IMPERIAL COLLEGE LONDON
UNIVERSITY OF LONDON

A STUDY OF CURVATURE EFFECTS ON GUIDED ELASTIC WAVES

by

Ka Lok Jimmy Fong

A thesis submitted to the University of London for the degree of
Doctor of Philosophy

Department of Mechanical Engineering
Imperial College London
London SW7 2BX

October 2005

Abstract

Long range guided wave inspection of large engineering structures has been proven to be very effective. However, there are still many aspects of the guided wave behaviour which remain unknown. One of these aspects is the curvature effect which can substantially change the physical properties of the guided wave mode, especially in a leaky system where limiting the extent of energy radiation into the surrounding medium is critical for successful inspection.

This thesis examines the curvature effect on the guided wave properties using a 2-D curved plate system. Both unloaded and loaded cases are investigated systematically. Model studies comprise exact and asymptotic analyses, including investigations of their limits.

The curvature effect in an unloaded case is examined by comparing the phase velocity and the displacement mode shapes of fundamental modes between a straight case and curved cases of various curvature radii, at all frequencies. The percentage difference of these properties due to the curvature effect is found to increase exponentially with an increase in radius, and is frequency dependent. This provides a graphical tool to pick the best frequency at which the properties are least affected by the curvature. Results of Finite Element (FE) modelling and experiment prove the validity of the analytical predictions.

For the loaded case (leaky case), the analytical solution is substantially more complicated, partly due to the fact that the numerical calculations of the Bessel functions with a complex order are hard to implement. The solutions produce the dispersion relation of phase velocity and attenuation of an embedded curved plate system. The distribution of energy, determining the amount of coupling between the guiding layer and the surrounding medium, can be obtained, and can also be related to the changes of attenuation in a particular mode when the plate is curved. Experimental and FE validations are provided.

Acknowledgments

First and foremost, I would like to express my deepest gratitude to my supervisors Dr. Mike Lowe and Professor Peter Cawley for their inestimable guidance, and for offering me a PhD position within the well organised Non-destructive Testing Lab.

I would also like to thank my project collaborators, Professor Richard Craster, Dr. Dmitri Gridin and Mr. Alex Adamou, without whom the completion of this project would not have been possible. They have given me an insight into the world of mathematicians, and have dispelled some jokes regarding Engineers and Mathematicians.

My heartfelt thanks also goes to all my colleagues in the NDT group at Imperial College, in particular Thomas Vogt, Francesco Simonetti and Daniel Hesse, for their invaluable input during our numerous discussions, and for creating a such friendly working environment.

Not forgetting my parents and my sister who toiled through the years to give me the opportunity to study overseas, I thank you from the bottom of my heart. Last but not least, June, thank you for supporting me emotionally and mentally over the past years and giving me the strength and determination to produce my best works so far.

This work was funded by the EPSRC.

Contents

List of Figures

List of Tables

Chapter 1

Introduction

1.1 Motivation

Adequate roof support systems in underground coal mines are of vital importance to both the safety and productivity of the mining operation. Since the 1960s, a rockbolt technique to reinforce the roof in roadways and caverns in mines has become very popular [1].

The rockbolts are ribbed steel bars that are designed to stop and stabilise the rock movements, and therefore can be constantly subjected to a high level of stress, especially at locations where the surrounding rocks begin to fracture. As a result, regular inspections of the rockbolts are essential to ensure their integrity. Possible problems are fracture, severe bending distortion by rock movement, stress corrosion cracking, and loss of bonding between the bolt and the rock, all of which can lead to unsafe roof conditions threatening both personnel safety and production capacity.

A technique, based on a time response method using guided waves, has been developed by Beard [2, 3] to inspect the rockbolts. Guided waves are undoubtedly one of the most efficient Non-Destructive Evaluation (NDE) concepts to inspect and monitor elongated structures. The guided wave inspection is straightforward and is based on ultrasonic elastic waves that are excited at one location on the structure and propagate along its length. Any subsequent echoes can indicate the presence of defects and/or other discontinuities. For the rockbolt inspection, the setup is illustrated in Fig. 1.1.

A good understanding of the wave propagation properties for the specific structure, the embedded rockbolt in this case, is the key to any successful inspection using guided waves. There are many different wave modes which can propagate at different speeds, and they are, in general, frequency-dependent. These properties are usually calculated numerically and expressed in the form of frequency dependent dispersion curves for all the propagating

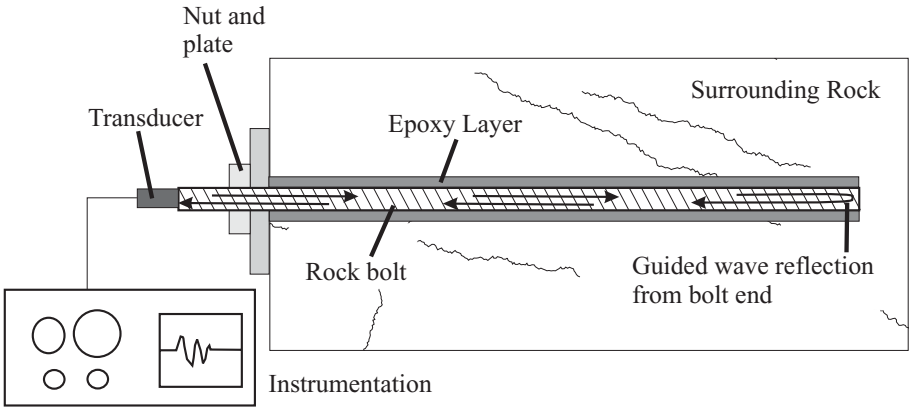

Figure 1.1: Schematic diagram of the experimental setup for the rockbolt inspection (after Beard [3]).

wave modes of the system, presenting phase velocities, group velocities and also attenuations in the case of a leaky system such as the rockbolt embedded in rock (Fig. 1.1). A leaky system is coupled with an infinite half space that the energy leaks into as the wave modes travel along the guiding medium.

The dispersion curves can provide vital information for choosing the most appropriate type of wave mode and frequency to achieve optimal excitation and propagation conditions for the inspection; in this case the key goals are long-range propagation without excessive attenuation and a good detectability of defects. In addition, the dispersion curves are very important to the post processing of the inspection results, from which the defects and other features of the structure can be identified, located and sized.

One major challenge for the rockbolt inspection is to achieve a good signal to noise ratio by minimising the radiation of the propagation energy into the surrounding rock. Wave modes are chosen at frequencies where the energy is concentrated at the core of the rockbolt [4]. This is to minimise the amount of energy at the interface between the bar surface and the surrounding medium, hence limiting the amount of attenuation due to the energy leakage.

The dispersion curves for the rockbolt have so far been calculated based on cylindrical waves propagating along a perfectly straight path (see for example Auld [5]). In reality, many of the rockbolts may be bent along their length by the external forces that are applied by movements of the rock layers, after they have been used for a period of time. These curvatures along the length of the rockbolt are usually sufficiently small that they have an insignificant effect on the wave propagation properties. However, the curvatures can be critical when the rock movements are severe and the prediction of the straight case can no longer correctly represent the curved case.

Beard [2] found that the wave modes, at a frequency thought to be optimum when the rockbolt is straight, undergo a mode conversion where the energy distribution in the cross

section shifts towards the surface close to either the inner or the outer radius of the curvature after the rockbolt is curved. This allows a greater coupling at the metal/rock interface, resulting in a higher amount of leakage as the wave propagates, and consequently the signal to noise ratio can become very low such that an inspection using the selected wave mode can no longer be possible. Therefore depending on this condition of detectability, a bend along the propagation direction can be categorised into either critical or non-critical. Fig. 1.2 shows a photograph of a rockbolt that was removed from the mine after being used for many years; the bolt has several bend sections including those of critical and non-critical natures. Currently, there is very poor understanding of the nature of the wave propagation around these bends.

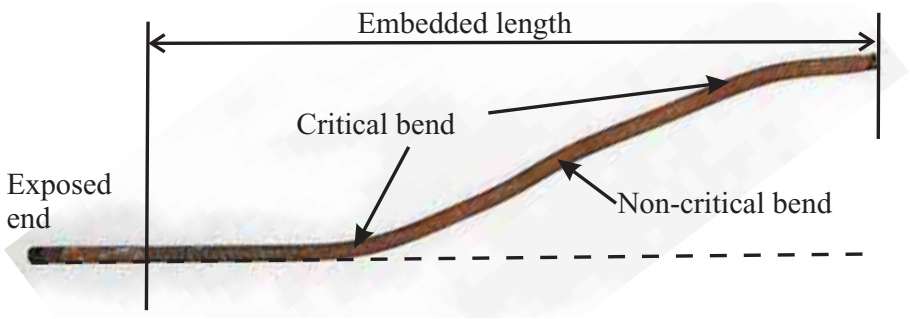

Figure 1.2: Photograph of a rockbolt extracted from a mine after being critically bent by the surrounding rock movements.

This curved rockbolt problem constitutes the motivation of the investigation in this thesis, of which the objective is to gain insight into the curvature effect on the propagation properties. This particular geometry for the curved rockbolt problem is complex because of double curvatures: the rockbolt is circular in section and is then curved also in the plane of bending. As a result, there has been relatively little research on such curved cylindrical geometries. A historical development of research in curved cylindrical geometries is presented in the next section.

There is much similarity of wave behaviour in plates and bars, therefore it has been shown by Beard [2] that it is possible to make inferences about wave behaviour in bars from the study of wave behaviour in a simpler 2-dimensional plate system. There have been some limited studies of the curvature effect recently by Beard [2], Wilcox [6] and Valle *et al.* [7], all of which have used plate structures for their studies. However, these studies do not address leaky problems which are fundamental to any potential guided wave applications in embedded structures, and nor do they present any result in the region where the frequency and "curvature radius to thickness ratio" are high. This is due to the fact that the analytical solution can be unstable in these regions. This thesis aims to exploit and extend on their ideas to resolve these omissions.

1.2 Properties of Waves in Plates, Pipes and Bars

The basic concept of guided waves is based on the acoustic plane waves (also known as bulk waves) of the material, propagating along a medium that is bounded by the regular boundaries of the structure. The acoustic plane waves are of either compressional or shear nature; in combination, they form specific types of frequency-dependent wave motions, with their own individual propagation properties, for the corresponding structural geometry. These wave modes have increasingly complex mode shapes with increasing frequency, and they only exist beyond their cut-off frequencies. The frequency dependence of these wave modes can be modelled analytically with dispersion curves, showing, for example, the phase velocity and group velocity.

The common geometries, for which the guided wave inspection technique has been used, are plates, pipes and bars. In each of the three cases, the wave motions can be categorised into families of wave modes according to their propagation nature. It is worth noting that pipes and bars have a similar geometry, and thus share the same families of wave modes.

For plates, the wave modes are either symmetric and antisymmetric along the mid-plane through the thickness, which is the characteristic used to group them into the corresponding families. For bars or pipes, the wave modes are, in general, divided into three families, namely the longitudinal modes: a purely axially symmetric wave motion, the flexural modes: an asymmetric mode involving a bending motion along the propagation direction, and the torsional mode: a twisting motion along the centre axis. The category of families for plates and pipes are illustrated in Figs. 1.3 and 1.4, of which the deformed mode shapes of the wave motions for each family of the geometry type are shown.

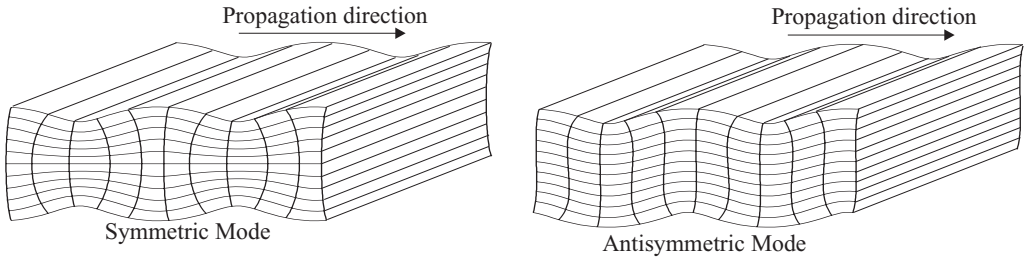

Figure 1.3: Families of wave motions of guided waves in plates (Diagram generated using Disperse [148]).

1.3 Background on Guided Waves in Curved Beams

An analytical model to predict the properties of guided waves is one of the fundamental needs when developing methods for guided wave inspection, as mentioned before. The

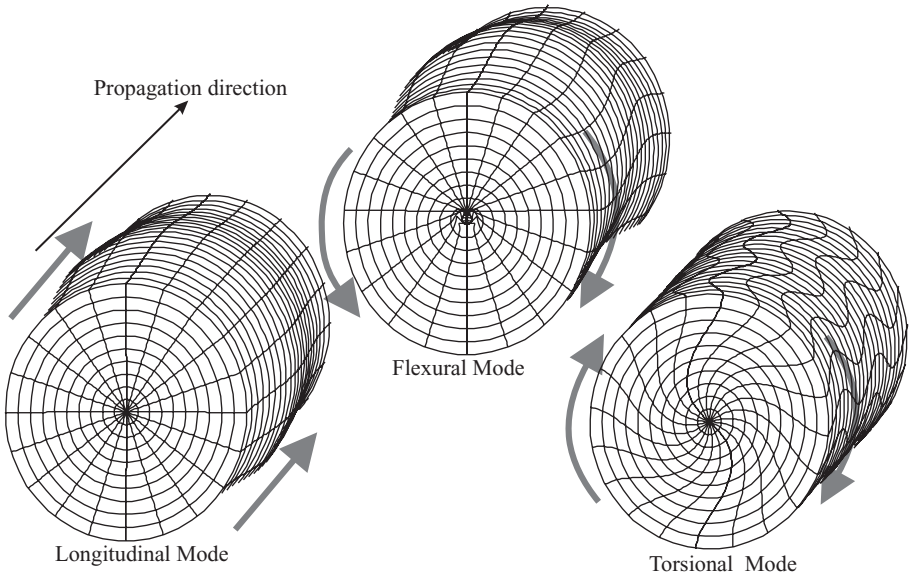

Figure 1.4: Families of wave motions of guided waves in bars/pipes (Diagram generated using Disperse [148]).The thick arrows indicate the general directions of particle movements in one instance corresponding to a particular wave family.

development of analytical models has spanned over more than a century and has included a wide variety of problems, ranging from the guided wave propagation in isotropic plates [8, 9, 10, 11, 12] and cylindrical structures [13, 14, 15, 16, 17], to those with additional complexities, such as multi-layered structures [18, 19, 20, 21, 22, 23], anisotropy of materials [24, 25, 26, 27, 28] and leaky wave problems [29, 30, 31].

Mathematically, all of these different cases are governed by the same set of partial differential equations, also called the wave equations, describing the behaviour of the waves in a 3-dimensional space. The only difference between these cases is the boundary conditions, and it is the introduction of these boundary conditions that makes the analytical solution difficult. The majority of the above studies have used an elegant classical partial waves technique to obtain modal solutions of guided waves in many structures with a simple cross section geometry; the partial waves technique decomposes the coupled partial differential equations into separable equations in terms of the shear and longitudinal partial wave potentials (see for example Achenbach [32] or Auld [33]).

The studies of propagation in curvilinear beam waveguides are difficult, and mathematical models developed to date are still incomplete and complicated. These studies can be roughly divided into two different branches concerning acoustic and elastic wave propagations. They correspond to many day to day physical applications such as the sound wave propagation in musical instruments and impact testing of structures with such curved geometry.

1.3.1 Acoustic Waveguides

Acoustic waveguides can be purely longitudinal in which the particle motion in the acoustic medium is polarised in the propagation direction, or purely shear in which the particle motion in the acoustic medium is polarised in the direction that is perpendicular to the propagation direction. Here it commonly refers to those wave modes that travel in a fluid medium where only the longitudinal motion is supported.

In 1957, Waldron [34] derived a set of general equations to describe the particle movements along a curved acoustic line. Later, Grigor'yan [35] extended on Waldron's idea to include acoustic propagation in an infinitely long bend with a rectangular cross-section. In addition, he demonstrated the acoustical field line diagram in the bent sections. In the earlier studies of curvilinear waveguides, the cross-section was confined to a rectangular shape. This is partly because their governing equations are separable, and thus can readily be solved.

In 1971, Rostafinski [36] successfully treated the acoustical problem of a curved rectangular section joined to a straight section. He theoretically investigated the acoustic velocity distribution of propagating and non-propagating modes in curved bends and presented a method for determining the non-propagating modes generated at discontinuities. However, his solutions were limited to very low frequencies. Subsequent study by Osborne [37] produced solutions for the higher order modes of the same geometry as Rostafinski's study.

The first experimental study of a curved acoustic waveguide with a rectangular cross section was carried out by Cummings [38] in 1974. In the same publication, Cummings derived the principle governing equations for a curved circular section acoustic waveguide in toroidal co-ordinates. However, toroidal co-ordinates, which are required to suit the boundary conditions of a circular section curved geometry, is not one of the eleven co-ordinate systems in which the governing wave equations are amenable to separable solutions, and thus cannot be solved directly. (Details of the separability of differential equations can be found in, for example, Morse and Feshbach [39], pp. 665-666). Cummings did not produce any solutions to the circular section curved problem which remained a stumbling block to progress for a long time. Other studies on various aspects of sound propagation in rectangular curved waveguides were also conducted [40, 41].

In 1983, Keefe *et al.* [42] was the first to attempt to address the toroidal problem by approximating the circular cross-section with appropriate sizes of rectangular slices stacked on top of each other. This was a very crude model, therefore it is not surprising that a high percentage of error was recorded. In the same year, Ting *et al.* [43] investigated the problem of the same toroidal geometry using a perturbation method where the results was solved asymptotically to the straight case, and the solution were therefore limited to cases

of slight curvature.

Recently, a sequence of publications by Félix *et al.* using multimodal analysis [44, 45, 46] produced the most promising solutions for analysing the acoustical characteristics in a bent pipe. The solutions allow calculations of steady and dynamic (transient) problems, including any kind of discontinuities. In addition, the reflection and transmission coefficients at the entrance and exit of the bend have also been studied.

1.3.2 Elastic Waveguides

Elastic waveguides transmit wave propagations in an elastic medium supporting both the longitudinal and/or shear wave motions that are coupled together. As expected, there have been substantially fewer studies on elastic curved waveguides than on acoustic curved waveguides because of the difficulty in obtaining the exact frequency dependent characteristic solutions. Any analysis has thus had to rely heavily on approximation approaches.

In 1960, Morley [47] derived a Timoshenko-like theory for the propagation of flexural elastic waves in an infinite curved rod. Morley's model included both the rotary inertia and radial shear deformation about the neutral axis as in the Timoshenko theory. However, the model is only valid for rods with a slight curvature, allowing the extension of the neutral axis to be neglected, and the governing equations can then be simplified significantly. In 1974, Crowley *et al.* [48] adapted from Morley's Timoshenko theory to study the propagation of light in a rectangular cross-section beam. The study involves numerical simulation of the fringe pattern generated by a continuous wave, which was then compared to one obtained experimentally from a transmitted light isochromatic technique, but strictly speaking, this should be regarded as an acoustic problem.

In 1966, Witrick [49] investigated elastic wave propagation in a helical spring using the same theory containing a small curvature, where he measured and identified two different velocities corresponding to the bending and the torsional elastic wave modes.

Subsequently, Britton *et al.* [50] put forward an approximate theory for longitudinal elastic waves in circular rings and helical springs. They have drawn a conclusion that a completely different approximate theory is required for each type of propagation (i.e. longitudinal, torsional and flexural). Frequency dependent dispersion curves for these fundamental types of modes were presented. Nevertheless, approximate theories, such as the Timoshenko theory, are subject to assumptions and can only accurately describe the behaviour of the few lowest order modes where the distribution of the motion in the cross-section is relatively simple. Some experimental validations were also produced in their late paper in 1971 [51], where short duration, wide band pulses were sent along a helical spring.

A similar experiment to investigate the distortion of longitudinal square pulses in slightly curved elastic rods was also performed by Hsieh *et al.* [52]. This was validated with results obtained from an elementary theory where the rotary inertia and radial shear deformation are neglected. Hsieh *et al.* demonstrated that a good agreement can be obtained when the wavelength of the pulse is large compared to the curvature of the rod, and thus all bending effects may be neglected. Then Bryan Moodie *et al.* [53] offered comparisons of several mathematical techniques to solve the elementary theory.

The immense difficulty in producing such solutions have deterred many researchers from considering this topic. Since Crowley's study, the author is not aware of any publication regarding this topic until a paper by Wu *et al.* [54] in 1996. Wu *et al.* derived the "non-trivial" characteristic equations for a bent bar. Although these equations were never solved in their publication, attention was paid to the calculation of the energy carried by wave modes that are reflected or transmitted at the bend. Nevertheless, a heavy assumption that the curvature radius goes to infinity was made to obtain solutions of the energy field in an uncoupled form. Both smooth and sharp bends were investigated, and experimental validations were carried out in a sequel paper [55]; carbon steel bars were bent at various curvatures, while strain that can be linked to the energy around the circumference was measured using diametrically opposite strain gauges.

Although the development of guided wave techniques to carry out long range inspection for structures, such as pipelines and rockbolts, has advanced rapidly in the past two decades [56], there are still many problems to be solved, one of which is the curvature effect. Demma *et al.* [57] examined the mode conversion phenomenon of the fundamental pipe modes at the straight/bend interfaces numerically and experimentally. Later, they [58] extracted the dispersion curves for a bent pipe in vacuum using a finite element toroid model; the dispersion curves and the characteristic mode shapes were subsequently compared with the straight case.

Recently, a new branch of guided waves, concerning quantum particles that propagate in nanoscale structures, such as thin wires, has attracted much attention. This has been driven by the race in the semiconductor industry to achieve a faster computer processor or other IC chips, where the electrons are transported between one component and the next in a confining potential. Waves of this kind of propagation through a curved wire have just been studied [59, 60] using an effective one-dimensional equation which can subsequently match the solutions of the three-dimensional waveguide case. The wave functions are constructed using a method similar to the multimodal technique which can be easily solved as an eigen-problem.

1.4 Project Collaborators

It is well known that the governing wave equations of a guided wave problem may be solved using a variety of mathematical approximation methods such as the Normal Mode Theory [61, 5], asymptotic method [62, 63], ray theory [64], JWKB expansion theory [65] and spectral method [66, 67]. Although, all of these methods can substantially simplify the numerical solutions of the problem, and thus may resolve the inseparable equations in toroidal co-ordinates, they are often based on heavy assumptions which may limit the solutions to specific conditions.

Due to the mathematical complexity in these alternative methods, it was decided in the beginning that great benefits would be gained from a close collaboration with Dr. Dmitri Gridin, Prof. Richard Craster and Mr. Alexander Adamou of the Mathematics Department at Imperial College London. This collaborative project was funded by the Engineering and Physical Science Research Council (EPSRC) [68]. This has provided a framework in which ideas have been exchanged regularly in many useful meetings to try to tackle the difficult mathematical problems. Some of the results obtained by the mathematics collaborators are included in summary form in this thesis, and wherever this is done, it is clearly identified as their work. Elsewhere, unless stated otherwise, all of the work in this thesis is the author's own. The followings are the list of publications as an outcome of this project by the collaborators:

D. Gridin, R.V. Craster, J. Fong, M.J.S. Lowe and M. Beard, "The high-frequency asymptotic analysis of guided waves in a circular elastic annulus", Wave Motion **38**, 67-90 (2003).

D. Gridin and R.V. Craster, "Quasi-modes of a weakly curved waveguide", Proceeding of Royal Society London, series A, **459**, 2909-2931 (2003).

D. Gridin and R.V. Craster, "Lamb-modes in curved plates", Proceeding of Royal Society London, series A, **460**, 1831-1847 (2004).

A.T.I. Adamou and R.V. Craster, "Spectral methods for modelling guided waves in elastic media", The Journal of the Acoustical Society of America **116**(3), 1524-1535 (2004).

D. Gridin, A.T.I. Adamou and R.V. Craster, "Electronic eigenstates in quantum rings: Asymptotics and numerics", Physical Review B **69**, 155317 (2004).

D. Gridin, R.V. Craster and A.T.I. Adamou, "Trapped modes in curved elastic plates", submitted to Proceeding of Royal Society London, series A, in 2004.

The list of publications by the author can be found at the end of this thesis.

1.5 Outline of Thesis

This thesis studies the significance of the curvature effect in the propagation direction on the properties of the guided waves. The study has been carried out in a systematic approach of several steps, with an ultimate aim to gain insight into the leaky curved problem using a plate structure. Each of these steps describes a different aspect of the problem and constitutes roughly a chapter in the thesis in the following way.

In chapter 1, subsequent to an introductory remark for this investigation, a literature review on the wave propagations in curved beam structures, both acoustic and elastic waveguides, has been presented. This gives the historical background of waveguides in a curved beam, and details the difficulties of obtaining precise analytical solutions to the behaviour of the wave modes in such problems. These difficulties would also justify the use of plate structures initially to study the curvature effect, instead of starting out with the more complex cylindrical structures.

Chapter 2 reviews the circumferential guided waves in an unloaded curved plate and their engineering applications. Subsequently, the foundation theoretical concept of the dispersion relations of the circumferential waves in an unloaded plate is summarised, and the essential notations are introduced. Although, the analytical solution for these dispersion relations is well documented, numerical instabilities have prevented the calculation of solutions when the product of frequency and radius is large. A detailed study of these instabilities is presented. The dispersion curves were traced numerically using a scheme implemented in Matlab, for which the key steps are outlined.

The instability problem of the analytical solutions can be overcome using three asymptotic methods which were derived by our collaborators. The theory of these asymptotic methods has been published in a joint paper [63]. In first part of the Chapter 3, the equations of the asymptotic methods are summarised. Subsequently, in the second part of this chapter, the author studies numerical examples of these methods, while the accuracy and robustness of each of the asymptotic methods is investigated. However, the studies are limited to the lower order wave modes existing in the guiding system as they are fundamental to the calculation of the curvature effect in the later chapters.

In chapter 4, using the analytical solutions presented in the previous chapter, the curvature effect on the frequency dependent phase velocity of the fundamental modes in an unloaded plate is investigated. Since the dynamic interaction of the incident mode and the defect/discontinuity is vital to an inspection, we then examine how the curvature affects the through-thickness displacement distribution. A quantitative comparison between the phase velocities and the mode shapes of the propagating modes is also made.

Chapter 5 is divided into two separate parts, introducing numerical and experimental

techniques which were used to validate the analytical prediction of the curvature effect of an unloaded case. For the experimental part, a modification of the analytical model is presented; the modification was necessary to correctly represent the "real" situation of the experiment, and thus to enable experiment and model results to be compared.

A review of the existing studies of leaky circumferential waves is given in chapter 6. The exact analytical solution is extended to include the leaky curved plate cases. The routine to trace the dispersion curves for these cases is developed, and it is more difficult because of the complex roots. Using the analytical solutions, the prediction of the curvature effect on the frequency dependent attenuation of the fundamental modes is obtained.

In chapter 7, the curvature effect on the attenuation of the wave modes in a loaded coupled plate case is validated experimentally and by finite element modelling. An immersed pipe experimental technique is proposed for the validation, and the results are explained.

Lastly, the concluding remarks are presented in the final chapter.

Chapter 2

Circumferential Guided Waves in Unloaded Plates

The effect of curvature along the propagation direction on guided wave properties can be studied initially using plate structures in plane strain (2-D). This provides a sensible alternative to 3-D beam structures because of the relative simplicity in obtaining the analytical solutions. The aim of this chapter is to provide the underlying analytical theory, from which the frequency dependent (dispersive) propagation characteristics of wave modes in a curved plate are calculated. The characteristic solutions can be numerically evaluated, although they are unstable in certain combinations of input parameters. A detailed study is also presented to investigate the circumstances in which these analytical solutions become unstable.

2.1 Background

This section reviews the historical development of circumferential guided waves, and their use in engineering applications.

2.1.1 Historical Background on Circumferential Waves

The study of waves propagating in the circumferential direction of a structure can be traced back to as early as the 1920s, mainly inspired by the field of seismology. Researchers such as Sezawa investigated the earthquake phenomena of surface waves propagating along the slightly curved earth surface in both cylindrical [69] and spherical [70] coordinates.

In 1958, Viktorov [71] formulated the fundamental theory for the Rayleigh wave that

propagates on both convex and concave cylindrical surfaces. He derived and solved the governing differential equations, and introduced the concept of angular wavenumber. Subsequently, in 1964, Keller *et al.* [72] used a first-order asymptotic approximation of the "geometrical theory" to construct the surface wave field at high frequencies, however, the effect of dispersion was not taken into account. In addition to the Rayleigh wave, there are other modes of surface waves that are confined to propagating near curved boundaries. One of these modes is the "whispering gallery" wave mode, which was studied by Brekhovskikh [73] in 1968. The mode was named after the whispering-gallery phenomenon in large circular buildings such as St. Paul Cathedral, London, where the mode was first discovered. In addition, there exist many more studies on curved surface waveguides since the 1960s, concerning a wide spectrum of fields [74, 35, 75] which cover elasticity, electromagnetics, hydrodynamics, optics and other fields.

In 1962, Horton *et al.* [76] were the first to demonstrate experimentally that circumferential waves can exist in an aluminium cylinder. Subsequently, the first mathematical theory for the Lamb-type elastic waves travelling around a solid cylinder was derived by Viktorov [77] in 1963. Later, in a letter to the Journal of the Acoustical Society of America, Grace *et al.* [78] attempted to extend on Viktorov's work to include the attenuation due to the leakage of energy as the waves propagate around the circumference of an immersed pipe. However, the complex parameter which was used to account for the attenuation decay is thought to be incorrectly used. The reason for such mistake will be explained in detail later in Ch. 6.

Recently, Viktorov's work was revised by Qu *et al.* [79] and Liu *et al.* [80], both of whom introduced non-dimensional parameters to the formulations. One obvious advantage for using these parameters is that the dispersion curves could be used universally for structures with the same material properties and "thickness to radius" ratio. In 1999, Valle *et al.* [7] utilised these formulae to model multilayered solid cylindrical structures using continuous boundary conditions between layers. In the same year, Kley *et al.* [81] demonstrated experimentally the effectiveness of a technique to extract the dispersion curves for circumferential guided waves. The waves were generated by a laser-ultrasonic method in a two-layered cylinder. Subsequently, Maze *et al.* [82] used the same solution type to calculate for the case of fluid filled pipes.

Despite the formulae of the circumferential Shear Horizontal (SH) waves being simpler compared to those for the Lamb-type waves, the mathematical derivation of the characteristic function for circumferential SH waves was only published by Gridin *et al.* [63] in 2003, and later was also reported by Zhao *et al.* [83] in 2004.

The usage of composite materials has increased steadily in the past decade, driven primarily by substantial demands in the aerospace industry. As a result, research on circumferential waves in anisotropic composite multilayered structures has also been receiving

attention in recent years, in order to come up with a reliable fast inspection technique. Deriving from the classical elasticity theory, Towfighi *et al.* treated the problem of elastic waves in anisotropic cylindrical curved plates [84], and later for spherical curved plates [85]. In 1998, Babich *et al.* [86] formulated an explicit expression for the amplitude of a wave mode travelling along a curved inhomogeneous layer where the material properties vary through the thickness. Additionally, Sharma *et al.* [87] examined the wave propagations that are generated by the thermoelastic effect in a transversely isotropic curved plate.

2.1.2 Engineering Applications using circumferential guided waves

The general review by Chimenti [12], which focuses on guided wave inspection techniques for plates in particular, describes the developments in this area up to 1997. In addition to plates, elongated cylindrical structures, such as pipelines, can be inspected successfully using axially propagating cylindrical guided waves [56]. Guided wave techniques have the advantage of long range coverage, and only a small area needs to be exposed for excitation. However, an axially propagating guided wave technique is only for the screening of pipelines, and thus does not give definite information about defects.

Therefore for local detailed inspection, the axially propagating guided wave technique may not be applicable. In this case, conventional through-transmission ultrasound methods have been used to measure the local wall thickness losses, as shown in Fig. 2.1. Although this technique can pin-point the exact location and the severity of the defect accurately, it can be very time consuming, especially when the pipe diameter is large. Alternatively, guided waves propagating in the circumferential direction can potentially offer a robust option for inspecting these cases. Theoretically the technique can inspect the full circumference from a single point around the circumference of a structure, though this can only be achieved if the excitation frequency and the excitation mode are carefully chosen to obtain the best propagation characteristics.

Other than pipes, large curved metal plates are used in many engineering applications such as those used in the construction of the cylindrical shell of a large oil tank, as illustrated in Fig. 2.2. Techniques to inspect flat plates using Electro Magnetic Array Transducers (EMATs) have been well developed [88]. A similar technique may be easily adapted for inspecting the curved structures. Alers [89] considered using EMATs that are mounted either on the outer surface of the pipe or inside of the pipe via a 'pig' moving platform, to generate circumferentially propagating Rayleigh waves for the inspection. Subsequently, Hirao *et al.* [90] applied circumferential Shear Horizontal (SH) waves to inspect gas pipelines in a setup analogous to Alers'. In addition, pressure vessels can potentially be inspected using guided circumferential waves around the circumference.

The method is particularly attractive for the inspection of areas that are difficult to access such as directly above supports.

Figure 2.1: Photograph of a conventional point by point through-transmission inspection technique around a small diameter water pipe.

Figure 2.2: Photograph of a large oil tank that is assembled by many large slightly curved plates.

Nevertheless, applications using circumferential waves remain novel, where much of the work progressed merely over the past decade. In 1994, Nagy *et al.* [91] reported using circumferential creeping waves to detect radially grown fatigue cracks on the far side of so-called "weep" holes in thin airframe stiffeners, though the fuel contained in the wing must be drained before any inspection. Later, Hassan *et al.* [92] investigated the possibility of detecting these cracks in a fuel filled "weep" hole, and assessed the attenuation caused by the radiation of energy into the fluid.

In 1998, Cheeke *et al.* [93] instigated an intrinsic technique to sense the fluid level contained inside the pipe; the technique takes advantage of the sizeable difference in group velocity of the Lamb type circumferential waves between a filled and an empty pipe, Later, Li *et al.* [94] invented a method to detect fatigue cracks in complex components that are used in aging helicopters, such as the rotor hub, connecting links and pitch shaft. Subsequently, Valle *et al.* [95] and Qu *et al.* [96] demonstrated that radial cracks in an annular structure can be located and sized accurately using the Lamb-type circumferential guided waves.

Employing an optimisation process, Chen *et al.* [97] reported recently that the characteristic parameters, such as the elastic constants, thickness and curvature radius, can be measured using the low-frequency circumferential Lamb waves. This has a potential application of evaluating the characteristic parameters for thin layers of protective materials coated on the surface of pipelines.

2.2 Exact Theoretical Analysis of Circumferential Waves

A comprehensive version of the exact analytical characteristic formulae has been reported by Qu *et al.* [79]. In this section, these equations are modified by the introduction of new notations which are in-line with a recent publication [63], in such a way that they may be easily adapted for various situations with the appropriate boundary conditions (see Sec. 2.2.4); the equations are also consistent with those derived for the leaky cases in Ch. 6.

The approach for solution in the circumferential geometry is similar to that in the straight plate, where Bessel functions being used instead of exponential functions. The SH and Lamb-type circumferential wave solutions are entirely independent (uncoupled), therefore it is valid to treat them separately. Formulae for both the SH and Lamb-type circumferential waves are presented in this section.

2.2.1 Wave Equations

To study waves propagating circumferentially, a system of cylindrical co-ordinates, in the r, θ and z direction, is used throughout this thesis. A schematic diagram showing the cylindrical system is illustrated in Fig. 2.3. The governing mathematical equations of elastic wave propagation in a bulk material are well documented; these equations will be referred to as the wave equations (see for example Auld [5]). Previously, the wave equations expressed in cylindrical coordinates have also been studied extensively for wave propagations in the axial direction of a pipe [56]. The fundamental wave equations which

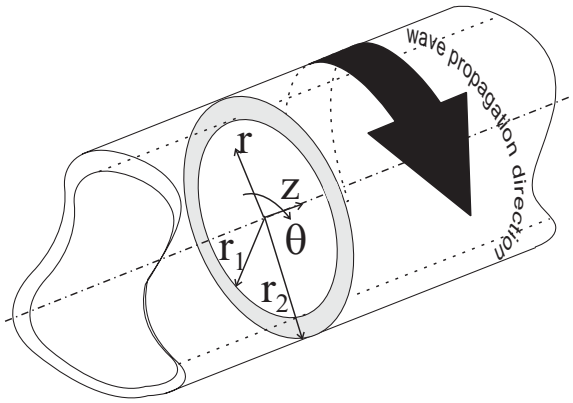

Figure 2.3: The geometry of the circumferential waves problem (after Wilcox [5]).

are not subject to any external body forces, are considered:

$$\rho\left(\frac{\partial^2 \bar{u}}{\partial t^2}\right) = \nabla \cdot \sigma_{ij}. \tag{2.1}$$

where $\bar{u} = (u_r, u_\theta, u_z)$ is the displacement vector in cylindrical coordinates, and ∇ is the divergence operator. Eqn. 2.1 may be expressed in term of non-tensor equations which are given in App. A.1. The Cauchy stress tensor σ_{ij} can be related to the strain tensor ε_{ij} by Hooke's law (Eqn. 2.2); and furthermore the strain tensor may be expressed in terms of the displacement vector, $\bar{u}$ (defined in App. A.2).

$$\sigma_{ij} = \lambda \delta_{ij} \phi + 2\mu \varepsilon_{ij}. \tag{2.2}$$

where δ_{ij} is the Kronecker delta which is equal to one for $i = j$ and is equal to zero for $i \neq j$, while dilatation $\phi = \varepsilon_{rr} + \varepsilon_{\theta\theta} + \varepsilon_{zz}$.

For circumferential propagation, the field in the elastic medium does not depend on the z direction, and therefore any z direction dependent terms are omitted. As a result, the displacement vector $\bar{u}$ is only a function of r and θ. Furthermore, the field is dependent on a time harmonic in the propagation direction, represented by $e^{-i\omega t}$, where ω is the angular frequency. In general, the time harmonic function is common to all field quantities and therefore is suppressed throughout the formulation. The displacement field may be reduced to the following form:

$$\bar{u}(r, \theta) = \bar{U}(r) e^{i\nu\theta}. \tag{2.3}$$

where ν is the angular wavenumber and $\bar{U}$ is the wave displacement amplitude along the radial line. For the non-attenuative problem considered in this chapter, both ν and ω are assumed to be purely real quantities. Although the model depicts a pipe structure

with waves propagating around its circumference, the circumferential continuity condition is not considered theoretically. The waves are assumed to propagate along an infinite circular cylinder, or along a cylindrical cavity of circular cross section in an infinite elastic medium. Therefore ν may vary between zero and infinity.

2.2.2 Shear Horizontal (SH) Circumferential Waves

SH circumferential waves propagate in the θ direction and are polarised in the z direction. The particle movements can be described by Eqn. A.3, corresponding to the equation of motion in an infinite medium in the z direction. Eqn. A.3 may be expressed in terms of the displacement in the SH direction, u_z, in the following form:

$$\left(\frac{\partial^2}{\partial r^2} + \frac{1}{r}\frac{\partial}{\partial r} + \frac{1}{r^2}\frac{\partial^2}{\partial \theta^2}\right)u_z + k_T^2 u_z = 0. \tag{2.4}$$

where $k_T = \omega/C_T$ is the bulk shear wavenumber, and C_T is the bulk shear velocity. Substituting the z component of Eqn. 2.3 into Eqn. 2.4 yields the following Bessel's differential equation for U_z:

$$(k_T r)^2 \frac{\partial^2 U_z}{\partial (k_T r)^2} + (k_T r)\frac{\partial U_z}{\partial (k_T r)} + ((k_T r)^2 - \nu^2)U_z = 0. \tag{2.5}$$

The general solutions of Eqn 2.5 may be satisfied by several combinations of Bessel functions, each of which represents the oscillatory behaviour of the shear partial bulk wave propagating towards and away from one point in the medium respectively. The three valid combinations are the normal Bessel functions (J and Y), the modified Bessel functions (I and K) and the Hankel functions ($H1$ and $H2$) which are linear combinations of normal Bessel functions of the first and second kinds. The general solution for U_z may be written in the following form:

$$U_z = a_1 W_\nu(k_T r) + a_2 Z_\nu(k_T r). \tag{2.6}$$

where W and Z are placeholders for the solutions of a Bessel equation (after Pavlakovic [14]), and may be substituted by any of the combinations discussed, and a_1 and a_2 are the unknown field constants for the incident and reflected shear partial bulk waves respectively.

2.2.3 Lamb-Type Circumferential Waves

The exact formulation of the fields in a Lamb-type problem is analogous to that of the SH waves. Particles of the circumferentially propagating Lamb-type waves polarise in

both the radial and circumferential directions (u_r and u_θ). Therefore two coupled waves equations in those directions, Eqn. A.1 and Eqn. A.2, are considered; the equations may be simplified by using the convenient Helmholtz decomposition technique. The technique separates the coupled equations in terms of two scalar potentials, φ and ψ, associated with the longitudinal and shear motions respectively. The displacement field of Eqn. 2.3 may be expressed as follows:

$$u_r = \frac{\partial \varphi}{\partial r} + \frac{1}{r}\frac{\partial \psi}{\partial \theta}, \qquad u_\theta = \frac{1}{r}\frac{\partial \varphi}{\partial \theta} - \frac{\partial \psi}{\partial r}. \tag{2.7}$$

And the equations of motion become two uncoupled Helmholtz equations:

$$\begin{aligned} &\left(\frac{\partial^2}{\partial r^2} + \frac{1}{r}\frac{\partial}{\partial r} + \frac{1}{r^2}\frac{\partial^2}{\partial \theta^2}\right)\varphi + k_L^2 \varphi = 0, \\ &\left(\frac{\partial^2}{\partial r^2} + \frac{1}{r}\frac{\partial}{\partial r} + \frac{1}{r^2}\frac{\partial^2}{\partial \theta^2}\right)\psi + k_T^2 \psi = 0. \end{aligned} \tag{2.8}$$

where $k_L = \omega/C_L$ and $k_T = \omega/C_T$ are the bulk longitudinal and shear wavenumbers respectively. C_L and C_T are the longitudinal and shear bulk velocities of the material, and may also be expressed in terms of the material properties, such as the Lamé constants (λ, μ) and the density (ρ):

$$C_L = \sqrt{\frac{\lambda + 2\mu}{\rho}}, \qquad C_T = \sqrt{\frac{\mu}{\rho}}. \tag{2.9}$$

The modal solutions of the potentials may be assumed as follows:

$$\varphi(r,\theta) = \Phi(r) e^{i\nu\theta}, \qquad \psi(r,\theta) = \Psi(r) e^{i\nu\theta}. \tag{2.10}$$

where $\Phi(r)$ and $\Psi(r)$ are the amplitude distributions of their corresponding modal solution across the plate thickness. Then substituting these modal representations into Eqn. 2.8, the wave equations may be rewritten for Φ and Ψ:

$$\begin{aligned} &(k_L r)^2 \frac{\partial^2 \Phi}{\partial (k_L r)^2} + (k_L r)\frac{\partial \Phi}{\partial (k_L r)} + ((k_L r)^2 - \nu^2)\Phi = 0, \\ &(k_T r)^2 \frac{\partial^2 \Psi}{\partial (k_T r)^2} + (k_T r)\frac{\partial \Psi}{\partial (k_T r)} + ((k_T r)^2 - \nu^2)\Psi = 0. \end{aligned} \tag{2.11}$$

where the first and second equations correspond to the longitudinal and transverse wave propagations in an infinite medium. As in the SH formulation, the general solutions of Equations 2.11 may be expressed with the Bessel function placeholders, W and Z:

$$\Phi = a_1 W_\nu(k_L r) + a_2 Z_\nu(k_L r), \qquad \Psi = a_3 W_\nu(k_T r) + a_4 Z_\nu(k_T r). \tag{2.12}$$

where a_{is}, with $i = \{1, 2, 3, 4\}$ are the unknown partial bulk wave amplitudes.

2.2.4 Boundary Conditions

The general solutions of the waves equations presented in the previous sections give the basis for calculating the SH and Lamb-type circumferential guided waves. The solutions are formulated in such a way that they can be easily adapted to form the characteristic functions of both non-attenuative and attenuative homogeneous cases provided that the appropriate boundary conditions are satisfied at the interfaces between different materials. The formulation of circumferential waves continues from the work started by Lowe [98] and Pavlakovic [14] for the plate and cylindrical guided waves respectively, therefore the interfaces considered are in-line with those considered by them; the interfaces considered are solid-solid, solid-vacuum, and solid-fluid. Only the non-attenuative cases are considered in this chapter, while the attenuative case of a leaky system will be presented in Ch. 6.

It is worth noting that only an ideal fluid, which does not support any shear wave propagation, is considered. In addition, only the boundary conditions that are relevant to the formation of the characteristic functions are summarised in this section. There should be an adequate number of conditions to set up a finite set of equations in the same unknown field amplitudes of which the common solutions in the frequency-wavenumber domain $(\omega - \nu)$ can be determined. Since SH waves have polarisation in the z direction and the fluid does not support any shear propagation, a slightly different boundary condition at the interfaces would have to be used compared to those used for the Lamb-type wave propagation. The boundary conditions for the SH waves are summarised in Tab. 2.1 where σ_{zr} is the tangential stress.

Interface types		
solid-vacuum	**solid^1-solid^2**	**solid-fluid**
$\sigma_{zr_{solid}} = 0\|_{r=a}$	$u_{z_{solid^1}} = u_{z_{solid^2}}\|_{r=a}$ $\sigma_{zr_{solid^1}} = \sigma_{zr_{solid^2}}\|_{r=a}$	$u_{z_{solid}} = 0\|_{r=a}$ $\sigma_{rr_{solid}} = 0\|_{r=a}$

Table 2.1: Boundary conditions for the circumferentially propagating SH waves at the interface, $r = a$, between two types of materials.

For the circumferential Lamb-type waves, all the field components are z independent, since there is no z direction polarisation in these waves. The four fields that are valid at these interfaces where the radius r is equal to a distance a, are the normal radial stress σ_{rr}, the tangential stress $\sigma_{r\theta}$, the radial displacement u_r, and the circumferential displacement u_θ. A summary of the boundary conditions for the Lamb case at various types of interface is shown in Tab. 2.2.

Interface types		
solid-vacuum	**solid^1-solid^2**	**solid-fluid**
$\sigma_{rr_{solid}} = 0\|_{r=a}$	$u_{r_{solid^1}} = u_{r_{solid^2}}\|_{r=a}$	$u_{r_{solid}} = u_{r_{fluid}}\|_{r=a}$
$\sigma_{r\theta_{solid}} = 0\|_{r=a}$	$u_{\theta_{solid^1}} = u_{\theta_{solid^2}}\|_{r=a}$	$\sigma_{rr_{solid}} = \sigma_{rr_{fluid}}\|_{r=a}$
	$\sigma_{rr_{solid^1}} = \sigma_{rr_{solid^2}}\|_{r=a}$	$\sigma_{r\theta_{solid}} = 0\|_{r=a}$
	$\sigma_{r\theta_{solid^1}} = \sigma_{r\theta_{solid^2}}\|_{r=a}$	

Table 2.2: Boundary conditions for the circumferentially propagating Lamb-type guided waves at the interface, $r = a$, between two types of material.

2.2.5 Characteristic Functions for an Unloaded Single Layer

The modelling of guided waves for a particular curvature of a single curved solid layer in vacuum is fairly simple. This involves satisfying the traction-free boundary conditions listed in the previous section with the general solutions for the specific types of propagation; the general solutions for the SH and Lamb-type waves are given in Eqn. 2.6 and Eqn. 2.12 respectively.

The choice of the combination of Bessel functions for these general solutions in the axially propagating cases has been studied extensively by Pavlakovic [14] who concluded that the right choice of Bessel functions could improve the numerical stability. However, for the circumferential case, the parameters used in the Bessel functions are very different, where the order of the functions are not necessarily integer and can be very large. In this case, there are little differences in the numerical stability when using various combinations of Bessel functions, therefore the normal Bessel functions (J and Y) will be used throughout this thesis for the general solutions of non-attenuative cases. On the other hand, for waves propagating along a layer that is coupled with an infinite half space where the energy leaks into the surrounding half-space medium and vanishes in distance, the solutions cannot be correctly represented by the normal Bessel functions. Further detail on this can be found in Sec. 6.2.

SH Circumferential Waves

The traction-free boundary conditions at the inner and outer surfaces for the SH waves can be reduced to:

$$\frac{\partial u_z}{\partial r} = 0; \qquad r = r_1, r_2. \tag{2.13}$$

This condition is known as the homogeneous Neumann boundary condition, which is also used in acoustic propagation problems. Substituting the general solutions into Eqn. 2.13

creates a homogeneous system of two equations:

$$a_1 J'_\nu(k_T r_1) + a_2 Y'_\nu(k_T r_1) = 0, \quad a_1 J'_\nu(k_T r_2) + a_2 Y'_\nu(k_T r_2) = 0. \tag{2.14}$$

Then the dispersion relation for the modal solutions can be simplified to the following elegant form:

$$J'_\nu(k_T r_1) Y'_\nu(k_T r_2) - J'_\nu(k_T r_2) Y'_\nu(k_T r_1) = 0. \tag{2.15}$$

For every frequency ω, there is a finite number of real roots ν of Eqn. 2.15, relating to the number of propagating modes. Substituting the root of a $\omega-\nu$ pair back into Eqn. 2.14, the field amplitudes a_1 and a_2 may be evaluated. The general through-thickness displacement field is subsequently obtained:

$$u_z(r,\theta) = U_z(r) e^{i\nu\theta} \propto \left\{ J_\nu(k_T r) - \frac{J'_\nu(k_T a)}{Y'_\nu(k_T a)} Y_\nu(k_T r) \right\} e^{i\nu\theta}. \tag{2.16}$$

Lamb-Type Circumferential Waves

Similarly, for the Lamb-type waves, the traction-free boundary conditions need to be satisfied in order to set up a characteristic function. First, the stresses σ_{rr} and $\sigma_{r\theta}$ have to be re-written in terms of the displacement potentials, φ and ψ (see Eqn. 2.17). This can be obtained by substituting the displacement field (Eqn. 2.7) into the strain tensor (Eqn. A.2), while the Hookes Law relation (Eqn. 2.2) is used to obtain the stress-strain relationship.

$$\begin{aligned} \sigma_{rr} &= -\lambda k_L^2 \varphi + 2\mu \left(\frac{\partial^2 \varphi}{\partial r^2} - \frac{1}{r^2}\frac{\partial \psi}{\partial \theta} + \frac{1}{r}\frac{\partial^2 \psi}{\partial r \partial \theta} \right), \\ \sigma_{r\theta} &= \mu \left(\frac{2}{r}\frac{\partial^2 \varphi}{\partial r \partial \theta} - \frac{2}{r^2}\frac{\partial \varphi}{\partial \theta} + \frac{1}{r^2}\frac{\partial^2 \psi}{\partial \theta^2} - \frac{\partial^2 \psi}{\partial r^2} + \frac{1}{r}\frac{\partial \psi}{\partial r} \right). \end{aligned} \tag{2.17}$$

By expressing the traction-free conditions at the inner and outer surfaces using Eqn. 2.17, a 4×4 homogeneous characteristic eigen-matrix for the 4 unknown field amplitude constants $\mathbf{a} = (a_1, a_2, a_3, a_4)^T$ is obtained:

$$D(\nu, \omega) \cdot \mathbf{a} = \mathbf{0}. \tag{2.18}$$

The eigen-matrix D is a function of the frequency ω and angular wavenumber ν. The roots of the characteristic eigen-matrix, given by the ω-ν pairs, can be evaluated when the determinant of the matrix, D, is set to zero. The elements of matrix D for the unloaded Lamb-type circumferential case are given in App. B. To solve for the unknown

amplitudes, **a**, as an eigenvector, one of these unknowns must be assumed as an arbitrary value. Subsequently, using the general solutions and Eqn. 2.7, the displacement fields can be rearranged as the following:

$$\begin{aligned} u_r(r,\theta) &= \left\{ a_1 k_L J'_\nu(k_L r) + a_2 k_L Y'_\nu(k_L r) + a_3 \frac{i\nu}{r} J_\nu(k_T r) + a_4 \frac{i\nu}{r} Y_\nu(k_T r) \right\} e^{i\nu\theta}, \\ u_\theta(r,\theta) &= \left\{ a_1 \frac{i\nu}{r} J_\nu(k_L r) + a_2 \frac{i\nu}{r} Y_\nu(k_L r) - a_3 k_T J'_\nu(k_T r) - a_4 k_T Y'_\nu(k_T r) \right\} e^{i\nu\theta}. \end{aligned} \tag{2.19}$$

2.3 Instabilities of Exact Analytical Solutions

With the derivations in the previous sections, dispersion curves for both the SH and Lamb-type cases may be calculated and traced numerically using the characteristic functions, Eqn. 2.15 and Eqn. 2.18 respectively. The computation requires finding of the roots in the $\omega - \nu$ domain. The root convergence is achieved using a bi-section iteration technique and together with a summary of the tracing routine, will be discussed later in Sec. 3.2.

One major problem with the exact analytical dispersion relation of the circumferential waves is that the solutions can become unstable numerically at high frequencies or when the curvature radius of the system is large. This instability is associated with the very large value of either, the elements of the characteristic function (Eqn. 2.18) or the determinant of D. An unavoidable numerical breakdown is results, where values above the machine precision being obtained. There are both upper and lower limits on the magnitude of floating point numbers in each computer. All computation was carried out in a commercial software, Matlab^{TM}, where all variables are defined using double precision that has an overflow limit of $\pm 1.79769313486232 \times 10^{308}$ and an underflow limit of $\pm 4.94065645841247 \times 10^{-324}$.

As an example, the dispersion curves of a 3mm thick and 20mm inner radius curved plate are plotted for the SH and Lamb-type circumferential waves in Figs. 2.4 and 2.5 respectively. The material used for this example is steel and has material properties of $C_L = 5960m/s$, $C_T = 3260m/s$ and $\rho = 7932kg/m^3$. It can be seen in these figures that no solution can be obtained in the higher-frequency region of the dispersion curves because of the numerical instabilities which are caused by two related circumstances.

2.3.1 "Large $f - d$" Problem

The first type of the instabilities is the "ill-conditioning" of the eigen-matrix characteristic function, D. It is also commonly known as the "large $f - d$" problem (f is frequency and d is the plate thickness), which has been studied comprehensively in the straight plate case by Lowe [98]. As the name has suggested, the characteristic functions become unstable

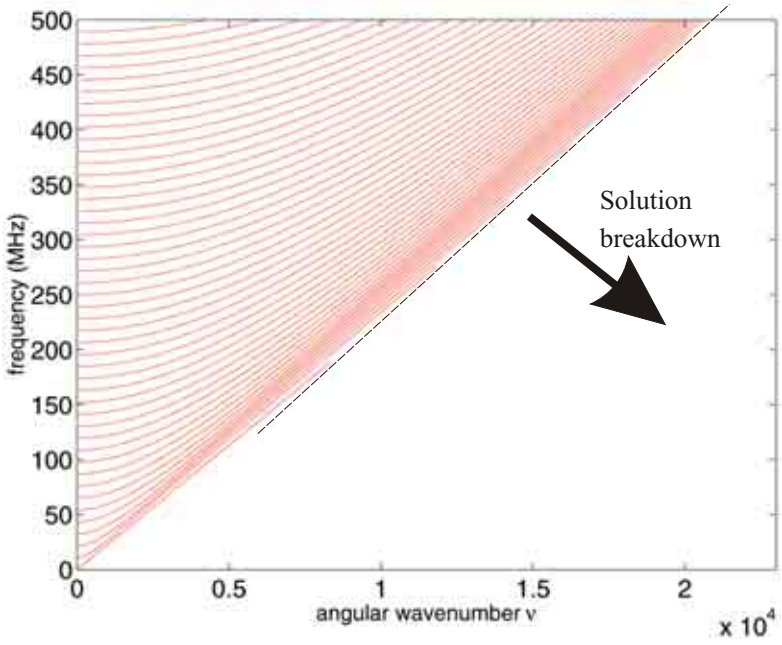

Figure 2.4: Every 20^{th} mode of the shear horizontal SH dispersion curves of a 3mm thick and 20mm inner radius steel curved plate.

when the combination of the frequency and thickness becomes very large. The "large $f - d$" problem is associated with the displacement decoupling of the inner and outer surfaces when the bulk partial waves become inhomogeneous (evanescent).

In the Lamb-type guided wave homogeneous system, the solution can be thought of as a superposition of 4 pairs of incident and reflected longitudinal and shear partial waves on both inner and outer surfaces. The natures of these partial waves are represented by the Bessel functions of the first and second kind (J and Y) with the arguments $\hat{\omega}_1$, $\hat{\omega}_2$, $\hat{\omega}_3$ and $\hat{\omega}_4$, which are defined as follows:

$$\hat{\omega}_1 = k_L r_1, \quad \hat{\omega}_2 = k_L r_2, \quad \hat{\omega}_3 = k_T r_1, \quad \hat{\omega}_4 = k_T r_2. \tag{2.20}$$

The amplitudes of these partial waves, $\mathbf{a}$, associated with a particular propagating wave mode can be determined by satisfying the boundary conditions at the inner and outer surfaces. Fig. 2.6 illustrates the partial waves concept for a curved plate system. Each type of partial waves strikes and reflects with the same angle from a normal radial line on both the inner and outer surfaces.

When both partial bulk waves on the same surface become inhomogeneous, the displacements and stresses of these modes at this surface begin to uncouple from the rest of the structure, as the energy decays exponentially away from that surface. This is what happens, for example, with the Rayleigh wave mode on a straight plate, when the solution transforms asymptotically from the A_0 and S_0 modes towards the Rayleigh mode at high

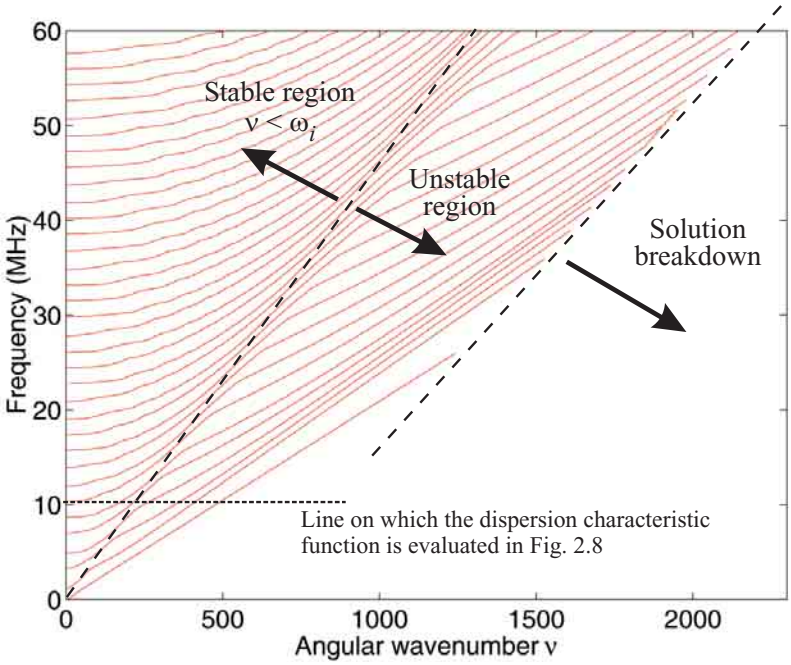

Figure 2.5: Every 5^{th} mode of the Lamb dispersion curves of a 3mm thick and 20mm inner radius steel curved plate.

frequencies. Unlike the symmetric boundary condition processed by the straight plate, a curved plate has different boundary conditions at the inner and outer surfaces due to the difference in curvature. It is worth stressing that as the frequency increases, each of these partial bulk waves become inhomogeneous sequentially. This results in the Rayleigh wave forming only on one surface at a time.

Once a partial wave in the system becomes inhomogeneous, elements in the solution matrix would have to adapt a combination of both decaying and growing coefficients in order to describe such decoupling behaviour, causing an ill-conditioning in the eigen-matrix D.

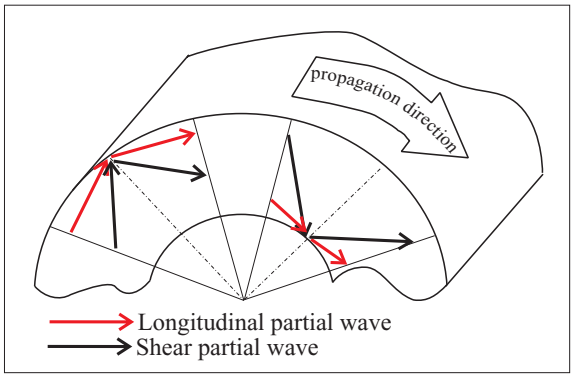

Figure 2.6: The concept of partial waves theory illustrating the uncoupled longitudinal and shear partial bulk waves at the inner and outer surfaces of a curved plate case.

In a strongly curved plate (i.e. the ratio thickness to radius is large), all propagating modes could become the surface Rayleigh-type waves at high frequencies (see Ch. 4). Fig. 2.7 demonstrates this asymmetry of the curved plate by comparing the through-thickness displacement mode shapes for the straight and curved cases for a plate of the same thickness. It can be clearly seen that the energy of the A_0 mode of the curved plate concentrates on the outer surface.

Thus the computation of the roots of a dispersion relation after any of the partial waves has become inhomogeneous, may be unstable. This area of stability can be illustrated in Fig. 2.8, where the dispersion function is evaluated at a constant frequency ω, and as a function of angular wavenumber ν, and corresponds to the calculation along the line shown in Fig. 2.5. It can be seen that the characteristic function has an oscillatory feature, where the zero crossings along the x-axis are the roots of the system. In the region $\nu < \omega_1$, the amplitude of these oscillations are more or less unvarying. In comparison, when $\nu > \omega_1$, one or more of the partial waves in the system would have become inhomogeneous; as a result, the amplitude of the function can become very large due to the "large $f-d$" problem, and may breakdown because of the large rounding error discussed before. Evaluating the roots in this region can be computationally expensive because of an increase in the number of iteration needed to obtain convergence.

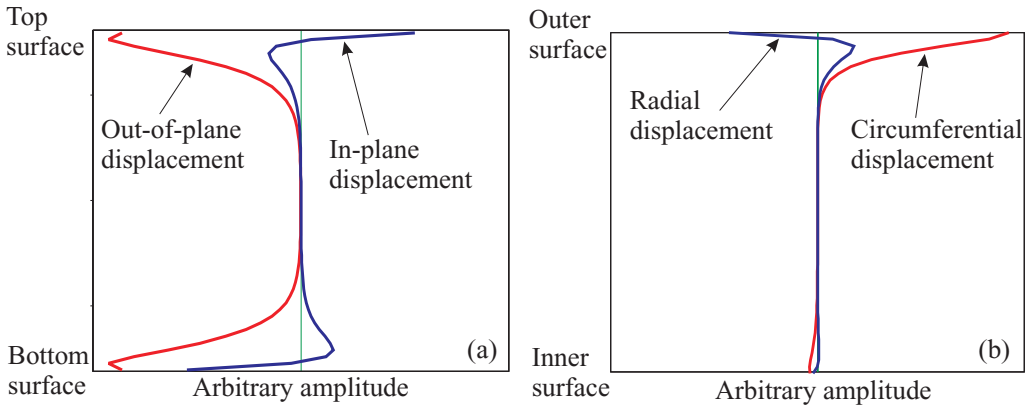

Figure 2.7: Displacement mode shapes of the A_0 mode at a frequency of 7MHz for (a) a straight steel plate, 3mm thick, and (b) a curved steel plate, 3mm thick and 20mm inner radius.

2.3.2 Breakdown of the Bessel Function

In addition to the "large $f-d$" problem, the second instability phenomenon is related to the breakdown of the Bessel functions contained within the eigen-matrix D of a curved plate system. this occurs when the argument is much larger than the order of the function [99]. The complicated Bessel functions offer unique solutions to the Bessel partial differential equations such as Eqn. 2.5. These equations appear in problems of vibrations, electric fields, heat conduction, fluid flow ...etc, in cylindrical geometry. Bessel functions of

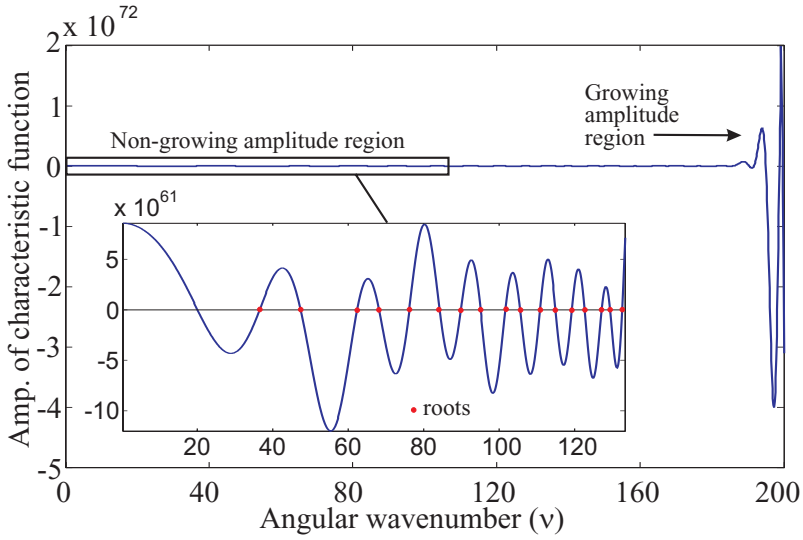

Figure 2.8: Lamb-type characteristic function calculated along the line shown in Fig. 2.5 for a curved steel plate, 3mm thick and 20mm inner radius. The frequency is kept constant at 10MHz

the first and second kind ($J_\gamma(x)$ and $Y_\gamma(x)$), and their derivatives, are used in forming the underlying dispersion relation equations (App. B), where γ and x are the order and argument of the Bessel functions respectively. Instability of the Bessel functions is a previously known problem and has been treated in much literature such as Abramowitz *et al.* [99] and Watson [100] using, for example, series expansions and several asymptotic expressions, but the accuracy of these schemes are generally conditional.

When $x > \gamma$, both $J_\gamma(x)$ and $Y_\gamma(x)$ functions have oscillatory profiles with a relatively low gradually changing amplitude, also the oscillation of the functions has a non-constant frequency, as shown in Fig. 2.9. On the contrary, when $x < \gamma$, $J_\gamma(x)$ has a zero value, while $Y_\gamma(x)$ grows exponentially. Therefore when the partial bulk waves in the Lamb-type case become inhomogeneous, i.e. $\nu < \omega_i$ with $i = \{1, 2, 3, 4\}$, the corresponding Bessel function of the second kind $Y_\nu(\omega_i)$ can become numerically very large.

This does not necessarily lead to an immediate solution breakdown once the order is larger than the argument of a Bessel function. As shown in Fig. 2.10, the Bessel function of the second kind remains computable in Matlab^{TM} even at a location of a high frequency value where the corresponding partial bulk wave has long turned inhomogeneous (i.e. when $\nu << \omega_i$). However, the amplitude of the Bessel function may eventually exceed the double precision limit at very high frequencies, corresponding to the spikes in Fig. 2.10 where the function may be evaluated but the result is inaccurate.

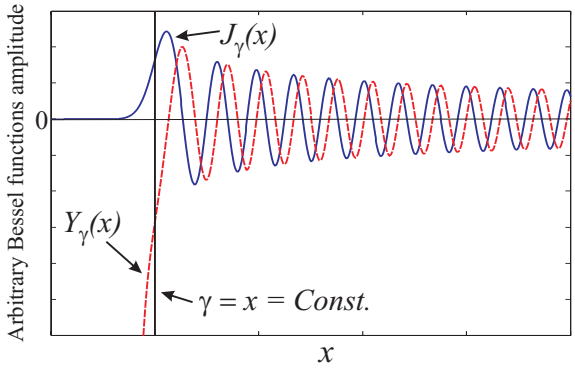

Figure 2.9: Amplitude of Bessel functions of the first $J_\gamma(x)$ and second $Y_\gamma(x)$ kind, with the argument γ assigned to be a constant. The $J_\gamma(x)$ and $Y_\gamma(x)$ are shown in solid and dotted lines respectively.

2.3.3 Comparison of the Two Instabilities

Although both the $Y_\gamma(x)$ and the "large f-d" problem could introduce instabilities to the numerical calculation of the characteristic functions at different frequencies, the fundamental causes of these breakdowns are evidently linked to the introduction of evanescent bulk partial waves in the solution. The order in which these two types of instabilities occur is dependent on both the geometrical and mechanical properties of the system. The only region where the solution is totally stable is where the partial waves in the system are completely homogeneous. Based on this observation, both the stable and unstable regions are indicated in Fig. 2.5.

The Bessel functions are the main building blocks of the characteristic eigen-matrix D, and are also used to describe the nature of the partial waves at the interfaces. Therefore analysing the absolute amplitude of the Bessel functions at a typical area of dispersion curves in the "$\omega - \nu$" domain can help us to visualise the causes of the two different types of instability.

Taking the first and last partial waves that become inhomogeneous for a particular mode with increasing frequency as an example, the absolute amplitude of their corresponding Bessel functions of the first and second kinds, with the arguments $\hat{\omega}_1$ and $\hat{\omega}_4$ respectively, are evaluated, as shown in Fig. 2.11. The Bessel functions of the first (J) and second kinds (Y) represent the decay rates of the incident and reflected partial wave amplitudes at the surfaces. The arguments of the Bessel function denote the type of partial wave and at which surface it is interacting, in such a way that the argument $\hat{\omega}_1 = k_L r_1$ correspond to the longitudinal partial wave at the inner surface, and the argument $\hat{\omega}_4 = k_T r_2$ correspond to the shear partial wave at the outer surface. A detail study of the partial wave analysis for this kind of system is presented in Sec. 3.1.4.

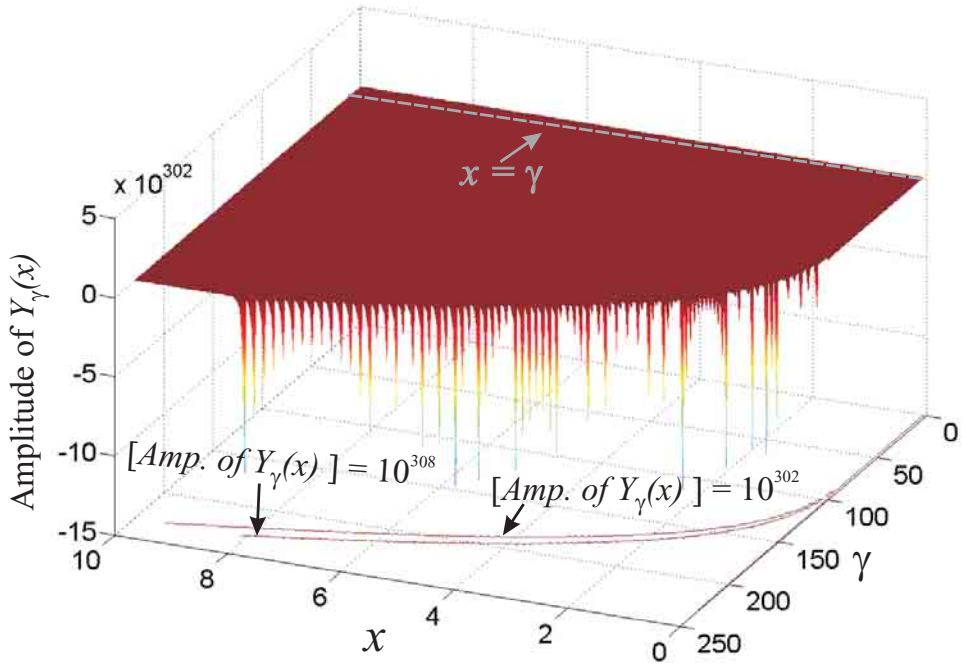

Figure 2.10: Three-dimensional plot of the second order Bessel function $Y_\gamma(x)$ evaluated using Matlab^{TM} around a numerically unstable region.

In addition, the lines $\nu = \hat{\omega}_i$ for i = {1,2,3,4} are plotted to indicate the positions where each of the partial waves transform from homogeneous to inhomogeneous. The plots are calculated for a 3mm thick and 20mm inner radius curved steel plate.

Fig. 2.11(a) shows the absolute amplitude of $Y_\nu(\hat{\omega}_1)$, where the amplitude on the left hand side of $\nu = \hat{\omega}_1$ remains moderate; whereas the amplitude on the right hand side of the line increases exponentially. Eventually the function breaks down at very high frequencies, covering a substantial area of the dispersion curves. The breakdown area of the Bessel function is indicated in white, and in grey if it is over an area of dispersion curves. It can also be seen that the width of this grey area increases with increasing frequency.

Additionally, the Bessel function of the second kind corresponds to the other partial waves, for instance the shear partial wave at the outer surface $Y_\nu(\hat{\omega}_4)$, shown in Fig. 2.11(c), has an amplitude which is typically much lower than that of $Y_\nu(\hat{\omega}_1)$. Furthermore, the numerical breakdown of $Y_\nu(\hat{\omega}_4)$ is almost always beyond the area of the dispersion curves. Therefore the precise reason of the Bessel function breakdown can actually be pinpointed to the breakdown of $Y_\nu(\hat{\omega}_1)$ of the system.

On the other hand, the "large $f - d$" problem is most likely to occur when $Y_\nu(\hat{\omega}_1)$ has a very high amplitude, indicated in Fig. 2.11(a), compared to amplitudes of other Bessel functions in the same locations. This creates an "ill-conditioning" of D. In this area, both $J_\nu(\hat{\omega}_1)$ (Fig. 2.11(b)) and $J_\nu(\hat{\omega}_2)$ have zero values, and therefore have no effect on

the "large $f-d$" problem; whereas $J_\nu(\hat{\omega}_3)$ and $J_\nu(\hat{\omega}_4)$ (Fig. 2.11(d)) can have very small absolute amplitudes in this area, especially where the partial waves are well coupled. As a result, the genuine cause of the "large $f-d$" problem is highly dependent on the relative difference in amplitudes between $Y_\nu(\hat{\omega}_1)$ and $J_\nu(\hat{\omega}_4)$.

In general, it can be said that, if the "d/r_1" ratio of the curved plate system is small, the solution should breakdown due to the instability of the Bessel functions before the "large f-d" problem becomes influential, and vice versa for a system with a large "d/r_1" ratio. This is because the argument of the Bessel function is a product of the frequency (ω), the radius (r_1, r_2) and the reciprocal of the bulk wave speeds (C_T^{-1}, C_L^{-1}), therefore increasing the radius would proportionally reduce the value of frequency at which the Bessel function breaks down. Numerical examples demonstrating this dependence will be presented later in Sec. 3.3.

2.4 Summary

An extensive literature review on the development and current engineering applications of the circumferentially propagating wave modes has been presented.

A theoretical analysis of waves propagating circumferentially in an unloaded plate has been studied. The formulae of the SH and Lamb-type wave modes have been summarised separately because of the difference in their polarisation directions. Then the fundamental formulae in each type of propagation have been generalised to model a multilayered curved plate structure, including both fluid and solid layers, by adapting the appropriate boundary conditions listed in Sec. 2.2.4. As an example, the derivation of the characteristic functions and other field quantities has been presented for an unloaded curved single layer.

Numerical solutions of the circumferential SH and Lamb-type modes can become unstable at high frequencies. Depending on the geometrical and mechanical properties, the exact solutions may be limited to low frequencies, especial those of the lower order modes. This instability stems from the well known "large $f-d$" problem and the breakdown of the Bessel function of the second kind $Y_\gamma(x)$, and has been discussed in detail.

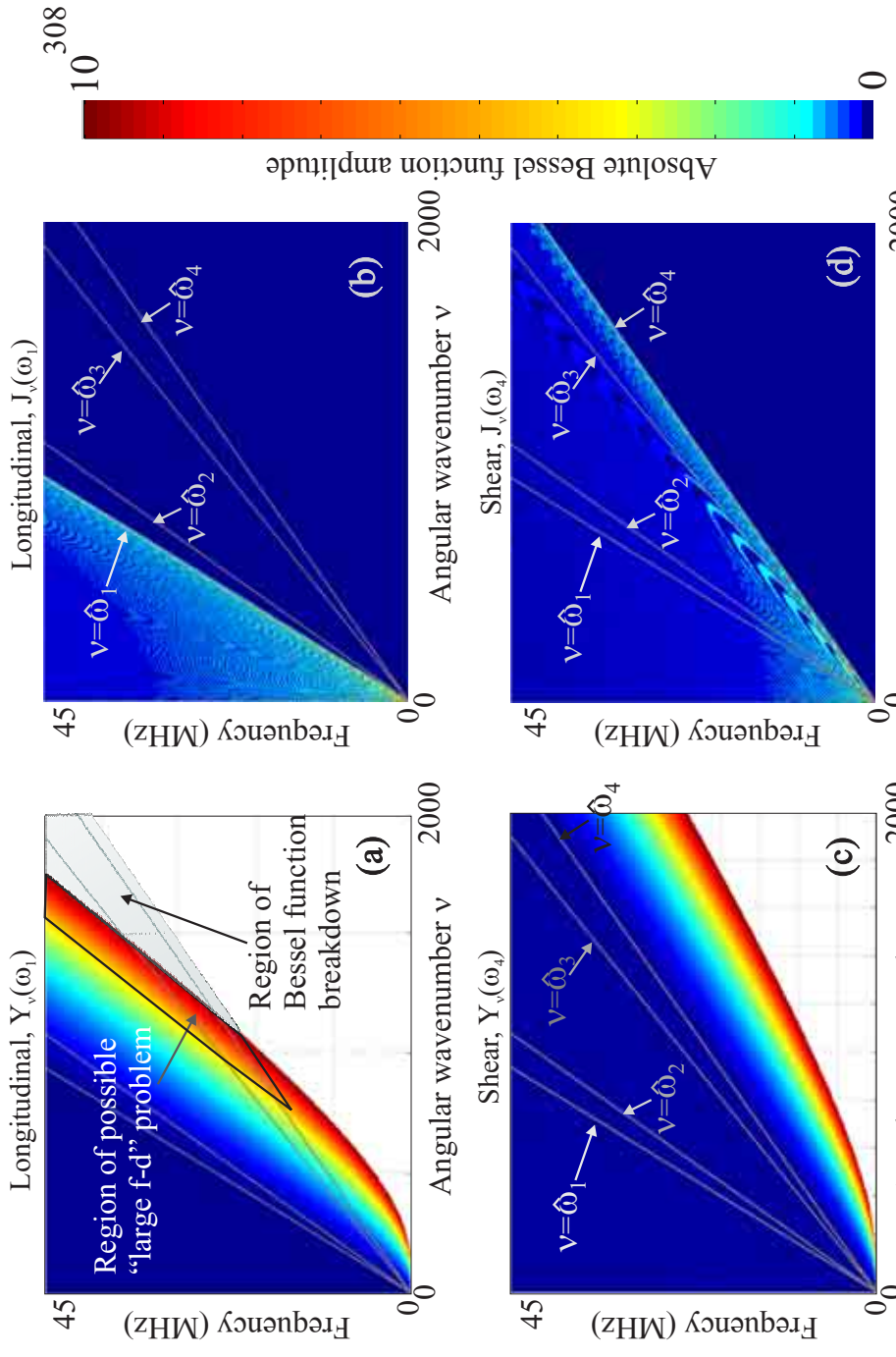

Figure 2.11: Absolute amplitude of the Bessel functions first and second kinds corresponding to the incident and reflected partial waves of the longitudinal kind at the inner surface, **(a)** $Y_\nu(\hat{\omega}_1)$ and **(b)** $J_\nu(\hat{\omega}_1)$, and of the shear kind at the outer surface, **(c)** $Y_\nu(\hat{\omega}_4)$ and **(d)** $J_\nu(\hat{\omega}_4)$. The calculation is based on a 3mm thick steel plate and 20mm inner radius, r_1. The grey and white areas indicate numerical overflow.

Chapter 3

Asymptotic Analysis of Circumferential Guided Waves in Unloaded Plates

The exact analytical dispersion characteristic function of the circumferential guided waves becomes unstable at high frequencies and large curvature radius as discussed in the previous chapter. Keeping the initial motivation of investigating the curvature effect using circumferential waves in mind, it is desirable to be able to calculate the analytical solutions for curved plate systems of any curvature, and at any frequency. For this reason, alternative methods to calculate the exact analytical solutions is a necessity for the completion of this thesis. Asymptotic analyses for those "ill-conditioned" characteristic functions has been studied, as part of the collaborative project with researchers in the Mathematics department at Imperial College. The asymptotic solutions have been derived by our collaborators, and subsequently have been implemented into a Matlab^{TM} program where the limits of these methods were further analysed by the author. This chapter is based on work published in Gridin *et al.* [63] and Fong *et al.* [101].

In this chapter, the derivation of the asymptotic methods, found by Dr. D. Gridin and Prof. R. Craster of mathematics department at Imperial College is summarised (Sec. 3.1). Subsequently, a numerical routine that has ben implemented to trace the dispersion curves for both the exact and asymptotic methods is outlined, and the dispersion curves of several curvatures are presented as examples. Lastly, the accuracy and the efficiency of these asymptotic methods are assessed.

3.1 Asymptotic Solutions

To address the instability problems of the exact analytical solution of circumferential waves in an unloaded curved plate, three asymptotic methods were proposed by our collaborators. For completeness of this thesis, the derivations of these methods are summarised in this section. The full details can be found in Gridin *et al.* [63].

The first method considered is the Uniform Asymptotic Method (UAM), with which the exact Bessel functions are replaced with an uniform asymptotic expansion that is expressed in terms of the Airy functions. The second method, the Regional Asymptotic Method (RAM), adapts a conditional asymptotic expansion which divides the calculations of the Bessel functions into three regimes depending on the order and the argument of the Bessel functions. With further mathematical manipulations, the dispersion curves can be subdivided into regions where the characteristic functions are expressed explicitly. In the last proposed method, the Simplified Region Asymptotic Method (SRAM) extends on the RAM by eliminating the exponentially small terms in the equations, to achieve a complete stability of the characteristic function.

3.1.1 Uniform Asymptotic Method (UAM)

The methodology of the UAM to obtain dispersion relations is the same as the exact method. Both methods require solving for roots in the $\omega-\nu$ domain when the determinant of this eigen-problem matrix is equal to zero, Eqn. 2.18. The only difference compared to the exact derivation is that the Bessel functions [$(J_\nu(k_{T,L}\cdot r_{1,2})$ and $Y_\nu(k_{T,L}\cdot r_{1,2})$] and their derivatives contained in the eigen-matrix D are replaced with the uniform asymptotes.

In the UAM, only the leading terms of the large-order asymptotes of the Bessel functions that are uniform for all arguments x (see pp.366 of Abramowitz [99]), are used.

$$
\begin{aligned}
J_\gamma(x) &\sim \left(\frac{4\zeta}{1-\frac{x^2}{\gamma^2}}\right)^{1/4}\frac{Ai(\gamma^{2/3}\zeta)}{\gamma^{1/3}}, \qquad Y_\gamma(x) \sim -\left(\frac{4\zeta}{1-\frac{x^2}{\gamma^2}}\right)^{1/4}\frac{Bi(\gamma^{2/3}\zeta)}{\gamma^{1/3}},\\
J'_\gamma(x) &\sim -\frac{2\gamma}{x}\left(\frac{1-\frac{x^2}{\gamma^2}}{4\zeta}\right)^{1/4}\frac{Ai'(\gamma^{2/3}\zeta)}{\gamma^{2/3}}, \qquad Y'_\gamma(x) \sim \frac{2\gamma}{x}\left(\frac{1-\frac{x^2}{\gamma^2}}{4\zeta}\right)^{1/4}\frac{Bi'(\gamma^{2/3}\zeta)}{\gamma^{2/3}}.
\end{aligned}
\tag{3.1}
$$

where ζ can be obtained using the following:

$$
\begin{aligned}
\frac{2}{3}\zeta^{3/2} &= \cosh^{-1}(\gamma/x) - \sqrt{1-\frac{x^2}{\gamma^2}}, \qquad x<\gamma,\\
\frac{2}{3}(-\zeta)^{3/2} &= \sqrt{\frac{x^2}{\gamma^2}-1} - \cos^{-1}(\gamma/x), \qquad x>\gamma.
\end{aligned}
\tag{3.2}
$$

Although the UAM does not resolve the instability problem at high frequencies since the nature of the Airy functions (Ai and Bi) is similar to that of the Bessel functions, a significant reduction in the complexity of calculating the Bessel functions is achieved. As a result, the calculation time required using the UAM is much reduced compared to that of the exact method.

3.1.2 Regional Asymptotic Method (RAM)

One fundamental assumption used in the RAM is that the wavelength of the shear bulk wave is much smaller than the inner radius of the curved plate (r_1):

$$k_T r_1, \quad k_L r_1 \gg 1. \tag{3.3}$$

This assumption ensures that the arguments of the Bessel functions used in the dispersion relations (2.15 and 2.18) are large. Consequently, the Bessel functions can be simplified using the large-argument large-order (Debye's) asymptotes that are expressed in 3 regimes depending on the order γ and the argument x of the Bessel functions in the following relationships:

$$\text{Regime I: } \gamma < x, \quad \text{Regime II: } \gamma \approx x, \quad \text{Regime III: } \gamma > x. \tag{3.4}$$

The leading terms of the large-argument large-order asymptotes of the Bessel functions, and their first derivatives are summarised in App. C.1.

Shear Horizontal (SH) Waves

By adapting the solution in the appropriate regime (Eqn. 3.4 to represent the Bessel functions in the dispersion relation, the SH dispersion curves can be sub-divided into five regions in which a real angular wavenumber ν can be situated:

$$\begin{aligned} &\text{Region I: } \nu < k_T r_1, \quad \text{Region II: } \nu \approx k_T r_1, \quad \text{Region III: } k_T r_1 < \nu < k_T r_2, \\ &\text{Region IV: } \nu \approx k_T r_2, \quad \text{Region V: } k_T r_2 < \nu. \end{aligned} \tag{3.5}$$

These regions can also be visualised graphically in the dispersion curves shown in the ν-ω domain of Fig. 3.1. Regions I and III are the main regions where the majority of the solutions are calculated; while Regions II and IV are the transitional regions, which are much narrower than Regions I and III. The purpose of these transitional regions is to ensure a smooth transition by using a solution that is equally accurate in both

neighbouring regions. The transitional areas surround the boundaries $\nu = k_T r_1, k_T r_2$, where the boundaries of this transitional area $(\tilde{\omega} - \nu)$ is calculated by taking the argument of the Airy function in Eqn. 3.1 equal to a constant, is defined in Eqn. 3.6 where the subscripts $T, L, 1, 2$ may be chosen according to the region in which the solution applies; the value of the constant dictates the width of translational area which increases with frequency, and a constant value of 3 is typically used. Eqn. 3.6 can be applied to the translational areas for the Lamb-type cases in the next section.

$$\pm\left|\left(\nu\left[\frac{3}{2}(\cosh^{-1}(\frac{\nu C_{T,L}}{\tilde{\omega} r_{1,2}}) - \sqrt{1-\left(\frac{\tilde{\omega} r_{1,2}}{\nu C_{T,L}}\right)^2}\right]\right)^{2/3}\right| = 3 \;\; (Const.) \tag{3.6}$$

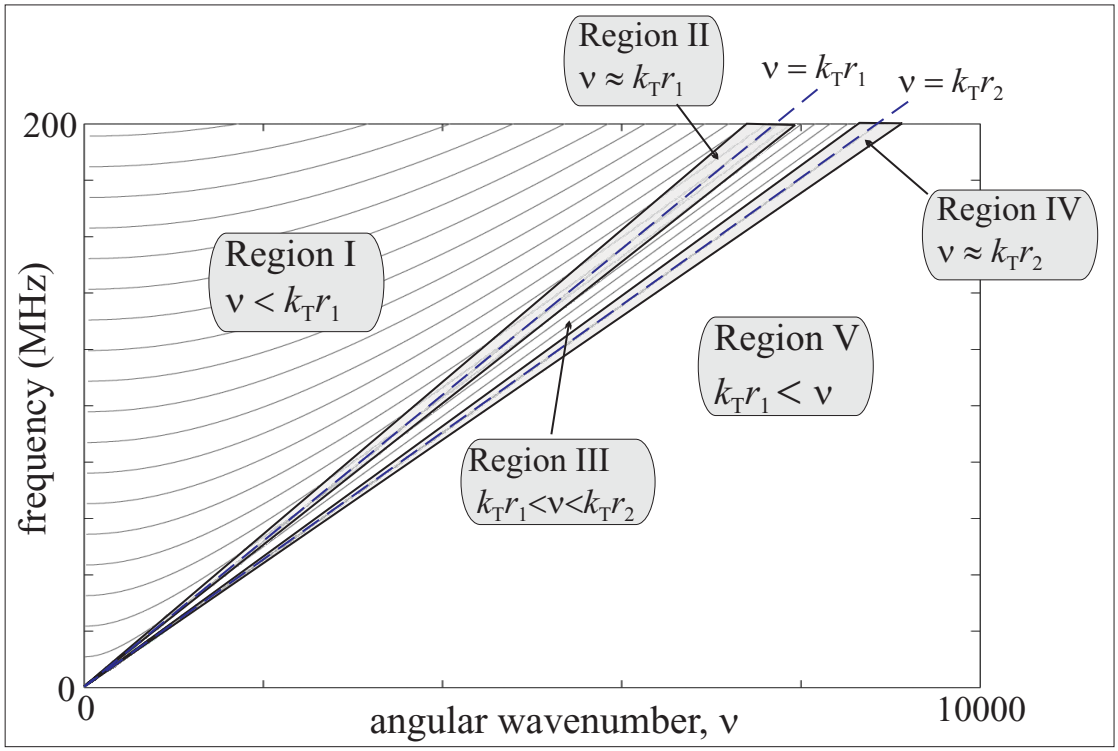

Figure 3.1: Shear horizontal (SH) circumferential dispersion curves and the regions defined for the Regional Asymptotic methods ($r_1 = 0.02$m and $r_2 = 0.023$m, Steel as an example).

Using the appropriate asymptotes (App. C.1), the dispersion relation may be expressed explicitly in each Region:

Region I: $\nu < k_T r_1$

$$\sin\left\{(k_T^2 r_1^2 - \nu^2)^{1/2} - (k_T^2 r_2^2 - \nu^2)^{1/2} - \nu\left[\cos^{-1}\left(\frac{\nu}{k_T r_1}\right) - \cos^{-1}\left(\frac{\nu}{k_T r_2}\right)\right]\right\} = 0. \tag{3.7}$$

Region II: $\nu \approx k_T r_1$

$$Ai'\left[\left(\frac{2}{k_T r_1}\right)^{1/3}(\nu - k_T r_1)\right]\cos\left\{(k_T^2 r_2^2 - \nu^2)^{1/2} - \nu\cos^{-1}\left(\frac{\nu}{k_T r_2}\right) - \frac{\pi}{4}\right\}$$
$$-Bi'\left[\left(\frac{2}{k_T r_1}\right)^{1/3}(\nu - k_T r_1)\right]\sin\left\{(k_T^2 r_2^2 - \nu^2)^{1/2} - \nu\cos^{-1}\left(\frac{\nu}{k_T r_2}\right) - \frac{\pi}{4}\right\} = 0.$$

Region III: $k_T r_1 < \nu < k_T r_2$

$$2\sin\left[\sqrt{k_T^2 r_2^2 - \nu^2} - \nu\cos^{-1}\left(\frac{\nu}{k_T r_2}\right) - \frac{\pi}{4}\right]$$
$$+\cos\left[\sqrt{k_T^2 r_2^2 - \nu^2} - \nu\cos^{-1}\left(\frac{\nu}{k_T r_2}\right) - \frac{\pi}{4}\right]e^{2[\sqrt{\nu^2 - k_T^2 r_1^2} - \nu\cosh^{-1}(\nu/k_T r_1)]} = 0. \tag{3.8}$$

Region IV: $\nu \approx k_T r_2$

$$e^{2[\sqrt{\nu^2 - k_T^2 r_1^2} - \nu\cosh^{-1}(\nu/k_T r_1)]}Bi'\left[\left(\frac{2}{k_T r_2}\right)^{1/3}(\nu - k_T r_2)\right]$$
$$+2Ai'\left[\left(\frac{2}{k_T r_2}\right)^{1/3}(\nu - k_T r_2)\right] = 0. \tag{3.9}$$

Lamb-type Waves

Under the assumption of Eqn. 3.3, the second terms of the elements in the solution matrix D (shown in App. B) are of higher asymptotic order, and therefore may be neglected. Additionally, the determinant of the eigen-matrix may be reduced and expressed in the following single equation:

$$f_5^2 f_6^2\{J_\nu(\hat{\omega}_2)Y_\nu(\hat{\omega}_1) - J_\nu(\hat{\omega}_1)Y_\nu(\hat{\omega}_2)\}\{J_\nu(\hat{\omega}_4)Y_\nu(\hat{\omega}_3) - J_\nu(\hat{\omega}_3)Y_\nu(\hat{\omega}_4)\}$$
$$+16\nu^4\hat{\omega}_1\hat{\omega}_2\hat{\omega}_3\hat{\omega}_4\{J'_\nu(\hat{\omega}_2)Y'_\nu(\hat{\omega}_1) - J'_\nu(\hat{\omega}_1)Y'_\nu(\hat{\omega}_2)\}\{J'_\nu(\hat{\omega}_4)Y'_\nu(\hat{\omega}_3) - J'_\nu(\hat{\omega}_3)Y'_\nu(\hat{\omega}_4)\}$$
$$-4\nu^2[f_5^2\hat{\omega}_1\hat{\omega}_3\{J_\nu(\hat{\omega}_2)Y'_\nu(\hat{\omega}_1) - J'_\nu(\hat{\omega}_1)Y_\nu(\hat{\omega}_2)\}\{J_\nu(\hat{\omega}_4)Y'_\nu(\hat{\omega}_3) - J'_\nu(\hat{\omega}_3)Y_\nu(\hat{\omega}_4)\}$$
$$+f_6^2\hat{\omega}_2\hat{\omega}_4\{J'_\nu(\hat{\omega}_2)Y_\nu(\hat{\omega}_1) - J_\nu(\hat{\omega}_1)Y'_\nu(\hat{\omega}_2)\}\{J'_\nu(\hat{\omega}_4)Y_\nu(\hat{\omega}_3) - J_\nu(\hat{\omega}_3)Y'_\nu(\hat{\omega}_4)\}]$$
$$+\frac{32}{\pi^2}\nu^2 f_5 f_6 = 0. \tag{3.10}$$

where $f_5 = 2\nu^2 - \hat{\omega}_4^2, \quad f_6 = 2\nu^2 - \hat{\omega}_3^2$.

Eqn. 3.10 has been expressed in such a way that a convenient form of asymptotes for the cross-products of the Bessel functions containing two different arguments (given in App. C.2), could be readily used. As in the SH waves, the dispersion characteristic function (Eqn. 3.10) is further simplified into nine regions by applying the appropriate cross-product asymptotes for the Bessel functions corresponding to the different regimes, the nine regions being:

Region I: $\nu < \hat{\omega}_1$, Region II: $\nu \approx \hat{\omega}_1$, Region III: $\hat{\omega}_1 < \nu < \hat{\omega}_2$,

Region IV: $\nu \approx \hat{\omega}_2$, Region V: $\hat{\omega}_2 < \nu < \hat{\omega}_3$, Region VI: $\nu \approx \hat{\omega}_3$,
Region VII: $\hat{\omega}_3 < \nu < \hat{\omega}_4$, Region VIII: $\nu \approx \hat{\omega}_4$, Region IX: $\hat{\omega}_4 < \nu$. (3.11)

where $\hat{\omega}_1 = k_L r_1$, $\hat{\omega}_2 = k_L r_2$, $\hat{\omega}_3 = k_T r_1$, $\hat{\omega}_4 = k_T r_2$. The graphical representation of

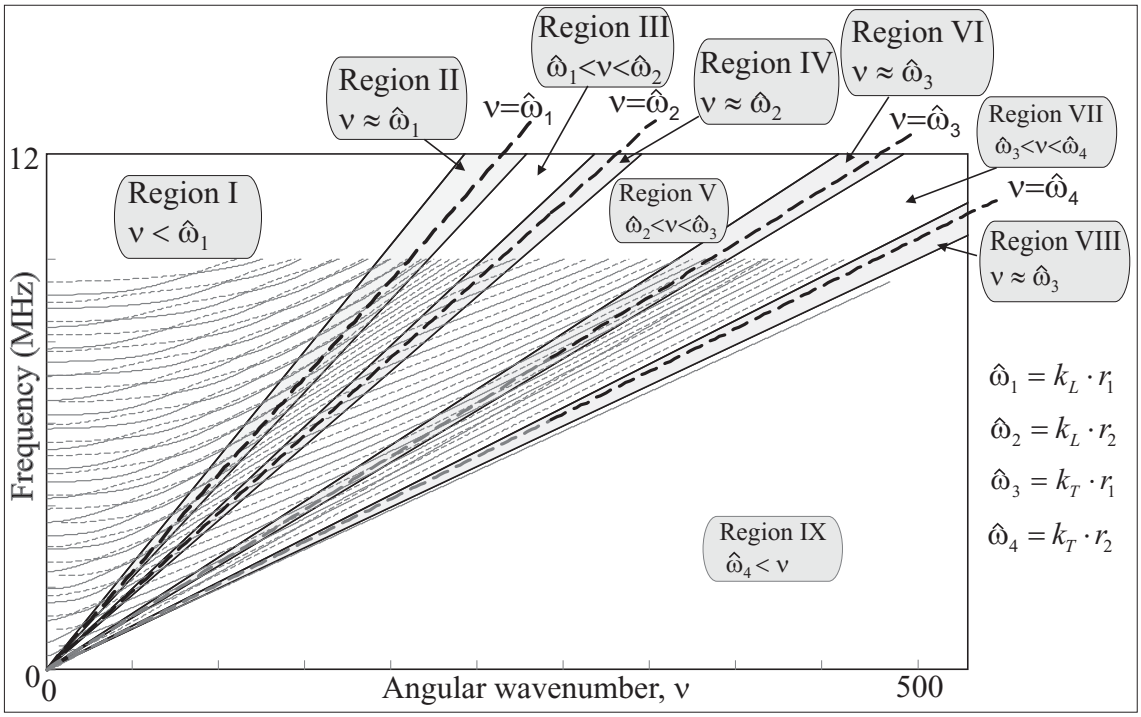

Figure 3.2: Lamb-type circumferential dispersion curves and regions defined for the Regional Asymptotic methods ($r_1 = 0.02$m and $r_2 = 0.025$m, Steel as an example).

these regions is illustrated in the dispersion curves of Fig. 3.2, where the dispersion relation is expressed explicitly for each region. Regions II, IV, VI, VIII are the transitional regions, where the solutions are derived in the same way as those of the SH case, and are shown in App. C.3. Regions I, III, V, VII and IX are expressed in terms of the fundamental trigonometric functions which can substantially reduce the complexity of the calculations. The key equations of the Regions are summarised below:

Region I: $\nu < \hat{\omega}_1$

$$c_1 \sin(\alpha_1 - \alpha_2)\sin(\alpha_3 - \alpha_4) + c_2 \cos(\alpha_1 - \alpha_2)\cos(\alpha_3 - \alpha_4) + c_3 = 0. \tag{3.12}$$

Region III: $\hat{\omega}_1 < \nu < \hat{\omega}_2$

$$-\Big\{\frac{f_5^2 f_6^2}{\tilde{f}_1 f_2 f_3 f_4}\Big(\cos\alpha_2 e^{-\beta_1} + \sin\alpha_2 \frac{e^{\beta_1}}{2}\Big) + 16\nu^4 \tilde{f}_1 f_2 f_3 f_4 \Big(\sin\alpha_2 e^{-\beta_1} + \cos\alpha_2 \frac{e^{\beta_1}}{2}\Big)\Big\}\sin(\alpha_3 - \alpha_4) - 4\nu^2\Big\{\frac{f_6^2 f_2 f_4}{\tilde{f}_1 f_3}\Big(-\sin\alpha_2 e^{-\beta_1} + \cos\alpha_2 \frac{e^{\beta_1}}{2}\Big) + \frac{f_5^2 \tilde{f}_1 f_3}{f_2 f_4}\Big(\cos\alpha_2 e^{-\beta_1} - \sin\alpha_2 \frac{e^{\beta_1}}{2}\Big)\Big\}\cos(\alpha_3 - \alpha_4) + c_3 = 0. \tag{3.13}$$

Region V: $\hat{\omega}_2 < \nu < \hat{\omega}_3$

$$c_4 \sinh(\beta_1 - \beta_2)\sin(\alpha_3 - \alpha_4) + c_5 \cosh(\beta_1 - \beta_2)\cos(\alpha_3 - \alpha_4) + c_3 = 0. \tag{3.14}$$

Region VII: $\hat{\omega}_3 < \nu < \hat{\omega}_4$

$$\begin{aligned}\sinh(\beta_2 - \beta_1)\Big\{ \frac{f_5^2 f_6^2}{\tilde{f}_1\tilde{f}_2\tilde{f}_3 f_4}\Big(\cos\alpha_4 e^{-\beta_3} + \sin\alpha_4 \frac{e^{\beta_3}}{2}\Big) - 16\nu^4 \tilde{f}_1\tilde{f}_2\tilde{f}_3 f_4 \Big(\sin\alpha_4 e^{-\beta_3} \\ + \cos\alpha_4 \frac{e^{\beta_3}}{2}\Big)\Big\} - 4\nu^2 \cosh(\beta_2 - \beta_1)\Big\{ \frac{f_6^2 \tilde{f}_2 f_4}{\tilde{f}_1\tilde{f}_3}\Big(- \cos\alpha_4 \frac{e^{\beta_3}}{2} - \sin\alpha_4 e^{-\beta_3}\Big) \\ + \frac{f_5^2 \tilde{f}_1\tilde{f}_3}{f_2 f_4}\Big(\cos\alpha_4 e^{-\beta_3} - \sin\alpha_4 \frac{e^{\beta_3}}{2}\Big)\Big\} + c_3 = 0.\end{aligned} \tag{3.15}$$

Region IX: $\hat{\omega}_4 < \nu$

$$c_6 \sinh(\beta_1 - \beta_2)\sinh(\beta_3 - \beta_4) + c_7 \cosh(\beta_1 - \beta_2)\cosh(\beta_3 - \beta_4) + c_3 = 0. \tag{3.16}$$

$$\begin{aligned}&\text{where} \quad c_1 = \frac{f_5^2 f_6^2}{f_1 f_2 f_3 f_4} + 16\nu^4 f_1 f_2 f_3 f_4, \quad c_2 = -4\nu^2\Big\{ \frac{f_5^2 f_1 f_3}{f_2 f_4} + \frac{f_6^2 f_2 f_4}{f_1 f_3}\Big\}, \\ &\quad c_3 = 8\nu^2 f_5 f_6, \quad c_4 = \frac{f_5^2 f_6^2}{\tilde{f}_1\tilde{f}_2 f_3 f_4} - 16\nu^4 \tilde{f}_1\tilde{f}_2 f_3 f_4, \quad c_5 = -4\nu^2\Big\{ \frac{f_5^2 \tilde{f}_1 f_3}{\tilde{f}_2 f_4} + \frac{f_6^2 \tilde{f}_2 f_4}{\tilde{f}_1 f_3}\Big\}, \\ &\quad c_6 = \frac{f_5^2 f_6^2}{\tilde{f}_1\tilde{f}_2\tilde{f}_3\tilde{f}_4} + 16\nu^4 \tilde{f}_1\tilde{f}_2\tilde{f}_3\tilde{f}_4, \quad c_7 = -4\nu^2\Big\{ \frac{f_5^2 \tilde{f}_1\tilde{f}_3}{\tilde{f}_2\tilde{f}_4} + \frac{f_6^2 \tilde{f}_2\tilde{f}_4}{\tilde{f}_1\tilde{f}_3}\Big\}, \\ &\quad \alpha_i = f_i^2 - \nu\cos^{-1}(\nu/\hat{\omega}_i) - \pi/4, \quad \beta_i = \tilde{f}_i^2 - \nu\cosh^{-1}(\nu/\hat{\omega}_i), \\ &\quad f_i = (\hat{\omega}_i^2 - \nu^2)^{1/4}, \quad \tilde{f}_i = (\nu^2 - \hat{\omega}_i^2)^{1/4}.\end{aligned} \tag{3.17}$$

The dispersion relations of the transitional regions contain Bessel functions associated only to partial waves that are homogeneous. This ensures that the Bessel function that is determined using the uniform asymptotes expressed in terms of the Airy functions (Eqn. 3.1), could not become unstable.

3.1.3 Simplified Regional Asymptotic Method (SRAM)

Although using the RAM resolves the instability problem of the Bessel functions, the dispersion relation equations derived using the RAM (Eqns. 3.7 - 3.9 and Eqns. 3.12 - 3.16), may still contain numerous exponentially small and large terms. These terms normally exist in the equations of the dispersion relation inside the "unstable Region" shown in Fig. 2.5, where some or all the partial waves are inhomogeneous, as discussed in Sec. 2.3. In fact, the very small and large terms in the equations, representing the exponential decay of the partial wave amplitudes, and thus having a similar effect to the "large f-d" problem. They can cause the dispersion relation function to grow exponentially, and eventually the solutions break down at very high frequency due to numerical overflow.

This "ill-conditioning" of the dispersion functions may be overcome simply by eliminating the exponentially small terms that describe the mild coupling condition of the partial waves between the surfaces when they become inhomogeneous. By doing so, a considerable reduction of the function amplitude and a removal of the exponential growth nature of the function can be achieved. This allows the iteration of the roots to be quicker and the solutions to be more stable.

As an illustration, a comparison of the Lamb-type dispersion characteristic functions for Region V between the RAM and SRAM is shown in Fig. 3.3; the roots of the function are where the curve crosses the x-axis. It can be seen that the nature of rapidly increasing oscillation amplitude is effectively removed when using the SRAM. Since only the zero crossing points of the function are of any interest, reducing the oscillation amplitude of the function would not in any way affect the accuracy of the results; this is reflected in the accuracy plots later in Sec. 3.4.

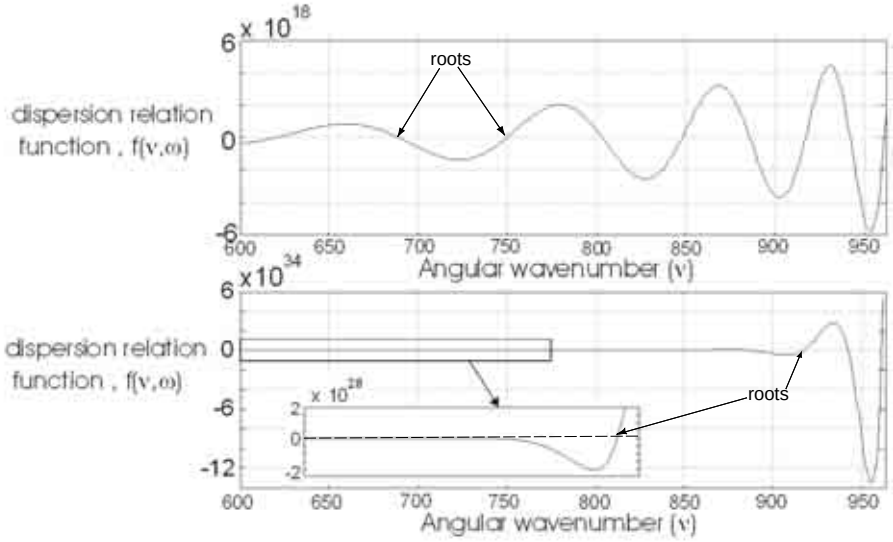

Figure 3.3: Lamb-type dispersion characteristic function of Region V at a frequency of 25MHz for a curved steel plate structure (3mm thick and 20mm inner radius) using RAM (bottom) and SRAM (top) with a "zoom-in" for low angular wavenumber values.

In Regions I and II of both the SH and Lamb-type systems, all partial waves are homogeneous or in the transition of becoming inhomogeneous. Therefore there are no exponentially small and large terms in the dispersion relation of these regions which may cause the "ill-conditioning" of the dispersion function; consequently, no further simplification of the dispersion result is necessary in these regions.

Shear Horizontal (SH) Waves

Region III: $k_T r_1 < \nu < k_T r_2$

In Eqn. 3.8, the second term is typically very small for all the parameters used in the solution, and therefore can be omitted. Doing so is equivalent to neglecting the boundary condition of inner wall completely, resulting in a simplified asymptotic dispersion relation for a curved plate:

$$\sin\left[\sqrt{k^2 r_2^2 - \nu^2} - \nu \cos^{-1}\left(\frac{\nu}{k_T r_2}\right) - \frac{\pi}{4}\right] = 0. \tag{3.18}$$

Region IV: $\nu \approx k_T r_2$

In this region, the first term of Eqn. 3.9 is exponentially small and therefore can be omitted, resulting in a reduced dispersion relation for the whispering gallery type modes in a curved plate:

$$Ai'\left[\left(\frac{2}{k_T r_2}\right)^{1/3}(\nu - k_T r_2)\right] = 0. \tag{3.19}$$

Lamb-type Waves

The dispersion relations for the transitional regions are shown in App. C.4, in which the exponentially small terms of the dispersion relations in the RAM (App. C.3) are identified and eliminated.

Region III: $\hat{\omega}_1 < \nu < \hat{\omega}_2$

In Eqn. 3.13, terms with $e^{-\beta_1}$, where β_1 is negative and large, are much larger than unity, therefore c_3 and the e^{β_1} terms can be neglected and the dispersion relation in this region becomes:

$$\begin{aligned}&\left\{\frac{f_5^2 f_6^2}{\tilde{f}_1 f_2 f_3 f_4}\cos\alpha_2\right) + 16\nu^4 \tilde{f}_1 f_2 f_3 f_4 \sin\alpha_2\Big\}\sin(\alpha_3 - \alpha_4)\\ &+4\nu^2\Big\{-\frac{f_6^2 f_2 f_4}{\tilde{f}_1 f_3}\sin\alpha_2 + \frac{f_5^2 \tilde{f}_1 f_3}{f_2 f_4}\cos\alpha_2\Big\}\cos(\alpha_3 - \alpha_4) + c_3 = 0.\end{aligned} \tag{3.20}$$

This simplification can be applied similarly to both Regions V and Region VII.

Region V: $\hat{\omega}_2 < \nu < \hat{\omega}_3$

$$-c_4 \sin(\alpha_3 - \alpha_4) + c_5 \cos(\alpha_3 - \alpha_4) = 0. \tag{3.21}$$

Region VII: $\hat{\omega}_3 < \nu < \hat{\omega}_4$

$$(f_6^2 - 4\nu^2 \tilde{f}_1^2 \tilde{f}_3^2)(f_5^2 \cos\alpha_4) = 0. \tag{3.22}$$

Region IX: $\hat{\omega}_4 < \nu$

With further simplification of Eqn. 3.16, its equation may be expressed as a combination of two Rayleigh equations describing waves on the outer and inner surfaces of the curved plate that correspond to the first and the second half of the equation respectively:

$$\begin{aligned}\{(2\nu^2 - k_T^2 r_2^2)^2 - 4\nu^2 \sqrt{\nu^2 - k_L^2 r_2^2}\sqrt{\nu^2 - k_T^2 r_2^2}\} \\ \times\{(2\nu^2 - k_T^2 r_1^2)^2 - 4\nu^2 \sqrt{\nu^2 - k_L^2 r_1^2}\sqrt{\nu^2 - k_T^2 r_1^2}\} = 0.\end{aligned} \tag{3.23}$$

3.1.4 Partial Wave Analysis

The partial wave analysis [102] is an elegant way of representing the concept of guided wave propagation. A guided wave of a particular wave mode may be decomposed into longitudinal and shear partial waves that have appropriate amplitudes to satisfy the boundary conditions at a given frequency. In a Lamb-type system, the physical behaviour of the partial waves corresponding to each region (shown in Fig. 3.2) is illustrated in Fig. 3.4. The length of the arrows in the figure indicates the amplitude of partial waves at the inner r_1 and outer r_2 radii, while the direction of the arrows show the angle of interaction between the partial waves and the boundary surfaces.

In general, the longitudinal and shear partial waves are reflected from the inner and outer surfaces of the curved plate at a reflected angle which is the same as the incident angle; an angle that is between the incident/reflected wave and the normal of the surface. However, in cylindrical coordinates, the general direction of the wave front of these partial waves rotates around the central axis. As a result, there is an infinite set of longitudinal-shear partial wave pairs along the surfaces that are dependent on the θ direction.

As the frequency increases, the incident and reflected angles increase simultaneously. At the point where the dispersion curve of a mode touches the line $\nu = \hat{\omega}_1$ in Region II (see Fig. 3.2), the longitudinal partial wave is tangential to the inner surface. Subsequently, as the dispersion curve crosses the line $\nu = \hat{\omega}_1$ into Region III, the longitudinal partial wave on the inner surface must change from homogeneous to inhomogeneous (i.e. from real to imaginary wavenumber) in order to ensure its resultant amplitude is the same as the other partial waves.

As the frequency increases, the rest of the partial waves become inhomogeneous waves sequentially as the dispersion curves cross the lines $\nu = \hat{\omega}_{2,3,4}$ in Regions IV, VI and VIII respectively, as shown in Fig. 3.4. The wave modes eventually converge into the surface

Rayleigh waves when both the longitudinal and shear partial waves become inhomogeneous. The behaviour of the partial waves that comprise the solution is in general very different in each region, and hence the asymptotic solutions of the Bessel function in the appropriate regime are used.

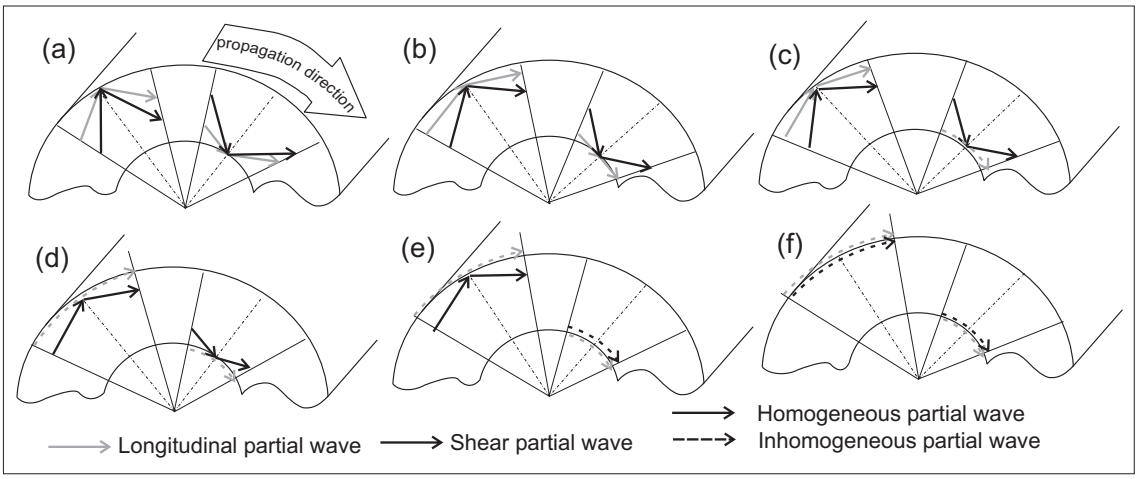

Figure 3.4: Partial wave pattern at the boundaries of a generalised curved plate structure corresponding to the various locations in the dispersion curves of Fig. 3.2. (a) Region I. (b) $\nu = \hat{\omega}_1$. (c) Region III. (d) Region V. (e) Region VII. (f) Region IX.

3.2 Implementation of Numerical Solutions

The analytical dispersion characteristic equations of both the exact and asymptotic methods for a single layered unloaded curved plate have been implemented in a Matlab^{TM} program, from which the modal solutions, also known as the roots of the characteristic equations, are computed. The program evaluates the solutions in the frequency-angular wavenumber ω-ν domain, and traces and joins the roots that belong to the same wave propagating mode. The tracing routine used is very similar to that used by Lowe [9] with some minor modifications, such as the choice of iteration and sweeping domains.

To trace the dispersion curves, a number of fundamental parameters defining the geometrical and mechanical properties of the problem must be first defined. The program then selects two close angular wavenumber values ($\nu_{1,2}$) chosen preferably in the region $\nu > \hat{\omega}_1$ where the gradient of the curves in the working domain $\nu - \omega$ is similar between wave modes.

There is in general an infinite number of frequencies ω that can satisfy the dispersion relation for any one angular wavenumber. Therefore an upper frequency limit must be specified to restrict the number of wave modes traced. The program steps and iterates in the ω domain up to the specified upper frequency limit, where a finite number of frequency

roots ω_m for both ν_1 and ν_2, is evaluated.

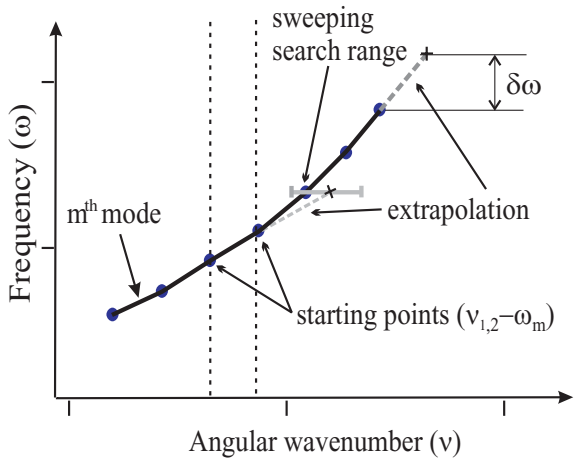

Figure 3.5: Illustration of a typical dispersion curves 1D-iteration and tracing procedure.

Each pair of these roots $\nu_{1,2}\omega_m$ provides the starting point for the first m modes, and is used to linearly extrapolate an estimated angular wavenumber value in a small frequency step $\delta\omega$. Convergence is obtained by iterating over a range of angular wavenumbers (sweeping) as demonstrated in Fig. 3.5. The program switches to a quadratic extrapolation once a third point is found. Doing so can usually provide a better estimation for the extrapolation, and thus a reduction in the overall number of iterations.

The stepping size in frequency $\delta\omega$ might be reduced when there are two closely located roots found in the sweeping range, or when the gradient is very extreme to extrapolate accurately. In general, a large step can be used in the regions where $\nu > k_T r_1$ for the SH case and $\nu > k_L r_1$ for the Lamb-type case. This is because the dispersion curves in these regions have gradients that vary little with frequency. The tracing process is repeated for all m modes.

In addition, Matlab^{TM} automatically registers the value of double precision variables with "*Inf*" or "0" when they become overflow or underflow respectively, as discussed in Sec. 2.3. Using these properties, it would possible to distinguish if the instability is caused by the Bessel functions or the "large f-d" problem; the Bessel function breakdown causes the value of $Y_\nu(\hat{\omega}_1)$ in the solution (Eqn. B.1) to become *Inf*, while the determinant of the solution matrix becomes *Inf* if the solution breakdown is caused by the "large f-d" problem.

When using the regional methods, extra procedures are included to determine the region in which the estimated ω-ν is located, allowing an appropriate dispersion relation to be used. Nevertheless, there is one obvious difficulty in applying such a regional scheme. Since the equation of the dispersion relation is different for each region, a discontinuity

may occur at the boundary of any two regions. By increasing the sweeping range, the discontinuity problem of the curves can often be resolved, but this may just as easily cause the extrapolation to track the neighbouring mode. To rectify this problem, a much smaller frequency step $\delta\omega$ for the extrapolation is automatically applied near the boundaries when regional schemes are used. The general concept of the tracing routine is summarised with the flow chart shown in Fig. 3.6.

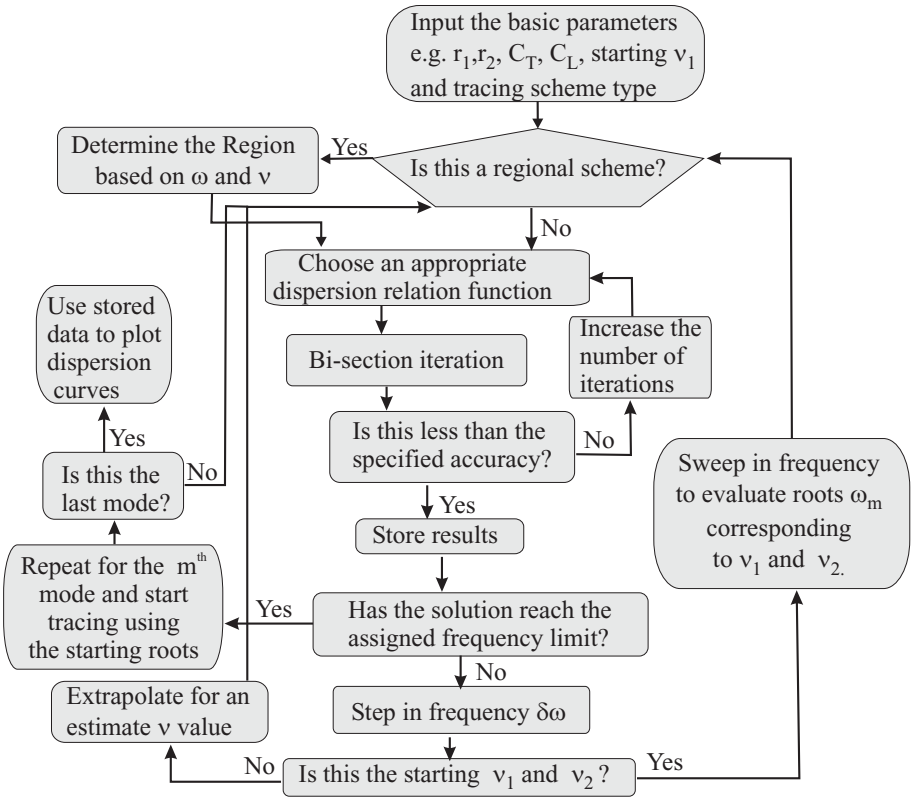

Figure 3.6: Flow chart of the tracing routine that has been implemented in a Matlab^{TM} program.

A Bi-Section Method (BSM) [103] is used for the iteration in this program; the BSM is a very simple method to use but is regarded as inefficient. Other potentially more efficient methods such as the Newton's method ([104]) have been considered. However due to the exponential growth nature of the dispersion functions (Fig. 2.8), these methods often add and subtract extremely unequal numbers, resulting in higher numerical rounding errors compared to the BSM. It appears that the BSM has provided a much more stable scheme for this kind of problem as it only makes use of the polarity of the function at each evaluation, while ignoring the solution magnitude. The solutions are iterated until a minimum accuracy of a specified value is obtained. In all the calculations of this chapter, an accuracy of 1×10^{-9} was used; the value was chosen so that the numerical error is many orders less than the error caused by using the asymptotic methods.

Additionally, the routine has been programmed to solve the characteristic function of a

multilayered curved plate using the classical exact global matrix method [98]. The Global Matrix [**G**] forms a secular equation that relates the partial waves amplitudes {**A**} at each layer boundary to the external boundary conditions of the system in the following form:

$$[\mathbf{G}]\{\mathbf{A}\} = 0. \tag{3.24}$$

However, as there are currently no asymptotic solutions available for multilayered structures, solutions are likely to suffer from instabilities at high frequencies due to the reasons discussed previously in Sec. 2.3.

3.3 Numerical Examples

As an example, numerical results of the dispersion curves for the circumferential SH and Lamb-type waves of a curved plate were calculated using the exact solution and the three asymptotic approximation methods with the tracing routine described in the previous section. The curved plate structure investigated was composed of steel that has material properties of $C_L = 5960m/s$, $C_T = 3260m/s$ and $\rho = 7932kg/m^3$. To demonstrate the effect of curvature, three geometries have been carefully chosen so that the solution corresponding to the same mode breaks down at different frequencies; these example geometries are tabulated in Tab. 3.1. The curvature of a plate is defined by the "d/r_1" ratio in this thesis, where d is the thickness and r_1 is the inner radius.

	$r_1(m)$	$r_2(m)$	Curvature: $\frac{d}{r_1}$	$\frac{r_2}{r_1}$
geometry **1**	0.02	0.021	0.05	1.05
geometry **2**	0.02	0.023	0.15	1.15
geometry **3**	0.02	0.025	0.25	1.25

Table 3.1: Geometries of the curved plate used for the case study in this thesis.

SH waves

Fig. 3.7(a) shows four dispersion curves of the SH type wave modes that are calculated for the geometry **2**. Due to the large number of modes existing in the frequency range of interest, only every 20^{th} mode is presented in the graph to give a better visual quality. Using the exact method (top graph), it is evident that the solutions break down at the high-frequency high-angular wavenumber region as expected. Replacing the Bessel functions in the dispersion relation with the uniform asymptotes (Sec. 3.1.1), as shown in the second graph, did not result in any improvement in the stability of the solutions. This is shown

by comparing the frequency at which these curves break down to those of the exact case in graph 1; the breakdown point of each curve is marked with a cross in Fig. 3.7. As mentioned earlier, the time required to trace these curves using the UAM was significantly reduced.

By using the RAM (shown in the third graph from the top in Fig. 3.7(a)), the dispersion relation function becomes more stable and its solution could consequently be obtained at higher frequencies. Nevertheless, despite the improvement in stability compared to the UAM, the solutions can be seen to break down at even higher frequencies. The RAM eliminates the instability of the Bessel functions, therefore any further breakdown of the RAM solutions would have to be caused by the "large f-d" problem.

This is further confirmed by the SRAM, shown in the bottom graph of Fig. 3.7(a), where solutions are obtained for dispersion curves of all three geometries at any frequencies. Further investigation has indicated that there are no signs of any solution breakdown up to a frequency that is twice of that shown in Fig. 3.7(a). The dispersion functions of the SRAM do not grow exponentially with increasing frequency; as a result, there should not be any frequency limit at which the solutions become unstable.

Lamb-type waves

Figs. 3.7(b - d) present the Lamb-type dispersion curves that were calculated using the exact and asymptotic methods for geometry 1 to 3 respectively; the red and blue curves in the figures are used to distinguish between the neighbouring modes. Again for clarity, only every 5th mode is plotted here in the figures of the Lamb-type cases.

In order to compare dispersion curves of different geometries, both the frequency ω and the angular wavenumber ν must be scaled with the thickness d and the radius corresponding to the mid-point through the thickness of a curved plate r_{mid} (Eqn. 3.25). By doing so the circumferential wave dispersion curves are located in a similar location of the graph regardless of their geometry. However, it is worth stressing that the dispersion curves are only universal for geometries with the same r_2/r_1 ratio. All graphs in the Lamb-type case (Figs. 3.7(b - d)) were traced to an upper frequency-thickness (fd) limit of 0.18MHz-m. This is to ensure that a similar number of modes are presented in each graph to provide a good visual comparison.

$$\text{Scaled frequency}, \bar{\omega} = f \cdot d, \quad \text{Scaled wavenumber}, \bar{\nu} = \frac{\nu \cdot d}{r_{mid}}. \tag{3.25}$$

As in the SH case, the UAM does not improve the stability of the dispersion curves in the Lamb-type case. The solutions of both UAM and exact method fail at exactly the same frequencies, as illustrated in the top two graphs of Figs. 3.7(b - d) for all three

geometries. In general, the value of the fd product at which the exact solutions of a particular mode break down, increases with increasing curvature, though the cause of this solution breakdown in each geometry case might vary between the "large $f-d$" problem and the breakdown of the Bessel functions.

In the case of $r_2/r_1 = 1.05$ (Fig. 3.7(b)), the exact solution breakdown is caused by the instability of the Bessel functions. Using the RAM, a dramatic improvement in the solution stability is achieved in the dispersion curves. Nonetheless, the lower order modes still break down at very high fd products.

In the case of $r_2/r_1 = 1.15$ (Fig. 3.7(c)), though the breakdown of the exact solutions is caused by the instability of the Bessel functions, the elements of the characteristic eigen-matrix D at the point of the breakdown contain some extremely large and small terms. Because of this, the solutions are as likely to fail by the "large f-d" problem as much as by the breakdown of the Bessel functions. It is not surprising that only a very little extent of the dispersion curves is further traced when the RAM is used, compared to the exact method.

As the curvature increases, such as in the case of $r_2/r_1 = 1.25$ (Fig. 3.7(d)), the "large f-d" problem becomes dominant. It can be seen that there is no improvement compared to the exact method when using either UAM or RAM. This suggests that any solution breakdown at this geometry is purely caused by the "large f-d" problem. Such trend of increasing domination of the "large $f-d$" problem over the breakdown of Bessel functions can also be observed in the graphs (3) of Figs. 3.7(b - d), corresponding to r_2/r_1 increasing from 1.05 to 1.25. In this sequence of figures, the fd product values at which the solutions break down decreases.

Finally, by using the SRAM (graphs (4) of Figs. 3.7(b - d)), any instability nature of the dispersion relation is removed, and it is possible to trace solutions for all modes, and at all frequencies. The asymptotic methods have unquestionably solved the numerical instability problem discussed earlier in Sec. 2.3.

The dispersion curves in this chapter are plotted along the frequency-angular wavenumber ω-ν axes. Other forms of dispersion curves such as the tangential phase velocity V_{ph} and the group velocity V_{gr}, are sometimes more commonly used because of their physical meanings to certain applications. The tangential V_{ph} and V_{gr} of the wave modes can be easily converted from the ω-ν domain, using the following relationships:

$$V_{ph}(rad/s) = \frac{\omega}{\nu}. \tag{3.26}$$

$$V_{gr}(rad/s) = \frac{\partial\omega}{\partial\nu}. \tag{3.27}$$

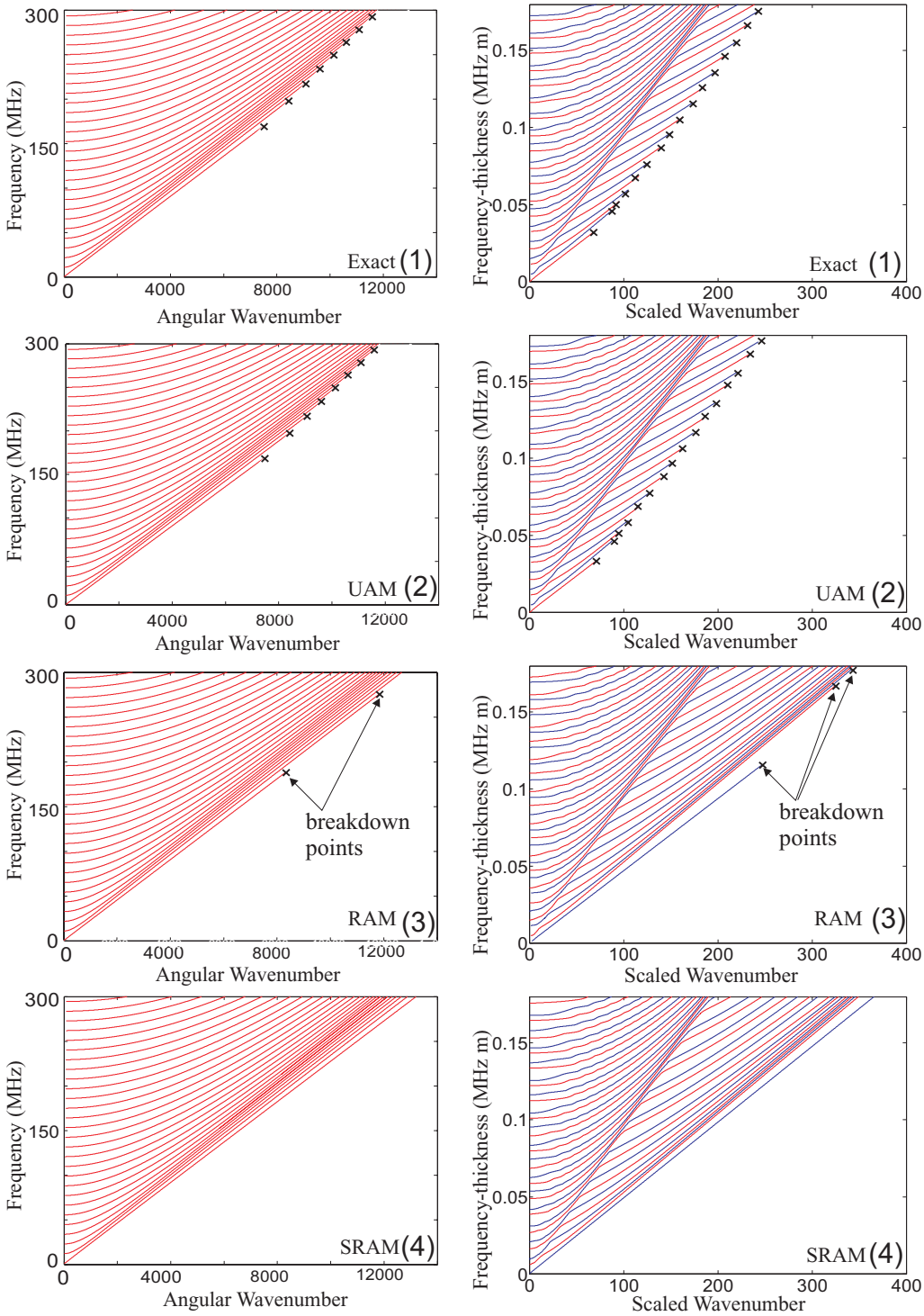

(a) Every 20^{th} mode of **SH** circumferential waves: $r_2/r_1 = 1.15$.

(b) Every 5^{th} mode of Lamb-type circumferential waves: $r_2/r_1 = 1.05$.

Figure 3.7: Frequency-Angular wavenumber dispersion curves using various analytical methods (1) Exact, (2) UAM, (3) RAM, (4) SRAM, where the breakdown points of the solutions are marked with crosses (x).

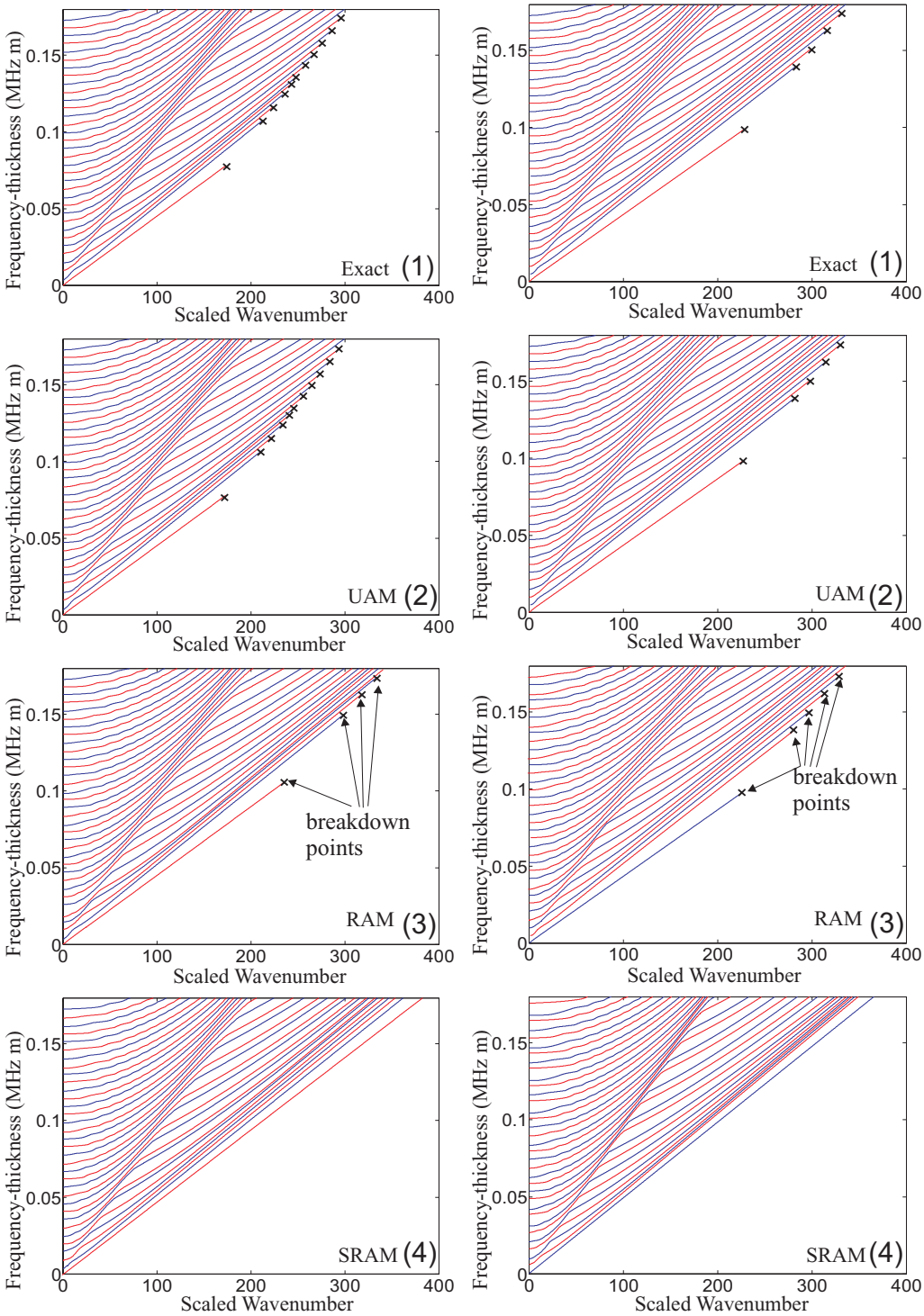

(c) Every 5^{th} mode of Lamb-type circumferential waves: $r_2/r_1 = 1.15$.

(d) Every 5^{th} mode of Lamb-type circumferential waves: $r_2/r_1 = 1.25$.

Figure 3.7: (**Continued**) Frequency-Angular wavenumber dispersion curves using various analytical methods (1) Exact, (2) UAM, (3) RAM, (4) SRAM, where the breakdown points of the solutions are marked with crosses (x).

3.4 Comparison of Asymptotic Methods

3.4.1 Accuracy

A simple observation of the dispersion curves reveals few differences between the results obtained using the exact method and the asymptotic methods, shown in Fig. 3.7. However, some errors at very low frequencies are expected as noted in Sec. 3.1. This is because the Debye's asymptotes used for the substitution of the Bessel functions are intended for large-orders and large-arguments, and thus they could easily hit their limits at low frequencies. Although the exact solution, which is extremely stable at low frequencies, can in theory be used instead of the asymptotic solutions at these frequencies to achieve an all-round accuracy for the dispersion curves, but for comparison purposes of each asymptotic method, this is not implemented at this stage.

To investigate the accuracy of various asymptotic methods preciously, a more specific analysis is conducted to measure the relative error of the dispersion curves. The relative error is defined as the absolute percentage difference in angular wavenumbers ν between the asymptotic ($\nu_{(asymptotic,m,\omega)}$) and the exact ($\nu_{(exact,m,\omega)}$) methods, and it is normalised by the angular wavenumber of the exact method:

$$\text{Relative Error}(\%) = \frac{\nu_{(asymptotic,m,\omega)} - \nu_{(exact,m,\omega)}}{\nu_{(exact,m,\omega)}} \cdot 100. \tag{3.28}$$

The percentage error is measured for every mode m at a frequency step, $\delta\omega$. This percentage error can then be mapped over the area of the corresponding dispersion curves for each asymptotic method, presented in a three-dimensional plot.

Unfortunately, the calculations of the relative error are limited to positions where the exact solution is computable. As a result, only modes which exist at frequencies that are lower than the breakdown frequency of the first fundamental mode when using the exact method are compared. The area of investigation is indicated by the rectangular boxes in the dispersion curves, shown in the plot (a) of Figs. 3.8 to 3.11.

As the asymptotic solutions become increasingly accurate with increasing frequency, the comparison in these rectangular boxes between various asymptotic and exact methods should have higher errors relatively compared to that at higher frequencies; therefore the comparison is representative of the investigation of the accuracy for these methods in the worse case scenario.

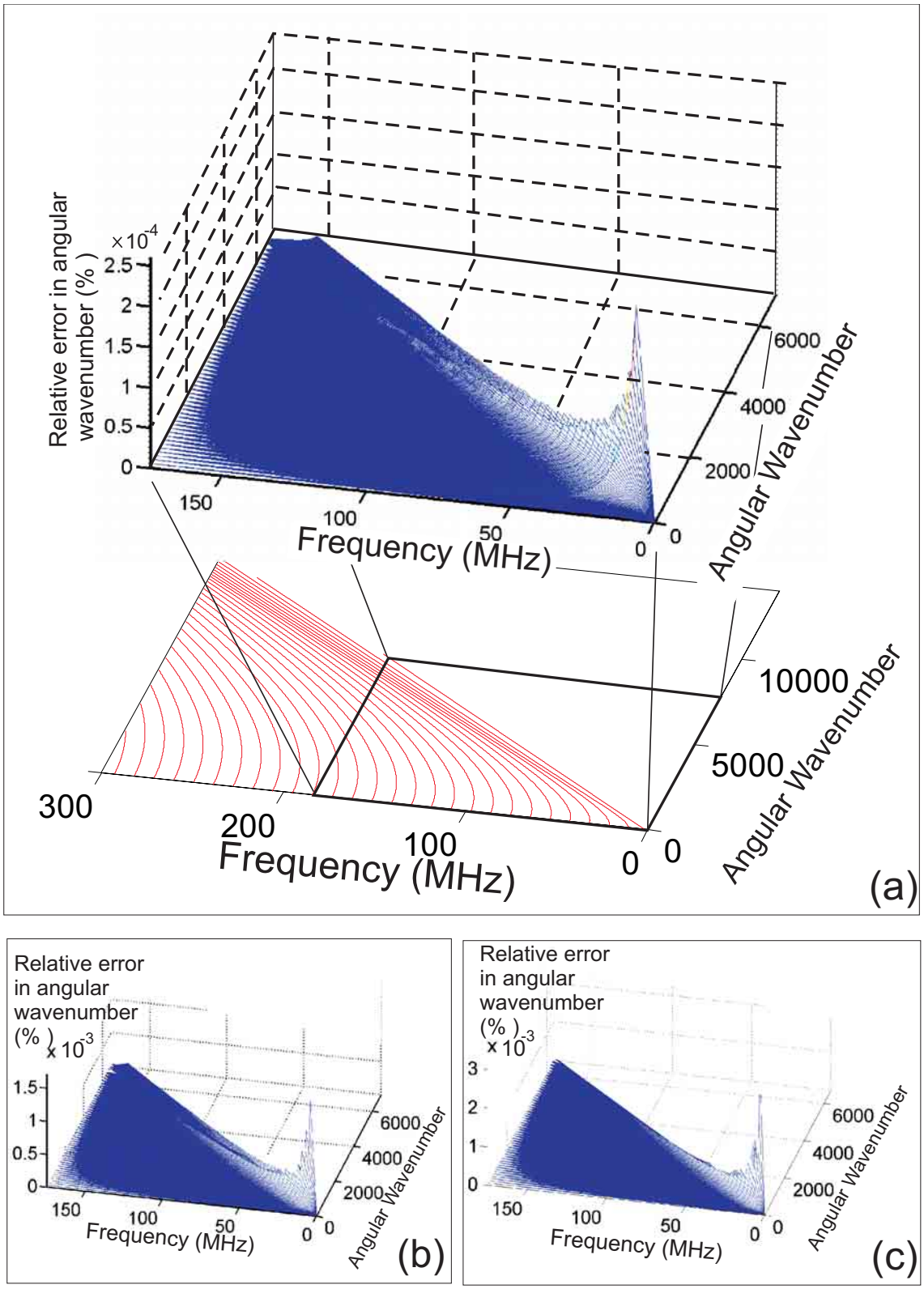

Figure 3.8: Measurements of the relative percentage error in angular wavenumber ν of the circumferential shear horizontal dispersion curves in an annular steel structure (geometry 2 : $r_2/r_1 = 1.15$). (a) 3-D error plot of the UAM, projecting over the calculation area of the exact dispersion curves. (b) 3-D error plot of the RAM. (c) 3-D error plot of the SRAM.

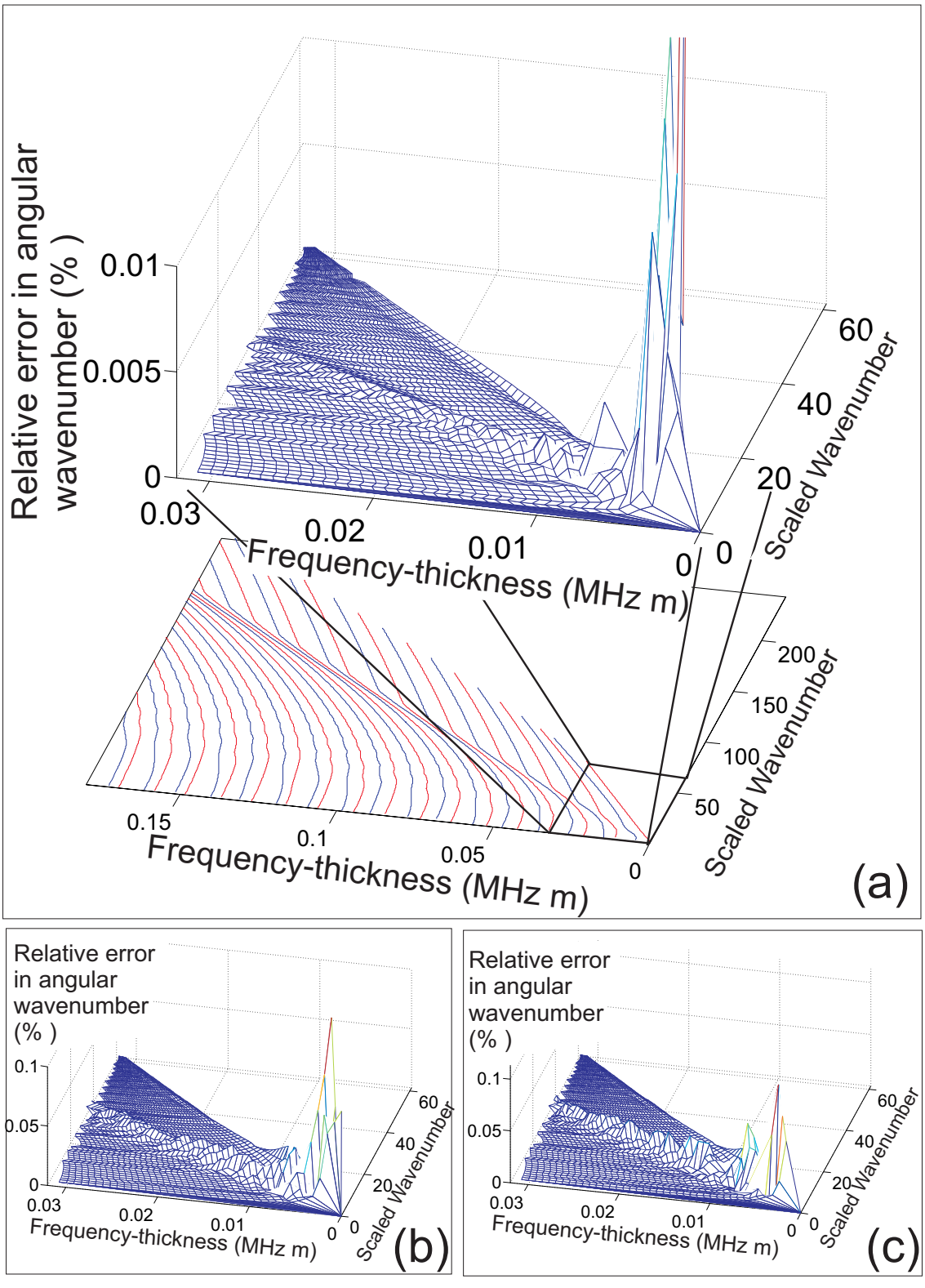

Figure 3.9: Measurements of the relative percentage error in angular wavenumber ν of the circumferential Lamb-type dispersion curves in an annular steel structure (geometry 1 : $r_2/r_1 = 1.05$). (a) 3-D error plot of the UAM, projecting over the calculation area of the exact dispersion curves. (b) 3-D error plot of the RAM. (c) 3-D error plot of the SRAM.

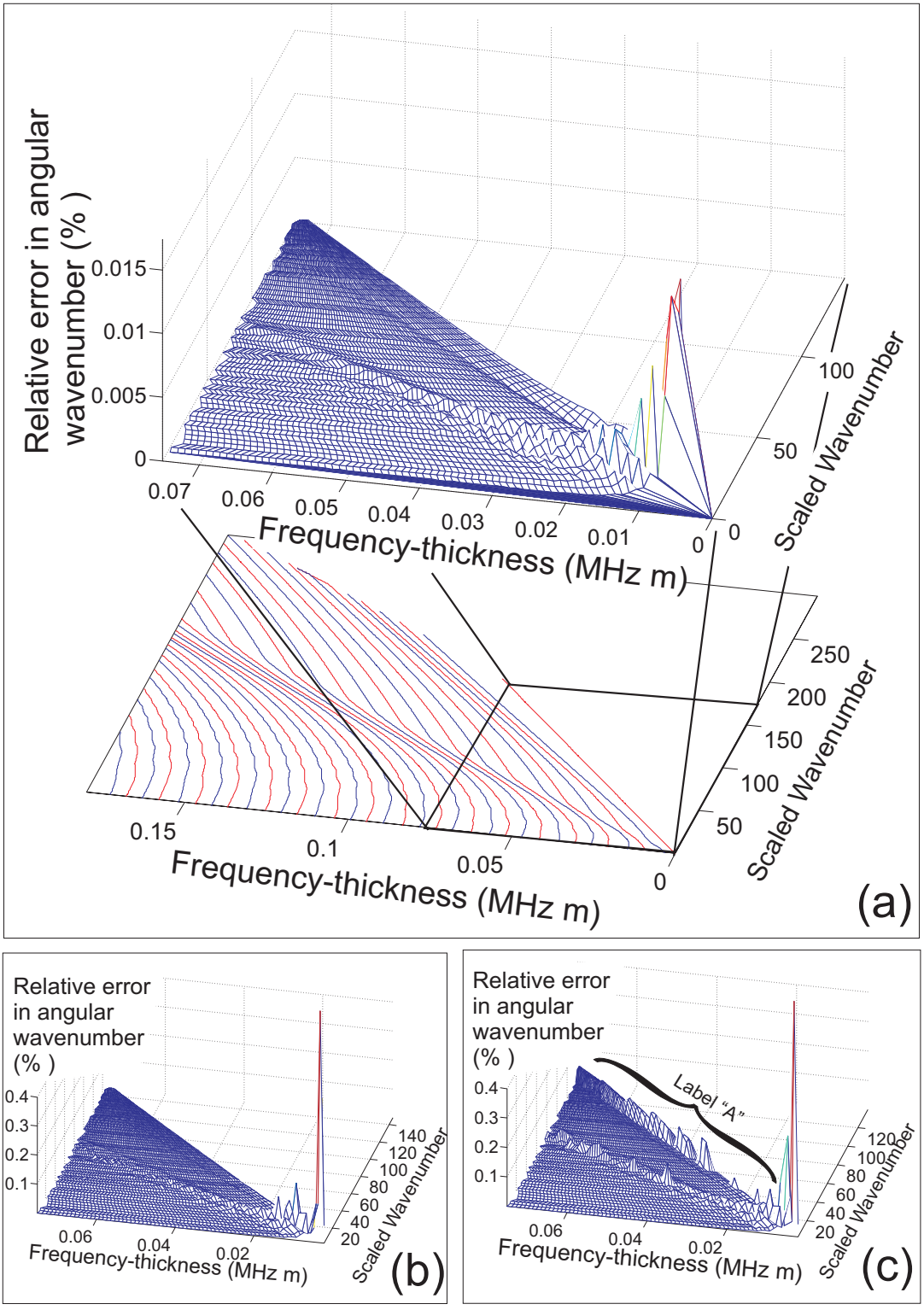

Figure 3.10: Measurements of the relative percentage error in angular wavenumber ν of the circumferential Lamb-type dispersion curves in an annular steel structure (geometry 2 : $r_2/r_1 = 1.15$). (a) 3-D error plot of the UAM, projecting over the calculation area of the exact dispersion curves. (b) 3-D error plot of the RAM. (c) 3-D error plot of the SRAM.

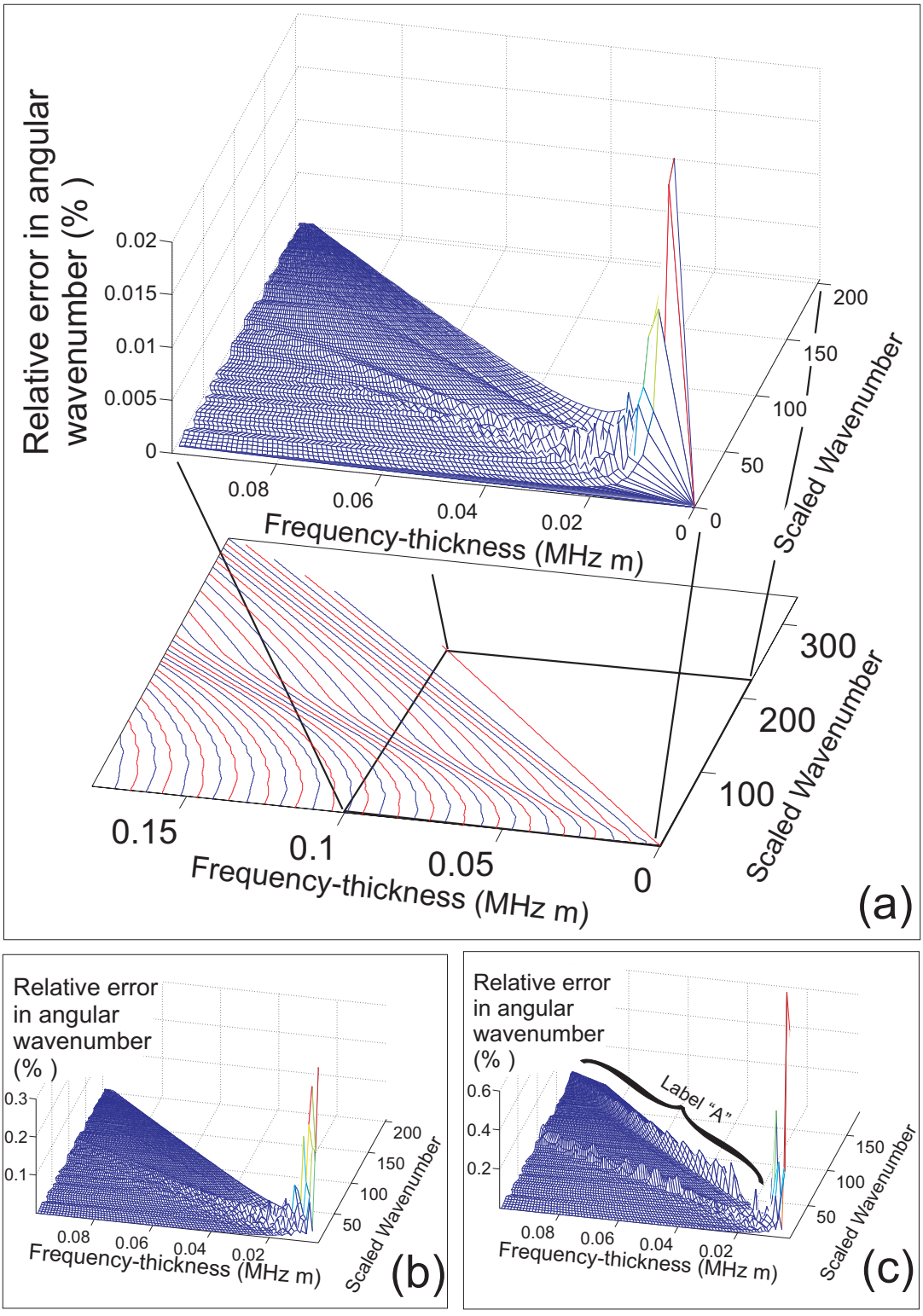

Figure 3.11: Measurements of the relative percentage error in angular wavenumber ν of the circumferential Lamb-type dispersion curves in an annular steel structure (geometry 3 : $r_2/r_1 = 1.25$). (a) 3-D error plot of the UAM, projecting over the calculation area of the exact dispersion curves. (b) 3-D error plot of the RAM. (c) 3-D error plot of the SRAM.

SH waves

Fig. 3.8 shows a three-dimensional error plot of the SH mode using geometry 2 and all three asymptotic methods; the 3-D error plot is assembled using approximately 500 grid points in each axis. For the UAM shown in Fig. 3.8(a), the solutions are extremely accurate, having a relatively error of less than 0.00005% generally. The relatively high level of error in the very low frequency region is anticipated because of the use of high-order high argument asymptotes for the Bessel functions.

For the regional asymptotic methods (i.e. the RAM and SRAM shown in Figs. 3.8[b - c]), it can be seen that the level of error is in general slightly higher than that of the UAM. This is attributed to the further simplification of the dispersion relation used in these methods. Additionally, a relatively high level of error is also detected at which the boundaries between the two neighbouring regions are located, for example at $\nu = c_T r_1$. This is caused by the fact that the expressions of the dispersion relation in different regions become less accurate at these boundaries where they reach their limits. This results in a slight discontinuity between any two regions. The effect of this discontinuity has been minimised by using the dispersion relations of the transitional regions in which their solutions are typically uniform across the neighbouring regions. This effect may further reduce by taking a higher constant value in Eqn. 3.6 to increase the size of the transitional region area, however this increases the complexity of the calculations at the same time.

Lamb-type waves

Figs. 3.9 to 3.11 present the three-dimensional error plots of the Lamb-type modes for the various asymptotic methods associated with the geometries 1, 2 and 3 respectively. These 3-D plots are assembled using a different number of grid points depending on the fd range of investigation. In the Lamb-type case, the percentage error is significantly higher than that of the SH case. This is because the Lamb-type dispersion relations are far more complex than those of the SH case.

In general, the accuracy of the solution depends on the accurate description of each term in the dispersion relation. In the asymptotic methods, these terms are substituted with asymptotes, and in cases of the SRAM, these terms may even be further simplified by utilising only the leading orders of the asymptotes. It can be seen that the total error can be easily accumulated when calculating the dispersion function that comprises many asymptotic terms.

The sharp peaks of the error amplitude at the very low frequencies are due to the same reason as the SH case. The amplitude of these sharp peaks has been truncated to enhance

the visual details in the 3-D error plot for the rest of the dispersion curve area. The high level of error at the boundaries between the regions is clearly visible. This is even more obvious in Regions VIII and IX of the SRAM (Fig. 3.2), where the dispersion relations have been heavily simplified as the partial waves on the inner and the outer surfaces become weakly coupled; this areas are indicated by label "A" in, for example, Figs. 3.10(c) and 3.11(c).

The solutions for the UAM generally have an error of less than 0.001% in most parts of the dispersion curves, and a slightly higher level of error is observed at locations where the curves are very close to each other. On the other hand, for the regional methods, solutions have an error of typically less than 0.01%, except at locations near the boundaries between two regions. Overall, the RAM appears to behave better near the boundaries than the SRAM. In spite of this, the worst accuracy near the boundaries occurs at a very low frequency and has a value of no more than 0.1%, which in most cases is sufficient to provide an extremely good prediction to the dispersion relation.

To sum up, simplification of the dispersion relations using all three asymptotic methods has been shown to retain a high degree of accuracy. This accuracy generally increases further with increasing frequency. Therefore even in the area near to the boundaries, the accuracy is exceptionally high in the high frequency region.

3.4.2 Speed

On top of the asymptotic methods being accurate, they are also extremely robust. The speed of the tracing routine is compared between the exact and asymptotic methods. Fig. 3.12 shows a comparison of the time in seconds that is required to trace the first 45 Lamb-type modes of the dispersion curves for the geometry 1 using various methods. An upper frequency limit is set at 32MHz. The calculations were performed with the tracing routine described in Fig. 3.6 using a computer with a Pentium IV 2.4GHz processor and 512MBytes of random access memory.

In the UAM, Airy functions are used instead of the Bessel functions; they are much easier to compute numerically, resulting in halving the tracing time compared to the exact method. A further reduction in the tracing time is achieved when using the RAM which expresses the dispersion relations in each region separately; this eliminates the need to assemble the eigen-problem matrix D in each iteration, allowing the RAM to speed up significantly. In the case of tracing the dispersion curves using SRAM, the solutions are well-conditioned, where the moderately oscillating amplitude can substantially allow the number of iterations needed for convergence to be reduced.

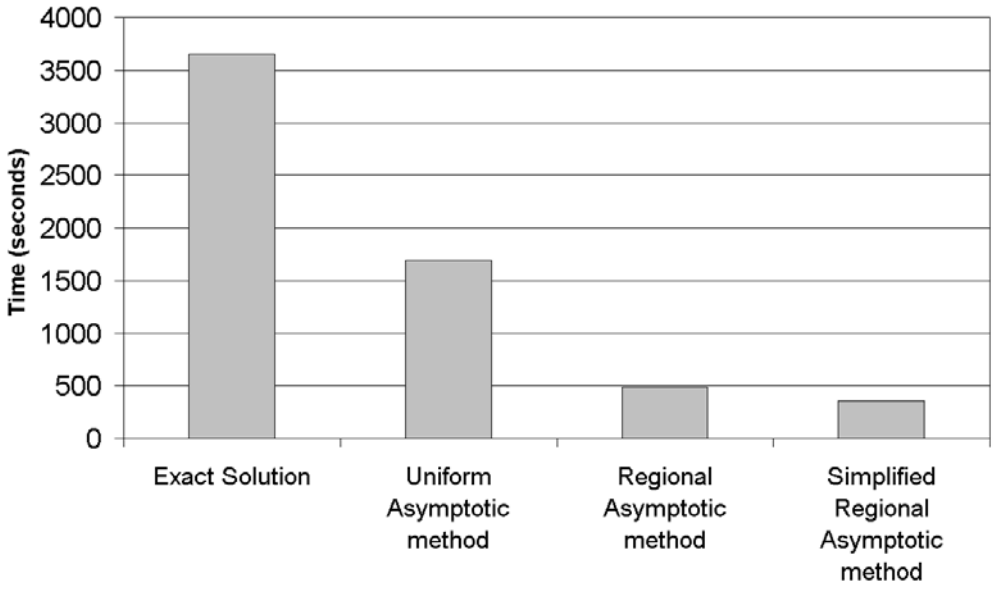

Figure 3.12: Time for tracing the Lamb-type circumferential dispersion curves for a 1mm thick, 20mm inner radius annulus steel structure using exact and Asymptotic methods.

3.5 Summary

This chapter has shown that the normally unstable exact dispersion relation of the circumferential guided elastic waves can be made stable by using asymptotic methods, allowing the solution to be extracted at all frequencies and geometries. The dispersion relations in these asymptotic methods can, in general, be related to the nature of the partial waves at different parts of the dispersion curves.

The steps of a numerical scheme to trace dispersion curves have been summarised. Using this tracing routine, numerical examples of several curvature radius cases, using both the exact and asymptotic methods, have been presented. Subsequently, the type of instability that causes the breakdown of the exact dispersion relation have been analysed using these examples. Furthermore, both the accuracy and the robustness of the solutions have been examined thoroughly for all three asymptotic methods.

Chapter 4

Curvature Effect on Propagation Properties in Unloaded Plates

Having demonstrated the accuracy and the effectiveness of the asymptotic methods in the previous chapter, the curvature effect on the propagation properties can now be thoroughly analysed at any frequency and for any wave mode using these solutions. In this chapter, a quantitative method to calculate the difference in phase velocity between straight and curved plates is introduced. The outcome of this provides a plain graphical interpretation representing the influence of the curvature at various frequencies for a particular mode; these graphs subsequently allow one to pick the best excitation frequency at which the mode is best suited for a particular engineering application.

In the second half of this chapter, the physical behaviour of the wave modes in a curved plate, such as the mode shapes, is examined; this behaviour may then be related to the propagation properties. Additionally, the features of the dispersion curves for a curved plate are explained using the" method of bounds". This chapter is based on work published in Fong *et al.* [105].

4.1 Analytical Predictions of the Curvature Effect

To analyse the effect of curvature, the phase velocities of wave modes in both straight and curved plates must first be calculated numerically. In the case of the straight plates, solutions of the dispersion curves can be readily obtained from a general purpose commercial program, Disperse [98]; whereas for the case of the curved plates, the solutions are evaluated numerically in the $\omega - \nu$ domain using the numerical tracing routine described in Sec. 3.2, and are subsequently converted into the $V_{ph} - \omega$ domain using Eqn. 3.26. The solutions were calculated using the exact formulation (Sec. 2.2.5) where possible, and

the asymptotic methods (Sec. 3.1) where the exact solution becomes unstable. This ensured that the calculations of these dispersion curves in any frequency range are extremely accurate.

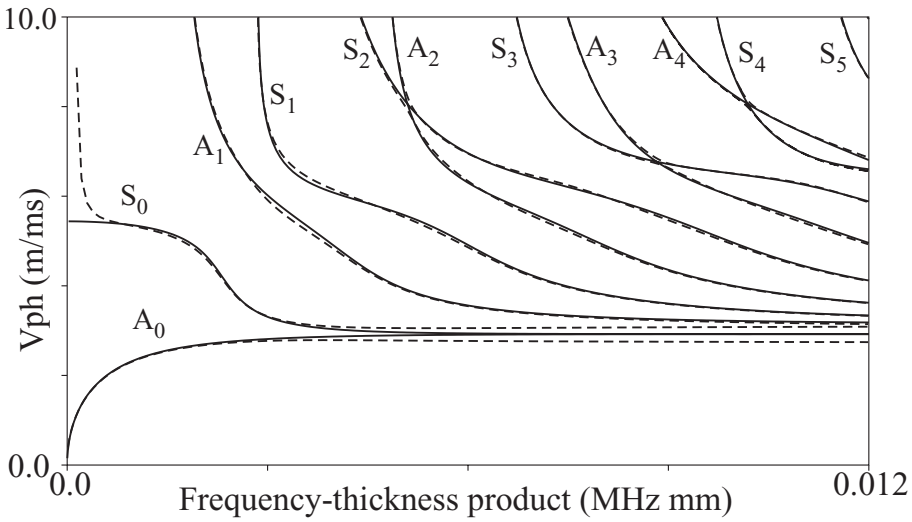

Figure 4.1: Phase velocity dispersion curves of an aluminium straight plate (Solid lines) of 3mm thickness (d) and an aluminium curved plate (Dashed lines), d = 3mm and r_1 = 0.02mm. The curves are labelled according to the straight plate system.

Fig. 4.1 shows the phase velocity dispersion curves for both straight and curved plate cases. The Lamb modes in a straight plate can, in general, be separated into two families depending on the symmetry of the displacement mode shapes with respect to the mid-plane of the plate. The labelling of Lamb modes in a straight plate is in accordance to this symmetry property, with A and S correspond to the antisymmetric and symmetric modes. Only the curves for the straight plate are labelled in Fig. 4.1. However, although dispersion curves of the curved plate may be found at locations close to those of their straight plate counterparts as can be seen in Fig. 4.1, these modes cannot be labelled in the same way.

For a curved plate system, there is no absolute distinction between symmetric and anti-symmetric mode shapes, due to the difference in curvature between the inner and outer surfaces. The plate no longer possesses a symmetry through the thickness and thus these modes become "quasi plate modes". As a result, the through-thickness displacement fields of these curved plate modes correspond only to "near symmetric" or "near anti-symmetric" distribution, and these two natures may interchange from one section to another along the dispersion curve of a specific curved plate mode. This interchanging of symmetrical natures is linked to a repulsion phenomenon of the dispersion curves, which will be discussed later in Sec. 4.3.3. Nevertheless, the dispersion curves are often very similar to those of the straight plate case.

The difference between these curves can be very subtle, and may be detected only upon careful inspections at certain frequencies. Therefore the significance of the curvature effect on wave modes in an unloaded plate may be quantified by comparing the phase velocity V_{ph} directly as a function of frequency between straight and curved plates over a range of curvatures using the following relationship:

$$\text{Normalised diff. in } V_{ph}(\%) = \frac{abs[V_{ph}(\text{straight pl.}) - V_{ph}(\text{curved pl.})]}{V_{ph}(\text{straight pl.})} \cdot 100. \tag{4.1}$$

In a curved plate system, the wave properties such as the linear phase velocity calculated using Eqn. 3.26 vary depending on the radial position at a particular frequency. Therefore before the phase velocities between the straight and curved plates can be compared, the circumferential wave speed must be recalculated along the mid-line position through the plate thickness (r_{mid}) so that it is compatible with that of the straight case; the corresponding equations for calculating the linear phase and group velocities are:

$$V_{ph}(m/s) = \frac{\omega}{\nu} \cdot r_{mid} \tag{4.2}$$

$$V_{gr}(m/s) = \frac{\partial\omega}{\partial\nu} \cdot r_{mid} \tag{4.3}$$

As an example, the first four fundamental modes are investigated here in this chapter, namely the A_0, S_0, A_1 and S_1 modes in the straight plate; these modes are commonly used for non-destructive evaluation, therefore have a higher investigation value. Additionally, their dispersion curves are of the least complicated nature as they intersect with other modes in the phase velocity-frequency domain for both the straight and curved cases, thus allowing a direct comparison between these two cases easily. By contrast, it would be a lot harder to compare the higher order modes directly because the symmetric and the neighbouring anti-symmetric modes cross each other typically at phase velocity higher than the longitudinal bulk velocity in the straight case, while the curved plate counterparts do not cross. A detailed examination of the mode crossing phenomenon is presented in Sec. 4.3.3.

The comparisons are carried out using dispersion curves calculated for a 1mm thick aluminium plate, and with the material properties of $C_L = 6320m/s$, $C_T = 3130m/s$ and density, $\rho = 2700kg/m^3$. The comparison of the phase velocity for each of these modes forms a three-dimensional surface plot, shown in Fig. 4.2, with a frequency range of 0 to 6MHz, and an inner radius range of 0 to 0.1m, where the parametric surface represents the amount of the phase velocity differences between the straight and curved plates.

In all four cases, the dispersion profile of the normalised phase velocity difference is not dependent on the inner radius which also known as the curvature radius in this thesis;

their amplitudes decay rapidly with increasing radius, showing as expected, that the phase velocity converges to the velocity of the straight plate case as the curvature reduces. Additionally, it can be observed that the velocity difference is significantly higher in all four cases at the very low frequencies.

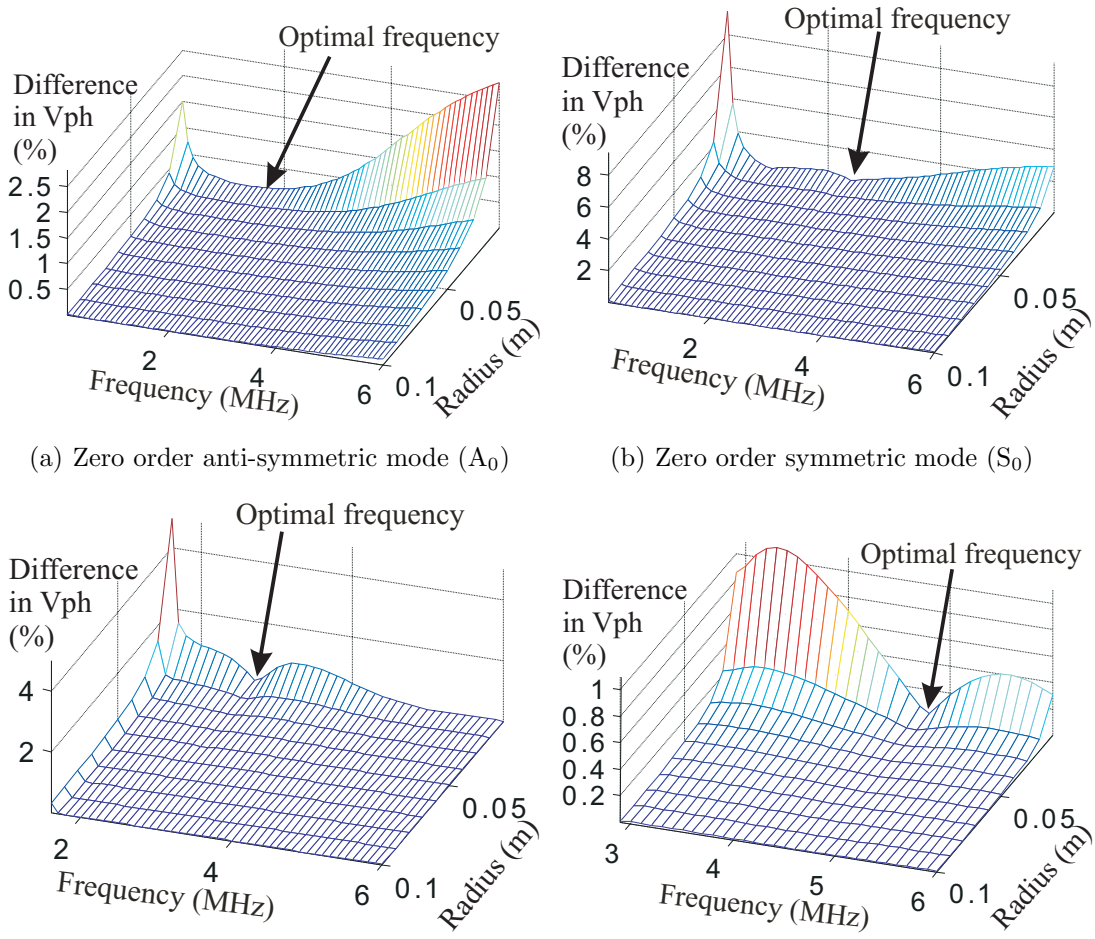

(a) Zero order anti-symmetric mode (A_0)

(b) Zero order symmetric mode (S_0)

(c) First order anti-symmetric mode (A_1)

(d) First order symmetric mode (S_1)

Figure 4.2: Effect of curvature on the phase velocity of (a) A_0, (b) S_0, (c) A_1 and (d) S_1 modes. The surface plots show the percentage difference in phase velocity V_{ph} between the straight and curved plates as a function of frequency at the mid-wall radius (r_{mid}) for a 1mm thick aluminium plate. The solutions of the phase velocity were calculated using analytical methods detailed in the previous chapters.

In the case of the A_0 mode, its phase velocity tends to zero as the frequency reduces, as a result, the percentage differences may appear to be substantially larger when the absolute phase velocity difference is normalised with this phase velocity value at these low frequencies.

In the case of all other modes, both wave modes of the curved and straight plates become non-propagating at their cut-off frequency (for example shown in Fig. 4.1), and their phase velocity tends to infinity. Additionally, the "out of plane" (radial) displacement field of this

"quasi-S_0" mode becomes antisymmetric, while the "in-plane" (tangential) displacement, which usually has a very small amplitude, remains symmetric. This mode corresponds to the vibration "breathing mode" of a pipe, where it can only vibrate as a whole and no energy can be transmitted from one location to another around the circumference. Below the cut-off frequency, the surface boundary condition can no longer support this type of wave motion.

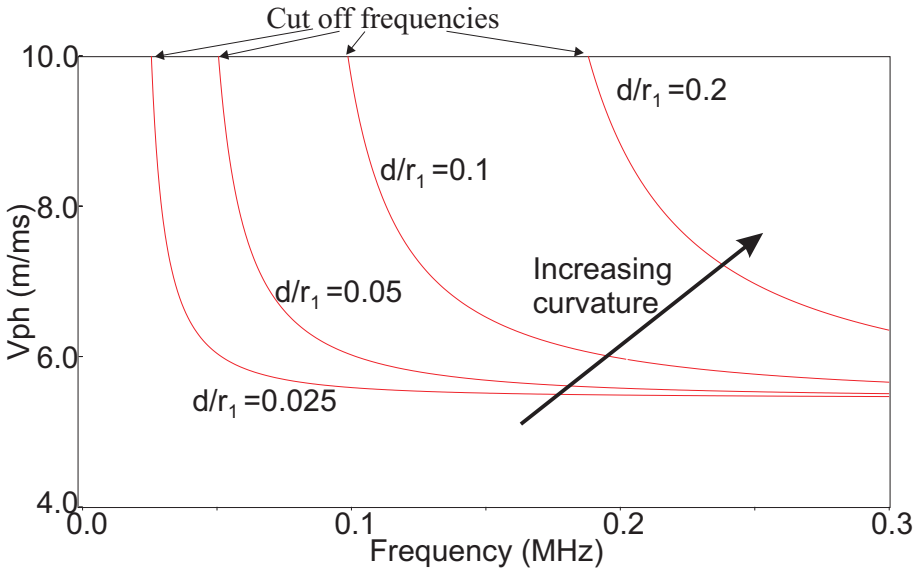

Figure 4.3: Dispersion curves of the "quasi-S_0" mode for aluminium plates of a range of thickness to radius ratios (d/r_1) at location near their cut off frequency.

The cut-off frequency of the curved case in general increases with increasing thickness to radius ratio of the curved plate (i.e. $\propto$ curvature), as shown in Fig. 4.3. This phenomenon can be attributed to the change of curvature in the plate system, and consequently alters the nature of the waves that interact with the boundaries of the propagation system, resulting in a shift of cut-off frequency of the wave mode. The phase velocity changes rapidly close to the cut-off frequency; for this reason, the difference between the straight and curved cases at location close to their cut-off frequency can appear to be very large in the higher order mode cases when comparing.

Using the dispersion profile in these three-dimensional plots shown in Fig. 4.2, it is possible to locate a frequency at which the mode is least sensitive to the curvature. The advantage of performing NDT inspection at this frequency is that the received echoes would allow one to locate the corresponding features precisely regardless of whether curvature exist along the propagation direction. These frequencies for the four modes of interest are labelled as "optimal frequency" and are indicated in Fig. 4.2.

4.2 Physical Properties of Waves in Curved Waveguides

As shown earlier in the previous sections, the phase velocity depends on both the frequency and curvature radius. The through-thickness displacement mode shapes of a particular mode can govern its phase velocity at a given frequency. In this section, the relationship between the change of the mode shapes and that of the phase velocity as the plate curvature changes is investigated.

One major factor of this curvature dependency is the difference in curvature between the boundaries at the top and bottom surfaces. As a result, the displacement mode shape distribution for the curved plate modes tends to shift towards either surface compared to the straight plate case; there is no longer a symmetry in distribution along the mid-line of the thickness. The level of this mode shape shift might generally increase with increasing curvature.

As an illustration, the displacement mode shapes of the fundamental zero order symmetric (S_0) and anti-symmetric (A_0) modes at the selected frequencies may be compared visually between the straight (thickness: 1mm) and curved (thickness: 1mm, inner radius: 10mm) plates, as shown in Fig. 4.4.

It can be seen that both the A_0 and S_0 modes in the case of the straight plate converge to the surface Rayleigh wave speed at high frequencies, however these wave modes do not behave in the same way as soon as the curvature is introduced. Once again using the partial waves technique, discussed in Sec. 3.1.4, to decompose a mode into longitudinal and shear partial waves that interact with the boundaries at the inner and outer surfaces, it is possible to comprehend the physical behaviour of these two modes.

The idea of the asymptotic regions in Fig. 3.2 and the corresponding behaviour of the partial waves in Fig. 3.4 will be referred to considerably in this section for the explanation of various phenomena. Here the behaviour of the "quasi-A_0" and "quasi-S_0" modes in three different curvature ranges is considered, including a moderately curved case, and cases when the curvature is either very large or very small.

Moderate Curvature Radius

When a plate is moderately curved, the dispersion curve of the "quasi-S_0" mode appears in Region VIII (Fig. 3.2) at high frequencies; in this region, only the partial waves at the inner surface are completely inhomogeneous and have amplitudes much greater than that at the outer surface. As a result, most of the energy concentrates only on the inner surface at these frequencies as shown in Fig. 4.4, hence the corresponding phase velocity can be thought of as the phase velocity for the Rayleigh wave on the concave surface [74].

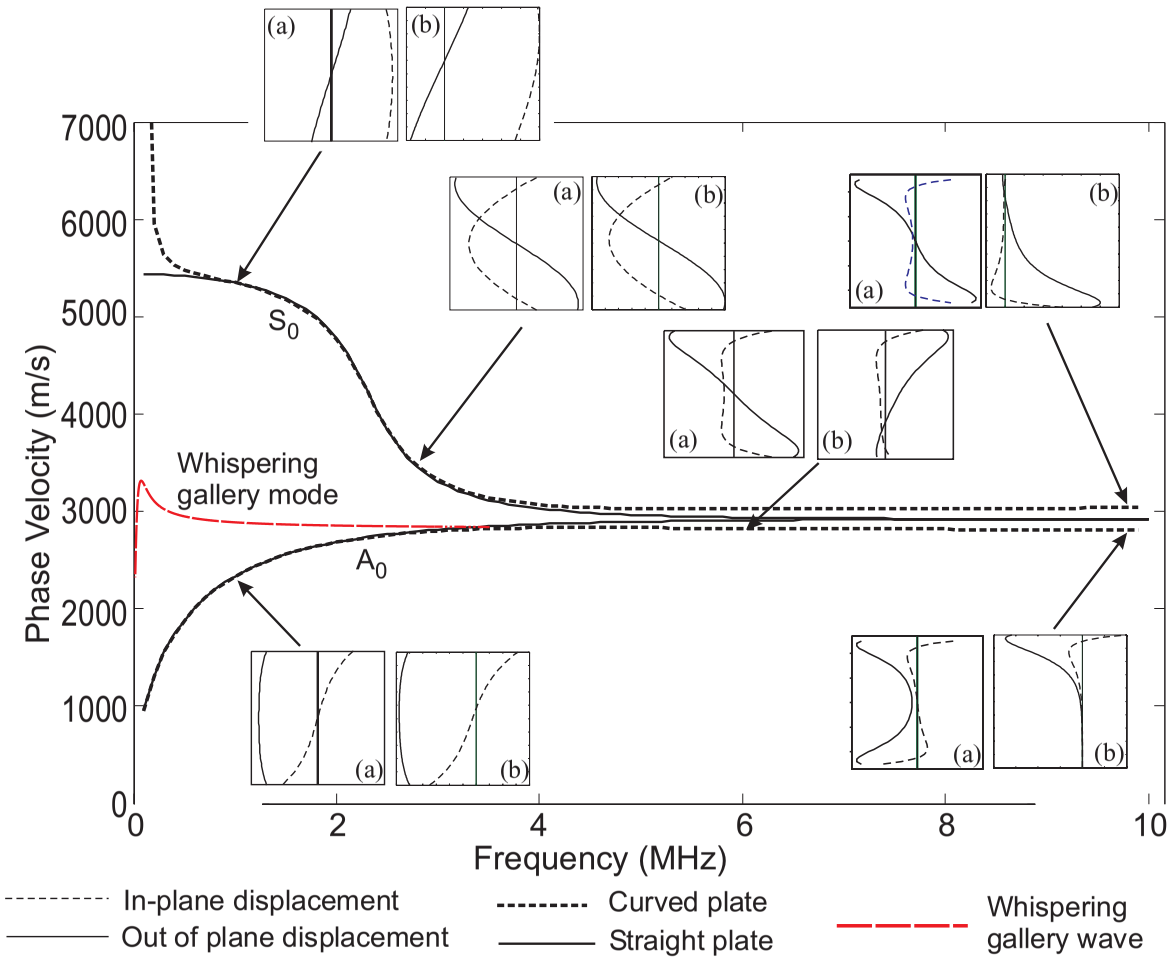

Figure 4.4: Phase velocity dispersion curves of the two fundamental Lamb type modes for an aluminium straight plate (1mm thick, solid lines) and the equivalent "quasi-modes" of the curved plate (1mm thick, 10mm radius, dotted lines). The through-thickness displacement mode shapes are also shown at selected frequencies for (a) a straight plate and (b) a curved plate, where the top and the bottom of the graph correspond to the outer and inner surfaces of the curved plate respectively and the horizontal axis shows the arbitrary amplitude of the out-of-plane displacement (solid line) and in-plane displacement (dashed line).

Small Curvature Radius

On the other hand, when the curvature of a plate is large such as that used for Fig. 3.7d (d/r_1=0.25), all higher order modes tend asymptotically to the "quasi-S_0" mode in Region VIII at high frequencies, where they share the same physical behaviour. And as a result, when the curvature of the system is large, these higher order modes would eventually become the Rayleigh wave on the concave surface in the same way as the "quasi-S_0 mode as the frequency increases.

Large Curvature Radius

When the curvature of the system is small, the width of Region VIII narrows and the "quasi-S_0" mode crosses the boundary $\nu = \hat{\omega}_4$ into Region IX, where partial waves on both the inner and outer surfaces become inhomogeneous. As expected, the mode shapes of the "quasi-S_0" and "quasi-A_0" modes and their corresponding linear phase velocities may become similar to each other in this region. In addition, the curves of the higher order modes can no longer converge to the "quasi-S_0" mode at high frequencies, but instead they converge asymptotically to a single wave speed in the Region VIII.

As $r_1 \rightarrow \infty$, the properties of the "quasi-S_0" and "quasi-A_0" modes would eventually coincide and Region VIII disappears as the boundaries $\nu = \hat{\omega}_3$ and $\nu = \hat{\omega}_4$ merge, while the higher order modes converge to the shear bulk velocity.

Whispering Gallery Wave

For the "quasi-A_0" mode, the partial waves become inhomogeneous on both surfaces at high frequencies. Therefore the displacement decays exponentially towards the mid-plane from both surfaces; the decay is represented by the nature of the Bessel function of the second kind $Y_\gamma(x)$ where $\gamma > x$. However, due to the curvature effect, the decay of displacement amplitude away from the outer surface decays much faster than that on the inner surface. In this case, as the frequency increases, most of the energy concentrates relatively on the outer surface, forcing the phase velocity to match the velocity of the Rayleigh wave on the outer surface, or the whispering gallery wave [106].

The pure whispering gallery wave can be easily calculated by considering a rod where waves propagate in the circumferential direction. This eliminates the boundary condition at the inner surface to simulate the condition where the partial waves are decoupled from the inner surface of the curved plate at high frequencies. Furthermore, since the boundary conditions ($\sigma_{\theta\theta}$ and $\sigma_{r\theta} = 0$) are axially symmetric, the components associated with the outgoing radiation are not required and the general solutions (Eqn. 2.12) can be reduced

to the following forms:

$$\varphi(r,\theta) = [a_1 J_\nu(k_L r)]e^{i\nu\theta}, \qquad \psi(r,\theta)_{\text{solid}} = [a_2 J_\nu(k_T r)]e^{i\nu\theta}. \tag{4.4}$$

The secular equation of the dispersion relations is constructed by substituting these general solutions back into Eqn. 2.17. The solution of first fundamental mode of this secular equation is the whispering gallery wave. The dispersion curve can then be extracted as described in Sec. 3.2.

It can be seen in Fig. 4.4 that at high frequencies the "quasi-A_0" mode converges to the speed of the whispering gallery mode, indicating that the energy of the "quasi-A_0" mode is trapped very close to the outer surface.

Mode Shapes Comparison

In general, the degree of difference in the displacement mode shapes between the straight and curved plates can be linked directly to the difference in the phase velocity. This is further illustrated, for example, in Fig. 4.2(a), at 1MHz and 6MHz for the "quasi-A_0" mode, where the differences in phase velocity correspond roughly to the minimum and maximum respectively within the range of interest. At these two frequencies, the "quasi-A_0" mode, as shown in Fig. 4.4, is found to have the minimum and maximum differences in displacement mode shapes between the straight and curved plates when compared visually. It is thought that the study of the mode shape similarity can provide an interesting insight into the curvature effect.

The similarity of the mode shapes can be investigated using a "displacement dot product" method modified from Beard [2], which involves comparing the two "out-of-plane" ($\bar{u}_x$ and $\bar{u}_r$), and the two "in-plane" ($\bar{u}_z$ and $\bar{u}_\theta$) through-thickness displacement vectors between the straight and curved plates. The $\bar{}$ denotes the vector of through-thickness amplitudes, and x and z are the "out -of-plane" and "in-plane" directions of a straight plate respectively, while r and θ are the corresponding directions of a curved plate (see Fig. 4.5 for illustration).

Mathematically the similarity of the displacement vectors between the straight and curved plates can be described by a similarity factor "S" which is evaluated by taking the average dot product of the vectors in the "in-plane" and "out-of-plane" directions in turn (Eqn. 4.5). The similarity "S-factor" equals zero if the mode shapes under comparison are identical, and equals one if they are completely different.

$$S = 1 - \frac{1}{2}\left(\frac{(\bar{u}_z \cdot \bar{u}_\theta)}{|\bar{u}_z||\bar{u}_\theta|} + \frac{(\bar{u}_x \cdot \bar{u}_r)}{|\bar{u}_x||\bar{u}_r|}\right). \tag{4.5}$$

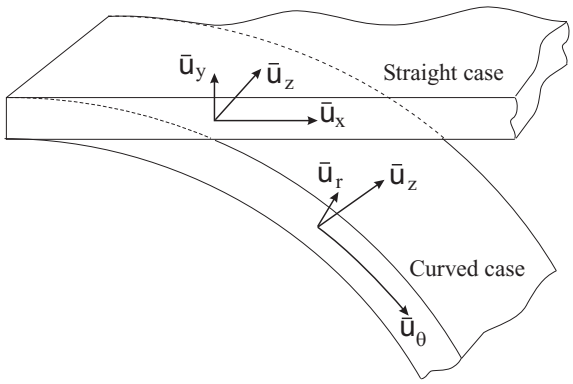

Figure 4.5: Coordinates system of the straight and curved plates.

The "S-factor" was calculated for the S_0 and A_0 modes for a 1mm thick, 10mm inner radius curved aluminium plate compared with a straight 1mm thick aluminium plate, in a frequency range of 0-10MHz. The displacement mode shapes vectors were discretised into 101 equal distance points across the wall thickness. The results, together with the phase velocity percentage differences for the corresponding curvature and frequency range, are presented in Fig. 4.6.

In both cases, the "S-factor" follows the trend of the phase velocity percentage difference. Additionally, the amplitude of the "S-factor" can be roughly correlated to that of the phase velocity percentage difference. Although there is a qualitative similarity between the two parameters where an "S-factor" of 0.3 is approximately equivalent to 4% of phase velocity difference (shown in Fig. 4.6), they are not in a simple relationship; this may be quantified by taking the ratio of the difference in phase velocity to the "S-factor", as shown in Fig. 4.7. Note that the vertical scale of the figures has been magnified to reveal the differences. It can be seen that the difference between the two parameters is bigger particularly at frequencies where there are subtle changes in the phase velocity, such as 4-6MHz for the A_0 mode and 2-4MHz for the S_0 mode.

Nevertheless, this sudden increase in amplitude of the "S-factor" and the phase velocity difference can provide a fairly good indication of the frequency at which the modes start to converge to the Rayleigh wave. This is because in this frequency range, the curved plate mode has the majority of its energy shifted towards one surface as discussed earlier, while the straight plate mode remains symmetric, causing a sudden increase in the property difference between these two cases.

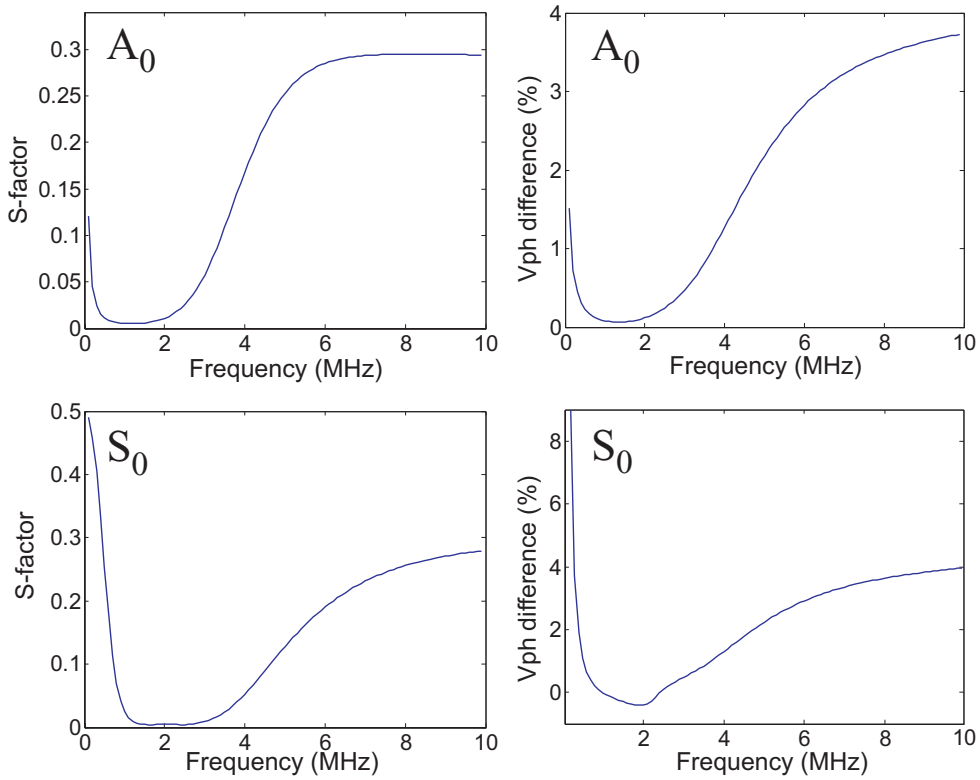

(a) Mode shape difference: "S-factor" (b) Phase velocity difference

Figure 4.6: Difference in mode shapes between a curved (1mm thick and 10mm inner radius) and a straight (1mm thick) plates for the A_0 (top) and S_0 (bottom) modes.

4.3 Characteristics of Dispersion Curves in Curved plates

4.3.1 Concept of the Method of Bounds

For the Lamb wave dispersion curves of a straight plate in vacuum, Mindlin [107] instigated an ingenious method to characterise the basic features of the curves using the "method of bounds". The idea of this method is based on mapping the so-called "bounds" to the dispersion curves of the coupled guided wave system. In the case of Lamb-type propagation in a straight plate, Mindlin defined the "bounds" as:

- the dispersion curves of an uncoupled guided wave system, supporting purely one of their fundamental wave propagation types (i.e. either the longitudinal or shear type propagation) that satisfy all two traction-free boundary conditions at the plate surfaces.

The system of "bounds" allows one to visualise the asymptotic behaviour of the curves to the "bounds" according to their physical characteristics, and to a large extent the "bounds" guide the dispersion curves of the coupled system.

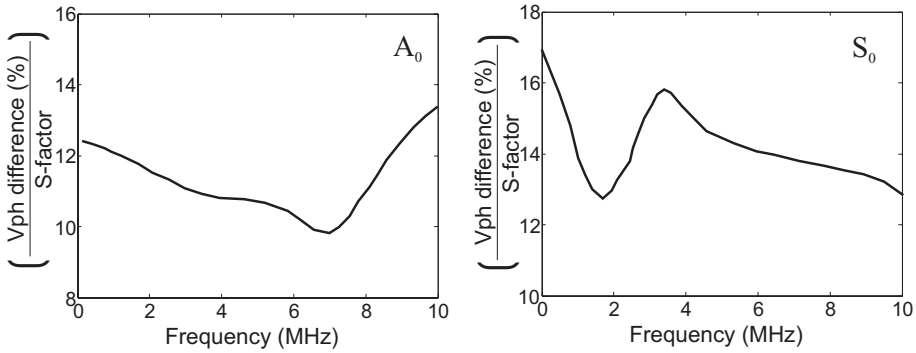

Figure 4.7: Ratio of the difference in phase velocity to the "S-factor" for the A_0 and S_0 modes taken from data presented in Fig. 4.6.

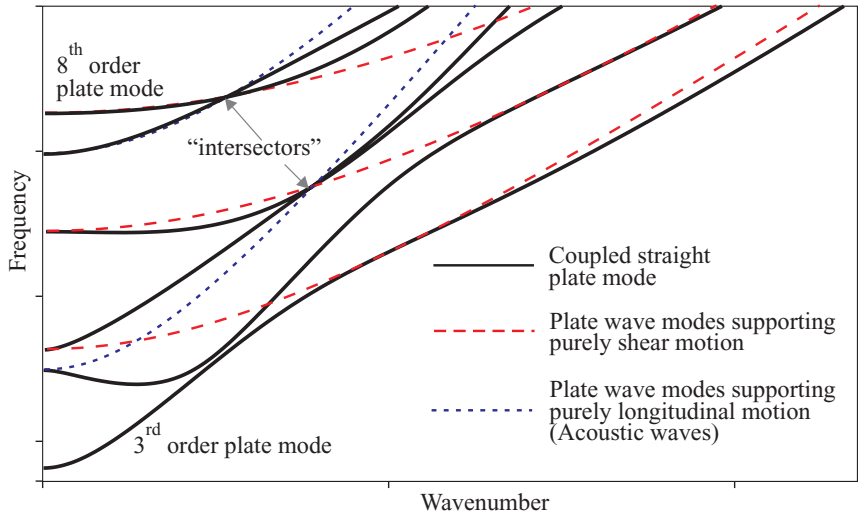

Figure 4.8: An illustration of the method of bounds by Mindlin [107] , showing the dispersion curves of a plate system and those supporting purely longitudinal and shear motions known as "bounds".

To study the more complex dispersion curves one must often be satisfied with successive approximations starting from the cases for which solutions are familiar. Fig. 4.8 illustrates the concept of the method of bounds, where it can be seen that the Lamb wave dispersion curves in a plate are closely related to the "bounds". A more detailed examination of the "bounds" is provided later in Sec. 4.3.3. In this section, using a comparable method to Mindlin's method of bounds, various features of dispersion curves in a curved plate in vacuum may be identified in a similar fashion.

4.3.2 Shear Horizontal (SH) Dispersion Curves in Curved Plates

The SH wave modes in the straight plate contain purely shear motion polarised in the z direction, while satisfying the symmetric traction-free boundaries on the top and the

bottom surfaces. As a result, they are themselves the "bounds" of the wave system. However, unlike the straight case, the boundary conditions in the curved case are not symmetric. Therefore unless the dispersion curves are calculated from solutions satisfying each of the two boundary conditions individually, the dispersion curves of SH waves in curved plates cannot qualify to be true "bounds" as defined by Mindlin [107].

It would not be possible to decompose these dispersion curves further in satisfying each of the two boundary conditions in turn, since the two boundary conditions define also the geometry of the waveguide system such as the thickness; both boundary conditions are therefore needed in any solution. However, it would be possible to assume that the thickness of the plate is infinitely small and the curvatures on the inner and outer surfaces tend towards being identical. With this assumption in mind, two sets of dispersion curves can be obtained as a shell system for curvature corresponding to thin plates with radius equal to the value of either the inner or outer surface.

The dispersion relation of the M^{th} SH shell mode of curvature radius of $r_{1,2}$ and shell thickness d may be modified from the straight case which is taken from Auld [5], and is given as:

$$\omega(M) = \sqrt{\left[((M-1)\pi)^2 + (\nu(M) \cdot r_{1,2} \cdot d)^2\right]} \times C_T/d. \tag{4.6}$$

where $\nu(M) \cdot r_{1,2}$ are the linear wavenumber at the inner (r_1) and outer (r_2) surfaces of the curved plate respectively.

As an example, the dispersion curves are plotted in Fig. 4.9 for a curved steel plate with inner and outer radii of 10mm and 20mm respectively; the large curvature difference between the inner and outer surfaces is used to exaggerate the features in the dispersion curves that are caused by the two boundary conditions. The figure shows the dispersion curves of the curved plate SH wave modes calculated using Eqn. 2.15, together with a selected number of modes for the two shell systems with radius equal to the either boundary curvature (i.e. $r = r_{1,2}$).

When only one of the curvature radii is considered in the solutions of the shell systems, the dispersion curves maintain the same cut-off frequencies as those of the curved plate system. This suggests that these cut-off frequencies of the SH modes cannot be affected by the change in curvature, and they are only dependent on the thickness of the plate.

It can be seen that the 1^{st} order shell modes correspond to the linear bulk velocity at the inner and outer surfaces (i.e. $\nu = k_T r_{1,2}$) respectively. Additionally, all the modes of the two shell systems converge to the linear bulk velocity corresponding to the shell curvature radius at high frequencies (i.e. $\nu = k_T r_1$ and $\nu = k_T r_2$ for the inner and outer surfaces).

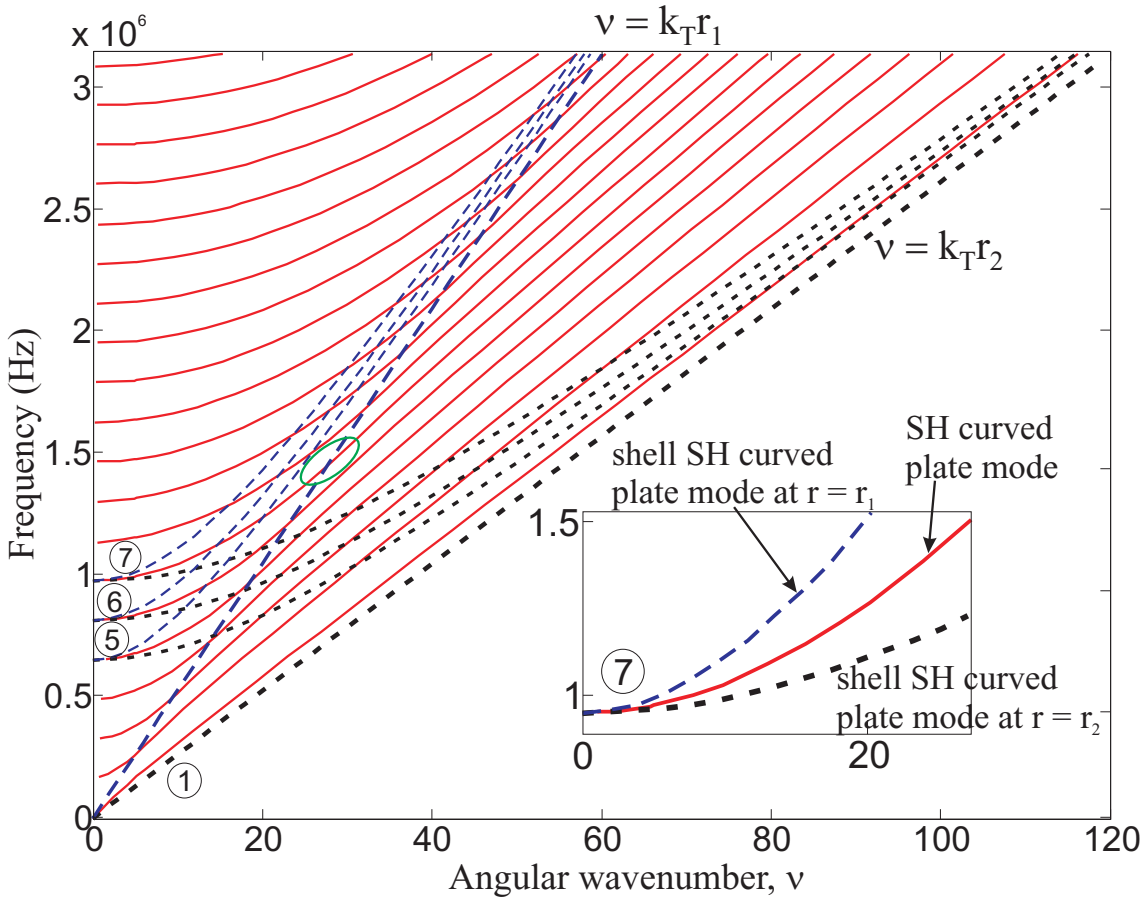

Figure 4.9: Angular wavenumber dispersion curves of SH modes in a steel curved plate (thickness: 10mm, inner radius: 10mm), and dispersion curves of the 1^{st}, 5^{th}, 6^{th} and 7^{th} modes of the shell system in which both curved boundary surfaces have their radius matched either to r_1 or to r_2. A zoom-window shows the 7^{th} mode in the region $\nu < k_T r_1$.

The mapping of the shell modes in the dispersion curves helps to visualise the amount of effect by each of the boundary conditions.

The two sets of shell modes can only coexist in the region $\nu < k_T r_1$ where the SH curved plate modes are affected by both boundaries. In the region $\nu > k_T r_1$, only the dispersion curves of the shell modes corresponding to the curvature radius of the outer surface r_2 are related to the SH curved plate modes; hence SH wave modes in this region may be considered as the Whispering Gallery waves of a purely shear nature.

Taking the 7^{th} order mode as an example, shown in the zoom-in window of Fig. 4.9, the SH curved plate mode has a dispersion profile sandwiched in between the two shell cases, showing that in this region the dispersion curves of the plate mode are influenced roughly the same by the boundary conditions on both surfaces. And as the plate mode moves towards $\nu = k_T r_1$, the curves change their normal trajectory and linger along $\nu = k_T r_1$ momentarily before changing their trajectory once again as they move into the region

$\nu > k_T r_1$. This region is marked by the green circle in Fig. 4.9.

In this region, there are no SH shell modes of the inner curvature radius $r = r_1$ present since the partial wave on the inner surface has turned inhomogeneous. However, this does not lead the plate dispersion curves to converge asymptotically to the shell modes of the outer curvature radius $r = r_2$. When $\nu > k_T r_1$, the fields disconnect from the inner surface, therefore having solutions that are bounded by the both inner and outer surfaces would not correctly describe their physical behaviour.

In order to model the asymptotic solution of modes in this region, one would have to consider the SH wave mode solutions that propagate in a rod with radius of r_2. The solutions for such wave propagation may be reduced directly from the RHS of Eqn. 2.14 where the outgoing partial wave term is eliminated, and the dispersion relation may be expressed as the following:

$$a_1 J'_\nu(k_T r_2) = 0. \tag{4.7}$$

Fig. 4.10 shows the dispersion curves of SH modes in a curved steel plate, and those in a steel rod. It can be clearly seen that in the region $\nu > k_T r_1$, the dispersion curves of SH modes in a rod agree exactly to those of the plate case. This shows that solutions bounded by only the outer surface are relevant in this region.

4.3.3 Lamb-type Dispersion Curves in Curved Plates

According to Mindlin's method of bounds, the "bounds" of the coupled Lamb-type system are constituted of the dispersion curves of wave modes in the same geometry, which support either the purely shear motion or the purely longitudinal motion in the circumferential direction. These "bounds" can easily be calculated numerically using a similar analytical approach to that of the SH mode, detailed in Ch. 2. The dispersion relations for these two sets of "bounds" are:

$$\text{Shear modes: } J'_\nu(k_T r_1)Y'_\nu(k_T r_2) - J'_\nu(k_T r_2)Y'_\nu(k_T r_1) = 0. \tag{4.8}$$

$$\text{Longitudinal modes: } J'_\nu(k_L r_1)Y'_\nu(k_L r_2) - J'_\nu(k_L r_2)Y'_\nu(k_L r_1) = 0. \tag{4.9}$$

A set of "bounds" of the coupled Lamb-type dispersion curves should have the following properties:

1. the "bounds" pass through a family of cut-off frequencies at $\nu = 0$.
2. the crossing of the any two "bounds" forms the "intersectors", as shown in Fig. 4.8.

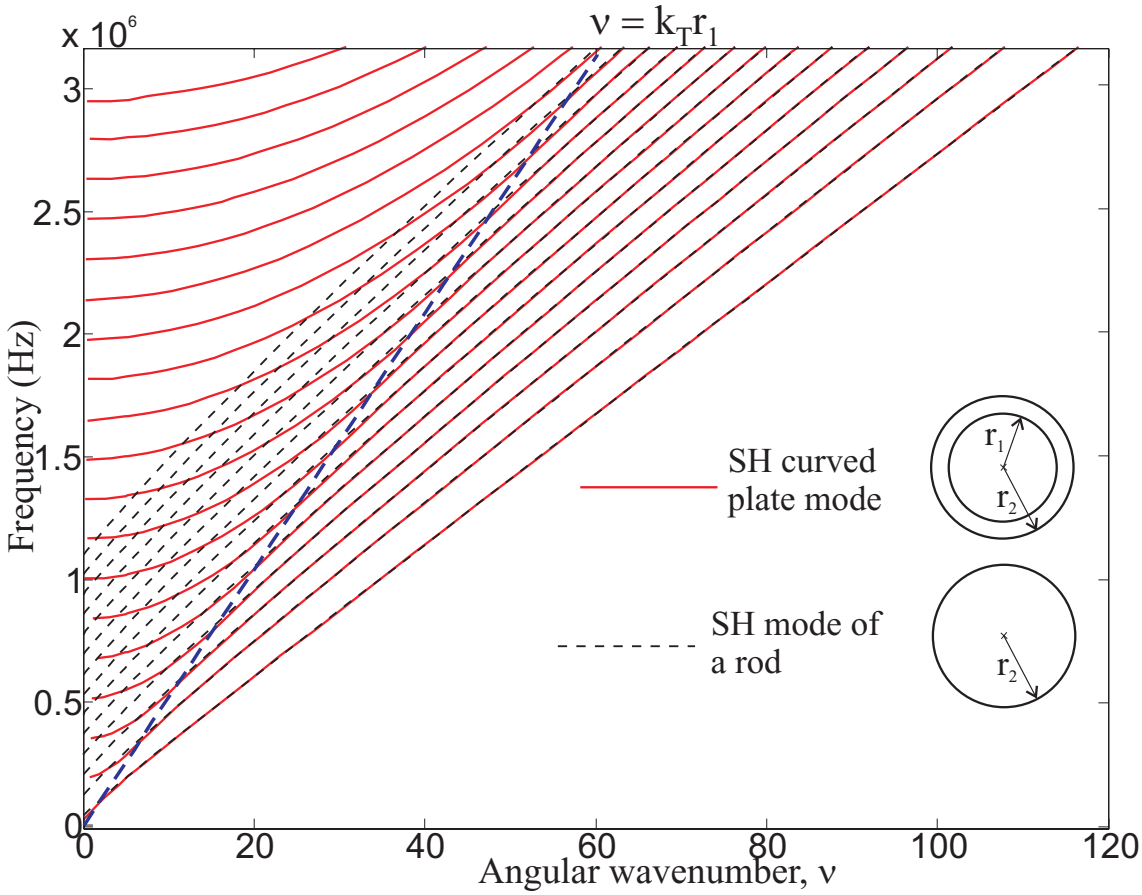

Figure 4.10: Angular wavenumber dispersion curves of SH modes in a steel curved plate (thickness: 10mm, inner radius: 10mm), and dispersion curves of SH mode in a steel rod (outer radius: 20mm).

3. the dispersion curves of the coupled Lamb-type wave modes are separated by the "bounds", and they only cross the bounds at the "intersector".

Fig. 4.11 shows the dispersion curves of the Lamb-type wave modes in a steel curved plate (thickness: 3mm, inner radius: 10mm). Additionally, it shows the sets of uncoupled longitudinal and shear curved plate modes of the corresponding curved plate system, which form the diamond like pattern of "bounds".

It can be seen that the uncoupled wave modes satisfy the first two properties of the "bounds" at all frequencies, whereas the third property is valid everywhere except inside the region $\hat{\omega}_1 < \nu < \hat{\omega}_2$ where $\hat{\omega}_1$ and $\hat{\omega}_2$ are $(\omega r_1/C_L)$ and $(\omega r_2/C_L)$ respectively. In this region (marked in Fig. 4.11), the dispersion curves of the coupled system do not seem to establish any connection with those of the uncoupled systems. This is because in this region the dispersion curves of the uncoupled longitudinal case do not depend on the inner surface of the curved plate; this phenomenon is similar to that in the region $\nu > k_T r_1$ of the SH case, shown in Fig. 4.9 of the previous section. Thus the "bounds" of these

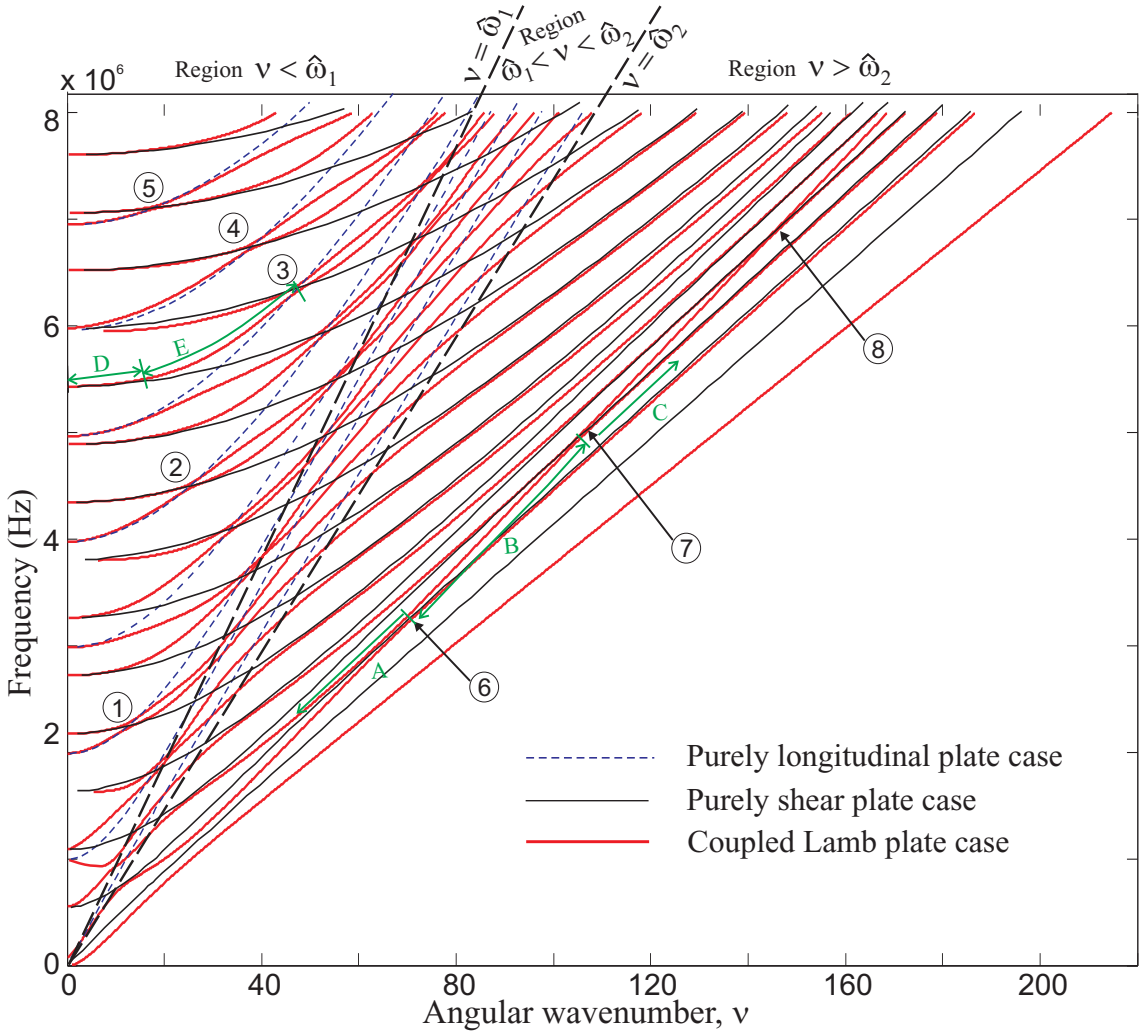

Figure 4.11: Angular wavenumber dispersion curves of the Lamb-type waves, and of the uncoupled purely longitudinal plate waves and purely shear plate waves, in a steel curved plate (thickness: 3mm, inner radius: 10mm). The location labels are marked inside the circles.

uncoupled plate modes would not be relevant in this region.

In the region $\nu > \hat{\omega}_2$, the "bounds" are made up solely of the dispersion curves of the purely shear case. A peculiar phenomenon may be observed in this region for the dispersion curves of a plate when curvature along the propagation direction is introduced. Since the dispersion curves of the curved plate case cannot cross the "bounds", it can be seen in Fig. 4.11 that these curves first run asymptotically along one "bound" (label "A"); they subsequently move towards the neighbouring "bound" with increasing frequency (label "B"), coming close range to neighbouring mode at the location 7 before repelling each other to run asymptotically along "bound" (label "C"). This repulsion phenomenon is also highlighted by the location labels 5-7 in Fig. 4.11, additionally, the zoom-in of location 7 is shown in Fig. 4.12.

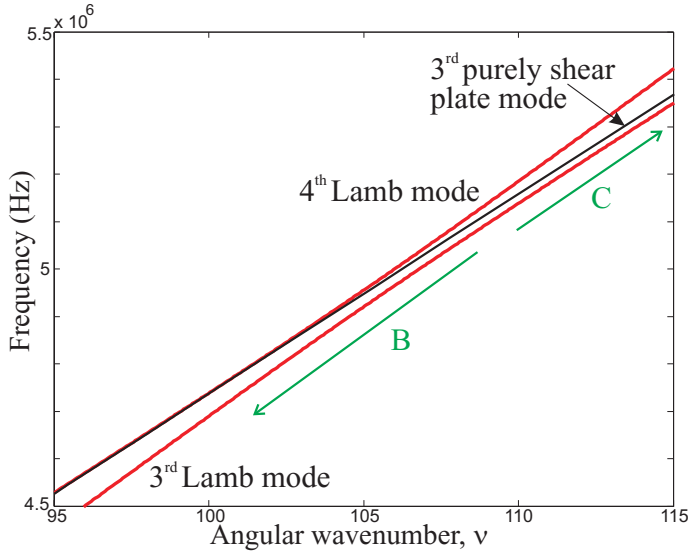

Figure 4.12: A zoom-in window of the angular wavenumber dispersion curves, showing the repulsion phenomenon at location correspond to the label 7 of Fig. 4.11 in the region $\nu > \hat{\omega}_2$.

On the other hand, in the region $\nu < \hat{\omega}_1$, the dispersion curves of the coupled Lamb case behave similarly to the straight plate case (see for example pp. 19 of Mindlin [107]). The dispersion curves follow asymptotically along the "bounds" at positions between the cut-off and the first set of "intersectors" (label "D"), the two neighbouring modes then come in close range at the intersector before repelling back towards the previous "bound". Thereafter they establish a parabolic profile between two "intersectors" in a terrace-like grid (label "E") until they reach the boundary of $\nu = \hat{\omega}_1$.

In the Lamb dispersion curves of the straight plate case, a mode crossing phenomenon, where a symmetric mode and a neighbouring anti-symmetric mode intersect, occurs typically at the "intersectors". However, this phenomenon vanishes in a curved plate case (see, for example, location labels 1-5 in Fig. 4.11, and a zoom-in of label 2 is shown in Fig. 4.13).

It has been shown by Zhu *et al.* [108] that the crossings of "bounds" are in fact "discontinuity points" of the coupled system in the straight case. These "discontinuity points" coincide with the so-called "intersection" and "near intersection" features in the Lamb dispersion curves. The results from Zhu's investigation indicated that no two propagating modes of one system travelling at the same speed and frequency can coexist. The same hypothesis may be applied to the curved plate system here.

Noting that the "intersectors" exist only in the region $\nu < \hat{\omega}_1$, it would be possible to make use of the Region Asymptotic Method (RAM) discussed in Sec. 3.1.2 to evaluate the values of the (ω_I, ν_I) roots at the "intersectors" in this region. The formulation of the asymptotic solutions of the purely longitudinal and shear circumferential curved plate

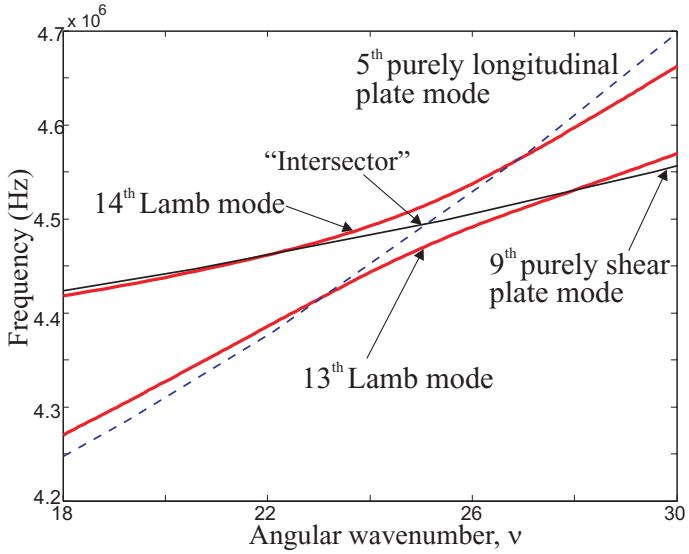

Figure 4.13: A zoom-in window of the angular wavenumber dispersion curves, showing the repulsion phenomenon at the "intersector" correspond to the label 2 of Fig. 4.11 in the region $\nu < \hat{\omega}_1$.

modes are analogous to that of the SH wave, shown in Eqn. 3.7, and they are given in the following forms:

$$\begin{aligned}
\text{Shear modes:} \quad & \sin\left\{\left[\left(\frac{\omega_I}{C_T}r_1\right)^2 - \nu_I^2\right]^{1/2} - \left[\left(\frac{\omega_I}{C_T}r_2\right)^2 - \nu_I^2\right]^{1/2} \right. \\
& \left. -\nu_I\left[\cos^{-1}\left(\frac{\nu_I C_T}{\omega_I r_1}\right) - \cos^{-1}\left(\frac{\nu_I C_T}{\omega_I r_2}\right)\right]\right\} = 0. \\
\text{Longitudinal modes:} \quad & \sin\left\{\left[\left(\frac{\omega_I}{C_L}r_1\right)^2 - \nu_I^2\right]^{1/2} - \left[\left(\frac{\omega_I}{C_L}r_2\right)^2 - \nu_I^2\right]^{1/2} \right. \\
& \left. -\nu_I\left[\cos^{-1}\left(\frac{\nu_I C_L}{\omega_I r_1}\right) - \cos^{-1}\left(\frac{\nu_I C_L}{\omega_I r_2}\right)\right]\right\} = 0.
\end{aligned} \tag{4.10}$$

The unknown values of (ω_I, ν_I) at the "intersectors" are evaluated by finding the zeros of a system of the two above equations. To validate the existence of the "discontinuity points" in the curved plate system, the (ω_I, ν_I) was first calculated numerically for the "intersectors" at the locations labelled 1-5 in Fig. 4.11. The calculation was performed with a tolerance factor of 1×10^{-12} and the results are summarised in Tab. 4.1.

Subsequently, the Lamb-type dispersion function (Eqn. 2.18) was evaluated based on the results of (ω_I, ν_I) at the "intersectors", where a perturbation in the frequency domain was carried out, while ν_I was fixed. Figs. 4.14 and 4.15 shows the amplitude of the Lamb-type dispersion function over a small range of frequencies at locations close to the "intersectors" label 1 and 4 respectively for comparison. In both graphs, the dispersion function does

"Intersector" location label	Frequency (Hz) at "intersector", $\omega_{\mathbf{I}}$	Angular wavenumber at "intersector", $\nu_{\mathbf{I}}$
1	2248180.1763508	12.6391630164712
2	4496360.35270159	25.2783260329422
3	6357612.76403117	47.616506606474
4	6744540.52905239	37.9174890494132
5	7109763.21793554	17.8257820710146

Table 4.1: (ω_I, ν_I) roots of the intersectors, corresponding to the case presented in Fig. 4.11.

not pass through the x-axis at the frequency of the "intersector". This indicates that the dispersion curves of the curved plate do not possess a root at the "intersector", thus illustrating the condition of the "discontinuity points" at the "intersectors".

In general, the dispersion curves of the two neighbouring modes in a curved plate case cannot cross each other, however, they may come close to each other at the "intersector", then repel each other as they move beyond this point (see Fig. 4.13). This is also shown in Figs. 4.14 and 4.15 where ω_I of the "intersector" is located in between two Lamb-type roots, each of which corresponds to one of the two neighbouring modes. The gap between these two neighbouring roots in these plots increases with increasing curvature, and vice versa as the curved plate system moves towards the straight case.

The condition on whether any two modes should intersect or repel each other at the "intersector" has been investigated by Überall *et al.* [109], who linked this character, though with little evidence, to that encountered for the energy levels of atoms during a molecular formation based on a perturbation theory.

Nevertheless, Überall concluded that if the neighbouring two modes belong to a different through-thickness symmetry near the "intersector", like the case of the symmetric (S) and antisymmetric (A) modes in straight plates (these two families are represented by independent orthogonal solutions), they may intersect each other. On the other hand, if the two neighbouring modes have similar mode shapes (i.e. belonging to the same orthogonal family), as in the case of two neighbouring modes of the same symmetry in straight plates, they repel each other after a near intersection, exchanging the nature of the corresponding modes simultaneously.

By contrast, the solutions of the curved plate case, though they satisfy the orthogonality condition, cannot be divided into two independent orthogonal families due to asymmetry of the boundary conditions. Based on the argument by Überall, the repulsion phenomenon between two neighbouring modes must occur at all "intersectors", which can be observed in Fig. 4.11. Moreover, the physical character of curved plate modes changes between

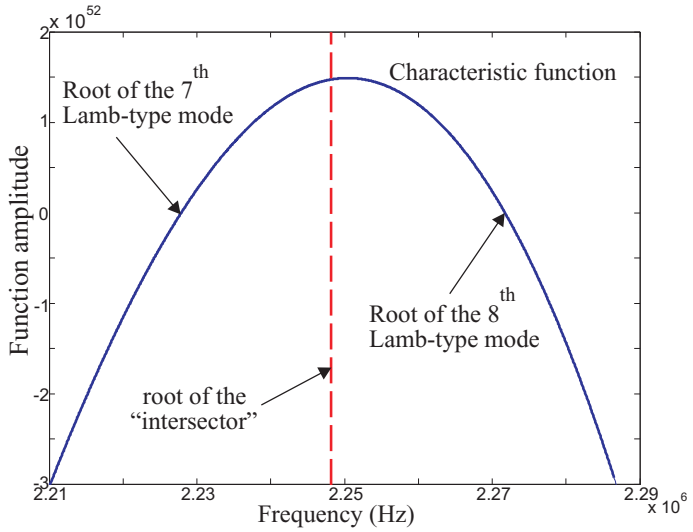

Figure 4.14: Lamb-type characteristic function of a curved plate (blue solid line), calculated as a function of a small range of frequencies near the "intersector" label 1 shown in Fig. 4.11, while an angular wavenumber is fixed at ν_{I1} of location 1. The frequency at which the corresponding "intersector" occurs, is indicated with the red dashed line.

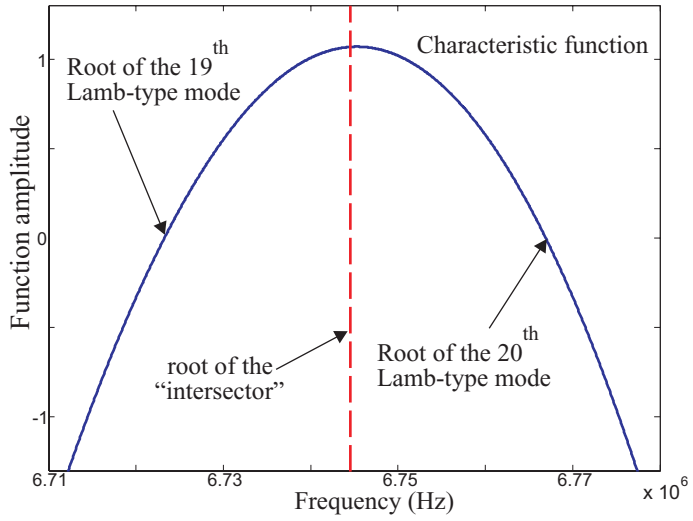

Figure 4.15: Lamb-type characteristic function of a curved plate (blue solid line), calculated as a function of a small range of frequencies near the "intersector" label 4 shown in Fig. 4.11, while an angular wavenumber is fixed at ν_{I4} of location 4. The frequency at which the corresponding "intersector" occurs, is indicated with the red dashed line.

the "near symmetric" and the "near anti-symmetric" mode shapes as they pass by each "intersector".

4.4 Summary

Using the asymptotic methods, the difference in phase velocity between the straight and curved plates as a function of radius and frequency has been studied for the first few fundamental plate modes in this chapter. The results of this comparison are presented in a 3-D plot for each individual mode, where an optimal frequency can be picked for a given engineering application.

The energy distribution of a wave mode can shift towards either the inner or outer surface when the curvature is present. Using this property, one could increase the sensitivity of the detection of defects at certain through thickness locations. The change in mode shapes between the straight and curved plates has been investigated using a "dot product" technique, which can be used to compare directly with the corresponding change in phase velocity at a particular frequency and curvature radius.

In this chapter, we have shown that various features of the dispersion curves in the curved plate may be identified using a modified version of the "method of bounds"; a system of uncoupled dispersion curves supporting primarily shear and longitudinal waves. These features include a family of cut-off frequencies, the near intersection points between two neighbouring modes and the asymptotic behaviours of the dispersion curves. Moreover, the repulsion phenomenon in the dispersion curves has been examined numerically.

Chapter 5

Confirmation of Curvature Effect in Unloaded Plates

The purpose of this chapter is to test the validity of the theoretical background, developed in the previous chapters, for the curvature effect on the propagation properties of guided waves in an unloaded plate. The confirmation cases are divided into two main sections where the analytical solutions are compared to results obtained using independent Finite Element (FE) modelling and experimental measurements respectively.

In the first section, a cyclic periodic FE model is utilised to extract the phase velocity dispersion curves numerically for plates of a range of curvature radii. Since the difference in phase velocity can be tiny when the curvature is small, it is extremely important that the accuracy of the numerical approximation in the FE modelling, which relates to the size of the elements, is ensured. A convergence analysis to pinpoint the limiting case of the element size is therefore performed. The solutions of the FE modelling are subsequently used for evaluating the curvature effect by comparing with the straight case as a function of frequency for each curvature radius.

An experimental technique to illustrate the curvature effect has proven to be very difficult because of the relatively small changes in velocity. In the second section, a simple technique to investigate the effect of curvature on the waveguide properties is presented. The technique involves thin aluminium strips bent to different curvatures within its material yield limit. In addition, permanently attached transducers were used for exciting and gathering of the wave signals to improve the accuracy of the experiment. This method allows sensitive measurements of the percentage difference in phase velocity between curved and straight plates.

However, since the curvature radius was restricted to the elastic limit of the plate material, the change in the phase velocity due to the curvature effect can be as little as in the order of

a hundredth of a percent. As a result, any other influences, such as the change of through-thickness local density and stress, may become significant. These additional influences are investigated, leading to an appropriate adjustment to the analytical model. Good agreements are obtained when the experimental results are correlated with the improved analytical predictions.

5.1 Finite Element (FE) Modelling

5.1.1 Introduction

Many problems in engineering are either difficult or impossible to solve analytically due to the complexity involved in describing the geometry of a real life structure. As a consequence, analytical solutions can be obtained only for limited simple situations. For complex systems, engineers therefore resort to numerical methods, which provide an appropriate approximation to the solution. Most numerical methods, such as the Finite Element (FE) method [110], employ a technique of discretisation in which the solutions are formulated based on a constituent set of elements or nodes, which are then combined to obtain the solution for the whole structure. In the case of FE, as the size of the elements becomes smaller, the model forms a continuum which represents the real structure with increasing accuracy. This numerical technique takes advantage of the recent rapid advance in the processing power of digital computers to include enormous complexity while being able to analyse the solution efficiently.

FE procedures have been employed extensively in solid and fluid structures for analyses of heat transfers, stress, flow ...etc. Recently, they have been used increasingly in simulating ultrasonic waveguide propagations [111, 112, 113]. This method provides a vital research tool for both academic and industrial use.

The use of standard commercial FE programs to calculate the guided wave dispersion curves for structures with complicated arbitrary cross-section has been previously reported by Gavrić [114], and subsequently adapted by Wilcox *et al.* [115], so only a brief description of the method is given in this section. Coincidentally, Wilcox's FE method was originally formulated to approximate solutions of a straight case based on an annular structure. Therefore it would be possible to apply a specific curvature radius to the annular structure to model the curved plate cases exactly.

The procedure of the modelling is analogous to that by Wilcox *et al.* [115] who used a so-called cyclic symmetry model, where a given order of periodic variation around the circumference is prescribed. This axially harmonic condition allows a 3-D structure problem to be modelled with 2-D axi-symmetric harmonic elements representing the cross section

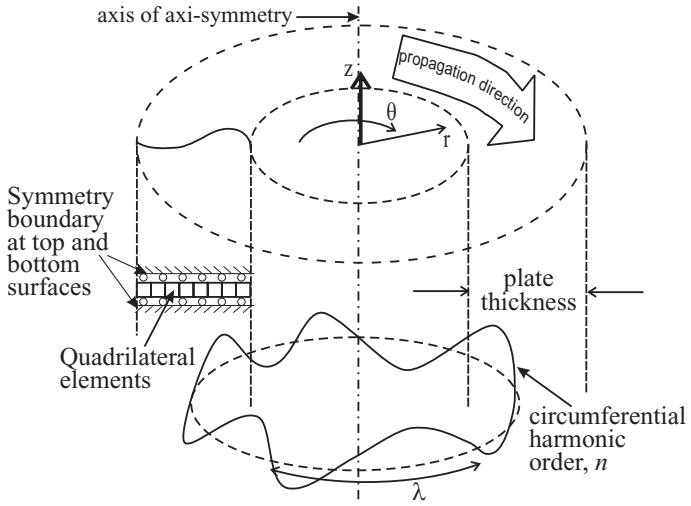

Figure 5.1: Schematic diagram of a 2-D cyclic symmetry FE model for the evaluation of dispersion curves.

of the structure normal to the propagation direction.

The model consists of discretising the thickness of the plate into a row of a desired number of 2-D axially symmetric elements, such that the radial length of the row corresponds to the thickness of the plate (see Fig. 5.1). Symmetric boundary conditions are subsequently applied to the top and the bottom of the row of elements to simulate an infinitely wide plate (the width direction is vertical in Fig. 5.1). Noting that there is no variation of the displacement field in the z direction for circumferentially propagating Lamb modes. An illustration of the modelling is shown in Fig. 5.1.

Assuming the waves propagate in the circumferential direction, θ, the circumferential periodic cyclic order, n, of the FE model related to the angular wavenumber, ν, by

$$2\pi\frac{r_{mid}}{\nu} = \text{wavelength, } \lambda = \frac{\text{Circumference}}{\text{Cyclic order, } n} = \frac{2\pi r_{mid}}{n}. \tag{5.1}$$

For a model with fixed radius, varying the periodic cyclic order, n, around the circumference would therefore force the propagating modes to propagate at a certain wavelength λ. As in the analytical calculations (Eqn. 3.25), the dispersion relation is calculated along the mid-line through the plate thickness (r_{mid}).

This unloaded system subsequently forms an eigen-problem of an equilibrium relation between the internal stiffness matrix $\mathbf{k}$, global mass matrix $\mathbf{M}$, nodal displacement $\hat{u}$ and nodal acceleration $\hat{\ddot{u}}$ in a local scale, expressed as a set of linear simultaneous algebraic equations of the following type:

$$[\mathbf{M}]\hat{\ddot{u}} + [\mathbf{k}(n, \omega_m)]\hat{u} = 0. \tag{5.2}$$

The natural frequencies (ω_m) of the plate corresponding to the m^{th} propagating mode can be solved using the eigensolver routine available in most commercial FE packages. The results presented in this section were obtained using the program Finel [116], a FE program developed at Imperial College, with which the periodic cyclic order, n can be specified and the corresponding ω_m solved. Finel finds the roots, $n - \omega_m$, of the specific system using the Lanczos method of eigenvalue extraction.

By solving for ω_m over the first m modes and a range of periodic cyclic orders, n, a complete set of eigen-solution (ω_m, n) discrete points are obtained (shown, for example, in Fig. 5.2), and can then be joined to form dispersion curves. The only drawback with this technique is that the periodic cyclic orders n which can be analysed are restricted to integers, and this may result in a low resolution at the region where the phase velocity is high.

5.1.2 Accuracy of the FE Model

To ensure the accuracy of the FE solution, there should be enough elements across the thickness to closely represent all mode shapes in the real structure. In this section, the checking of the accuracy is divided into two parts. In the first part, a convergence analysis is performed, from which an optimal number of elements through the thickness to obtain an adequate level of accuracy is evaluated. Additionally, since the mode shapes, which can be highly distorted due to the curvature, are linked to the propagation properties as discussed in Sec. 4.2, it is important that the mode shapes calculated analytically match those extracted using the method. This comparison in mode shapes is presented in the second part of this section.

Convergence Analysis

The through-thickness displacement mode shapes become more complicated with increasing in both the mode and periodic cyclic orders (i.e. m and n respectively) shown in Fig. 5.2 for the Lamb circumferential dispersion curves of an aluminium curved plate (thickness: 1mm, inner radius: 20mm). Therefore the results can quickly become inaccurate when the product of mn grows larger.

As a rule of thumb, practice has shown that at least 6 elements should be used for each displacement harmonic cycle across the thickness. However, with such a small difference in phase velocity between the straight and curved plates in the case when the curved plate has small curvature, the accuracy of the FE modelling should be at least a factor of the higher than the changes due to the curvature effect. In this section, a study is carried out to determine the number of elements required to model the wall thickness in order

to ensure an acceptable level of accuracy. For simplicity, only four noded quadrilateral elements with unity aspect ratio are considered throughout the FE study.

As an illustration of the effect where the thickness of the model is constructed with less than the appropriate number of elements, Fig. 5.3 shows two dispersion curves for a 1mm thick, 20mm inner radius aluminium curved plate composed of two different element sizes corresponding to 34 and 47 elements through the plate thickness respectively.

With 34 elements through the thickness (Fig. 5.3(a)), the solutions do not resemble those calculated using exact solution at high values of nm product where the displacement mode shapes become complicated; this indicates a breakdown of the FE solution. In this case, there is simply an inadequate number of elements to resemble the full displacement field across the thickness, resulting in distorted displacement mode shapes. To extract the full dispersion curves up to $n = 1400$ without any obvious solution breakdown, 47 elements through the thickness (Fig. 5.3(b)) was found to be the absolute minimum.

Taking the 20^{th} mode at $n = 1200$ as an example, both the in-plane and the out-of-plane displacement mode shapes have approximately 10 harmonics across the thickness, therefore there should be at least 60 elements across the thickness according to the "rule of thumb". Nonetheless, the results generated using 60 elements are generally less accurate than is acceptable for the investigation of the curvature effect. In addition, for a given number of elements used, the level of the accuracy decreases with increasing m and frequency ω_m.

To demonstrate those points, the percentage error in frequency of the 20^{th} propagating mode is calculated in relation to the exact analytical solutions for a 1mm thick and 20mm inner radius curved aluminium plate. The result, shown in Fig. 5.4, is calculated at every n with $n = \{1, 2, 3 \ldots etc.\}$ and over a range of number of elements through the wall thickness.

With 2000 elements used across the wall thickness in the model, a typical percentage error of less than 0.001% was obtained for all locations of the dispersion curves (maximum range: $n = 1400$ and $m = 20$). In comparison, the small percentage difference caused by the curvature effect discussed in Sec. 4.1, even in the case of the smallest curvature investigated (inner radius: 0.1m), is approximately one order bigger than the error due to the finite element (FE) approximation.

This clearly indicates that many more elements than that according to the "rule of thumb", are required to ensure the accuracy level for predicting the curvature effect on the propagation properties. However, keeping in mind that the calculation time necessary for an eigen-matrix calculation depends mainly on the total number of Degree of Freedom (DOF) which increases proportionally with increasing number of elements. Therefore a model with a high number of elements can be computational expensive. This is especially

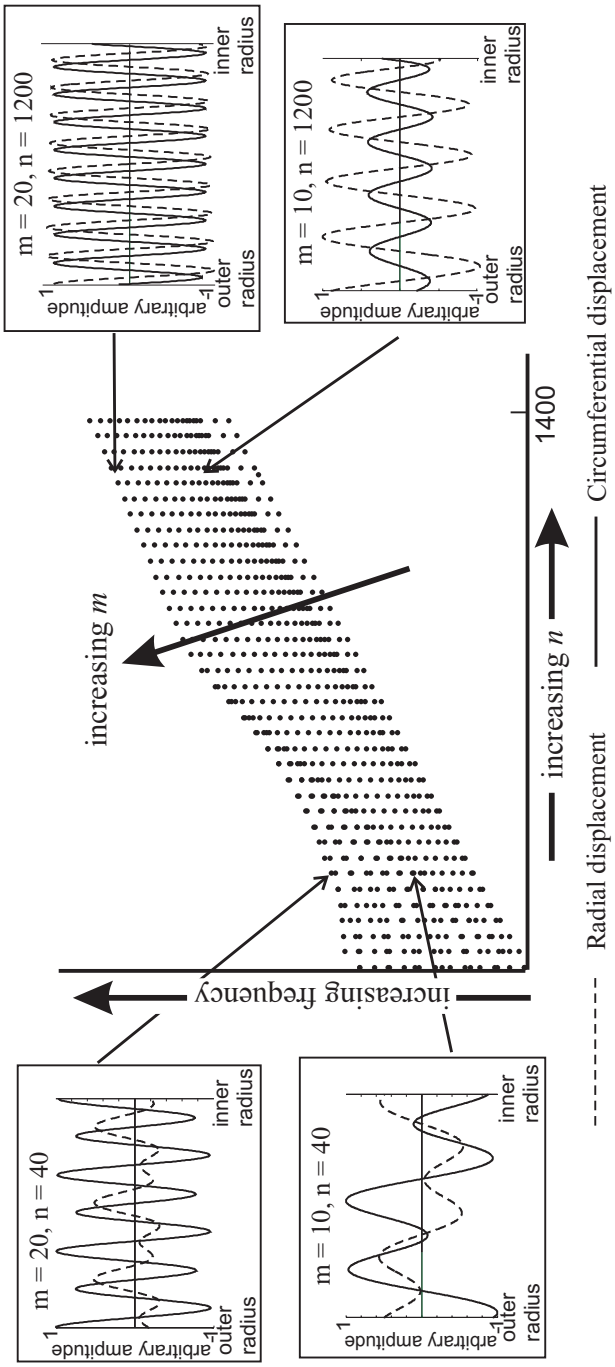

Figure 5.2: Eigen-solutions in the angular wavenumber-frequency domain extracted using a FE method and the mode shapes for the 10^{th} and the 20^{th} modes at $n = 40$ and $n = 1200$, where n is the cyclic periodic order around the circumference. The model is based on an aluminium curved plate (thickness: 1mm, inner radius: 20mm).

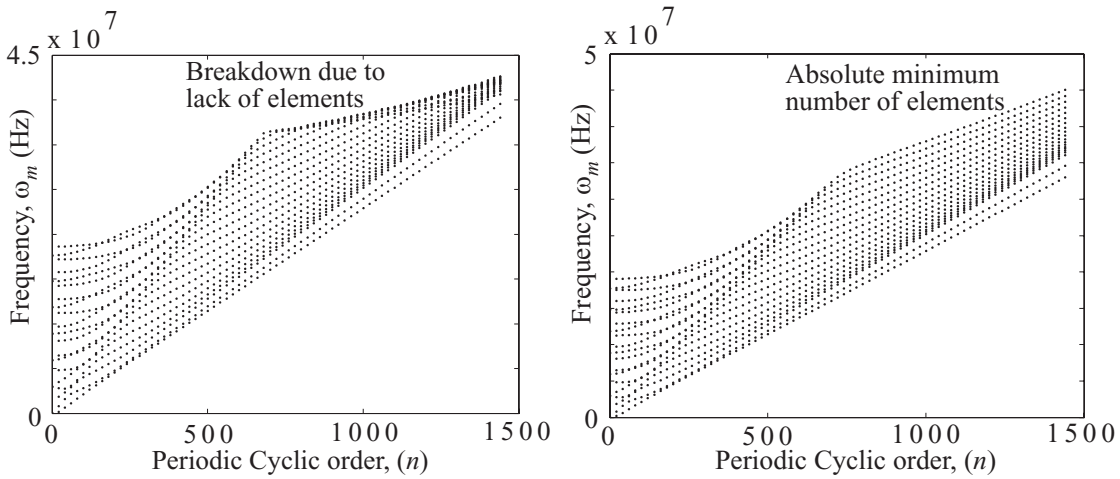

(a) 34 elements through the thickness

(b) 47 elements through the thickness

Figure 5.3: Dispersion curves extracted using the FE axially cyclic symmetric model with two different sizes of elements for an aluminium curved plate (thickness: 1mm, inner radius: 20mm).

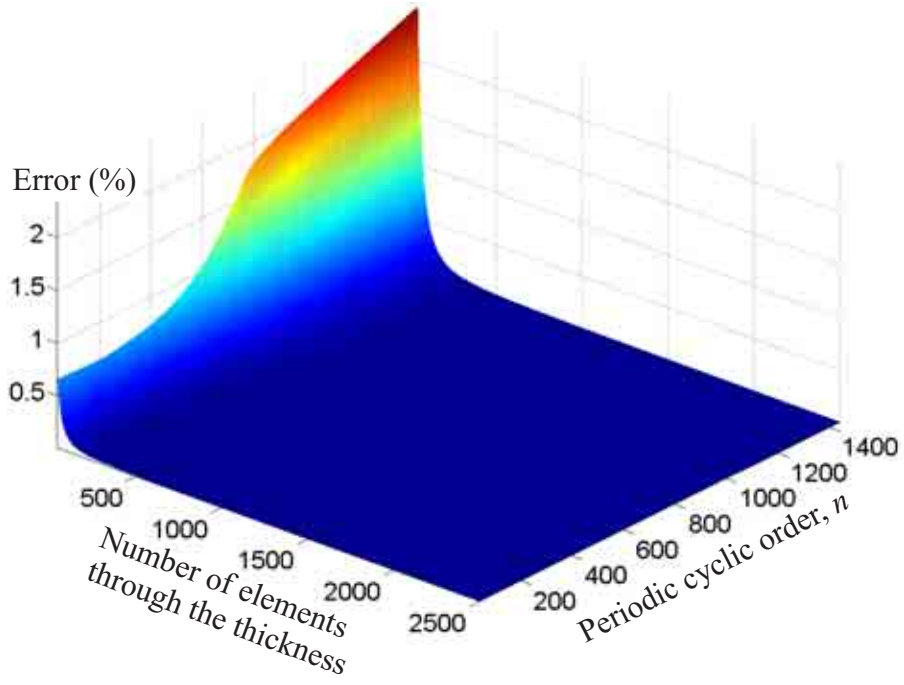

Figure 5.4: Percentage error in frequency of the 20^{th} mode as a function of the periodic cyclic order n and the number of elements through the thickness for an aluminium curved plate (thickness: 1mm, inner radius: 20mm).

important if the modelling is to be repeated many times over the range of periodic cyclic orders, n, in order to extract the dispersion curves.

Fig. 5.5 demonstrates the calculation time required to solve the eigen-problem using models with increasing elements, which were calculated using the FE program, Finel; the linear relationship shown in the figure is due to the fact that a substantial proportion of the reported time is for assembling the stiffness matrix of the problem. In reality, the relationship is likely to be an exponential best fit.

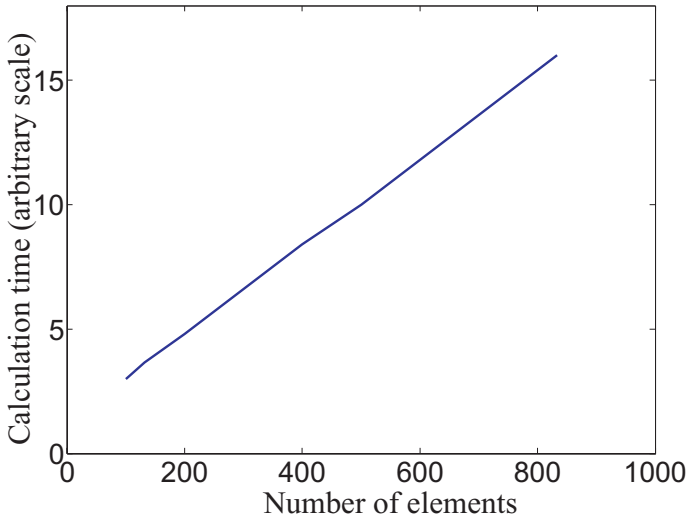

Figure 5.5: Calculation time required to solve the eigen-matrix for the first 20 modes at $n = 1200$ for an aluminium curved plate (thickness: 1mm, inner radius: 20mm) with the thickness of the model assembled using various numbers of elements according to Fig. 5.1. These calculations were carried out using the FE program Finel.

Nevertheless, if only the lower order fundamental modes are being considered in the FE simulation of the curvature effect, 1000 elements through the thickness should be more than adequate to obtain the necessary high accuracy.

Mode Shapes

The displacement mode shapes of a cyclic symmetry FE model can be obtained by means of solving the eigenvector $\hat{u}$ in Eqn. 5.2 for the corresponding $n - \omega_m$ pair. The through-thickness displacement field is then acquired from these displacement amplitudes at the nodal points along either the top or the bottom symmetry boundary (see in Fig. 5.1).

Two different types of mode shapes, one having many harmonics through its thickness with the other being highly asymmetric, have been considered for investigation in this section. A 1mm thick and 10mm inner radius aluminium curved plate was modelled using FE; the FE model was constructed using 1000 elements through the thickness. Figs. 5.6 and

5.7 present the through-thickness displacement mode shapes using every 10^{th} nodal point across the thickness, and those calculated using the exact displacement field equations of Eqn. 2.19.

It can be seen that the mode shapes of the 10^{th} mode in Fig. 5.7 are very much more complicated than those of the "quasi-A_0" mode in Fig. 5.6, and hence each harmonic through the thickness is constructed with a less number of nodal points compared to the lower order modes, resulting in a reduction in accuracy. In the case of Figs. 5.6 and 5.7, there are no noticeable discrepancies between the mode shapes calculated using the exact and the FE methods in both plots. Additionally, mode shapes having dominant amplitudes on the outer surface have been accurately modelled using the FE method.

5.1.3 Results of FE Simulations

This section deals with the confirmation of the curvature effect using the solutions obtained from the FE modelling of various curvature radii. The FE calculations are based on aluminium curved plates that have material properties of $C_L = 6320m/s$, $C_T = 3130m/s$ and density, $\rho = 2700kg/m^3$.

Prediction of the Curvature Effect using FE

The effect of curvature on the phase velocity is examined as a function of curvature radius and frequency in a similar manner as the analytical comparison detailed in Sec. 4.1. Although the accuracy of the FE solutions in the curved plate case is highly dependent on the number of elements used across the thickness, for a given thickness, a change in the radius should not in theory affect the accuracy of the FE results. It is therefore possible to assume that the convergence analysis in the Sec. 5.1.2 is correct for 1mm thick curved aluminium plates of any given curvature radius.

For a crude visual comparison between the exact and FE methods, the eigen-solutions of periodic cyclic order n (angular wavenumber ν) - frequency ω_m pair have been calculated using the FE cyclic symmetry model for 1mm thick curved aluminium plates of curvature radii in the range found in Fig. 4.2. The percentage differences in phase velocity were calculated according to Eqn. 4.1, which requires the eigen-solutions to be converted first into the phase velocity-frequency ($V_{ph} - \omega$) domain using Eqn. 4.2, and are subsequently interpolated at a regular frequency interval. The accuracy was ensured by using quadratic interpolation on FE solutions that are extracted at sufficiently close n intervals.

The phase velocity at each curvature radius was then compared with the exact solution of the straight case obtained from Disperse at the same regular interval. The overall results

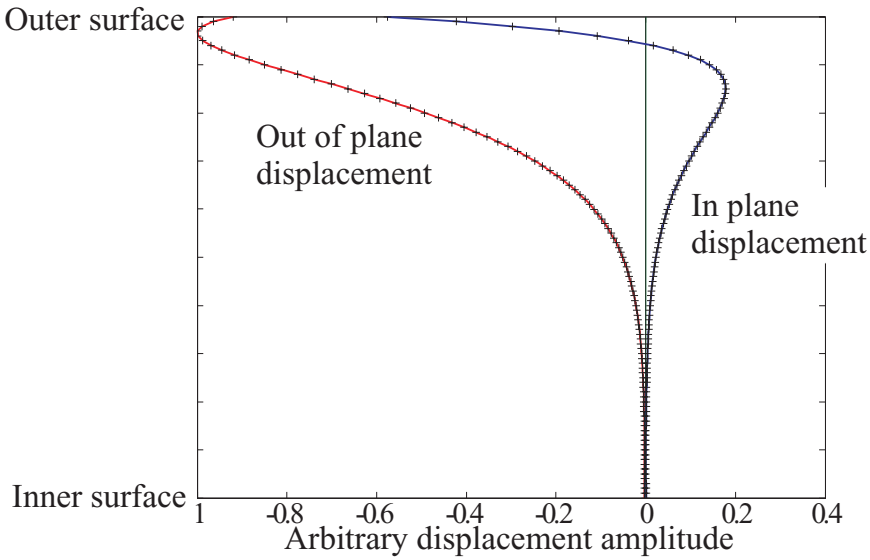

Figure 5.6: Displacement mode shapes of the "quasi-A_0" mode at 8.53MHz for a 1mm thick and 10mm inner radius aluminium curved plate, extracted using the exact (solid lines) and the FE (cross points) methods. The FE model is constructed using 1000 elements through the thickness.

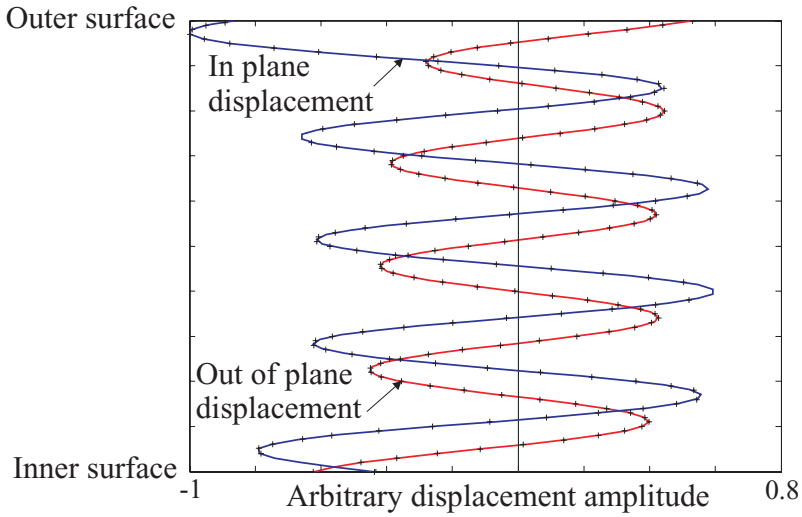

Figure 5.7: Displacement mode shapes of the 10^{th} "quasi-mode" at 8.53MHz for a 1mm thick and 10mm inner radius aluminium curved plate, extracted using the exact (solid lines) and the FE (cross points) methods. The FE model is constructed using 1000 elements through the thickness.

generate 3-D plots of the percentage difference as a function of radius and frequency for each individual propagating mode in a similar way to Fig. 4.2. Figs. 5.8 and 5.9 show the percentage difference between the straight and curved plate cases for the A_0 and A_1 modes respectively. Both plots appear to bear a striking resemblance to their exact solution counterparts (Figs. 4.2(a) and 4.2(c)) in terms of their shapes and amplitudes.

A direct comparison between the FE and exact methods, shown in Figs. 5.10 and 5.11 for the A_0 and A_1 modes respectively, reveals that the solutions are, in general, extremely accurate with an absolute difference in percentage ($\Delta\%$) between the exact and FE methods of less than 0.001%, except near their cut-off frequencies. One obvious explanation of this reduced level of accuracy is that the cut-off frequencies vary with the curvature radii, and their gradients near these frequencies can change dramatically from one point to another, hence introducing higher errors when interpolating their eigen-solutions at the regular frequency intervals.

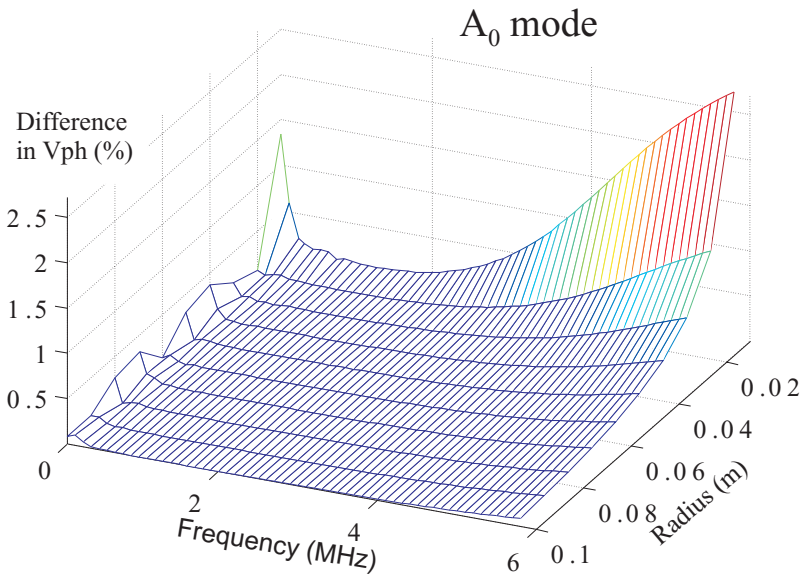

Figure 5.8: Percentage difference in phase velocity V_{ph} of the A_0 mode as a function of frequency and curvature radius for a 1mm thick aluminium plate calculated using a cyclic symmetric FE model.

At frequencies other than the cut-off frequency, the accuracy of the FE method as a function of radius may be demonstrated by plotting the percentage difference of the A_0 mode at 4MHz calculated using the exact and FE methods concurrently, as shown in Fig. 5.12. It can be seen that the FE eigen-solutions overlay the solutions of the exact method for any curvature radius at this frequency, and a similar accuracy can, in general, be obtained across the whole frequency spectrum except near the cut off frequencies for the reasons mentioned.

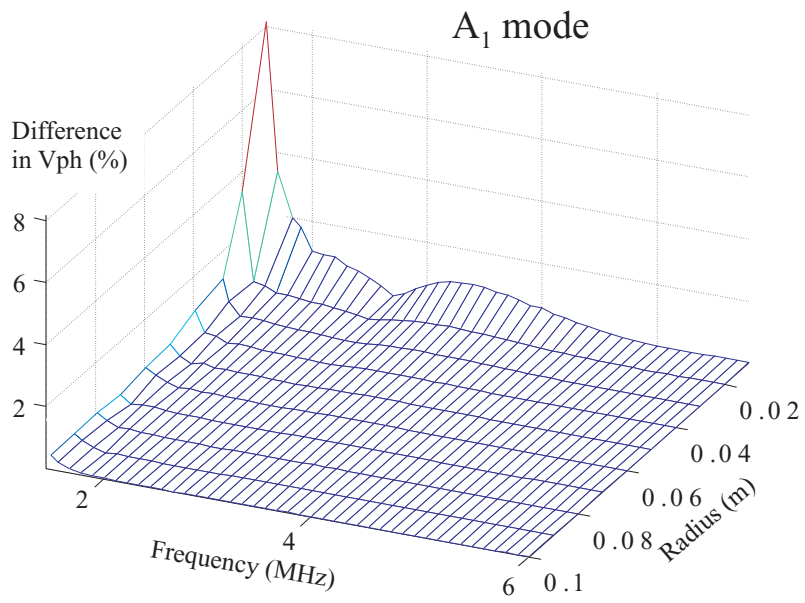

Figure 5.9: Percentage difference in phase velocity V_{ph} of the first order anti-symmetric mode (A_1) as a function of frequency and radius for a 1mm thick aluminium plate calculated using a cyclic symmetry FE model.

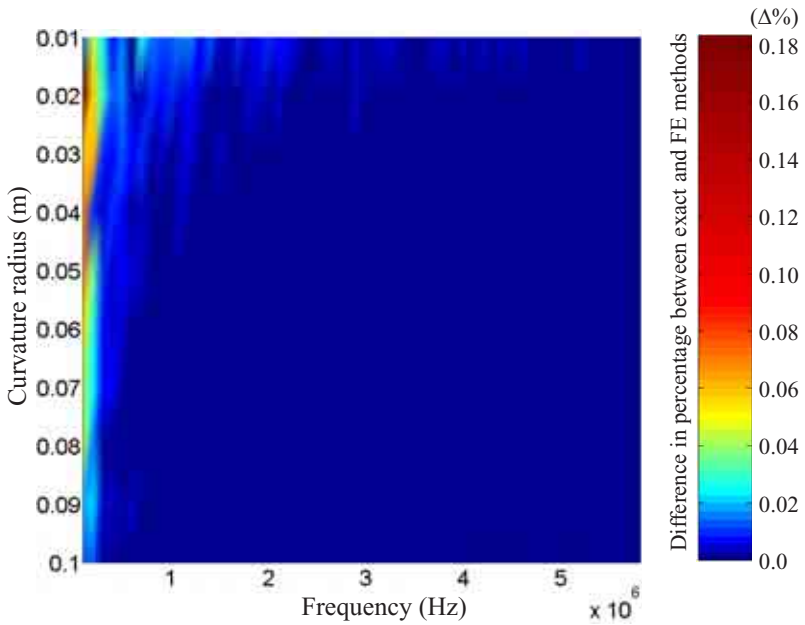

Figure 5.10: Absolute difference in percentage of the phase velocity difference of the A_0 mode between the exact (Fig. 4.2(a)) and the FE (Fig. 5.8) methods in a 1mm curved aluminium plate.

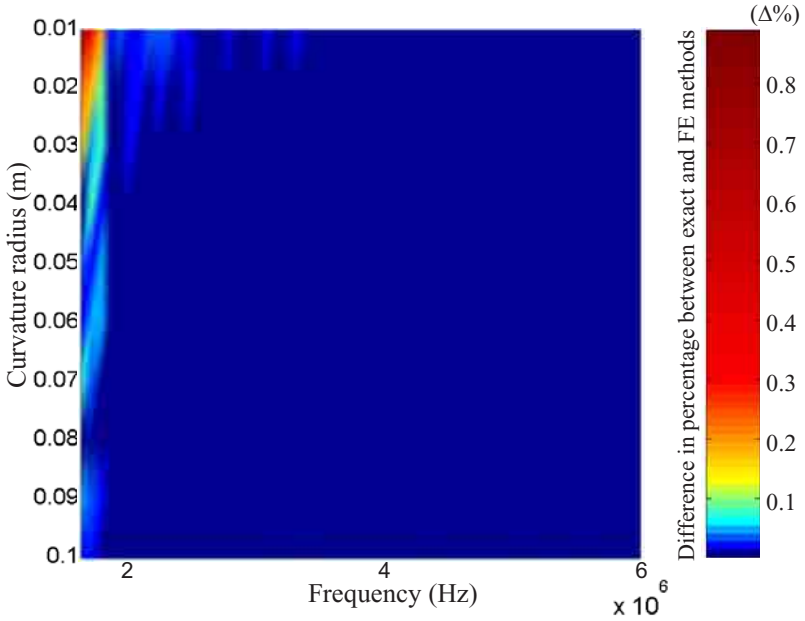

Figure 5.11: Absolute difference in percentage of the phase velocity difference of the A_1 mode between the exact (Fig. 4.2(c)) and the FE (Fig. 5.9) methods in a 1mm curved aluminium plate.

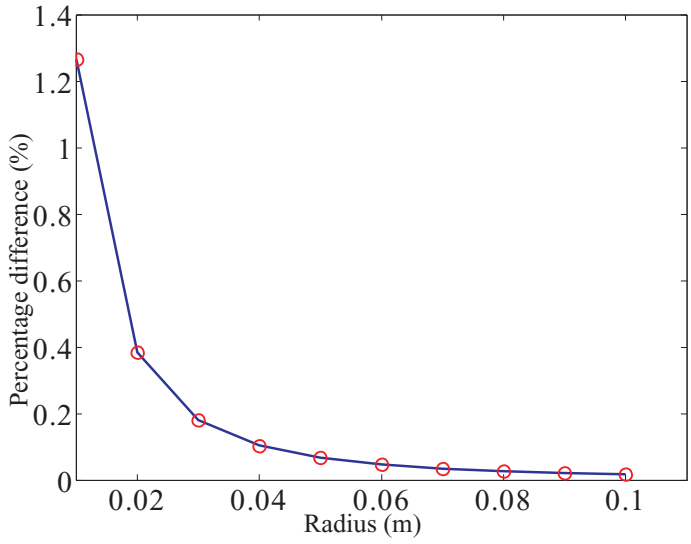

Figure 5.12: Percentage difference due to the curvature effect as a function of radius for the A_0 mode of a 1mm thick aluminium plate at 4MHz using exact analytical (solid line) and FE (circles) methods.

5.2 Experimental Studies

In this section, experimental techniques to illustrate the effect of curvature on the Lamb-type plate wave propagation properties are presented. Furthermore, many of the issues raised during the experiments, such as the excitability of a pure mode, are investigated and discussed.

5.2.1 Experimental Samples

The experiment was carried out with thin high-grade aluminium alloy (Al-2014A-T4) strips that are 0.97mm thick. The thin Al-2014A-T4 aluminium alloy plate has a high ultimate tensile strength that allows one to bend the strips to a tight curvature without passing the yield limit. It is also easier to handle than, for example, steel because of its lower Young's modulus. The material properties of the Al-2014A-T4 aluminium alloy [117] are summarised in Tab. 5.1.

Material	Al-2014A-T4
Young's modulus (MPa)	69500
Ultimate Tensile Strength (MPa)	385
0.2% Proof stress (MPa)	85
Elongation (%)	18

Table 5.1: Material properties of the Al-2014A-T4 aluminium alloy strip [117] used for the experiments.

The theory of circumferential waves developed in the previous chapters were for wave modes propagating in an infinitely wide plate, but of course this is not achievable in practise. Therefore finite width strips must be used, as shown in Fig. 5.13. Strips with a large aspect ratio (H/d) would be favourable in this experiment. However, it is more difficult to bend a wide strip, and furthermore, to achieve a consistent curvature across its length.

Recently, in 2002, Mukdadi *et al.* [118] have discovered that for plates with a small aspect (H/d) ratio, plate modes corresponding to the width of the strip H can be coupled with the normal plate modes of thickness d, creating a guiding system for a rectangular cross section. The extent to which the dispersion relation for this guiding system differs from the infinitely wide plate case of thickness d is highly dependent on the H/d ratio used. Currently there is no literature addressing either the relationship between the H/d ratio and the dispersion relation, or whether it is appropriate to use the modes of a rectangular cross section to approximate those of the infinitely wide plate. To address these questions, guided waves in the rectangular section will be investigated later in Sec. 5.2.4.

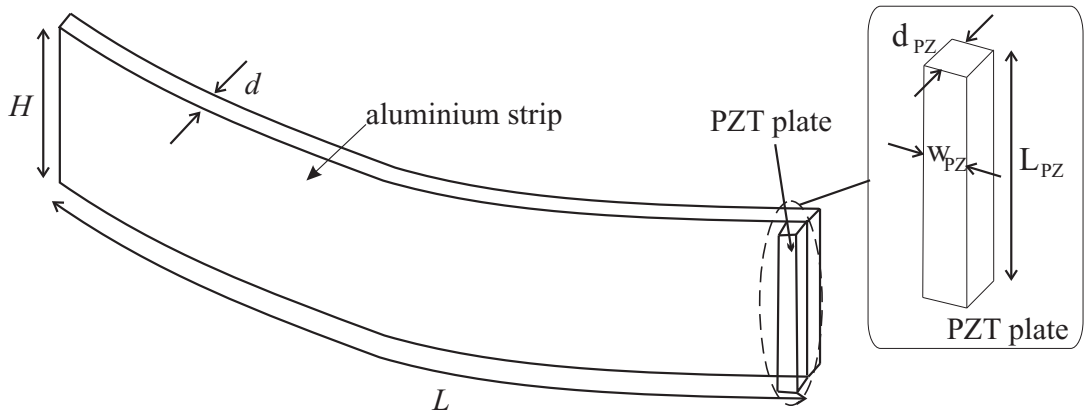

Figure 5.13: Schematic diagram of a thin curved aluminium strip, attached with a PZT plate.

For now, it is assumed that two sets of modes exist: those that are guided purely or almost purely by the width edges of the strip will be referred to as "width modes", while those that are guided by the thickness edges of the strip will be referred to as "thickness modes".

The width of the strip sample for the experiment was chosen so that the H/d ratio is large enough that the "width modes" have minimum interference with the "thickness modes" of the plate. The excitation of the width modes could also be minimised by exciting the strip in such a way that the excitation force does not match the mode shapes of any of the width modes; this will be discussed in the next section. Ideally, only the wave mode for the investigation should be excited, but this is not always easy to achieve. Therefore the sample strip should also be long enough so that it can act as a delay line where the received signals of different modes are well separated from each other in time.

Taking all of these into consideration, an aluminium strip 0.97mm thick (d), 30mm wide (H) and 700mm long (L) was selected for the experimental investigation of the curvature effect.

5.2.2 Excitation Technique

As shown in Fig. 4.2, the curvature effect on the phase velocity of any chosen mode is generally very small, especially when the curvature radius is large. Therefore the excitation method should always provide the same reference signal at different curvatures in order to eliminate any unnecessary error due to the shifting in excitation positions, and this is achieved using a permanently attached PZT transducer.

The mode for the investigation should be easy to excite. The A_0 mode has predominantly "out of plane" displacement at almost all frequencies and for plates of any curvature. Additionally, its properties are significantly influenced by the curvature effect and it is

thus ideal for the investigation. Exciting this mode requires driving the plate with a strong normal force, which is relatively easy to achieve efficiently using two thickness expansion PZT ceramic plates attached to the surfaces on either side of the plate, one excited 180 degrees out of phase to the other.

A commercially available lead based piezoelectric ceramic material Pz27 with properties shown in Tab. 5.2 was used for the experiment. When a voltage is applied to the PZT plates, one contracts while the other one expands, and vice versa in turn, generating a normal force on both surfaces in a synchronised fashion.

The size of the PZT plate used in this experiment is chosen based on the fact that the excitation frequency range is near the centre resonant frequency Cf_{PZ} of the PZT plate, calculated using the relationship given by Eqn. 5.3, where d_{PZ} is the PZT plate thickness and V_{PZ} is the compressional bulk velocity of the PZT material (see Fig. 5.13).

$$Cf_{PZ} = \frac{V_{PZ}}{2d_{PZ}}. \tag{5.3}$$

The experiment was performed at below the cut-off frequencies of the higher order Lamb wave modes ($\approx<$ 2MHz) to minimise any multimodal excitation of the "thickness modes". The PZT elements was 1mm thick (d_{PZ}), 3mm wide (W_{PZ}) and 30mm long (L_{PZ}); the centre frequency Cf_{PZ} of the PZT element is approximately 1.3MHz.

Ceramic Properties	**Pz27**	
Density (kg/m^3)		7740
Compression Velocity (m/s)		2760
Mechanical losses		0.02
Dielectric losses		0.02
Coupling factors	k_p	0.59
	k_t	0.47
	k_{33}	0.70

Table 5.2: Ceramic properties of the piezoelectric plate transducer, Pz27 used in the experiment.

The PZT plates could be attached at the end of the aluminium strip (shown in Fig. 5.14) using either a silver loaded glue or a fast cure epoxy, both of which have advantages and disadvantages. The silver loaded glue, though highly conductive, contains relatively large particles which causes a thick coupling layer in between the PZT plates and the aluminium plate. On the other hand, the fast cure epoxy is easy to manipulate and also gives a much thinner coupling layer than the silver loaded glue, but the epoxy is not conductive. Either the thick or non-conductive coupling layer can cause a significant voltage drop across the adhesive layer when a voltage is applied between the plate and the PZT, leading to a

reduction in the signal to noise ratio. Overall the fast cure epoxy was found to have a better performance than the silver loaded glue, and therefore was used for the experiment.

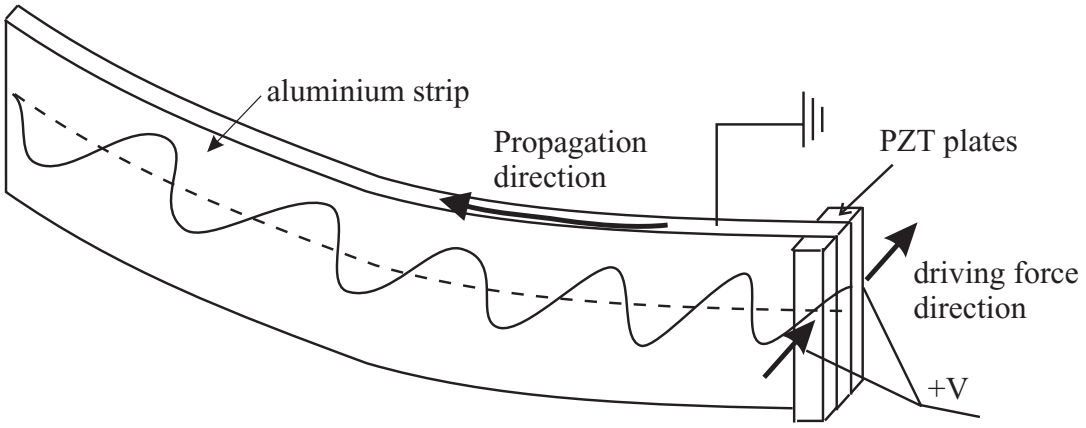

Figure 5.14: Schematic diagram of exciting the A_0 mode in an aluminium strip using PZT plates.

5.2.3 Experimental Setup

The aluminium strip may be bent at different curvatures by mean of fixing the length of the strip onto a set of plastic fixtures that are pinned on a wooden board along a specific curvature radius. A photograph of the experimental setup is shown in Fig. 5.15. In order to allow the plate to deform reversibly, the curvature radius of the experiment is limited by the fact that the sample material should not yield during the bending process. Using the material properties listed in Tab. 5.1, one can calculate the smallest curvature of the aluminium alloy strip, at which the stress applied on the strip during bending is within the yield limit of the material. This relationship between the yield stress σ_y and the minimum curvature radius r_{min} can be readily obtained from standard equations of the stress analysis in the following form:

$$\frac{2\sigma_{yield}}{d} = \frac{E}{r_{min}} \tag{5.4}$$

where E and d are the Young's modulus and plate thickness respectively. The smallest curvature radius r_{min} for which the sample plate remains elastic is approximately 0.09m.

The measurements were taken in a pulse-echo configuration where a signal is transmitted and received through the same set of PZT plates. A 30 cycle Hanning windowed wave packet, which provides a smooth narrow band signal, was used for the excitation. The equipment for generating such a signal involves a pulse generator, a function generator, a power amplifier and a receiver amplifier, all of which have been integrated into a single machine, "WaveMaker-Duet" [119]. Additionally, an oscilloscope and a computer are

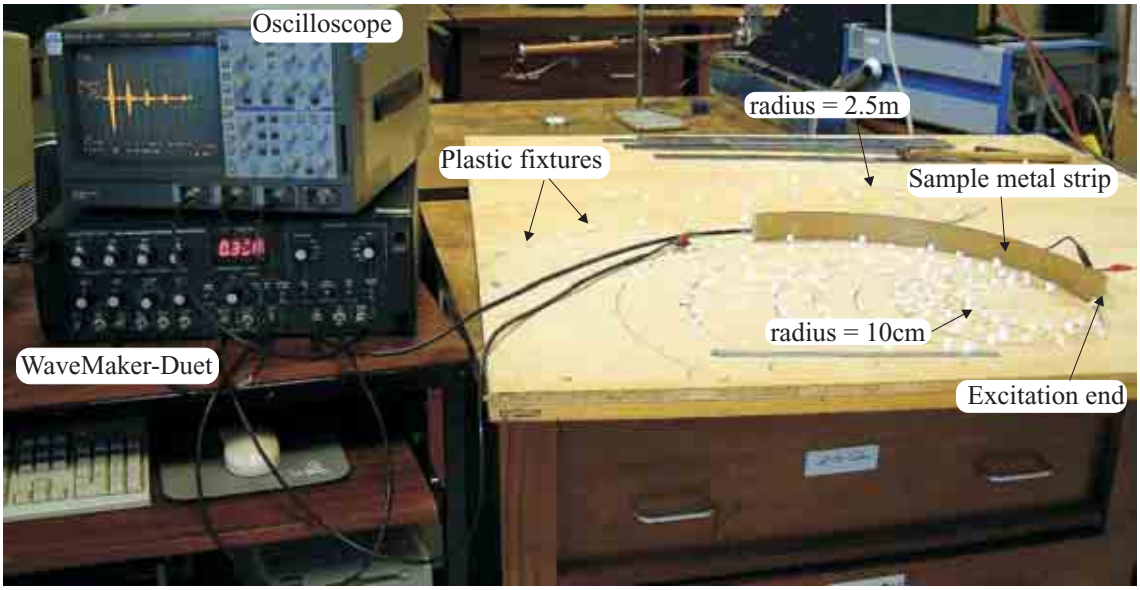

Figure 5.15: A photograph of the experimental setup for the investigation of the curvature effect.

used to save the data of the receiving wave signal for further processing. Fig. 5.16 shows a schematic diagram of the experimental setup.

The pulse generator triggers the oscilloscope simultaneously, while the function generator delivers a tone burst signal with an integer number of cycles to the PZT plates via the power amplifier. The toneburst signal travels back and forth along the aluminium plate after reflecting from the end of the plate, and subsequently being picked up by the same PZT plates. The received signal is amplified and displayed on an oscilloscope and may then be captured digitally in a computer via a GPIB connection.

5.2.4 Excitation Issues of Strip with a Rectangular Cross Section

Due to the presence of the width boundaries in a rectangular cross-section strip, the plate modes in a finite width plate strip may be different to those predicted theoretically for an infinitely wide plate. In general, there are two known issues associated with a waveguide of a rectangular cross-section. In this section each of these two issues is addressed in turn.

"Width-Edges" Effect

The first issue is the so-called "width-edges" effect, where the displacement field across the width of the strip alters due to the presence of the width-edges of a metal strip. Fromme [120] measured the out of plane displacement field of the metal plate surface using a Laser Vibrometer with an excitation method similar to that described in the previous section.

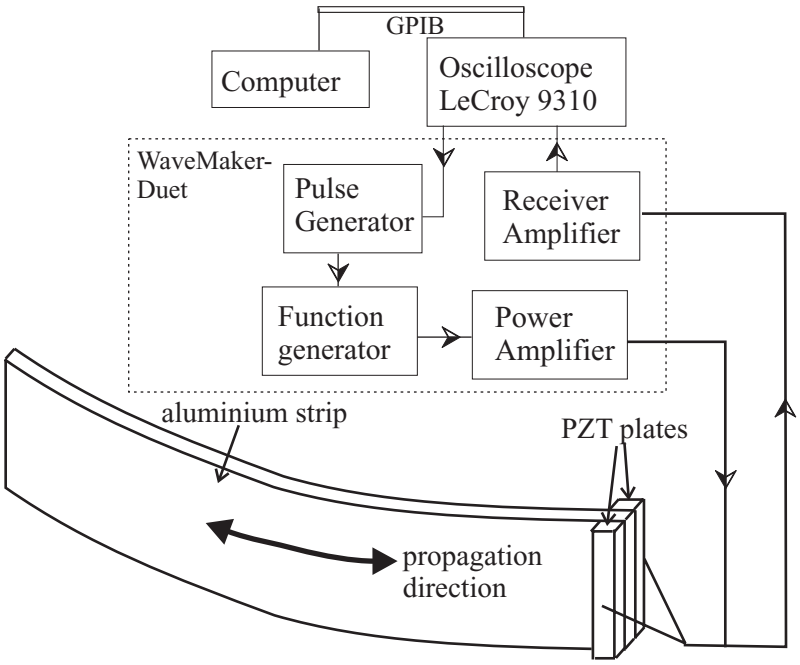

Figure 5.16: Schematic diagram of the experimental setup in a pulse-echo configuration.

He reported that the amplitudes of the out of plane displacement field is significantly higher close to the edges than elsewhere on the strip; the results are reproduced with permission in Fig. 5.17.

The "width-edges" effect has also been investigated on our experimental sample, where the out of plane displacement was measured across the width of the strip at several locations along its length using a Laser Vibrometer. The measurements were taken from the first arriving signal of the A_0 mode from the excitation source at 0.1mm intervals across the width of the strip at 450kHz, and the measured displacement amplitudes were normalised to the maximum amplitude across the width.

Fig. 5.18 shows the displacement amplitude variation across the width. It can be seen that the displacement field has a roughly constant amplitude in the central region of the strip at various locations away from the excitation, and as expected a much higher amplitude close to the width edges can be observed. Moreover, The actual amplitude along the edges was found to be dependent of its location along the strip, though, no further investigation was carried out. The high amplitude along the edges is thought to be caused by the fact that the particles are allowed greater movement due to the lack of constraint along the free boundary, while this is not the case in the central region. In general, the percentage of total energy at edges goes down as width goes up, therefore the "width-edges" effect would have less influence on the displacement field for a wider strip.

This suggests that the A_0 plate mode exists in both finite and infinitely wide plates, despite

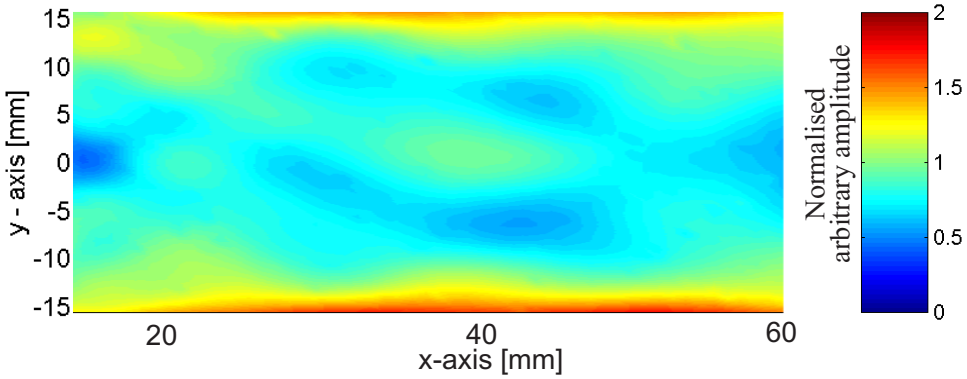

Figure 5.17: A reproduction of a scan measured by Fromme [120] (with permission). The scan shows the out of plane displacement field of the A_0 mode over the surface of a 1mm thick, 30mm wide aluminium strip. The A_0 mode is excited using the same method as described in Sec. 5.2.2 at 160kHz, and the field is measured using a Laser Vibrometer.

the presence of the "width-edges" effect, and they are travelling at the same velocity [118]. It also appears [118] that the A_0 mode has the same phase velocity regardless of the width of the strip at a particular frequency. However, based on the argument on the relationship between the phase velocity and the mode shapes discussed in Sec. 4.2, some influence of the "width-edges" effect should be expected, though they are thought to be insignificant.

This view was confirmed in the study by Gazis *et al.* [121] who used approximate equations of motion to investigate the influence of the width of a plate strip on the velocity of the lower order modes. Gazis *et al.* concluded that the width-edges of the metal strip have a significant influence on the phase velocity up to a large "H/d" ratio, after which the velocity converges asymptotically towards that of an infinitely wide straight plate. Although there is no specific value of "H/d" given to which the velocity is considered to be converge to that of the plate case. The velocity measurements of the A_0 mode taken from the 30mm wide strip match exactly to that of the analytical prediction, demonstrating that the strip has a "H/d" ratio where the velocity is asymptotic to that of the infinitely wide plate.

Rectangular Wave Modes

During the experiment, an excitation of a single pure A_0 plate mode was extremely difficult to achieve. Despite exciting at a frequency that is lower than the cut-off frequencies of the higher order modes, multimodal excitation was very common. Furthermore, many of the modes which are excited travel at velocities which do not correspond to either the A_0 or S_0 mode. This raises the suspicion that wave modes which are excited correspond to those of the rectangular cross section.

Every care has been taken to ensure that only the out of plane displacement field corre-

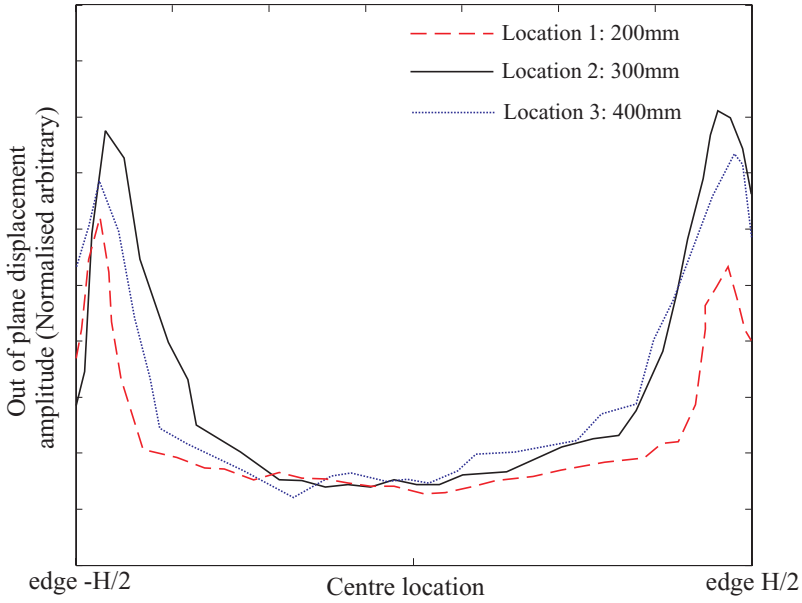

Figure 5.18: Measured out-of-plane displacement amplitude of the A_0 mode across the width of the aluminium strip sample at several locations along its length, at 450kHz.

sponding to the A_0 mode is excited. However, an imperfection of the PZT bonding to the strip surface is inevitable, resulting in an uneven distribution of the out of plane loading across the bond line of the PZT plate. This behaviour encourages the excitation of waves that are wholly or partially coupled with the waves reflecting back and forth between the boundaries of the width-edges. These coupled modes are referred to as the "rectangular-modes" in this thesis in recognition of their existence in a rectangular cross-section.

At many frequencies, the excitation of the "rectangular-modes" is unavoidable. However, at other frequencies these "rectangular-modes" may not be strongly excited. This is because the "rectangular-modes" become highly dispersive at these frequencies, where the different frequency components of the corresponding signal travel at different velocities, resulting in the energy of the dispersive mode being spread out in time. In this case a good clean signal of the A_0 mode can be obtained for the measurement of the phase velocity difference between the straight and curved waveguides. Fig. 5.19 shows the time responses at frequencies of 650kHz and 1MHz, at which the "width-modes" are strongly excited and are extremely dispersive respectively.

Using the FE cyclic symmetry modal analysis detailed in Sec. 5.1, the dispersion curves of the waveguide consisting of a rectangular cross-section with dimensions (thickness: 0.97mm, width: 30mm), as in the experiment, were obtained. The FE model used a large radius of 400mm to obtain the approximate solutions for the straight case. This technique of approximation had been verified by Wilcox *et al.* [115]. Figs. 5.20 and 5.21 show the frequency-angular wavenumber and phase velocity-frequency dispersion curves for such a rectangular waveguide. The presence of the edges introduces an extra dimension of

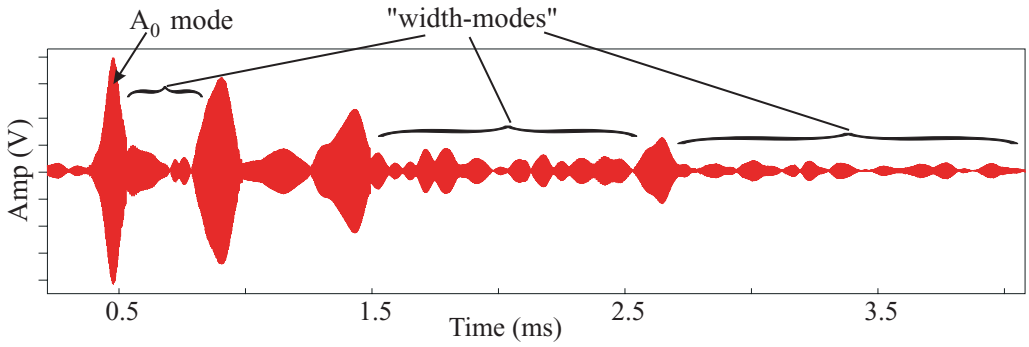

(a) 650kHz

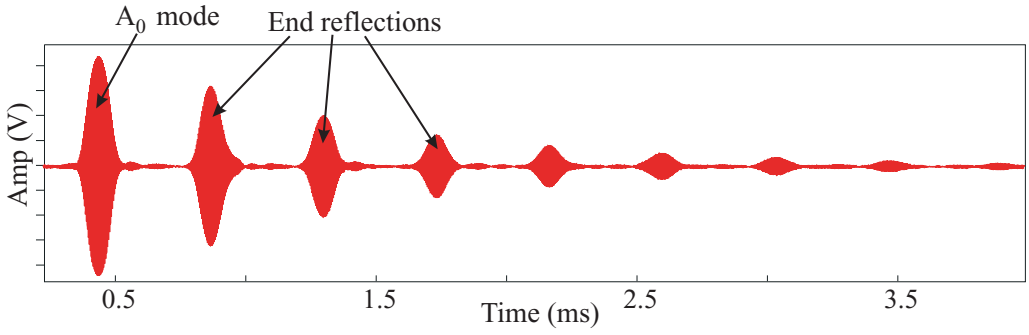

(b) 1.0MHz

Figure 5.19: Time responses of the experiment in a pulse-echo configuration using a straight aluminium strip (thickness:0.97mm, width: 30mm) which was excited with a 30 cycle Hanning windowed toneburst signal at one end of the strip.

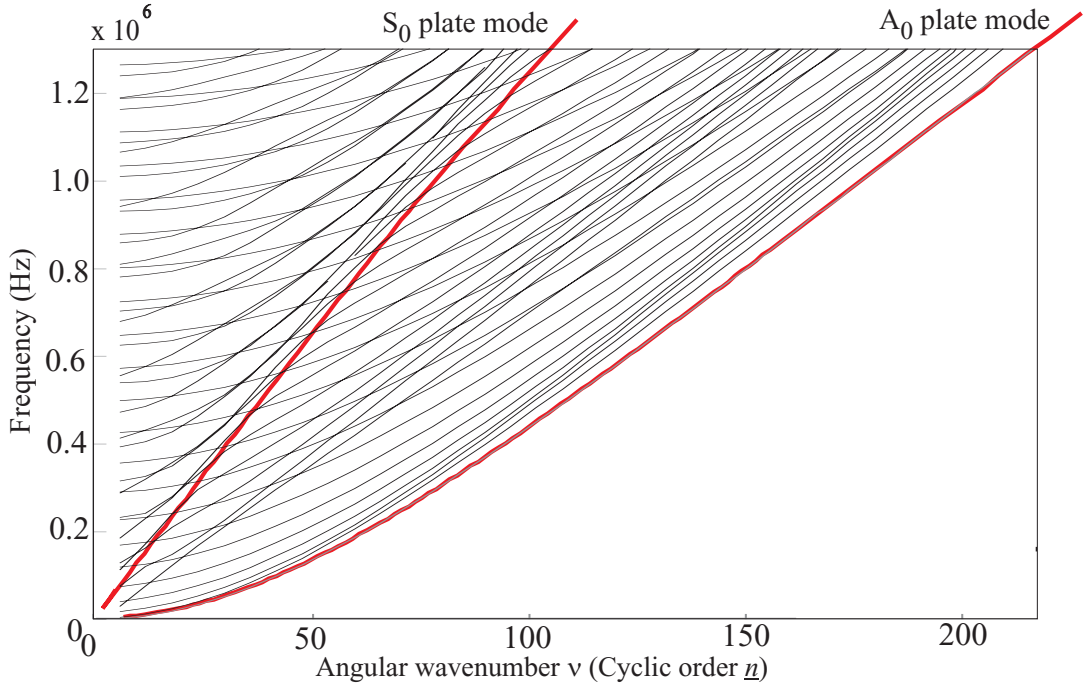

Figure 5.20: Frequency-angular wavenumber dispersion curves for a rectangular cross section aluminium strip (thickness: 0.97mm, width: 30mm, Black lines), and those of an infinitely wide aluminium plate (0.97mm, Red lines). The dispersion curves of the rectangular cross section were modelled using a cyclic symmetry FE model with an inner radius of 400mm.

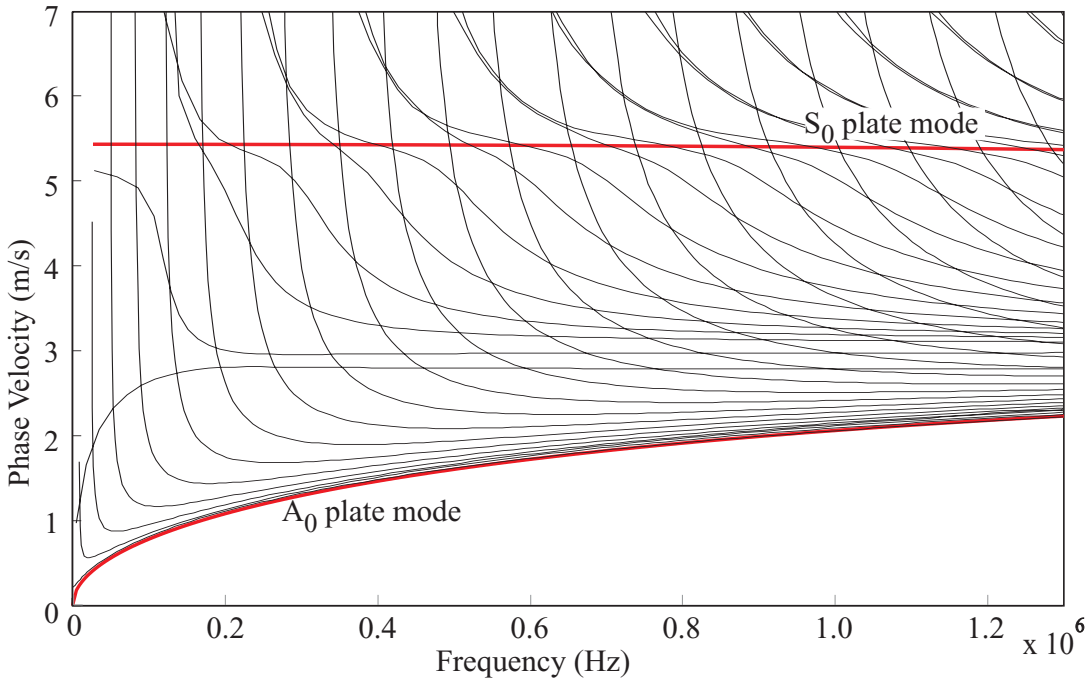

Figure 5.21: Phase velocity-frequency dispersion curves for a rectangular cross section aluminium strip (thickness: 0.97mm, width: 30mm, Black lines), and those of an infinitely wide aluminium plate (0.97mm, Red lines). The dispersion curves of the rectangular cross section were modelled using a cyclic symmetry FE model with an inner radius of 400mm.

movement, and the rectangular cross section system is therefore able to support a much higher number of wave modes in the frequency range below the cut-off frequency of the higher order infinite plate modes.

In general, the waves of a rectangular cross section waveguide can be divided into 3 types depending on their interaction with the different sets of boundaries.

1. **Thickness-plate modes:** These correspond to modes of an infinite plate whose thickness is the same as that of the strip and are subject to the edges effect. Only two exist in a frequency range of up to 1.4MHz in this case (see Fig. 5.20).
2. **Width-plate modes:** These correspond to modes of an infinite plate whose thickness is equal to the width of the strip and are subject to the edges effect. There are many in this frequency range.
3. **Twisting modes:** Modes that are coupled between the "thickness-plate modes" and the "width-plate modes", resulting in a twisting motion of the metal strip.

The dispersions curves of the latter two cases are shown in Figs. 5.22 and 5.24, while the mode shapes of the lower order modes of their corresponding type have been calculated at 300kHz from the eigen-vectors at the corresponding $\omega_m - n$ eigenvalues shown in Figs. 5.23 and 5.25. Although there are many wave modes of these two types in the frequency range of interest for this experiment, judging from their mode shapes, it can be easily seen that many of the higher order modes could not be excited because of very poor matching of the excitation force to their complex mode shapes. Furthermore, the "width-edges" effect is clearly visible from the mode shapes of the A_0 mode shown in Fig. 5.24.

Having the dispersion curves of the rectangular cross section, it is now possible to investigate the modes that have been excited during the experiment and their amplitudes at various frequencies, using a 2-dimensional Fourier transformation (2DFFT) technique [122]. The technique provides an indirect means of extracting the dispersion curves of the Lamb waves quantitatively from the experimental measurements of multimodal signals. This technique measures the signal of the time-responses at a certain known distance interval along the propagation direction using a Laser Doppler Vibrometer (LDV). An illustration of the setup can be found in Fig. 5.26. The measurement was performed in a "pitch-catch" configuration where the signal is excited with the PZT plates and subsequently picked up by the LDV after travelling a certain distance along the strip.

Generally, the measured results are in the time-spatial domain from which the 2DFFT is applied to transform the data into the frequency-wavenumber domain. The time-response data was measured with 32,000 time sampling points at every 1mm interval over a distance of 100mm in the propagation direction. The collected data formed a matrix, from which

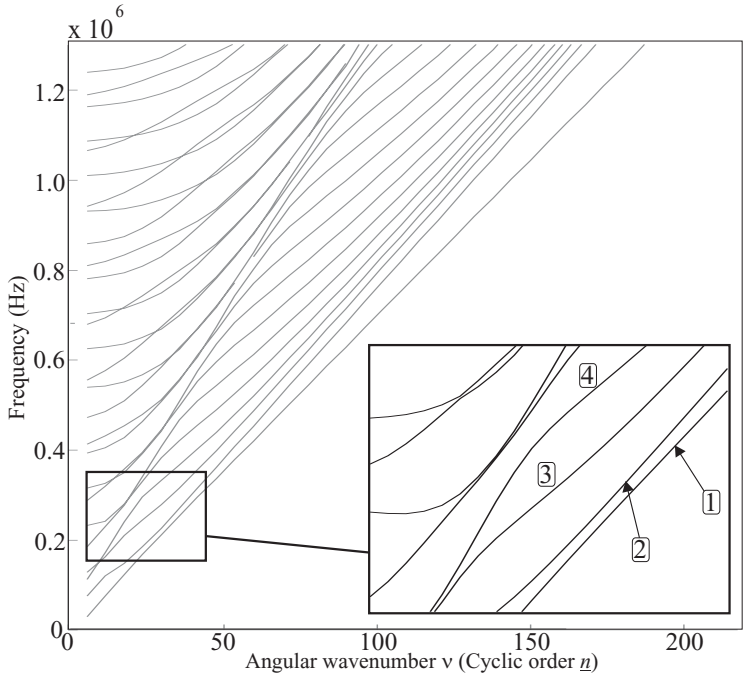

Figure 5.22: Dispersion curves of the "width-plate modes" for a rectangular cross section aluminium strip (thickness: 0.97mm, width: 30mm). The lower order modes are labelled in the zoom-in window, which correspond to the mode shapes in Fig. 5.23.

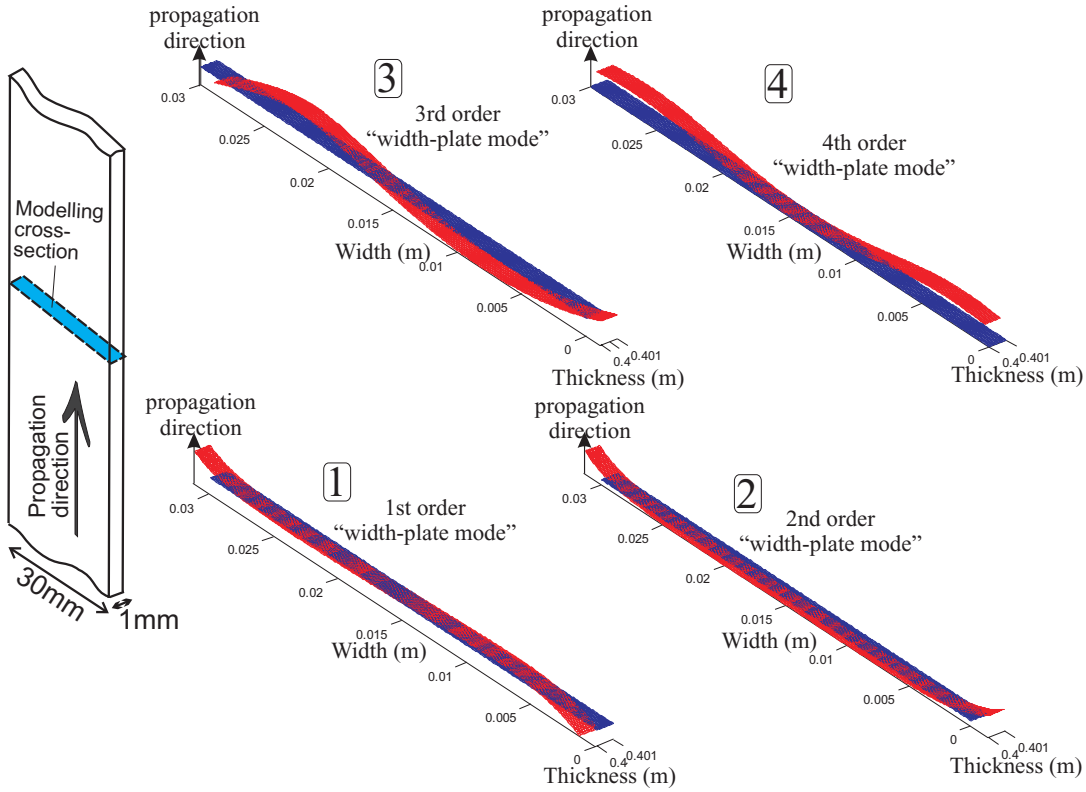

Figure 5.23: The displacement mode shapes (red mesh) of the "width-plate modes" corresponding to those labelled in Fig. 5.22 at 300kHz, while the undeformed mesh is shown in blue.

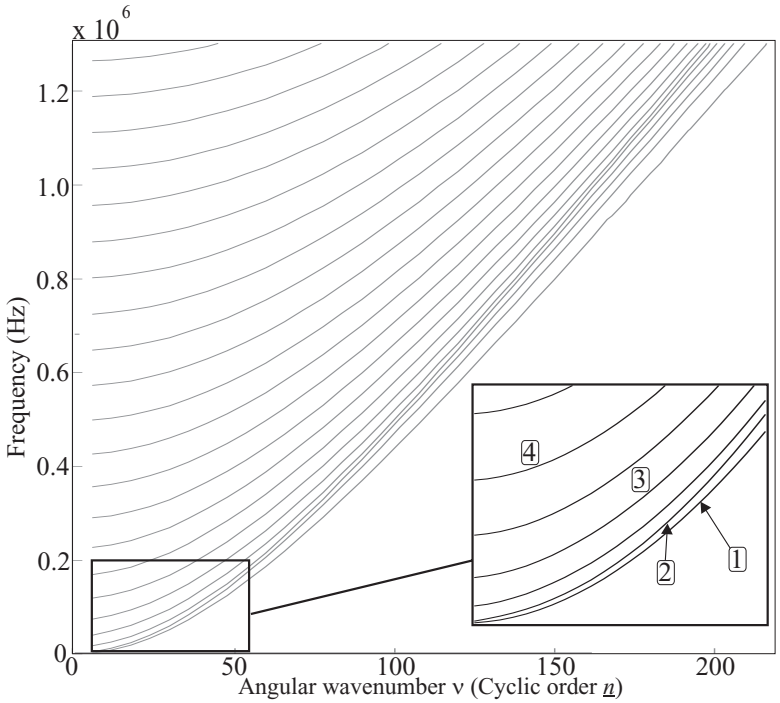

Figure 5.24: Dispersion curves of the "twisting modes" for a rectangular cross section aluminium strip (thickness: 0.97mm, width: 30mm). The lower order modes are labelled in the zoom-in window, which correspond to the mode shapes in Fig. 5.24.

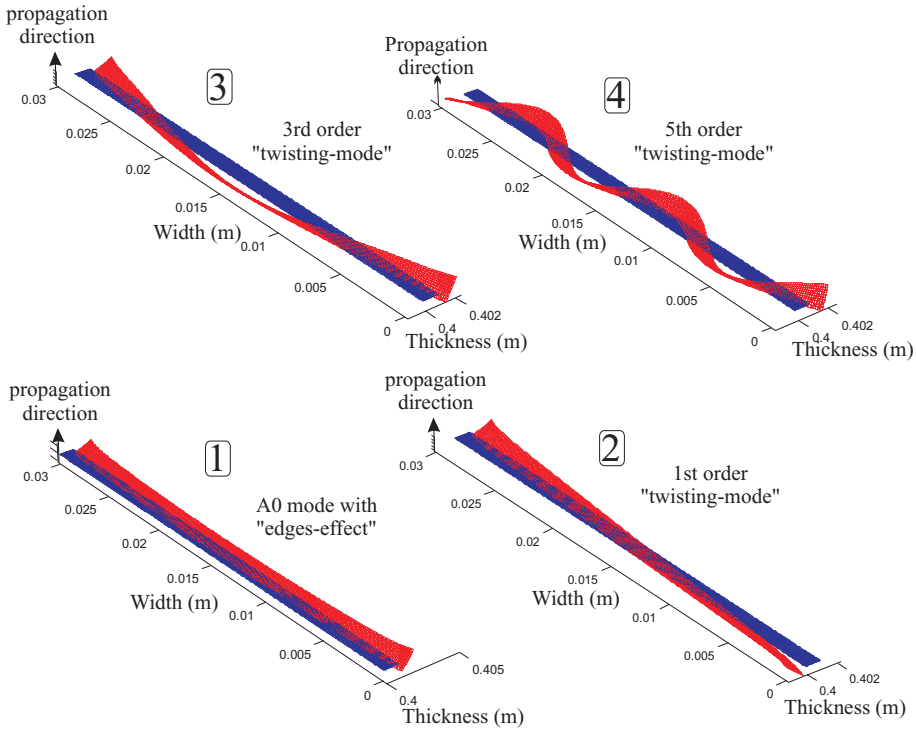

Figure 5.25: The displacement mode shapes (red mesh) of the "twisting modes" corresponding to those labelled in Fig. 5.24 and that of the A_0 mode at 300kHz, while the undeformed mode shapes is shown in blue mesh.

the 2DFFT was performed in a Matlab^{TM} program. The 2DFFT generates a 2-D colour map showing the distribution of energy and its amplitude at various locations in the frequency-wavenumber domain. By overlaying this colour map with the dispersion curves for the sample (Fig. 5.23), the modes that are strongly excited would be easily identified.

To visualise the contrast between the multimodal and the nearly pure-mode excitations, the 2DFFT technique was performed twice at the centre frequencies of 650kHz and 1.0MHz. These frequencies correspond to those used in obtaining the time responses of Fig. 5.19. At 650kHz (Fig. 5.27), as well as the A_0 mode, the S_0 and 1^{st} order "width-plate" modes have been strongly excited, although it is also clearly visible that there are numerous other "width-plate" modes being weakly excited. With such a multimodal excitation, it would be impossible to carry out any sensitive measurements of the curvature effect on the A_0 mode.

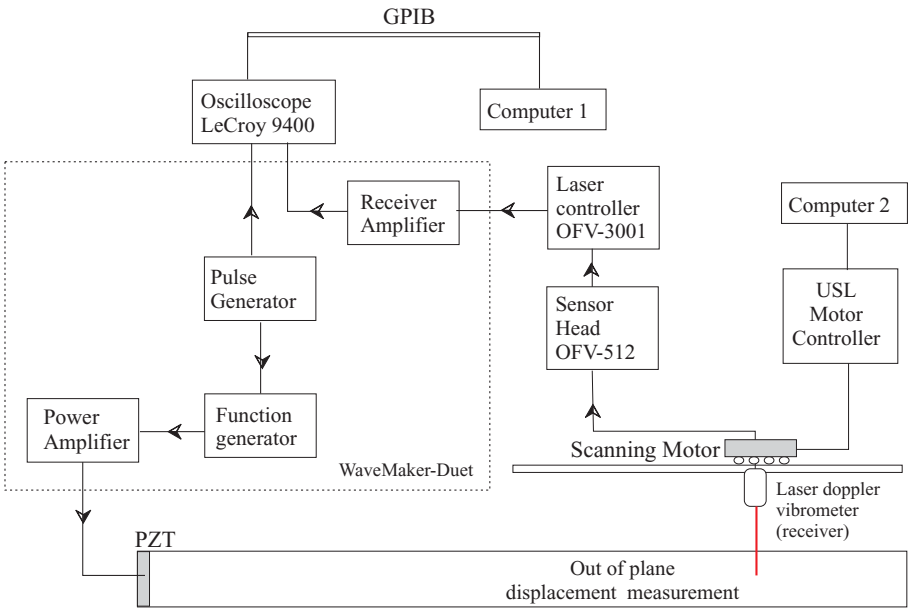

Figure 5.26: Schematic diagram of the experimental setup for measuring the time responses at a regular spatial interval along the propagation direction.

On the other hand, the 2DFFT result measured at 1.0MHz (Fig. 5.28) reveals that the S_0 and the "width-plate" modes have not been strongly excited. This confirms the observation of a nearly "pure-mode" excitation of the A_0 mode in the time response at this frequency shown in Fig. 5.19(b).

Typically, a good signal to noise ratio can be obtained in a relatively broad frequency range of approximately 300kHz to 2MHz using the PZT plates. Within this frequency range, there are many frequencies at which a nearly "pure-mode" excitation can be achieved and may be used for measuring phase velocity accurately.

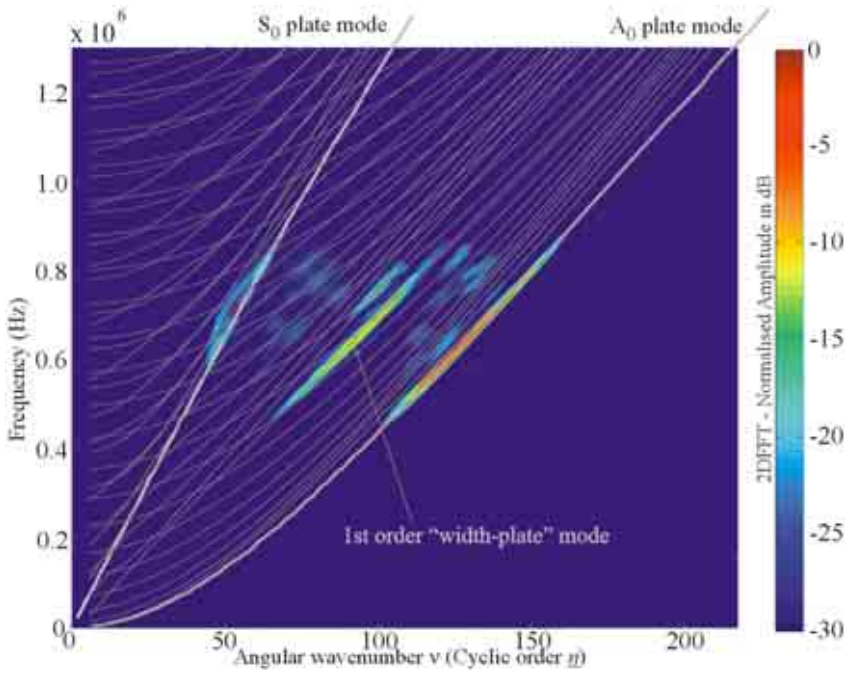

Figure 5.27: A colour map showing the result of the 2DFFT of the measurements obtained from the aluminium strip sample (thickness: 0.97mm, width: 30mm) with 32000 time and 100 spatial sampling points. The aluminium strip was excited at a centre frequency of 650kHz. The colour map overlays with the dispersion curves of the aluminium strip sample.

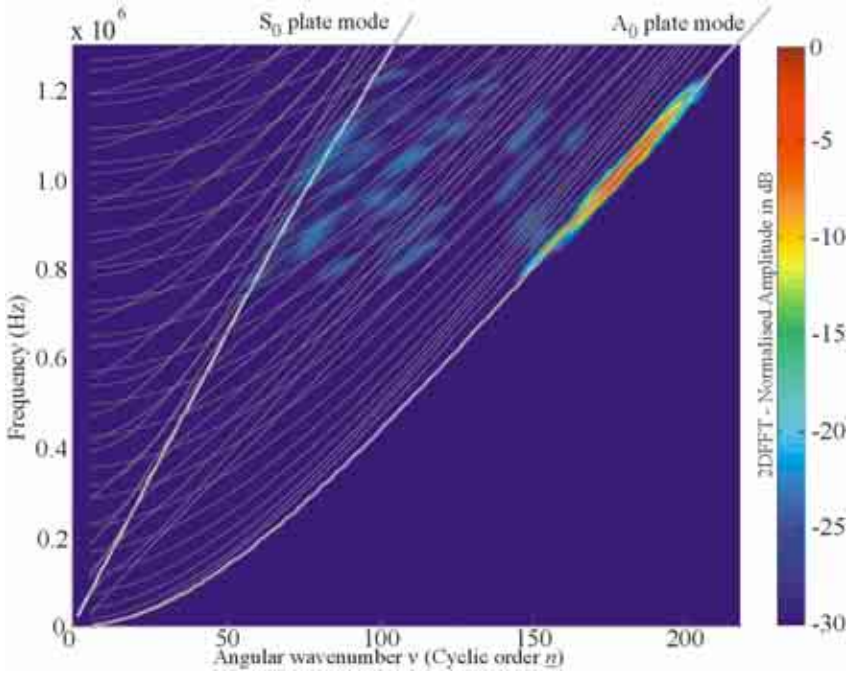

Figure 5.28: A colour map showing the result of the 2DFFT of the measurements obtained from the aluminium strip sample (thickness:0.97mm, width: 30mm) with 32000 time and 100 spatial sampling points. The aluminium strip was excited at a centre frequency of 1.0MHz. The colour map overlays with the dispersion curves of the aluminium strip sample.

5.2.5 Measurement of Relative Velocity

The permanently attached PZT plates allow the signal to be excited and received at the same reference locations, thus any shift in the time response should in theory, be caused by the difference in phase velocity of the A_0 mode travelling at different curvatures. The time response of the wave packet signal of both the straight and curved systems after travelling a certain distance, for example the first or the second end reflection of the metal strip, may be measured. Since the difference in phase velocity between the straight and curved cases is extremely small, as predicted in Sec. 4.1 (in most cases the difference is less than 1%), the actual difference in time between the straight and curved cases after travelling back and forth along the strip would still be much less than the time period of one wavelength.

The most reliable way to measure fractional changes in velocity is to identify the zero-crossing time of a particular sinusoid in the signal, as shown in Fig. 5.29. These two measured zero crossing points have the same phase, however, the difference in the measured times is caused by the velocity shift in the curved plate. Therefore the normalised phase velocity difference at the excitation frequency for a toneburst signal which had travelled a distance l, can be calculated using Eqn. 5.5. Vph_{st} is the phase velocity of the corresponding wave mode in a straight plate. This measurement relies on the signal being very narrow band, which can be treated practically as a single sinusoid.

$$\text{Difference in Vph}(\%) = \frac{l}{Vph_{st}} \cdot \frac{\text{abs}[t_c - t_f]}{t_c t_f} \cdot 100. \tag{5.5}$$

where t_c and t_f are the zero-crossing time of the curved and straight cases respectively.

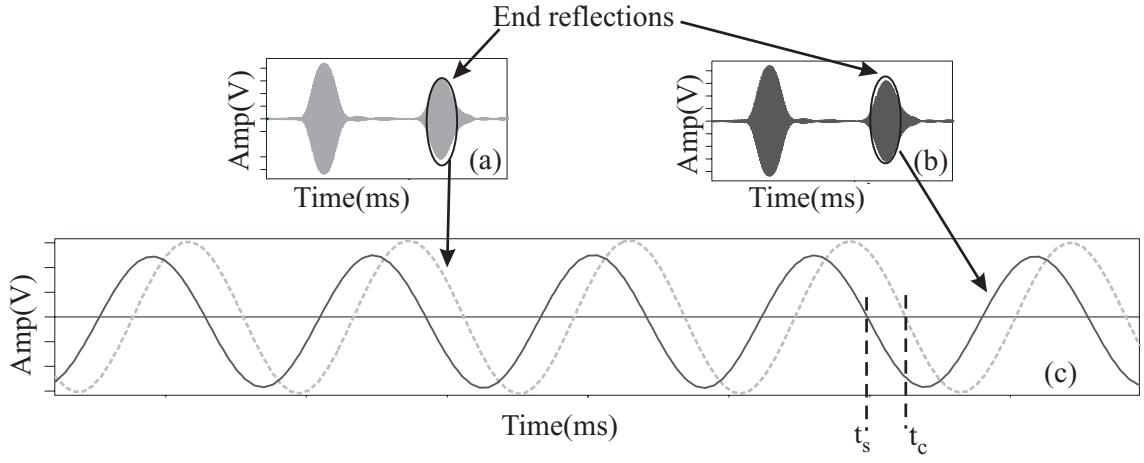

Figure 5.29: Time response of end reflection of the A_0 mode, (a) for a straight and (b) for a curved waveguide, and (c) the detail of their overlay, showing the arrival time of the striaght t_s and curved t_c cases.

5.2.6 Preliminary Results on Velocity Measurements

As discussed in the previous chapter, numerical instability of the exact circumferential waveguide solution occurs at high frequencies. Therefore the experimental measurements were validated against solutions obtained using the exact method, and with the asymptotic method where exact solutions become unstable. Results were only measured at certain frequencies where a nearly "pure-mode" was obtained, as discussed earlier. At other frequencies, the excitation of the "rectangular modes" interfered with the A_0 mode signal. Using several identical sample strips, experimental measurements were possible at 450kHz, 1.0MHz, 1.1MHz and 1.3MHz over a range of curvature radii, and these results together with those calculated from the analytical and FE methods are shown in Fig. 5.30.

The change of velocity from these predictions grows rapidly with reducing curvature radius as expected. Although the experimental results follow a similar upturn with reducing curvature radius at all four frequencies, the change of velocity from the experimental measurement was found to be higher than those from the analytical predictions. Additionally, these changes were also found to increase steadily with increasing curvature.

In general, there are two possible explanations for this discrepancy. First, it was difficult to force the aluminium strip into a constant curvature along the whole length with merely the plastic supports, especially at the ends of the strip, due to its elasticity. Nevertheless, this problem was thought to be minor and could be easily fixed. Secondly, the strip sample was constantly under stress when curved, which could change the material properties through the thickness. This was thought to be the significant cause of the error, and therefore further investigation was necessary.

5.2.7 Validation against an Improved Analytical Model

Bending of the metal strip can have two profound effects on the material properties through the thickness of the plate, which are discussed in this section. The effects are the local applied stress and the local density, both of which could affect the acoustical properties locally. The stress field varies linearly across the thickness in such a way that the inner and the outer surfaces have the highest compression and tension respectively at that particular curvature radius. Therefore the experimental validations could be improved either by taking into account the stress condition and the local density variation in the model, or by annealing the experimental samples to remove the variation of material properties permanently at each curvature.

The annealing idea is thought to be far too difficult to achieve without damaging the bonding of the PZT plates during the process, which could alter the reference signal, and thus reduce the accuracy of the measurements. For this reason, it would be sensible to

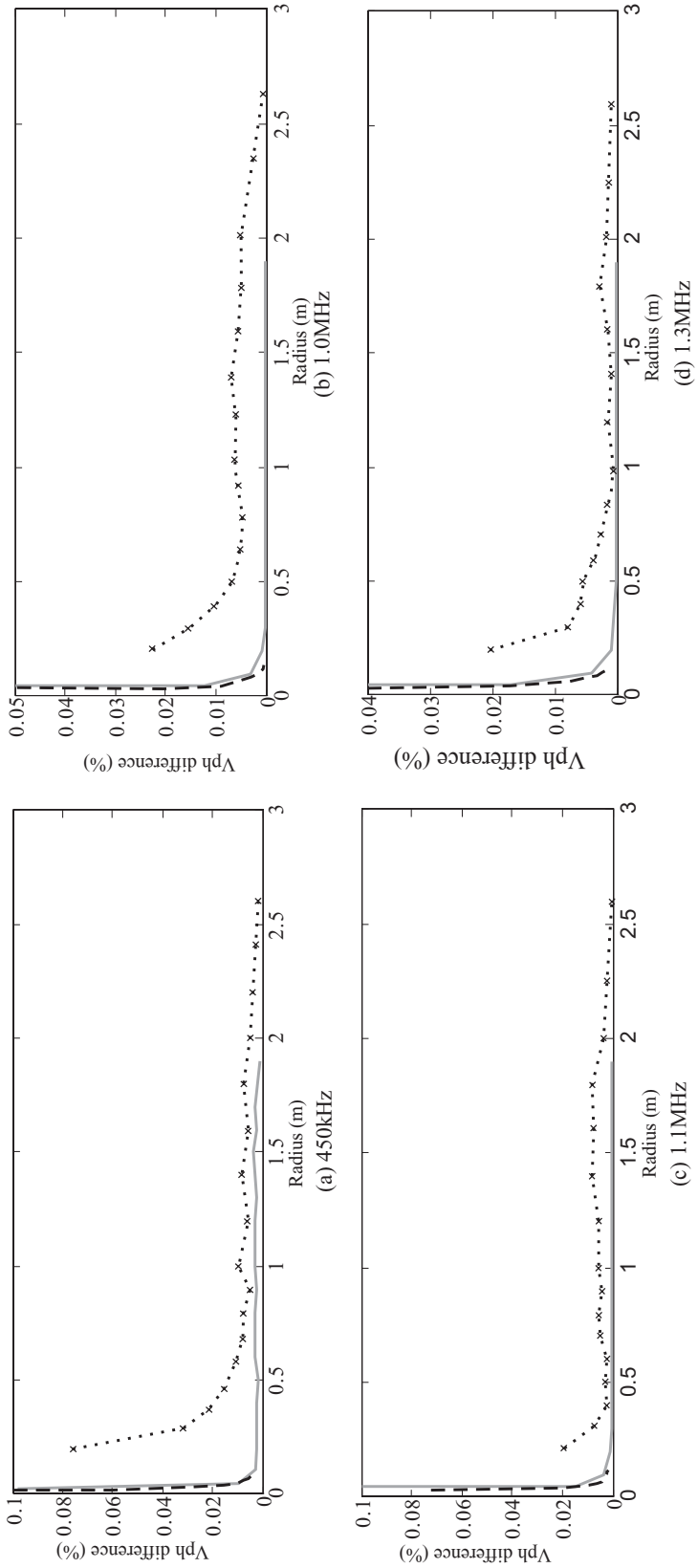

Figure 5.30: Percentage difference in phase velocity V_{ph} as a function of radius between 0.97mm thick aluminium straight and curved plates, calculated using exact analytical method (Dashed line), simplified Regional Asymptotic method (Solid line), and Experimental measurements (Dotted line).

simply include these "stress-induced" conditions into the analytical model. For this to be done, it is necessary to understand what parameters need to be updated in the analytical model.

The dispersion relation (Eqn. 2.18) is governed by the geometry properties of the thickness d and mean radius r_{mid}, and also the material mechanical properties of the Young's modulus E, poisson's ratio υ and density ρ. The latter are linked to the Lamé constants (λ, μ) in the following forms:

$$\lambda = \frac{\upsilon E}{(1+\upsilon)(1-2\upsilon)}, \qquad \mu = \frac{E}{2(1+\upsilon)}. \tag{5.6}$$

and thus Eqn. 2.9 of the bulk velocities, C_T and C_L become:

$$C_L = \sqrt{\frac{E(1-\upsilon)}{\rho(1+\upsilon)(1-2\upsilon)}}, \qquad C_T = \sqrt{\frac{E}{2\rho(1+\upsilon)}}. \tag{5.7}$$

Both the thickness d and the length of the mid-plane of the aluminium strip are assumed to be constant during bending. By contrast, the material properties can change significantly due to the acousto-elastic effect [123] where the bulk velocities of a material are sensitive to stress within the material, as well as the local density changes. The bulk velocities of a stressed structure may be calculated using the Murnaghan third-order elasticity theory [124]. The theory relates the stresses and the bulk velocities in the orthogonal directions of the cartesian coordinates.

Since the Lamb-type wave modes in an infinitely wide curved plate polarise only in the r and θ directions, which can be assumed to be orthogonal at a local level, the bulk velocity can then be recalculated using the following relevant equations [123]:

$$\begin{aligned}
\rho_0 C_{LP}^2 &= \lambda + 2\mu - \frac{P_{local}}{3K_0}(7\lambda + 10\mu + 6l + 4m) \\
\rho_0 C_{TP}^2 &= \mu - \frac{P_{local}}{3K_0}(3\lambda + 6\mu + 3m - \frac{n}{2}) \\
\rho_0 C_{LS}^2 &= \lambda + 2\mu + \frac{S_{local}}{3K_0}(\frac{\lambda+\mu}{\mu}(4\lambda + 10\mu + 4m) + \lambda + 2l) \\
\rho_0 C_{TS}^2 &= \mu + \frac{S_{local}}{3K_0}(4\lambda + 4\mu + m - \frac{\lambda}{\mu}\frac{n}{4})
\end{aligned} \tag{5.8}$$

The subscripts L and T indicate the longitudinal and shear wave motion respectively, and P_{local} and S_{local} are the compressional and tensional local stresses applied in the direction of propagation (i.e. on the inner and outer halves through the thickness respectively). μ, λ, l, m, and n are the first and third order global elastic constants, whereas K_0 is the global bulk modulus for an isotropic material defined as $K_0 = (\lambda + 2\mu/3)$, while ρ_0 is the

density of the material in the initial unstrained state. The third-order elastic moduli of solids account for the non-linear interaction of sound waves in solids that are caused by the applied directional stresses.

One basic assumption in the theory is that the material remains elastic throughout the deformation. This was investigated by measuring the stress as a function of strain for the aluminium sample in an Instron 5500 series tensile testing machine, and the results are shown in Fig. 5.31. It can be seen that the stress-strain relationship has remained virtually linear, even above the maximum stress level relating to that experienced by the aluminium strip with the smallest curvature radius investigated. The small offset in the graph could be caused by the slipping of the clamping jaws during the measurement.

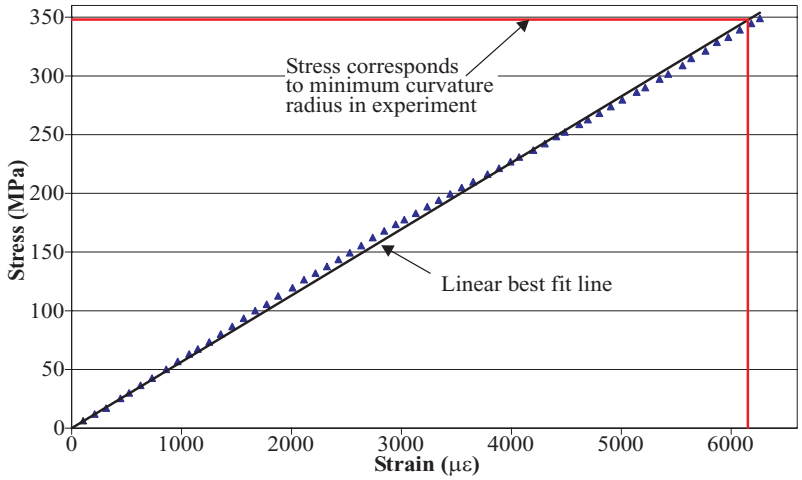

Figure 5.31: Stress strain relationship of the aluminium sample (Al-2014A-T4, thickness: 0.97mm, width: 30mm, length: 700mm). In addition, the highest stress level, corresponding to that in aluminium strip with the minimum curvature radius (10cm), is indicated in the graph.

The third-order elastic moduli of aluminium based alloys with various weight proportions of copper (Al-Cu) and Magnesium (Al-Mg) have been measured by Kesava Raju *et al.* [125]. The third-order moduli of the Al-2014A aluminium sample may be inferred from Kesava Raju's measurement results of the aluminium alloy that contains the closest metal compositions. The moduli were taken from the mean values of the measurements of a Al-4.8%Cu composition, compared to a Al-4.5%Cu-0.4%Mg composition for the Al-2014A aluminium sample, and they are listed in the Tab. 5.3 in the expression defined by Toupin *et al.* [126] which can be converted back to those used in Eqn. 5.8 by using the following [123]:

$$l = \frac{\nu_1}{2} + \nu_2, \qquad m = \nu_2 + 2\nu_3, \qquad n = 4\nu_3. \tag{5.9}$$

To include the conditions due to bending, an improved plate model with its thickness discretised into 9 layers has been analysed; each layer has a thickness of δd and is assumed

Toupin and Bernstein [126]		Murnaghan [124]	
ν_1	+ 6.0	l	-7.8
ν_2	-10.8	m	- 25.6
ν_3	-7.4	n	-29.6

Table 5.3: Mean value of the measured third-order elastic moduli of Al-4.8%Cu alloys at 298K in units of $10^{10}\mathrm{Nm}^{-2}$, obtained from Toupin *et al.* [126], and the corresponding moduli expressed by Murnaghan [124] .

to have the same curvature at the top and bottom of each layer. In addition, it is assumed that the plate is sufficiently wide compared to the thickness and the properties are uniform at all points in each layer. By doing so, the local density, ρ_{local} in each layer, due to strain while bending, may be calculated as a function of the local radius (r_{local}) shown in Eqn. 5.10.

$$\rho_{local} = \frac{\rho_0 \; r_{mid}^3}{r_{local}(r_{mid} + \upsilon r_{local} - \upsilon r_{mid})^2}. \tag{5.10}$$

Using Eqns. 5.8 and 5.10, the appropriate values of C_L, C_T and ρ_{local} corresponding to the local curvature radius in each layer of the model can be calculated to account for the through-thickness variations of density and velocity due to the local applied stresses. The solution of this analytical model of each layer is assembled using the Global Matrix method [98], with suitable boundary conditions between the layers (i.e. σ_{rr}, $\sigma_{r\theta}$, u_{rr} and $u_{\theta\theta}$ are continuous at the interface, while maintaining stress free conditions at $r = r_{1,2}$).

As a demonstration, the parameters of each of the 9-layers for the case of an aluminium sample that is bent to a curvature radius of 20cm are listed in Tab. 5.4. A negative value of stress in the table indicates compressional stresses P, while a positive value indicates tensional stresses S. The aluminum sample has unstrained material properties of: C_L = 6320m/s, C_T = 3230m/s and density $\rho_0 = 2700\mathrm{kg/m}^3$. Layer 5 is on the neutral axis and so has properties which have not been modified, while the local material properties are calculated at the mid-depth position in each layer. It can be seen from Tab. 5.4 that the bulk velocities are, in general, more sensitive to the compressional stresses than to the tensional stresses. Using these parameters, the dispersion curve of the A_0 mode of this multi-layered model was calculated and is shown in Fig. 5.32.

It is worth noting that although the percentage changes of longitudinal and shear bulk velocities, due to the stress and strain conditions on the outermost layers of the plate, are as high as 0.19% and 0.26% respectively, the change in phase velocity of the A_0 mode calculated with the stressed multilayered model compared to the unstrained single curved layer, is typically less then one thirtieth of a percent over the whole frequency range. The

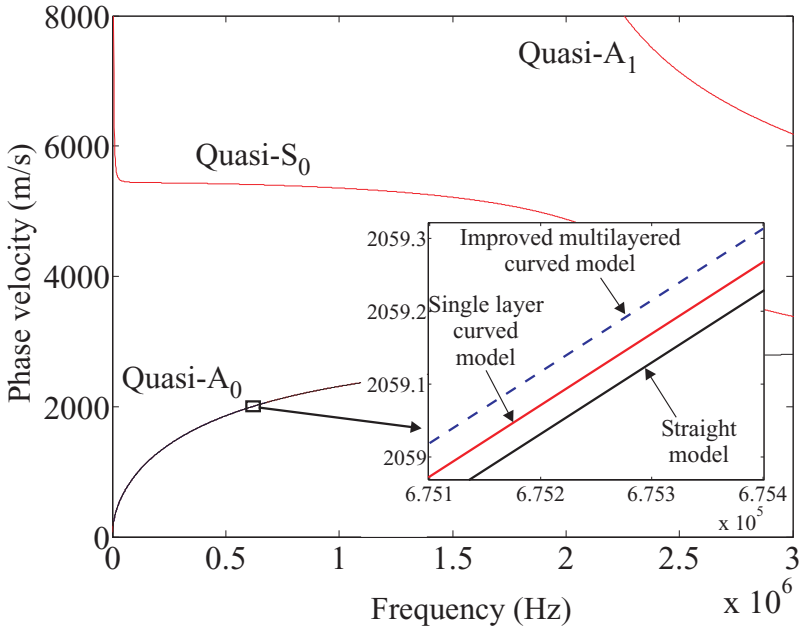

Figure 5.32: Phase velocity dispersion curves of an aluminium curved plate (thickness: 0.97mm, curvature radius: 20cm) using a single layer exact solution (Red solid line) and a multilayered improved model (Blue dashed line), and for an aluminium straight plate of the same thickness (Black solid line).

	Local radius (m)	Local applied stress P_{local} or S_{local} (MPa)	Local C_L (m/s)	Local C_T (m/s)	Local density ρ_{local} (kg/m^3)
Layer 1	0.199573	-74.1	6308.03	3125.21	2709.67
Layer 2	0.199680	-55.6	6311.02	3126.41	2707.25
Layer 3	0.199787	-37.1	6314.02	3127.61	2704.83
Layer 4	0.199893	-18.5	6317.01	3128.80	2702.41
Layer 5	0.2	0.0	6320.00	3130.00	2700.00
Layer 6	0.200107	18.5	6320.18	3132.02	2697.59
Layer 7	0.200213	37.1	6320.36	3134.04	2695.18
Layer 8	0.200320	55.6	6320.55	3136.06	2692.78
Layer 9	0.200427	74.1	6320.73	3138.07	2690.38

Table 5.4: Parameters of the 9 layers of a multi-layered model that is used to approximate the local variation of stress and density due to bending. The aluminium strip is 0.97mm thick and has a curvature radius of 20mm. Layer 5 is on the neutral axis and so has properties which have not been modified. The local parameters (P_{local}, S_{local}, Local C_L, Local C_T and ρ_{local}) are for the mid-depth position in each layer.

reason for such a small phase velocity alteration despite the larger changes of the bulk velocities may be understood to be the cancelling effect of the stress conditions where the overall stress is averaged out over the top and bottom halves through the thickness.

The dispersion curves of the 0.97mm thick aluminium plate were recalculated for curvature radii between 0.1m and 0.7m using the improved multilayered model, and subsequently used to compare again with the experimental results using Eqn. 4.1. The solutions are limited to curvature of small radii because of the solution breakdown when the curvature radius is large, as discussed in Sec. 2.3. It can be seen in Fig. 5.33 that the prediction of the experimental measurements using the analytical stressed model has improved significantly, compared to the single layer unstrained model used before in Sec. 5.2.6. The upturn of the velocity difference curve in Fig. 5.33 for the stressed curved plate case, occurs at a higher curvature radius. This is because when the curvature radius is small, the acousto-elastic effect becomes dominant, and therefore increases the difference greatly compared to the unstrained case.

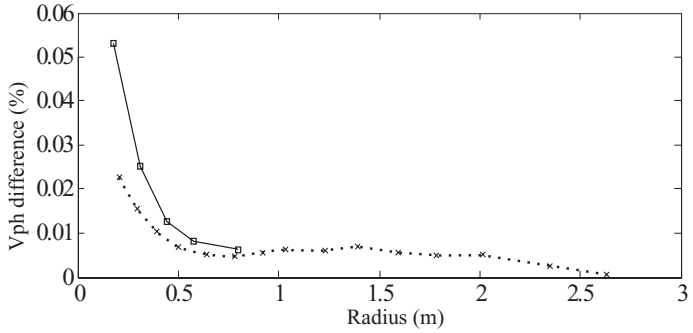

Figure 5.33: Percentage difference in phase velocity V_{ph} at 1.0MHz as a function of radius between 0.97mm thick aluminium straight and curved plates calculated with the multilayered analytical model (Solid line), and the experimental measurements (Dotted line).

5.2.8 Experimental Validation of the Displacement Mode Shapes

As discussed in Sec. 4.2, the displacement mode shapes can change substantially when the plate is bent from one curvature radius to another, and it is therefore interesting to measure such an effect experimentally. In general, it is rather difficult to measure the through-thickness displacement mode shapes directly and accurately, especially for plates with very small thickness. However, the curvature effect can shift the displacement field towards one surface, resulting an asymmetric mode shapes. Thus it is possible to validate the displacement mode shapes indirectly by comparing the ratio of displacement amplitudes taken on directly opposite sides faces of the plate.

The measurements was taken using the same aluminium sample and excitation method described earlier in Sec. 5.2.1 and Sec. 5.2.2 respectively. The toneburst signal of the

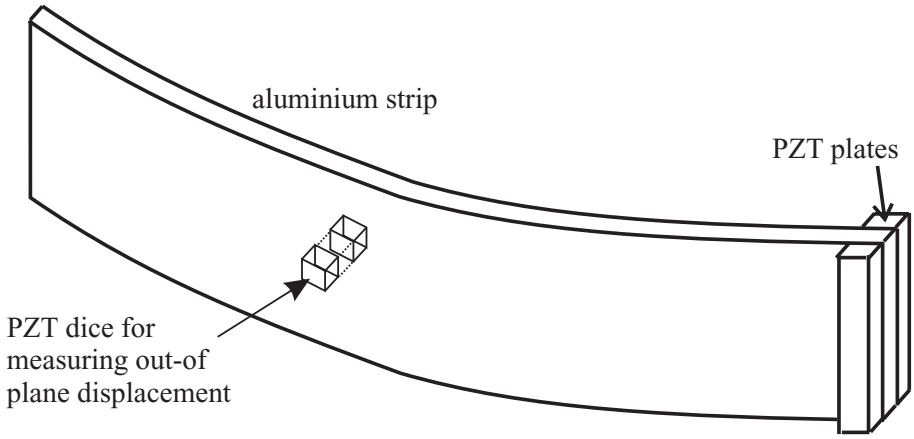

Figure 5.34: Schematic diagram of the PZT dice which are used to measure the out-of-plane displacement on the two surfaces.

A_0 mode was subsequently picked up by two small PZT dice elements (2mm cubes) that were glued directly opposite to each other on either side of the plate surfaces, as shown in Fig. 5.34. This allows the out-of-plane displacement amplitudes on both surfaces to be measured and are subsequently used for the validation of the phenomenon of asymmetric through-thickness mode shapes.

To compensate for any difference in the transducer sensitivity and coupling, each of the measured amplitudes was first normalised by the corresponding displacement amplitude taken when the plate is straight. The ratio of the amplitudes measured in the experiment were then compared with those calculated using the exact solution, and the results are shown in Fig. 5.35. The results of the measurements show a consistent trend with the analytical predictions. When the plate is straight, the ratio of the amplitude measured on the outer surface to that on the inner surface, is equal to one. As the curvature of the aluminium plate reduces, the displacement ratio reduces too, indicating that the displacement amplitude on the outer surface is becoming greater than that on the inner surface, hence shifting the displacement field as predicted.

5.3 Summary

The accuracy of using a cyclic symmetry finite element modelling technique to calculate dispersion curves of curved plates has been demonstrated; this requires that a sufficient number of elements be used to represent the through-thickness displacement mode shapes precisely. The number of elements required is dependent on the complexity of the mode shapes, which increases with increasing frequency and mode order. The asymmetric behaviour of the through-thickness mode shapes has been correctly presented in the modelling. The results of the FE modelling were then used to validate the exact prediction of

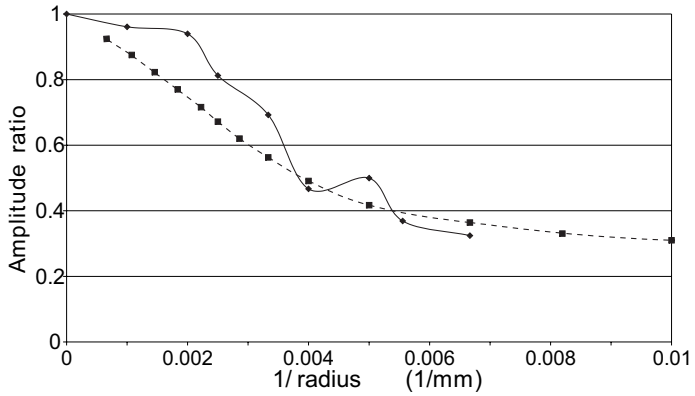

Figure 5.35: Ratio of the A_0 out-of-plane displacement amplitude between the outer and the inner surfaces as a function of curvature for a 0.97mm aluminium plate at 1.0MHz obtained experimentally (Solid line) and analytically (Dashed line).

the curvature effect on the phase velocity. In general, good agreement has been obtained, except near the cut-off frequency of the wave mode due to some minor numerical errors.

A simple experimental technique to validate the curvature effect has been introduced. Due to the small changes in phase velocity by the curvature effect, all aspects which could cause an inaccurate prediction have been carefully investigated. This includes the selectivity of the excitation wave mode and the local through-thickness variation of density and bulk velocities caused by the strain-stress conditions. The results of these investigations form the basis of an improved model, where conditions other than the curvature effect that were induced during the experiment, have been included into the analytical model. The experimental measurements match the prediction obtained from the improved analytical model reasonably well.

Chapter 6

Circumferential Guided Waves in Loaded Curved Plates

This chapter concerns the investigation of the curvature effect on the guided wave properties in curved plates coupled to an infinite half space of solid or fluid. This is an extension of the studies on the unloaded case detailed in the previous chapters, where it was found that the curvature has an insignificant effect on the wave propagation velocity when the curvature radius is moderately large. Thus predictions of a straight structure should in theory provide a sufficient accuracy for the inspection of a curved structure of the same cross section in most cases. In a loaded system, such as an embedded rockbolt, a dramatic increase in attenuation of some wave modes has been previously reported [2] when the rockbolt was curved, and thus the loaded curved system may still prove to be significantly different to the loaded straight system.

The aim of this chapter is to understand the effect of curvature on the attenuation due to the leakage of energy into the surrounding medium as the wave mode propagates along the structure. This study is of fundamental importance, especially to improve the understanding of some issues in the inspection technique of curved rockbolts (see Ch. 1).

To the best of the author's knowledge, there are currently no publications on the exact analytical solution of leaky circumferential Lamb-type waves, except a paper by Rousselot [127] dealing with circumferential wave propagation around thin shells. The reason for the lack of publications in this field is mainly the difficulty in solving the analytical solutions of this particular system; the analytical solution contains many complicated Bessel functions of complex order as part of the global solution. Currently, there is very little knowledge on how best this complex function is solved. In this chapter, both the analytical solution of the loaded curved plate problem and the solving of the Bessel functions with a complex order are addressed.

Numerical examples of the leaky case are presented in the second half of the chapter, which are subsequently used for predicting the curvature effect on the attenuation and phase velocity of the leaky plate modes. This chapter is based on work published in Fong *et al.* [128].

6.1 Literature Review on Leaky Circumferential Waves

Although, as mentioned earlier, there are currently very few papers studying the leaky circumferentially propagating guided waves, there is a relevant topic that is closely linked concerning leaky vibration modes scattering from pipes immersed in fluid; this topic has been studied extensively using a so-called "Resonance Scattering Theory" (RST) which was first derived in 1945 by Osborne *et al.* [129]. The difference between the studies of the leaky circumferentially propagating guided waves and the wave mode scattering problem using RST is that the former case addresses the waves travelling along a curved plate system, while their energy is leaked into the surrounding medium; on the other hand, the latter case addresses vibration, and does not correctly describe the attenuative nature of propagating modes due to leakage into the surrounding medium.

The general solutions for the displacement field ($\mathbf{U}$) of wave modes are typically given by Eqn. 6.1, where $\mathbf{A}$ is the field amplitude as a function of radial position through the thickness, and ν and ω are the angular wavenumber and angular frequency respectively.

$$\mathbf{U}(r,\theta) = \mathbf{A}(r) \cdot e^{i(\nu\theta - \omega t)}. \tag{6.1}$$

Either or both the wavenumber ν or frequency ω in Eqn. 6.1 can in theory be set to be complex, where the imaginary part accounts for the decay in the field amplitude as the wave modes propagate. However, these two complex quantities are in fact representing problems of two very different physical natures as reported by Bernard *et al.* [130].

The use of these two complex quantities can be easily mixed up, especially in a leaky curved plate system where the coupled half space medium has a much smaller impedance than the plate layer. For example, a metallic plate layer couples with a water half space. In this case, due to the mismatching of the impedance between the two coupled materials, the leakage is normally small. As a consequence, the imaginary part of the complex root, regardless whether a complex frequency $\bar{\omega}$ or a complex wavenumber $\bar{\nu}$ is used, is not the dominant part of the root. In fact, there is very little difference in the real part of the roots between solutions calculated using the complex frequency $\bar{\omega}$ and the complex wavenumber $\bar{\nu}$. For this reason, good agreement for an experimental validation have been reported [131] despite the experiment corresponding to one case and the analytical prediction to the other.

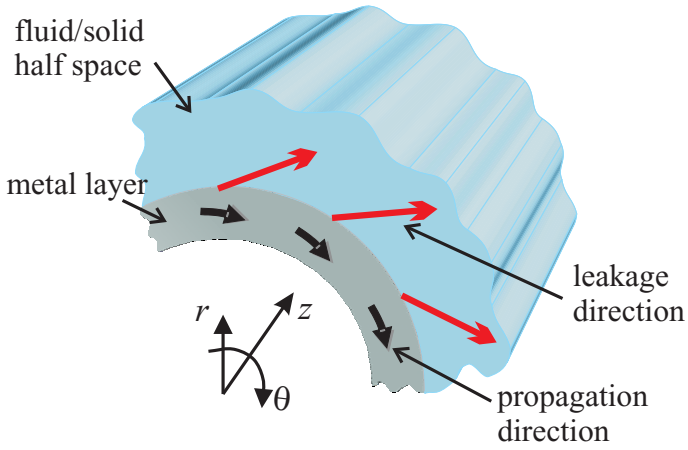

Figure 6.1: Illustration of the leaky circumferential wave problem and the coordinate system.

The RST uses a complex frequency ($\bar{\omega} = \omega_{real} + i\omega_{imag}$), and integer wavenumber; the solutions describe a steady state leaky system of the vibration modes of pipes with a certain integer number of harmonic cycles around the circumference at various frequencies. However, for a transient system (Fig. 6.1), a complex wavenumber ($\bar{\nu} = \nu_{real} + i\nu_{imag}$) and real frequency should be used; this would allow a correct description of the field amplitude that decays over distance while propagating around a curved waveguide.

The fundamental governing equations for these two problems are extremely similar, both of which contain Bessel functions. However, because of the use of a complex frequency $\bar{\omega}$ in the case of RST, only the Bessel functions of a complex argument and a real order are required to be solved; the solutions to the Bessel function with this combination of the argument and order are readily available (see for example Abramowitz *et al.* [99]).

On the other hand, problems represented by the Bessel functions with a complex order have not been studied thoroughly in the past; as a result, their nature is not yet clearly understood. Currently there are few numerical schemes available to calculate the Bessel functions of this combination of order and argument, and all of them are extremely difficult to implement; some of these issues are discussed later in this chapter.

Because of this obstacle in solving these Bessel functions, the investigation of the vibration scattering problem using the RST has become much more advanced compared to the leaky guided wave problem.

6.1.1 Complex Frequency - RST

All references listed in this section relate to solutions calculated using the complex frequency $\bar{\omega}$ while the wavenumber remains real throughout. The RST was originally de-

veloped for problems of acoustic-wave scattering from elastic cylinders and spheres which has subsequently been applied to the case of elastic wave scattering from cavities (see for example [132, 133, 134]).

Using the normal modal analysis, Breitenbach *et al.* [133] for the first time in 1983, plotted the phase velocity dispersion curves for the low-frequency modes in an aluminium cylindrical shell of various ratios of inner and outer radii.

Later, in 1984, Gaunaurd *et al.* [135] produced the phase velocity, group velocity and also attenuation dispersion curves for the first few circumnavigating surface waves using both the normal mode analysis and the RST. Subsequently, Talment *et al.* [136] extended this to the higher order modes, including the so-called "whispering gallery mode", the Rayleigh mode and the fluid-borne Stoneley mode.

In 1999, Maze *et al.* [137] examined the repulsion phenomena in the phase-velocity dispersion curves of the circumferential plate waves using a perturbation theory. The papers by Talment *et al.* [136] and Maze *et al.* [137] were later summarised in a publication by Bao *et al.* [138], together with a small extension which includes solutions for pipes that are both loaded and filled.

In 1998, Ahyi *et al.* [139] observed experimentally the acoustic excitation of the A_0 wave mode on a shell using long-pulse incident sound waves. The technique involves capturing in a photograph the wavefronts of the excited wave modes that are leaked into the surrounding fluid, from which it would be possible to evaluate the velocity of the corresponding wave mode.

6.1.2 Complex Wavenumber - Leaky Guided Circumferential Waves

Up until now, all analytical studies of the leaky circumferentially propagating guided waves have been limited to surface-type or interface-type waves. The first paper in which a complex wavenumber was used to account for the energy leakage of the surface Rayleigh wave on elastic cylinders into the surrounding fluid, was published in 1975 by Frisk *et al.* [140]. In the subsequent year, the same group of authors published two other papers on the solutions of two surface type circumferential waves on immersed pipes: one being the study of creeping waves [141] which are also known as the Franz modes, and the other being the "whispering gallery wave" [106]. The solutions of both cases were obtained using a heavily reduced form of the exact method, of which the limiting case corresponds to either of these two waves types.

Detailed experimental studies of the circumferentially propagating Rayleigh and Lamb waves have been previously examined on a cylinder immersed in water by Bunney *et al.* [142] in 1969. Additionally, in the same paper, Bunney *et al.* studied these waves on

cylinders with a range of different materials.

Later, in 1985, Rousselot [127] derived the dispersion curves of circumferentially propagating waves in a shell system (i.e. wall thickness $d \to 0$) using a modal theory. Despite the success in obtaining the analytical solutions to this case, the results shown in this paper are limited to the low frequency region of the dispersion curves.

In 1997, Hassan *et al.* [92] investigated a family of circumferential creeping waves around a fluid-filled cylindrical cavity in an elastic medium, where the phase velocity, group velocity and also attenuation dispersion curves were studied for this family of wave modes. The formulation of the analytical solution was adapted from that of the Rayleigh case on curved surfaces [74]. Later, in a sequel paper, Hassan *et al.* [143] examined the attenuation of the solid-borne Rayleigh waves and the fluid-borne Creeping waves in a fluid-filled cylindrical cavity, and some experimental validations of the analytical predictions were given.

6.2 Exact Analytical Model of the Leaky Circumferential Waves

A system may be considered to be leaky if a solid or fluid half space is coupled either on the inner (concave) or outer (convex) surface of the pipe or curved plate. However, it can readily be seen that for the filled case the energy leaking into the internal medium can be re-incident further around the pipe and so in fact is not lost, whereas for the externally loaded case, the leaking energy vanishes away from the interface. Therefore the convex case is the more interesting to study.

Fig. 6.1 shows the schematic diagram and the coordinate system of the problem of interest, where a curved metal plate couples with either a solid or fluid half space on the outer plate surface; this system will be referred to as the leaky case for the rest of this thesis.

The fundamental formulations of the wave equations used in this chapter are analogous to those presented in Sec. 2.2.2 and Sec. 2.2.3 for the unloaded SH and Lamb-type cases. For the SH case, the relevant equation of motion (Eqn. 2.4) is expressed in terms of the displacement u_z in the z direction. On the other hand, for the Lamb-type waves, the equations of motion are uncoupled into two separable equations in terms of the two scalar potentials, φ and ψ, corresponding to the longitudinal and shear motions respectively (Eqn. 2.7).

6.2.1 Displacement Field Equations

Solid layer(s)

As in Ch. 2, the common time harmonic factor ($e^{-i\omega t}$) in the general displacement field equations is suppressed throughout. The equations of motion (see Eqns. 2.4 and 2.8 for the SH and Lamb cases respectively) are expressed in terms of Bessel equations which can be solved using Bessel-type functions. For solid layer(s), Bessel functions of the first kind ($\boldsymbol{J}$) and second kind ($\boldsymbol{Y}$) with complex order may be used. The solution for the SH case become:

$$u_z(r,\theta)_{\text{solid}} = [a_{1s}J_{\bar{\nu}}(k_T r) + a_{2s}Y_{\bar{\nu}}(k_T r)]e^{i\bar{\nu}\theta}. \tag{6.2}$$

whereas for the Lamb-type case, the solutions are:

$$\begin{aligned}\varphi(r,\theta)_{\text{solid}} &= [a_{1s}J_{\bar{\nu}}(k_L r) + a_{2s}Y_{\bar{\nu}}(k_L r)]e^{i\bar{\nu}\theta}, \\ \psi(r,\theta)_{\text{solid}} &= [a_{3s}J_{\bar{\nu}}(k_T r) + a_{4s}Y_{\bar{\nu}}(k_T r)]e^{i\bar{\nu}\theta}.\end{aligned} \tag{6.3}$$

where a_{is}, with i={1,2...etc} are the unknown plane wave amplitudes in the solid layer (denoted by the subscript s).

Solid Half Space

A solid half space supports the propagation of both the shear and longitudinal bulk waves. Only the Hankel function of the first kind (H^1), corresponding to the outward propagating plane wave, is suitable to represent solutions in an infinite half space. The solution for the SH case becomes:

$$u_z(r,\theta)_{\text{solid}_{\text{hs}}} = [a_{1s_{hs}}H^1_{\bar{\nu}}(k_T r)]e^{i\bar{\nu}\theta}. \tag{6.4}$$

while the solution for the Lamb-type case is:

$$\begin{aligned}\varphi(r,\theta)_{\text{solid}_{\text{hs}}} &= [a_{1s_{hs}}H^1_{\bar{\nu}}(k_L r)]e^{i\bar{\nu}\theta}, \\ \psi(r,\theta)_{\text{solid}_{\text{hs}}} &= [a_{2s_{hs}}H^1_{\bar{\nu}}(k_T r)]e^{i\bar{\nu}\theta}.\end{aligned} \tag{6.5}$$

where $a_{is_{hs}}$, with i={1,2...etc} are the unknown plane wave amplitudes in the solid half space (denoted by the subscript hs).

Fluid Half Space

A perfect fluid half space cannot support any shear propagation, therefore any shear components in the solid layer would not be able to couple with the fluid layer, hence $u_{z_{fluid}} = 0$ in the SH case, while $\psi = 0$ in the Lamb-type case. As a result, the solutions of the leaky and non-leaky SH cases are both non-attenuative.

The solution for the fluid half space in the Lamb-type case, supporting only the longitudinal wave propagation, is reduced to the following form:

$$\varphi(r,\theta)_{\text{fluid}_{\text{hs}}} = [a_{f_{hs}} H^1_{\bar{\nu}}(k_L r)] e^{i\bar{\nu}\theta}. \tag{6.6}$$

where $a_{f_{hs}}$ is the unknown plane wave amplitude in the fluid half space of the Lamb-type case.

6.2.2 Solution of the Fluid-Loaded Solid Curved layer

As an example, the solution of Lamb-type waves in a solid curved plate coupled with a fluid half space on the outer surface (see Fig. 6.1) is presented in this section; the analytical solution is also in-line with the numerical and experimental validations presented in the next chapter. In all cases, the solution is obtained by applying the appropriate boundary conditions of each interface discussed in Sec. 2.2.4, and using the correct stress or displacement field equations. The stress field equations (Eqn. 2.17) can be obtained from the displacement field equations. According to Tab. 2.2, the five boundary conditions for the case of a fluid-filled solid curved layer are:

$$\begin{aligned}
&\sigma_{rr_{solid}} = 0|_{r=r_1} \\
&\sigma_{r\theta_{solid}} = 0|_{r=r_1} \\
&\sigma_{r\theta_{solid}} = 0|_{r=r_2} \\
&u_{r_{solid}} = u_{r_{fluid}}|_{r=r_2} \\
&\sigma_{rr_{solid}} = \sigma_{rr_{fluid}}|_{r=r_2}
\end{aligned} \tag{6.7}$$

where r_1 and r_2 are the radius at the inner and outer surfaces of the solid layer respectively. The overall solution of the layers can be assembled using the Global Matrix method (see for example Lowe [98]). This forms a homogeneous eigen-problem that relates the square

eigen-matrix [**D**] to the field amplitudes **a** in the form:

$$\begin{bmatrix} D_{11} & \cdots & \cdots & \cdots & D_{15} \\ \vdots & \ddots & & & \vdots \\ \vdots & & \ddots & & \vdots \\ \vdots & & & \ddots & \vdots \\ D_{51} & \cdots & \cdots & \cdots & D_{55} \end{bmatrix} \begin{Bmatrix} a_{1s} \\ a_{2s} \\ a_{3s} \\ a_{4s} \\ a_{f_{hs}} \end{Bmatrix} = \mathbf{0}. \tag{6.8}$$

It is worth noting that the eigen-matrix [**D**] is assembled with the boundary conditions in the order listed in Eqn. 6.7, and the elements of D are expressed explicitly as follows:

$$\begin{aligned}
D_{11} &= k_{L_s}^2[-\lambda J_{\bar{\nu}}(\hat{\omega}_1) + 2\mu_s J''_{\bar{\nu}}(\hat{\omega}_1)] \\
D_{12} &= k_{L_s}^2[-\lambda Y_{\bar{\nu}}(\hat{\omega}_1) + 2\mu_s Y''_{\bar{\nu}}(\hat{\omega}_1)] \\
D_{13} &= \tfrac{2\mu_s i\bar{\nu}}{r_1}[-\tfrac{1}{r_1} J_{\bar{\nu}}(\hat{\omega}_3) + k_{T_s} J'_{\bar{\nu}}(\hat{\omega}_3)] \\
D_{14} &= \tfrac{2\mu_s i\bar{\nu}}{r_1}[-\tfrac{1}{r_1} Y_{\bar{\nu}}(\hat{\omega}_3) + k_{T_s} Y'_{\nu}(\hat{\omega}_3)] \\
D_{15} &= 0 \\
D_{21} &= \tfrac{2\mu_s i\bar{\nu}}{r_1}[-\tfrac{1}{r_1} J_{\bar{\nu}}(\hat{\omega}_1) + k_{L_s} J'_{\bar{\nu}}(\hat{\omega}_1)] \\
D_{22} &= \tfrac{2\mu_s i\bar{\nu}}{r_1}[-\tfrac{1}{r_1} Y_{\bar{\nu}}(\hat{\omega}_1) + k_{L_s} Y'_{\bar{\nu}}(\hat{\omega}_1)] \\
D_{23} &= \mu_s[-k_{T_s}^2 J''_{\bar{\nu}}(\hat{\omega}_3) + \tfrac{k_{T_s}}{r_1} J'_{\bar{\nu}}(\hat{\omega}_3) - \tfrac{\bar{\nu}^2}{r_1^2} J_{\bar{\nu}}(\hat{\omega}_3)] \\
D_{24} &= \mu_s[-k_{T_s}^2 Y''_{\bar{\nu}}(\hat{\omega}_3) + \tfrac{k_{T_s}}{r_1} Y'_{\bar{\nu}}(\hat{\omega}_3) - \tfrac{\bar{\nu}^2}{r_1^2} Y_{\bar{\nu}}(\hat{\omega}_3)] \\
D_{25} &= 0 \\
D_{31} &= \tfrac{-2\mu_s i\bar{\nu}}{r_2}[-\tfrac{1}{r_2} J_{\bar{\nu}}(\hat{\omega}_2) + k_{L_s} J'_{\bar{\nu}}(\hat{\omega}_2)] \\
D_{32} &= \tfrac{-2\mu_s i\bar{\nu}}{r_2}[-\tfrac{1}{r_2} J_{\bar{\nu}}(\hat{\omega}_2) + k_{L_s} J'_{\bar{\nu}}(\hat{\omega}_2)] \\
D_{33} &= -\mu_s[-k_{T_s}^2 J''_{\bar{\nu}}(\hat{\omega}_4) + \tfrac{k_{T_s}}{r_2} J'_{\bar{\nu}}(\hat{\omega}_4) - \tfrac{\bar{\nu}^2}{r_2^2} J_{\bar{\nu}}(\hat{\omega}_4)] \\
D_{34} &= -\mu_s[-k_{T_s}^2 Y''_{\bar{\nu}}(\hat{\omega}_4) + \tfrac{k_{T_s}}{r_2} Y'_{\bar{\nu}}(\hat{\omega}_4) - \tfrac{\bar{\nu}^2}{r_2^2} Y_{\bar{\nu}}(\hat{\omega}_4)] \\
D_{35} &= 0 \\
D_{41} &= -k_{L_s} J'_{\bar{\nu}}(\hat{\omega}_2) \\
D_{42} &= -k_{L_s} Y'_{\bar{\nu}}(\hat{\omega}_2) \\
D_{43} &= \tfrac{-i\bar{\nu}}{r_2} J_{\bar{\nu}}(\hat{\omega}_4) \\
D_{44} &= \tfrac{-i\bar{\nu}}{r_2} Y_{\bar{\nu}}(\hat{\omega}_4) \\
D_{45} &= k_{L_f} H'^1_{\bar{\nu}}(\hat{\omega}_5) \\
D_{51} &= -k_{L_s}^2[-\lambda_s J_{\bar{\nu}}(\hat{\omega}_2) + 2\mu_s J''_{\bar{\nu}}(\hat{\omega}_2)] \\
D_{52} &= -k_{L_s}^2[-\lambda_s Y_{\bar{\nu}}(\hat{\omega}_2) + 2\mu_s Y''_{\bar{\nu}}(\hat{\omega}_2)] \\
D_{53} &= \tfrac{-2\mu_s i\bar{\nu}}{r_2}[-\tfrac{1}{r_2} J_{\bar{\nu}}(\hat{\omega}_4) + k_{T_s} J'_{\bar{\nu}}(\hat{\omega}_4)] \\
D_{54} &= \tfrac{-2\mu_s i\bar{\nu}}{r_2}[-\tfrac{1}{r_2} Y_{\bar{\nu}}(\hat{\omega}_4) + k_{T_s} Y'_{\bar{\nu}}(\hat{\omega}_4)] \\
D_{55} &= k_{L_f}^2[-\lambda_f H'^1_{\bar{\nu}}(\hat{\omega}_5) + 2\mu_f H''^1_{\bar{\nu}}(\hat{\omega}_5)]
\end{aligned} \tag{6.9}$$

where $\hat{\omega}_1 = k_{L_s} r_1$, $\hat{\omega}_2 = k_{L_s} r_2$, $\hat{\omega}_3 = k_{T_s} r_1$, $\hat{\omega}_4 = k_{T_s} r_2$, $\hat{\omega}_5 = k_{L_f} r_2$, and λ and μ are the Lamé constants of the material, while the subscripts s and f indicate the material

properties corresponding to the solid layer and the fluid half space respectively. The prime $'$ indicates the derivative of a function in respect to the radius r.

The solution to Eqn. 2.18 which consists of the complex wavenumber, $\bar{\nu}$, and the real frequency, ω, is obtained using a tracing routine written by the author and an optimisation routine available in the software Matlab^{TM}. The procedure of this 2-D tracing routine is discussed in Sec. 6.3.

The linear (tangential) phase velocity (V_{ph}) and the attenuation ($Atten$) of the wave modes are calculated at the mid-thickness of the plate (r_{mid}), and can be expressed in the following relationships:

$$V_{ph}(m/s) = \frac{\omega \cdot r_{mid}}{\nu_{real}}. \tag{6.10}$$

$$Atten(dB/m) = \frac{\nu_{imag}}{r_{mid}} \cdot 20log_{10}(e). \tag{6.11}$$

6.2.3 Bessel Function of the Complex Order

The numerical solution to Eqn. 6.8 was found to be extremely demanding, this is mainly because of the fact that an accurate calculation of the Bessel functions with a complex order is very complicated. As discussed in Sec. 2.3.2, the Bessel functions of the order γ and argument x are the unique standard solutions to the Bessel's differential equation in the following form:

$$y'' + \frac{1}{x}y' + (1 - \frac{\gamma}{x^2})y = 0. \tag{6.12}$$

Many engineering problems, especially those showing cylindrical symmetry, are described by the Bessel equation. In most circumstances, both the order and the argument of the Bessel function are real, or the order is real and the argument is complex. In this case, the Bessel equation can be easily treated using various methods, such as convergent series and asymptotic expansions ... etc. The details can be found in, for example, Ch. 9 of Abramowitz *et al.* [99].

However, the Bessel function of a complex order and a real/complex argument can arise in a few engineering problems such as acoustic wave propagations (see for example Frisk *et al.* [140]). Before computers were available, the theoretical treatment of the Bessel function of this kind relied heavily on asymptotic solutions that are subject to numerous conditions (details can be found in Langer [144]), and they are not always suitable for numerical calculations. Recently, the solutions of the Bessel function of this kind have been revised so that numerical schemes, such as Chebyshev expansions, recursion relations and numerical integration of the integral representation, can be applied.

The Chebyshev Expansions Technique (CET) [145] involves expressing the Bessel function in terms of the Chebyshev polynomial series. It has been reported [145] that the calculations using the CET can become uneconomical when the order and argument of the Bessel function are large.

On the other hand, the recurrence method has been shown [146] to provide the "most powerful" solution to the Bessel functions of complex order. The method takes advantage of the recurrence relations of the Bessel functions (Eqn. 9.1.27 of Abramowitz *et al.* [99]), from which the solution can be significantly simplified, and thus can easily be implemented and evaluated. Nevertheless, the accuracy of the numerical calculation using this method is highly dependent on the values of the orders and arguments used.

The theoretical background of the integral representation of the Bessel function has been examined briefly by Watson (pp. 46 of [100]). The numerical study of this Numerical Integration Scheme (NIS) has been investigated by one of the collaborators of the present work, Alexander Adamou, and the procedures of the method are summarised below.

In general, Bessel functions of the first kind $J_\gamma(x)$ may be expressed in the form of an integral in the following form (Eqn. 9.1.20 of [99]):

$$J_\gamma(x) = \frac{2(\frac{1}{2}x)^\gamma}{\pi^{\frac{1}{2}}\Gamma(\gamma+\frac{1}{2})}\int_0^1 (1-t^2)^{\gamma-\frac{1}{2}}\cos(xt)dt. \tag{6.13}$$

where Γ is the Gamma function. The formula is valid for $\Re(\gamma) > -\frac{1}{2}$, and can be numerically integrated. For $\Re(\gamma) < -\frac{1}{2}$, recurrence relations are used to express the Bessel function in terms of other Bessel functions with $\Re(\gamma) > -\frac{1}{2}$, which are then integrated as before.

The Bessel function of the second kind $Y_\gamma(x)$ can be evaluated using the following expression (Eqn. 9.1.2 of [99]):

$$Y_\gamma(x) = \frac{J_\gamma(x)\cos(\gamma\pi) - J_{-\gamma}(x)}{\sin(\gamma\pi)}. \tag{6.14}$$

The NIS was implemented in a Matlab^{TM} program where the accuracy of the solution can be specified. It is worth noting that the numerical integration breaks down for large x (at around $x > 100$) due to the rapid oscillations of the integrand.

In 1986, Thompson *et al.* [147] examined the Bessel functions of complex order using combination of both the CET and the recurrence relations to achieve a good accuracy in any range of the order and argument of the Bessel function. Based on his findings, Thompson outlined suitable choices of algorithms using a combinations of the above methods according to the $\gamma - x$ region, in order to achieve the best accuracy. This has subsequently been

implemented into a commercial program Maple^{TM} as a "ready-to-use" function (see for example http://www.maple.com); this Maple function can be linked to Matlab^{TM} from which the phase velocity and attenuation dispersion curves are calculated.

The accuracy of Thompson's method may be checked by comparing the numerical results with those calculated using the NIS with a tolerance value higher than the number of significant figures displayed by Matlab^{TM}. The numerical comparisons were performed using values of γ and x that fall into the three different regions: $\Re(\gamma) < x$, $\Re(\gamma) \approx x$ and $\Re(\gamma) > x$. The results are shown in Tab. 6.1, where the NIS has a theoretical tolerance in accuracy of at least 10×10^{-15}, therefore the differences of the solutions between these two methods correspond to the accuracy of CET (shown in Tab. 6.2). It can be seen that the results produced by Thompson's method for both the real and imaginary parts are extremely accurate in all regions. The solution is slightly less accurate in the region of $\gamma > x$, but nevertheless it has an accuracy of $1 \times 10^{-7}\%$. Therefore the method should in theory provide sufficient accuracy when evaluating the dispersion curves using the characteristic functions Eqn. 6.8 for the study of the curvature effect.

6.3 Two-dimensional Optimisation Routine

In an attenuative case, where the attenuation is due to leakage into a surrounding material, the roots of the system (Eqn. 6.8) are complex ($\bar{\nu}$, ω where $\bar{\nu} = \nu_{real} + \nu_{imag}i$), as discussed earlier, and can be treated as a system of three independent parameters. The tracing routine is, in general, very similar to that of the 1D problem detailed in Fig. 3.6 of Sec. 3.2.

The only difference compared to the non-attenuative case is that the roots of the characteristic function for the leaky case are searched in a plane of two independent parameters, while the remaining one is fixed. The plane in which a root is searched can be in any combination of the three parameters. In the author's implementation of the optimisation routine, a root is searched in the plane of imaginary part of wavenumber and frequency ($\nu_{imag} - \omega$), while the real part of the wavenumber ν_{real} is fixed.

As in the non-attenuative case, the first step of the routine is to locate two "initial roots" corresponding to the same mode at two real angular wavenumbers, $\mathrm{Re}(\nu_1)$ and $\mathrm{Re}(\nu_2)$ that have very close values. These roots provide the starting points of the line tracing routine in both the increasing and decreasing frequency directions. This searching of the "initial roots" may be repeated to search for a desired number of higher order modes.

To find a root of two parameters, the calculation may be treated as a minimisation problem

	Numerical Integration Scheme		Method of Thompson *et al.* [147]	
Parameters	$\mathbf{J}_\gamma(\mathbf{x})$	$\mathbf{Y}_\gamma(\mathbf{x})$	$\mathbf{J}_\gamma(\mathbf{x})$	$\mathbf{Y}_\gamma(\mathbf{x})$
$\gamma < x$	$-5.93644837574622 \times 10^{23} -$	$-6.21989546226278 \times 10^{23} +$	$-5.93644837574708 \times 10^{23} -$	$-6.21989546226677 \times 10^{23} +$
$\gamma = 30 + 50i, x = 70$	$6.21989546226278 \times 10^{23} i$	$5.93644837574622 \times 10^{23} i$	$6.21989546226677 \times 10^{23} i$	$5.93644837574708 \times 10^{23} i$
$\gamma \approx x$	$9.38713109974277 \times 10^{15} -$	$-2.04157148369613 \times 10^{15} -$	$9.387131099743 \times 10^{15} -$	$-2.04157148369597 \times 10^{15} -$
$\gamma = 30 + 50i, x = 31$	$2.04157148369613 \times 10^{15} i$	$9.38713109974277 \times 10^{15} i$	$2.04157148369597 \times 10^{15} i$	$9.38713109974300 \times 10^{15} i$
$\gamma = x$	$-1.95359736621662 \times 10^{15} -$	$-3.54953866450241 \times 10^{15} +$	$-1.95359736621661 \times 10^{15} -$	$-3.5495386645025 \times 10^{15} +$
$\gamma = 30 + 50i, x = 30$	$3.54953866450241 \times 10^{15} i$	$1.95359736621662 \times 10^{15} i$	$3.54953866450250 \times 10^{15} i$	$1.95359736621661 \times 10^{15} i$
$\gamma > x$	$-102.750648203869 +$	$21.6604641041049 +$	$-102.750648203871 +$	$21.6604626085221 +$
$\gamma = 30 + 50i, x = 10$	$21.6604279770704 i$	$102.750611005692 i$	$21.6604279770699 i$	$102.750609923256 i$

Table 6.1: Numerical calculations of the Bessel function of the first $J_\gamma(x)$ and second $Y_\gamma(x)$ kinds using both Numerical Integration Scheme (NIS), and a combination of Chebyshev Expansions Technique (CET) and recurrence method (detailed in Thompson *et al.* [147]at various regions depending on the relation between the order γ and the argument x of the Bessel function.

	Percentage Difference			
	$\mathbf{J}_\gamma(\mathbf{x})$		$\mathbf{Y}_\gamma(\mathbf{x})$	
Parameters	**Real Part**	**Imaginary Part**	**Real Part**	**Imaginary Part**
$\gamma < x$	1.45×10^{-11}	6.41×10^{-11}	6.44×10^{-11}	2.89×10^{-10}
$\gamma \approx x$	2.45×10^{-12}	7.84×10^{-12}	1.67×10^{-11}	2.45×10^{-12}
$\gamma = x$	5.12×10^{-13}	2.54×10^{-12}	2.54×10^{-12}	5.12×10^{-13}
$\gamma > x$	1.95×10^{-12}	2.31×10^{-12}	6.90×10^{-7}	1.05×10^{-7}

Table 6.2: Percentage different between solutions calculated using the Numerical Integration Scheme (NIS), and a combination of Chebyshev Expansions Technique (CET) and recurrence method at various regions based on values calculated in Tab. 6.1.

when the characteristic function of Eqn. 6.8 is expressed in the following way:

$$\text{Modified Characteristic Function (MCF)} = \log\left(\frac{\text{abs}[\Re(\det(D)) + \Im(\det(D))]}{10 \times 10^{100}}\right). \tag{6.15}$$

$\Re$ and $\Im$ indicate the real and imaginary quantities of the determinant of the characteristic function, D. Since the absolute quantity of D is usually very large, for clarity the amplitudes of D can be normalised with a very large number, such as 10×10^{100}, and expressed on a Log scale.

Fig. 6.2 illustrates the root finding routine of two independent parameters. The contour lines indicate the amplitude of the MCF. Having chosen the real part of the angular wavenumber ν_{real}, the amplitude of the MCF forms a sink at the corresponding root in the ν_{imag}-ω plane, showing a minimum of the function which corresponds to a root of the leaky system (Label A in Fig. 6.2).

The approximate location of a sink may be located by sweeping along the ν_{imag} and ω plane in turn to locate the general direction of the local minimum with respect to each parameter. This would subsequently allow the minima to be homed-in using a numerical algorithm of a two-dimensional steepest descent (see for example Press *et al.* [103]); the algorithm, as shown in Fig. 6.2, iterates to find the nearest local minimum of the MCF in the direction of the steepest descent gradient at a given starting point in the ν_{imag}-ω plane. The process is iterated as many times as required until a specified accuracy is achieved; a typical accuracy is set to 1×10^{-6} for the values of both ν_{imag} and ω.

Using the "initial roots", the second step of the routine traces the dispersion curves of the modes in the user specified frequency range, at every real angular wavenumber intervals $\text{Re}(\delta\nu)$. To trace a dispersion curve, an "initial guess point" is first identified by extrapolation in a step of $\text{Re}(\delta\nu)$ using previously found roots that can either be the "initial roots" or roots that are subsequently found. A linear extrapolation is used for the first 5 points on a curve, thereafter a quadratic extrapolation can be used to improve the efficiency of the scheme; this is similar to a technique used in Disperse [148].

In Fig. 6.2, the linear extrapolation of the tracing routine is demonstrated. It can be seen that an "initial guess point" at $\text{Real}(\nu + 2\delta\nu)$ is obtained by extrapolating using the two known roots at $\text{Real}(\nu)$ and $\text{Real}(\nu + \delta\nu)$, and the root is located using the steepest descent gradient iteration scheme. The extrapolation technique applies to both increasing and decreasing real wavenumber directions.

This tracing routine typically takes a lot longer than the 1D-tracing routine of the non-leaky case (Sec. 3.2). This can be attributed to the complexity of finding roots in the

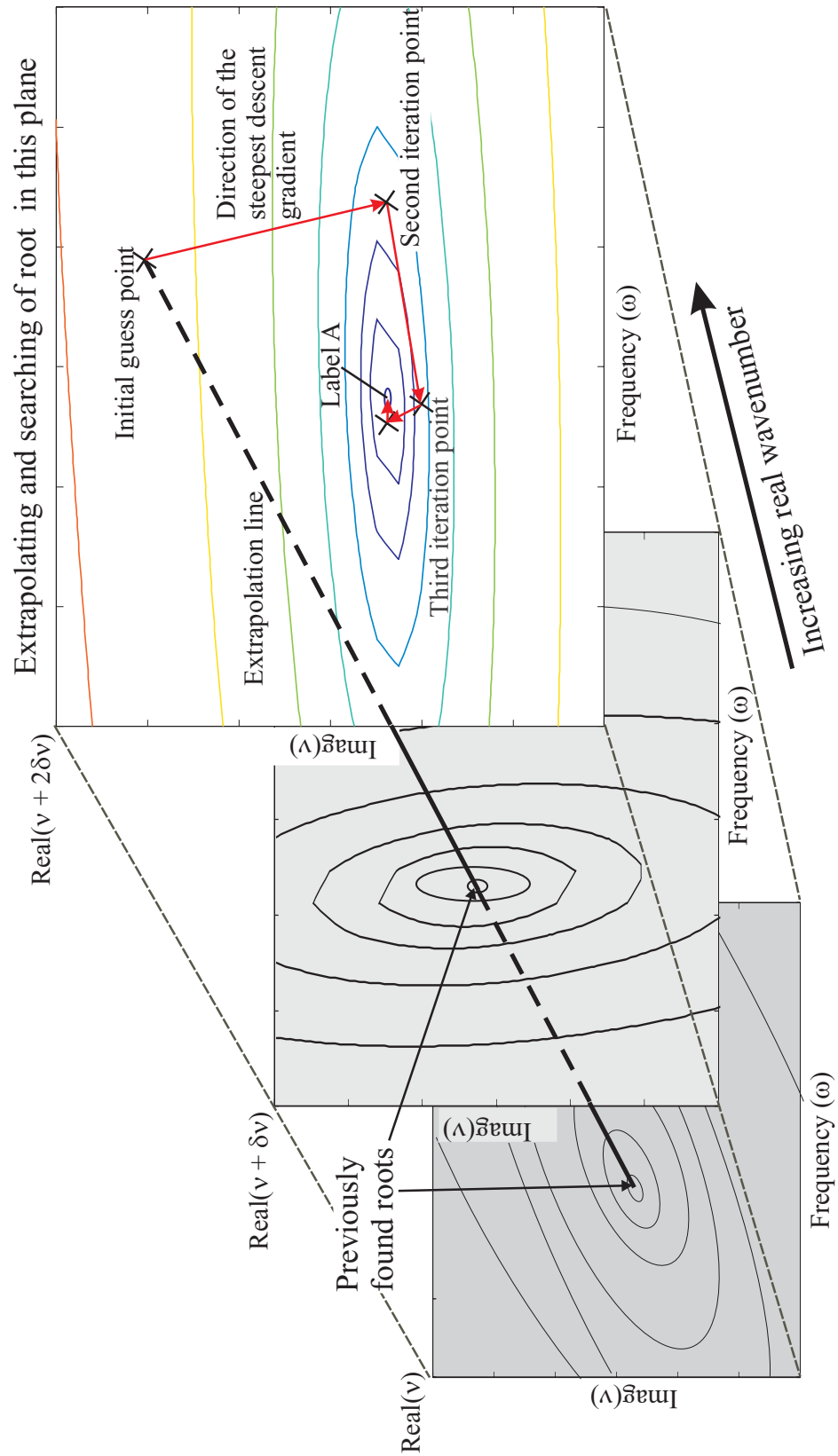

Figure 6.2: An illustration of a two dimensional root finding routine for a function of two independent parameters (ν_{imag} and ω) using a steepest descent scheme. The contour lines show the absolute amplitude of the characteristic function (Eqn. 6.8). The initial guess point can either be extrapolated linearly or quadratically from the previous roots. The illustration shown here is a linear extrapolation in the real angular wavenumber with a step of Real($\delta\nu$).

plane of two independent parameters, additional time is required during the first step of the routine to search for the "initial roots". For the 1-D problem of a non-attenuative case, the finding of the "initial roots" requires sweeping along one parameter within a particular range over n number of steps, whereas for the leaky problem, the searching of the "initial roots" requires sweeping along both parameters. If the same number of steps n is used in sweeping both parameters, the time needed to find the "initial roots" in an attenuative problem would be the square of that needed for the non-attenuative case.

The size of the step in each parameter for the initial sweeping is decided based on the size of the sink. The function MCF generates sinks that are localised, covering a small area in the Imag(ν)-ω plane. As demonstrated in Fig. 6.3, the direction of the steepest descent gradient does not always point towards the nearest root as one sweeps in the frequency along a particular Imag(ν). It can be seen that the direction of the steepest descent gradient points towards the sink along Im($\nu_1 + \delta\nu$), while it points away from the sink along Im(ν_1). Therefore the step size of imaginary wavenumber Im($\delta\nu$) must be small enough so that when sweeping along Im(ν_1) and Im($\nu_1 + \delta\nu$), the steepest decents are not both pointing away from the sink, which might result in the root not being identified. Similarly, the same criterion applies when choosing the step size for the frequency sweeping.

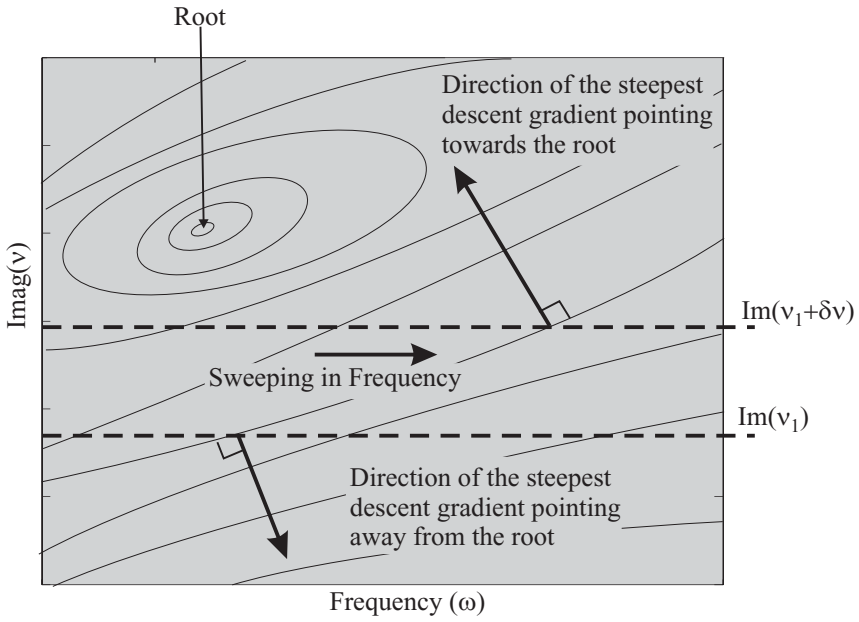

Figure 6.3: An illustration of the sweeping of the initial complex roots along a real wavenumber, Re(ν_1), in frequency $\delta\omega$ and in imaginary wavenumber, Im($\delta\nu$), steps.

6.4 Numerical Examples of a Fluid Loaded Case

As an example, numerical solutions of the dispersion curves for circumferential leaky Lamb-type waves in the system, illustrated in Fig. 6.1, were calculated using the solution detailed in Sec. 6.2.2, and with the tracing routine described in Sec. 6.3.

	Steel layer	**Water half space**
Longitudinal Vel. C_L, (m/s)	5959.6	1410.0
Shear Vel. C_T, (m/s)	3260.0	—
Density ρ, (kg/m^3)	7932	1000

Table 6.3: acoustical properties and density of the materials used in the numerical example of this chapter.

Figs. 6.4(a) and 6.4(b) show the phase velocity and attenuation dispersion curves of the Lamb type waves in a steel curved plate (thickness: 3mm, and inner radius: 40mm) coupled with a water half space on the outer surface. The acoustical properties and the density of these materials used in the numerical example are listed in Tab. 6.3. It can be seen that the phase velocity dispersion curves (Fig. 6.4(a)) are very similar to those of the non-leaky cases (see for example Fig. 4.1). This is because the solid layer remains as the dominant guiding layer in which the waves propagate at a similar speed to the non-leaky case, while some of their energy leaks into the water. The same phenomenon can also be found in the straight case when a water half space coupled to a solid layer would not change the physical properties of the wave modes significantly in the layer. The attenuation due to the energy leakage into the water for each individual mode is represented by the attenuation dispersion curves as a function of frequency, shown in Fig. 6.4(b). A comparison of the attenuation between straight and curved plates that are coupled with a water half space is given later in Sec. 6.5.

Figs. 6.5 and 6.6 show the mode shapes of the leaky and non-leaky cases for both the A_0 and S_0 modes respectively for a curved plate (thickness: 3mm, inner radius: 40mm). In both cases, despite the fact that they are calculated using different analytical solutions, the mode shapes of these two modes in the solid layer appear to be almost the same. This is because the water in the leaky case has a much lower impedance than the plate, thus has little effect on the mode shapes. Nevertheless, if the impedance between the plate and the water were similar, it would have a big effect on the mode shapes.

Furthermore as mentioned in Sec. 4.2, the change in mode shapes can be linked directly to the propagation properties such as the phase velocity. As a result, provided that the geometry of the main guiding medium (i.e. the solid plate) is kept the same, a matching in phase velocity of the wave modes between the leaky and non-leaky cases can be expected.

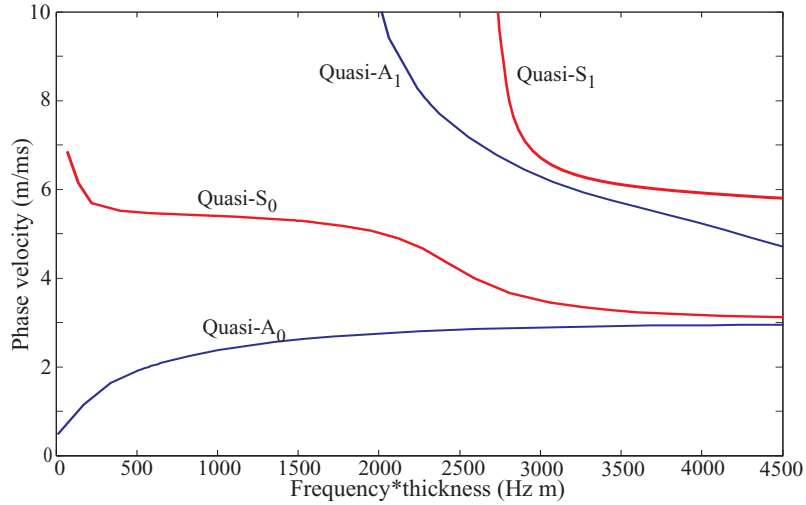

(a) Phase velocity

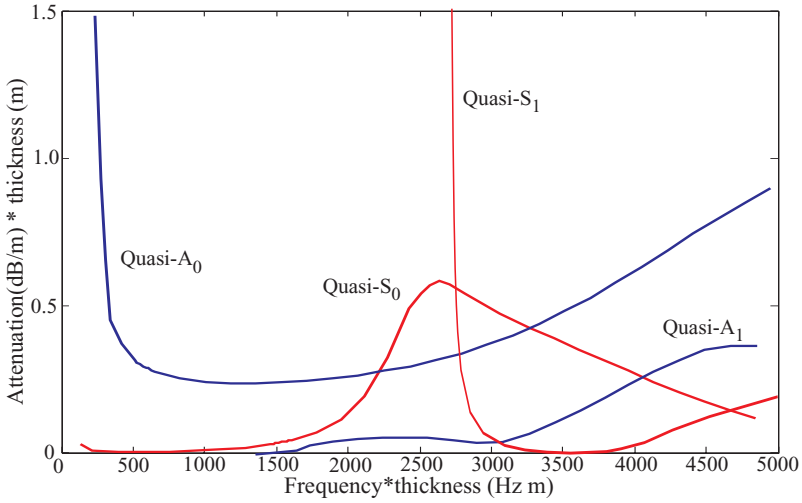

(b) Attenuation

Figure 6.4: Dispersion curves of the Lamb-type modes in a leaky curved plate systems of a 3mm thick, 40mm inner radius steel plate coupled with a water half space on the outside of plate.

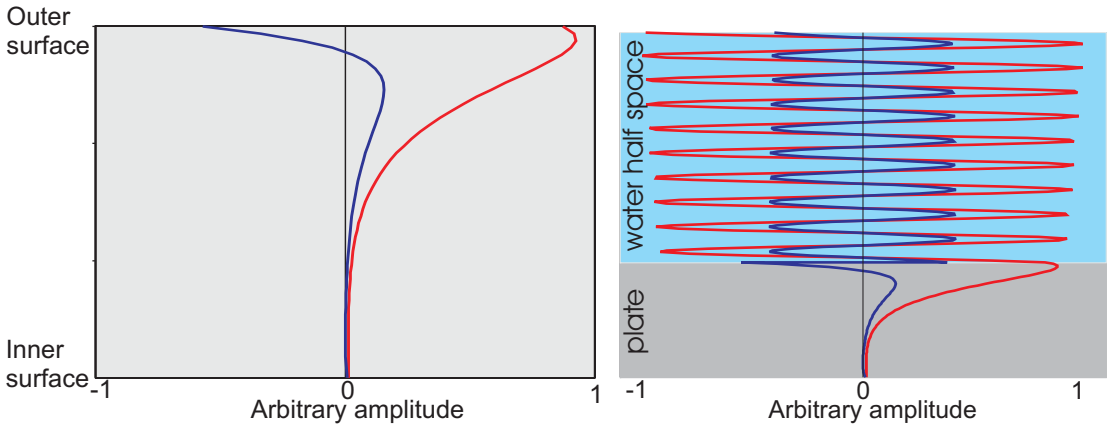

(a) Quasi-A_0 mode in non-leaky case (b) Quasi-A_0 mode in leaky case

Figure 6.5: Radial (Red) and circumferential (Blue) displacement field for the quasi-A_0 mode in a steel curved plate (thickness: 3mm, inner radius: 40mm) at 2.5MHz. Leaky case is for water on the outside of the plate.

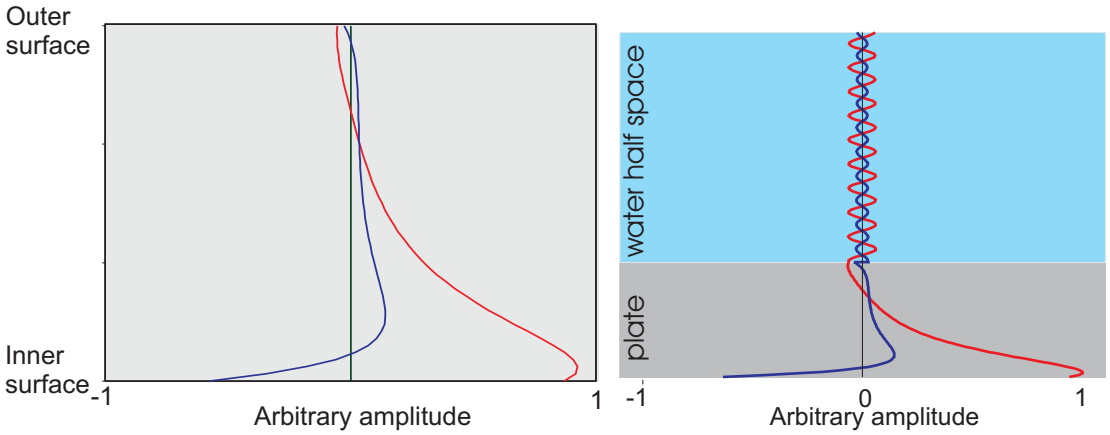

(a) Quasi-S_0 mode in non-leaky case (b) Quasi-S_0 mode in leaky case

Figure 6.6: Radial (Red) and circumferential (Blue) displacement field for the quasi-S_0 mode in a steel curved plate (thickness: 3mm, inner radius: 40mm) at 2.5MHz. Leaky case is for water on the outside of the plate.

In addition to the typical Lamb-type modes, the fluid-borne Franz modes [149] (also known as creeping waves) can also be calculated using the formulation derived in Sec. 6.2.2. Figs. 6.7(a) and 6.7(b) show the dispersion curves of the Franz modes in the same frequency range as those shown in Figs. 6.4(a) and 6.4(b). There is an infinite number of these modes at each frequency, all of whose phase velocity converge to the bulk speed of water as $\omega \rightarrow \infty$.

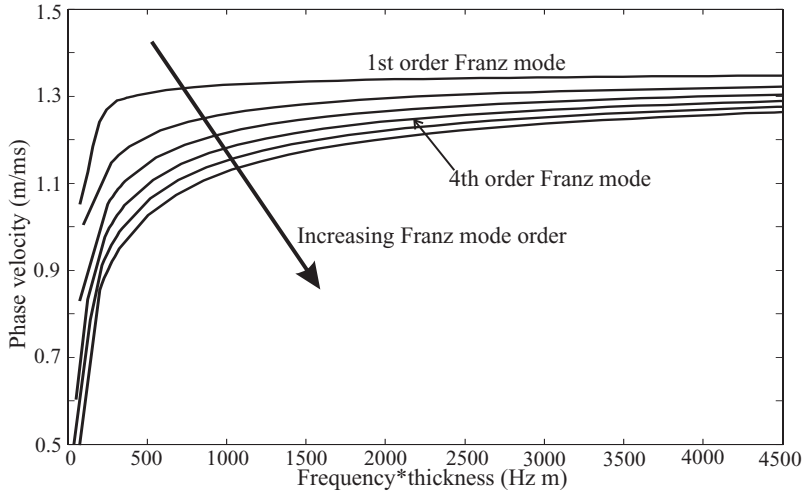

(a) Phase velocity

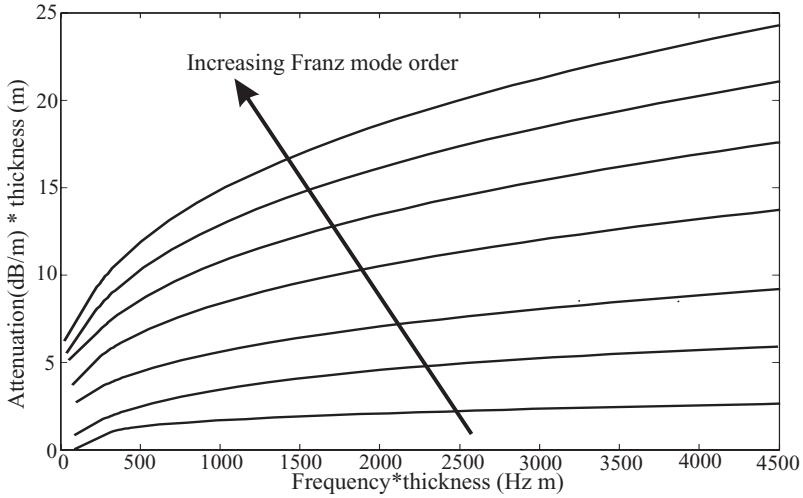

(b) Attenuation

Figure 6.7: Dispersion curves of the fluid-borne Franz modes in a leaky curved plate system of a 3mm thick, 40mm inner radius steel plate coupled with a water half space on the outside of plate.

Unlike the Sholte mode in the leaky straight plate system [150], the Franz modes propagate circumferentially in the fluid at a certain distance away from the solid layer surface, and have a large displacement component in the radial direction which leads to a large attenuation. Compared to the leaky Lamb-type curved plate modes, the Franz modes typically have a much higher attenuation. Fig. 6.8 shows the displacement mode shapes of the 1^{st} and 4^{th} order Franz modes. For a given Franz mode, the amplitude of the mode shapes

increases with distance from the plate surface; this increase in amplitude is associated to the curvature of the system, therefore a system with a large curvature would increase the rate at which the displacement amplitude radiating out from the surface. Additionally, it can be seen from Figs. 6.7 and 6.8 that the attenuation of the Franz mode increases with distance away from the solid surface where it propagates.

In practise these modes can be very difficult to detect as they are damped out completely in a very short distance compared to the typical Lamb-type curved plate modes, thus they do not normally interfere during experimental measurements.

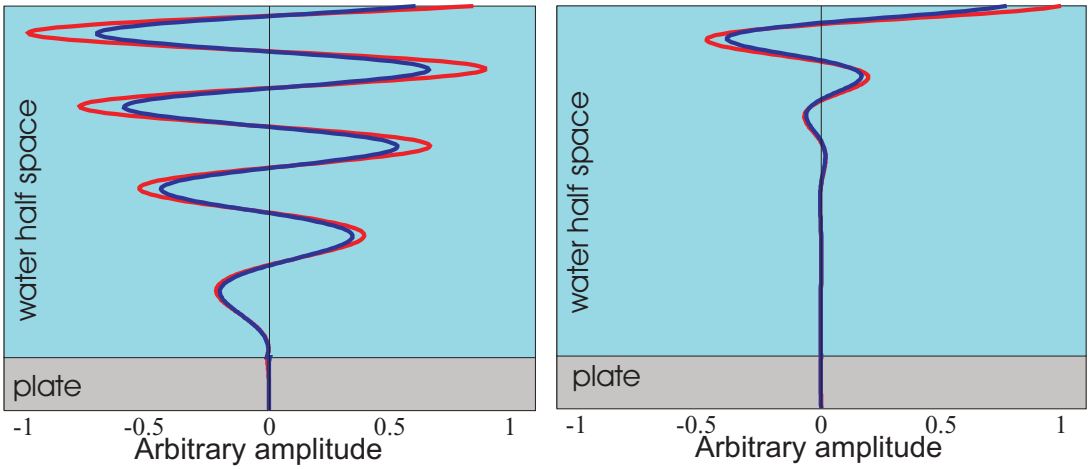

(a) 1^{st} order Franz mode (b) 4^{th} order Franz mode

Figure 6.8: Radial (Red) and circumferential (Blue) displacement field for Franz modes in a steel curved plate (thickness: 3mm, inner radius: 40mm) coupled with a water half space on the outer surface at 500kHz.

6.5 Curvature Effect on Propagation Properties in Loaded Plates

In this section, the curvature effect on the phase velocity and the attenuation of the wave modes in a loaded curved plate is investigated in a similar fashion to those investigated in Ch. 4 for the unloaded case. First, the phase velocity and attenuation dispersion curves may be compared visually between a straight (thickness: 3mm) and a curved steel plate (thickness: 3mm, inner radius: 40mm), both of which are coupled with a water half space on the outer surface, shown in Fig. 6.9. Only the first two fundamental Lamb-type wave modes are compared in Fig. 6.9, however, in the frequency range of this figure, there are other higher order plate modes as seen in Fig. 6.4(a), but for clarity these are not shown. The prefix "Quasi" is used in the figure to distinguish the wave modes belonging to the curved leaky plate system from those of the straight leaky system.

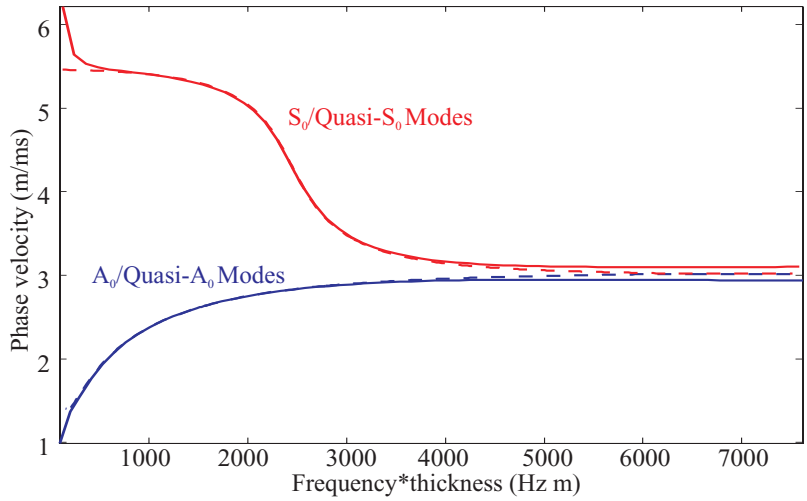

(a) Phase velocity

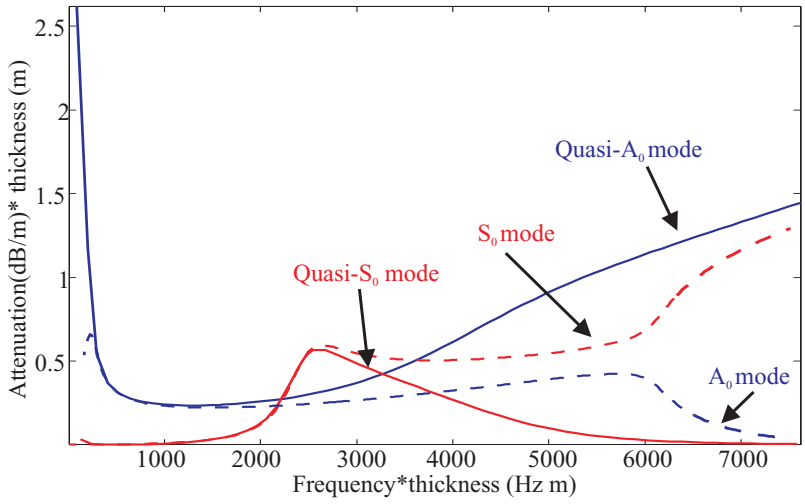

(b) Attenuation

Figure 6.9: Dispersion curves of the lowest two order Lamb-type modes in the straight (Dashed lines) and curved (Solid lines) leaky plate systems (3mm thick steel plate coupled with a water half space on the outer side of plate). The inner radius of the curved plate is 40mm.

Phase Velocity

As in the case of the non-leaky curved plate, the "quasi-A_0" and "quasi-S_0" modes do not converge to a single Rayleigh wave speed, but to two distinctively different speeds corresponding to the surface waves on the outer and inner surfaces respectively as $\omega \to \infty$. The displacement field of these two wave modes at low frequencies are similar, and hence their attenuation values are similar too. However, at higher frequencies, for example at 2.5MHz (shown in Figs. 6.5(b) and 6.6(b)) the displacement amplitude is confined to the area close to either the inner or the outer surface. As a result, the "quasi-A_0" mode can be strongly coupled with the water half space, and it can be seen in Fig. 6.9(b) that the attenuation becomes much larger than that of the A_0 mode towards higher frequencies due

to the increased leakage. On the contrary, as the energy distribution in the plate moves towards the inner surface, away from the water-solid interface, the "quasi-S_0" mode has a much smaller attenuation at higher frequencies compared to the straight plate S_0 mode.

Fig. 6.10 shows the normalised difference in phase velocity of the A_0 and S_0 modes between the straight and curved plates, using Eqn. 4.1, for a range of frequencies and inner radii of the curved plate. These figures have a striking resemblance to those analysed for the unloaded plate case (see Fig. 4.2) in terms of the pattern and the amplitude. The difference in phase velocity is typically less than a few percent even for a curved plate having a very small inner radius. This clearly suggests that the curvature has little effect on the phase velocity in both the leaky and the non-leaky systems.

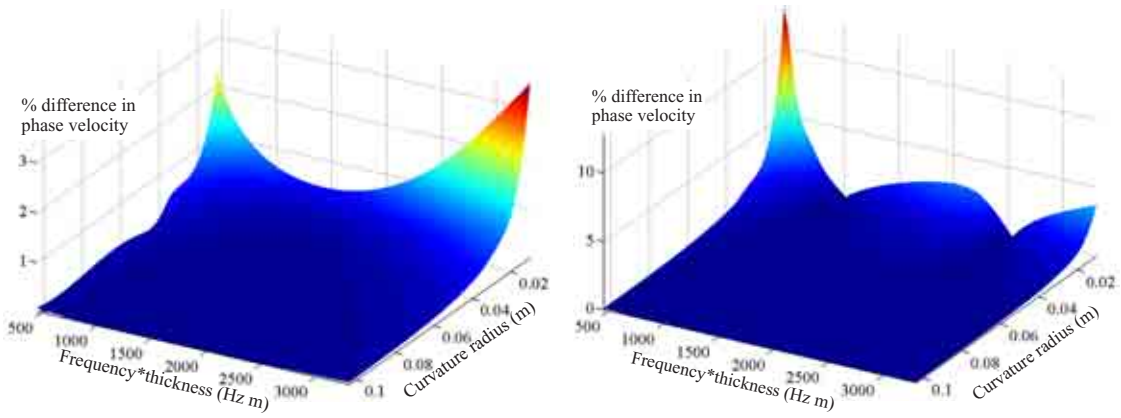

(a) A_0 mode (b) S_0 mode

Figure 6.10: Percentage difference in phase velocity between straight and curved steel plates (thickness: 3mm) as a function of frequency and inner radius of the curved plate. The plates are coupled on one side with water.

Attenuation

Similar 3-D plots (Fig. 6.11) have been produced for the comparison of the attenuation of the A_0 and S_0 modes over the same frequency and curvature radius range as those for the phase velocity comparison. It can be seen that the curvature effect on the attenuation varies over the range of frequencies in both cases, but most importantly, the curvature effect on the attenuation is substantially greater than that on the phase velocity.

Additionally, it is worth noting that the "quasi-A_0" mode has a greater attenuation which increases with increasing curvature, and this phenomenon is completely opposite for the "quasi-S_0" mode due to the reasons discussed earlier. Note that the percentage difference in attenuation of the S_0 shown in Fig. 6.11(b) is negative; a greater attenuation is shown as a positive percentage difference and vice versa. As Beard [2] reported, curvature can become problematic for inspection, especially in a leaky system. Typically the changes in

attenuation due to the curvature effect can increase and decrease by over 100% for the A_0 and S_0 modes respectively when the curvature radius is small.

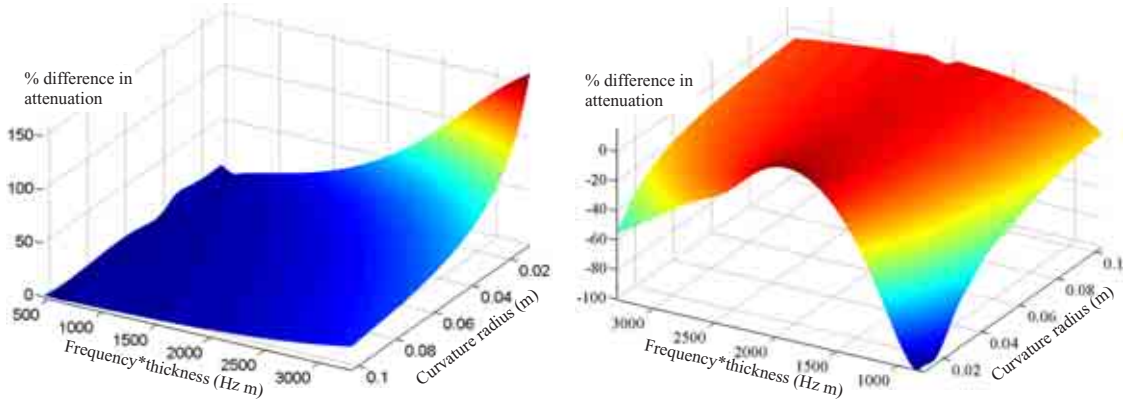

(a) A_0 mode (b) S_0 mode

Figure 6.11: Percentage difference in attenuation between straight and curved steel plates (thickness: 3mm) as a function of frequency and inner radius of the curved plate. The plates are coupled with a water half space on the outer surface of the plate.

Since the amount of leakage from the plate is related to the energy available to couple with the water half space at the surface of the plate, it would help to improve the understanding of the curvature effect on the attenuation by plotting the total energy density distribution across the plate thickness for a range of inner radii. The total energy density is a combination of the kinetic energy density (KED) and the strain energy density (SED). For the Lamb-type circumferentially propagating waves, the displacement field (Sec. 6.2.1) does not depend on the z direction, while $u_z = 0$. Therefore the formulae of the KED and SED (see for example Auld [5]), in terms of the relevant displacement and stress field vectors, can be reduced to the following forms:

$$\text{KED} = \frac{\rho}{4}\left\{\left(\frac{\partial u_r}{\partial t}\right)^2 + \left(\frac{\partial u_\theta}{\partial t}\right)^2\right\}. \tag{6.16}$$

$$\text{SED} = \frac{1}{4}\left\{\sigma_{rr}\frac{\partial u_r}{\partial r} + \sigma_{\theta\theta}\left(\frac{\partial u_\theta}{r\partial\theta} + \frac{u_r}{r}\right)\right\} + \frac{\sigma_{r\theta}}{8}\left\{r\frac{\partial}{\partial r}\left(\frac{u_\theta}{r}\right) + \frac{1}{r}\frac{\partial u_r}{\partial\theta}\right\}. \tag{6.17}$$

where u_r, u_θ, σ_{rr} and $\sigma_{r\theta}$ can be expressed in terms of the displacement scalar potentials φ and ψ using Eqns. 2.7 and 2.17 respectively, while the reduced version of $\sigma_{\theta\theta}$ can be expressed as follows:

$$\sigma_{\theta\theta} = \lambda\left[\frac{\partial^2\varphi}{\partial r^2} + \frac{1}{r^2}\frac{\partial^2\varphi}{\partial\theta^2} + \frac{1}{r}\frac{\partial\varphi}{\partial r}\right] + 2\mu\left[\frac{1}{r^2}\frac{\partial^2\varphi}{\partial\theta^2} - \frac{1}{r}\frac{\partial^2\psi}{\partial\theta\partial r} + \frac{1}{r}\frac{\partial\varphi}{\partial r} + \frac{1}{r^2}\frac{\partial\psi}{\partial\theta}\right]. \tag{6.18}$$

The through-thickness total energy density for the "quasi-A_0" and "quasi-S_0" modes at 500kHz is shown in Fig. 6.12, where the amplitude of the total energy density for a particular curvature radius has been normalised with the local maximum value. As expected,

the energy distribution is shifted towards the outer and inner surfaces for the quasi-A_0 and quasi-S_0 modes respectively as the curvature increases. This changes the amount of energy coupled with the water half space and consequently affects the attenuation value in the same way as occurs with increasing frequency.

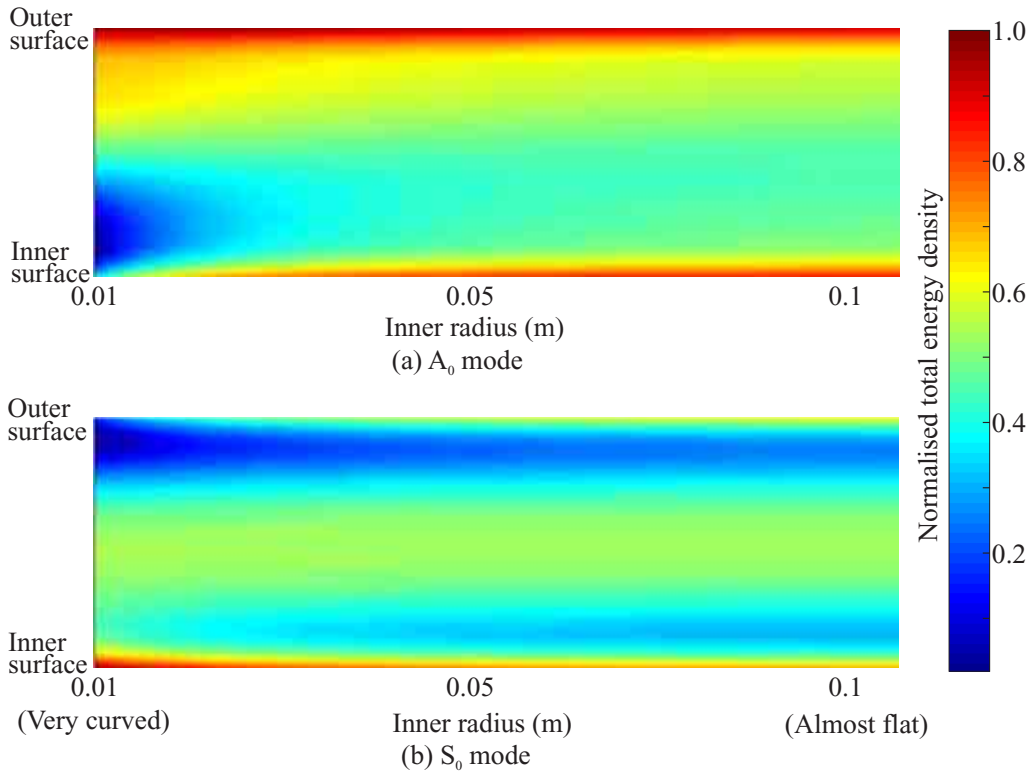

Figure 6.12: Through-thickness normalised total energy density calculated at 500kHz for the quasi-A_0 and quasi-S_0 modes in 3mm steel curved plates coupled with a water half space, over a range of inner radii.

6.6 Summary

In this chapter, leaky systems using solution that either have the angular wavenumber being real and the frequency being complex, or the angular wavenumber being complex and the frequency being real, have been thoroughly examined. In addition, a detailed literature review on these two kind of solutions has been performed.

For leaky guided circumferential wave propagation, the attenuation due to leakage can only be correctly described using the combination of complex wavenumber and real frequency roots. The general analytical solution for the circumferential guided waves of a loaded curved plate based on this combination of roots have been derived, and the formulation of a fluid-loaded case has been explicitly shown.

The Bessel function of complex order is the most important component in the solutions of leaky circumferential guided wave problems. However, few numerical schemes are available for the evaluation of these complex functions. The most promising numerical schemes include the robust Chebyshev Expansion Technique (CET), and the accurate Numerical Integration Scheme (NIS); both of these schemes have been evaluated in this chapter.

The finding of roots from the dispersion relation in a leaky case with two independent parameters can be carried out using a steepest descent scheme in a two-dimensional optimisation routine. This forms part of the global tracing routine, which has been summarised.

As an example, the phase velocity and attenuation dispersion curves, and the mode shapes, have been presented for a fluid loaded case, all of which were calculated using the numerical tracing routine. In general, there are two families of wave modes in the coupled plate case: the plate guided wave modes and the fluid-borne Franz modes.

The curvature of the plate was found to have much more effect on the attenuation than the phase velocity of the wave modes in the leaky case. The amount which the attenuation changes can be related to the amount of shift in energy distribution through the thickness due to the increasing in curvature. The shift of the energy distribution towards one surface or the other is wave mode dependent. In general, a higher attenuation is obtained if the energy shifts towards the half space-plate interface, and vice versa.

Chapter 7

Validation of Curvature Effect in Loaded Plates

The analytical solutions of a leaky system have been examined thoroughly in the previous chapter; the system consists of guided waves propagating circumferentially in curved plates that are coupled with either a solid or a fluid half space on the outer surface. The solutions were subsequently used to study the curvature effect in such systems. Before one uses the results, the validity of this solution must be established.

In this chapter, the analytical prediction of the curvature effect of the leaky curved plate case is validated using both the numerical FE method and experimental measurements. The model case for the validation in this chapter is a 3mm thick steel curved plate coupled with an infinite fluid half space on the outer surface (illustrated in Fig. 6.1). These geometrical dimensions are also the same as those investigated in Sec. 6.5 of the previous chapter.

In the first part of this chapter, a FE model analysed in the time domain using elastic and acoustic plane strain elements to represent the solid plate layer and the fluid half space respectively, is presented. Using this method, the attenuation can be evaluated from FE simulation results obtained over a range of curvature radii; the results are subsequently compared to that of the straight case to evaluate the curvature effect.

In the second part of this chapter, an experimental technique to measure the amount of attenuation due to the leakage into the surrounding medium is presented. Although the experimental technique, used in Ch. 5, can sensitively measure the difference in phase velocity due to the curvature effect, it would not be appropriate for the validation of the leaky case. This is because the experimental technique cannot be easily set up to allow only the outer surface of the metal plate to couple with a fluid half space. Nevertheless, since we expect the curvature effect on the attenuation to be significant, we do not need

such a sensitive setup as we did when studying the free case, as predicted in the previous chapter.

Instead, sufficiently accurate experimental measurements can be taken from a set of transducers attached permanently on the surface of a series of pipes of the same thickness and various curvature radii. The attenuation can then be measured by comparing the wave signals when the pipes are surrounded by water and when they are in air.

7.1 Finite Element (FE) Modelling of the Leaky Case

The general concept of numerical modelling using finite elements was discussed in Sec. 5.1.1. In this section, a FE technique to measure the difference in both the phase velocity and attenuation between the curved and straight cases is presented.

For a leaky system of a curved plate coupled with an infinite fluid half space (see Fig. 6.1), the dispersion curves cannot be extracted from the FE modelling technique in the same way as for the layered case with a finite thickness studied in Sec. 5.1. This is because for a non-leaky case, the FE calculation is based on a modal analysis where the natural frequencies corresponding to the ascribed geometry and boundary conditions are extracted; whereas for a leaky system, the geometry of an infinite half space is very difficult to model using a modal extraction scheme in finite element modelling.

Since the fluid half space has a very different impedance to the main guiding medium of the steel plate, and the wave modes of fluid and solid media can be considered as very weakly coupled, a close approximation in phase velocity may be obtained when the infinite half space is replaced with a thick finite layer. Although this idea of modelling the leaky system may correctly approximate the phase velocity of the wave modes in the plate layer by using the appropriate boundary conditions at the solid-fluid boundary, the model still would not be representative of the leaky system, as the leaky energy can re-enter the guiding medium after reflecting from the top of the fluid layer.

Alternatively, the wave mode propagation may be simulated in the time-domain, where a wave mode is excited at one end of the plate model and is subsequently measured at several locations along the plate before reflections from the top of the fluid layer appear. The results of this time response signal can then be used to calculate the attenuation of one particular wave mode.

7.1.1 FE model of the Leaky Case

Lamb-type wave mode propagation in both the straight and the curved plate cases involves polarisation only in the out-of-plane (u_y, u_r) and in-plane (u_x, u_θ) directions, as shown in Figs. 4.5 and 7.1. Therefore the simulation can be performed using 2-D elastic and acoustic plane strain elements to model a section through an infinitely wide steel plate and a fluid half space respectively. The plane strain elements are utilised in the plane of $x - y$ or $r - \theta$ for the straight or curved case respectively.

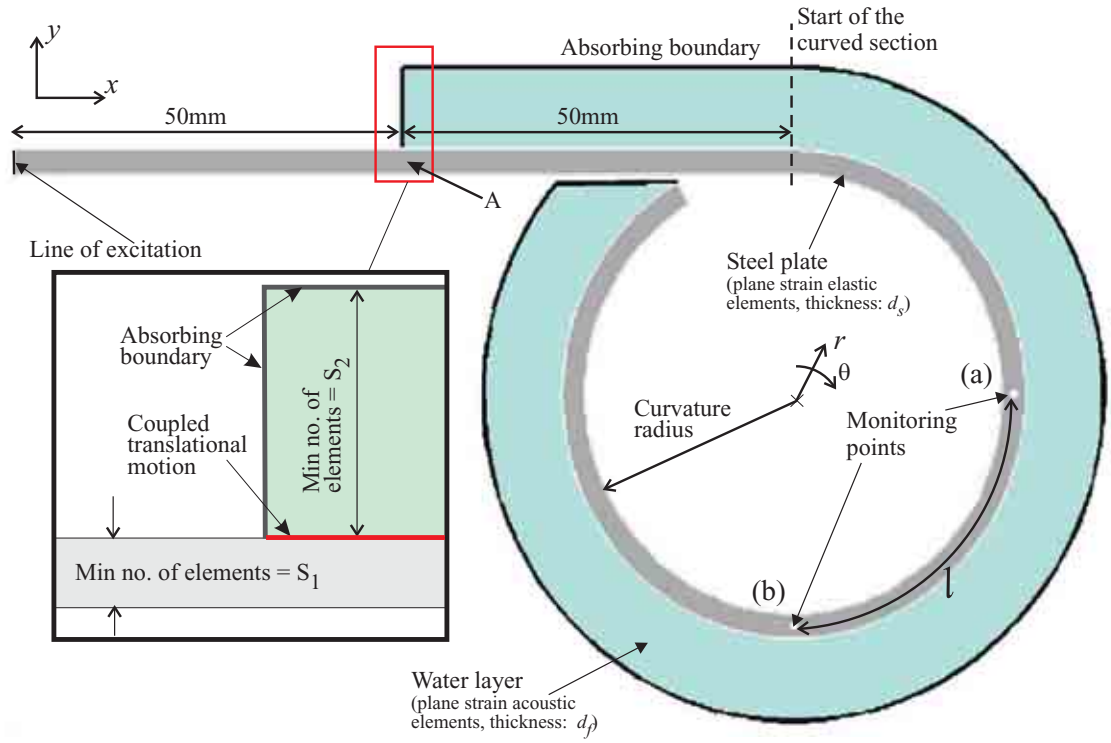

Figure 7.1: Schematic diagram of a two layered finite element model for the simulation of leaky wave mode propagation in the time domain.

Fig. 7.1 shows a schematic diagram of the FE model used for the time-domain FE simulation. The simulations were performed using Abaqus^{TM} but could equally have been done using many commercial FE programs. The model consists of a layer of steel plate (thickness: 3mm) coupled with a layer of water (thickness: 10mm). The two layers are tied together by coupling the translational motion, in the direction normal to the interface as expected for a perfect fluid. Additionally, absorbing boundaries are used on the external edges of the water layer to absorb any energy radiating away from the solid-fluid interface, hence simulating a fluid half space.

The material properties used are the same as those used in the previous chapter, and are listed in Tab. 6.3. The model is divided into two sections comprising an initial straight section and then a curved section of which the inner radius is fixed to a specific value

corresponding to the curvature radius that is under investigation.

A 5-cycle Hanning windowed toneburst signal is excited at the straight end of the steel plate by applying forces along the "line of excitation" with an appropriate amplitude either in the normal or in-plane direction to excite the A_0 or S_0 mode respectively; the "line of excitation" is the series of nodes along the free end of the straight section. To avoid transferring energy to the fluid-borne modes directly during the excitation of either the A_0 or S_0 mode, a 50mm long uncoupled single layered straight section is included to allow the specific excitation mode to fully develop before entering the leaky double layered section.

The choice of element sizes for the elastic and acoustic plane strain elements in the FE model follows the same criteria as those used in the modelling of the non-leaky cases discussed in Sec. 5.1. The general rule is that there should be at least 6 elements for one wavelength of the slowest propagating wave mode, including both guided and bulk wave types. Using these basic ideas, the minimum number of elements in the solid and fluid layers (S_1 and S_2) as illustrated in Fig. 7.1, can be determined using Eqns. 7.1 and 7.2. Additionally, for simplicity an aspect ratio ≈ 1 is used for all elements.

$$S_1 = \text{Round}\left[\frac{d_s}{6}\frac{\dot{V}_{ph}}{f_{ex}}\right], \tag{7.1}$$

$$S_2 = \text{Round}\left[\frac{d_f}{6}\frac{C_{L_{fluid}}}{f_{ex}}\right]. \tag{7.2}$$

where $\dot{V}_{ph}$ is the phase velocity of the wave mode under investigation, $C_{L_{fluid}}$ is the bulk translational velocity of the fluid, f_{ex} is the excitation frequency of the wave mode, and d_s and d_f are the thickness of the solid and fluid layers respectively.

The excitation signal can be reflected at any locations where there is a sharp change of impedance in the propagation direction; the impedance is dependent on both the material properties and the geometry. Therefore a reflection is expected to occur at location where the plate couples with the water layer, hence the initial straight section provides delay to separate the reverberating signals. Additionally, propagation velocities of the "quasi-A_0" and "quasi-S_0" modes vary little over the range of curvature radii in this study, therefore the length of the straight section (shown in Fig. 7.1) works well as a filtering length in all models.

As an illustration, the total energy density field of the system with a curvature radius of 40mm, at several time instances, is shown in Fig. 7.2. The fields were collected from the results generated from the time-domain simulation in Abaqus^{TM}, and subsequently plotted using Matlab^{TM}. The total energy density fields, which are the sum of the kinetic and potential energy density fields stored in the system (see for example pp.142-146 of Auld [33]), are plotted at four time instances corresponding to the propagation of the

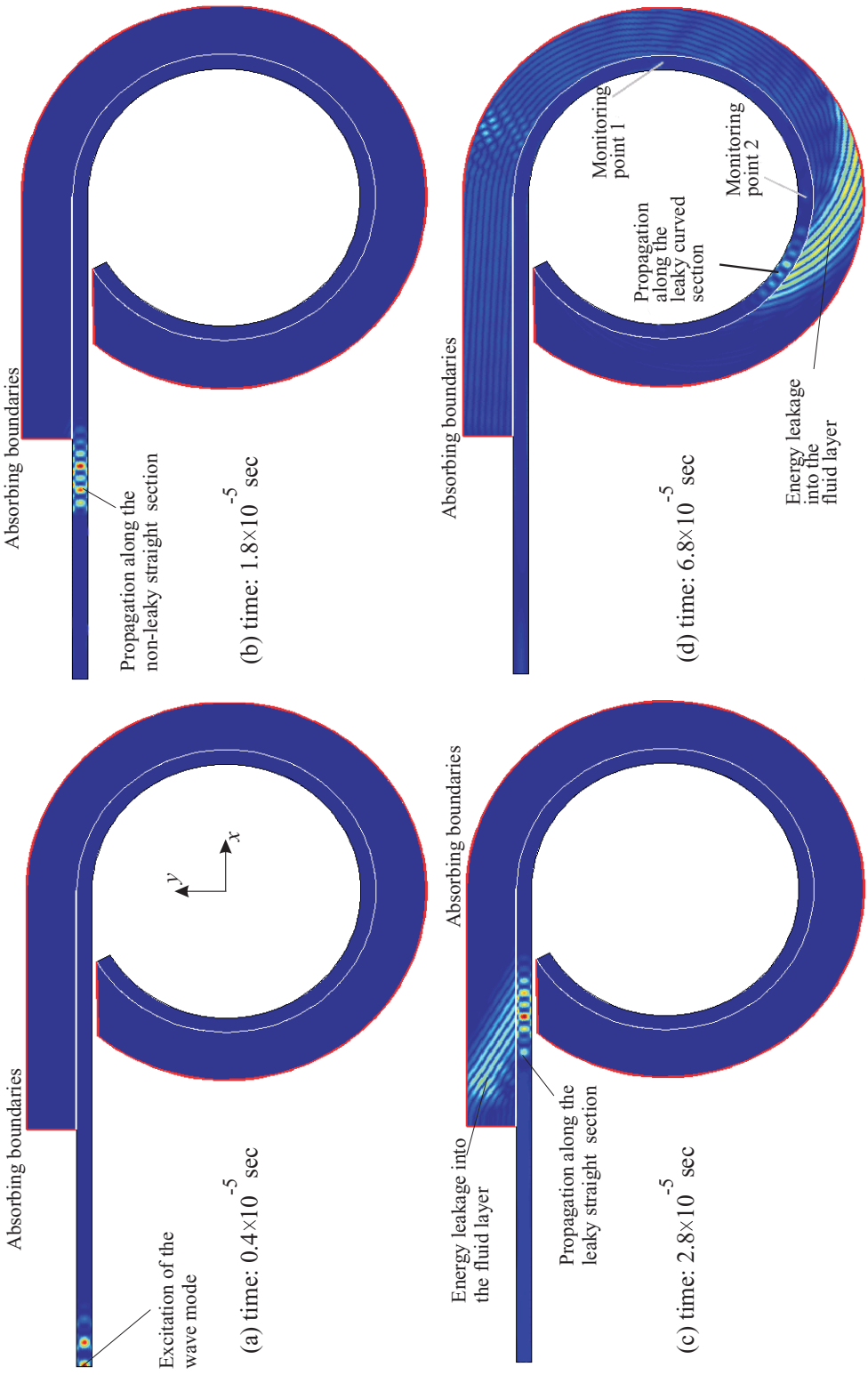

Figure 7.2: Output of the energy field from a time-domain simulation at several different time instants. The simulation is modelled using 2-D FE plane strain elastic or acoustic elements for the steel plate (thickness: 3mm) and the water layer (thickness:10mm) respectively. The model has a curvature radius of 40mm (see Fig. 7.1). The A_0 mode is excited with a 5 cycle Hanning windowed toneburst at time = 0.0sec and frequency = 500kHz.

A_0 wave mode in different sections of the FE model at times of 0.4×10^{-5}, 1.8×10^{-5}, 2.8×10^{-5} and 6.8×10^{-5} seconds respectively. The colour scales of the field amplitudes are different in all four time instances; the amplitudes of the energy level in the field are normalised to the maximum value for clarity. Therefore these images are illustrative but do not directly indicate the degree of attenuation.

Fig. 7.2(a) shows the A_0 mode being generated along the "line of excitation" at 500kHz to propagate in the non-leaky straight section of the model (Fig. 7.2(b)). As the wave packet enters the double layered straight section (Fig. 7.2(c)), the non-leaky A_0 wave mode converts into a leaky A_0 mode where some of its energy leaks into the fluid layer, and is subsequently absorbed by the absorbing boundary. The amount of this leakage is governed by the attenuation characteristic of the wave mode at the excitation frequency. Finally, the A_0 leaky wave mode enters the leaky curved sections, as shown in Fig. 7.2(d), where more energy is expected to leak into the surrounding medium for the reasons explained in Sec. 6.5 of the previous chapter. In this section of the model, the wave fronts of the leaky bulk waves appear to be curved in the fluid layer; the arc of the wave fronts has the same curvature as that of the outer surface of the plate.

A drawback with this approach is that the absorbing boundary condition works best when the radiating waves strike the boundaries at 90 degrees (details can be found in, for example, Engquist *et al.* [151]). As a result, the absorbing boundaries of the fluid layer do not absorb all the wave energy that reaches them; a small amount of the energy may be reflected back and re-enter the plate. However, the fluid layer acts as a delay line so any such re-incident waves are delayed with respect to the wave mode of interest.

Additionally, the propagation of the fluid-borne Franz modes can be observed in the fluid layer in Fig. 7.2(d). It can be seen that as the energy of the "quasi-A_0" mode leaks into the fluid layer, some of this leaky energy is converted continuously into the Franz modes, which are represented by the circular wave fronts in the fluid layer.

Abaqus^{TM} outputs the time response signal of the displacement only in the directions along the principal axes of the cartesian coordinates, x and y, in Fig. 7.2(a). For the investigation of the curvature effect on the attenuation of the leaky "quasi-A_0" mode, two time response signals are required, and they are measured at nodes located at the mid-point through the thickness of the steel plate in the out-of-plane direction at positions along the principal axes, indicated by the "monitoring points" 1 and 2 of Fig. 7.2(d).

The typical time response signals of the leaky "quasi-A_0" mode, measured in the out-of-plane direction at the "monitoring points" 1 and 2, for a 3mm thick steel plate with a 40mm curvature radius, are shown in Fig. 7.3.

In addition to the leaky "quasi-A_0" mode, a small amount of the leaky "quasi-S_0" mode

can also been seen ahead of the "quasi-A_0" mode. Since the excitation is asymmetric, there should not be any "quasi-S_0 mode excited at the "line of excitation". However, as the wave packet enters the coupled section (see location "A" in Fig. 7.1), the symmetry condition is destroyed. At this location, some of the energy for the "quasi-A_0" mode is converted to that of "quasi-S_0" mode; this is also know as the mode conversion phenomenon.

The same phenomenon occurs when exciting the S_0 mode where some of its energy is converted to that of the A_0 mode. However, it was found that a substantially higher amount of the A_0 mode is generated in this case, compared to the amount of S_0 mode generated during the excitation of the A_0 mode.

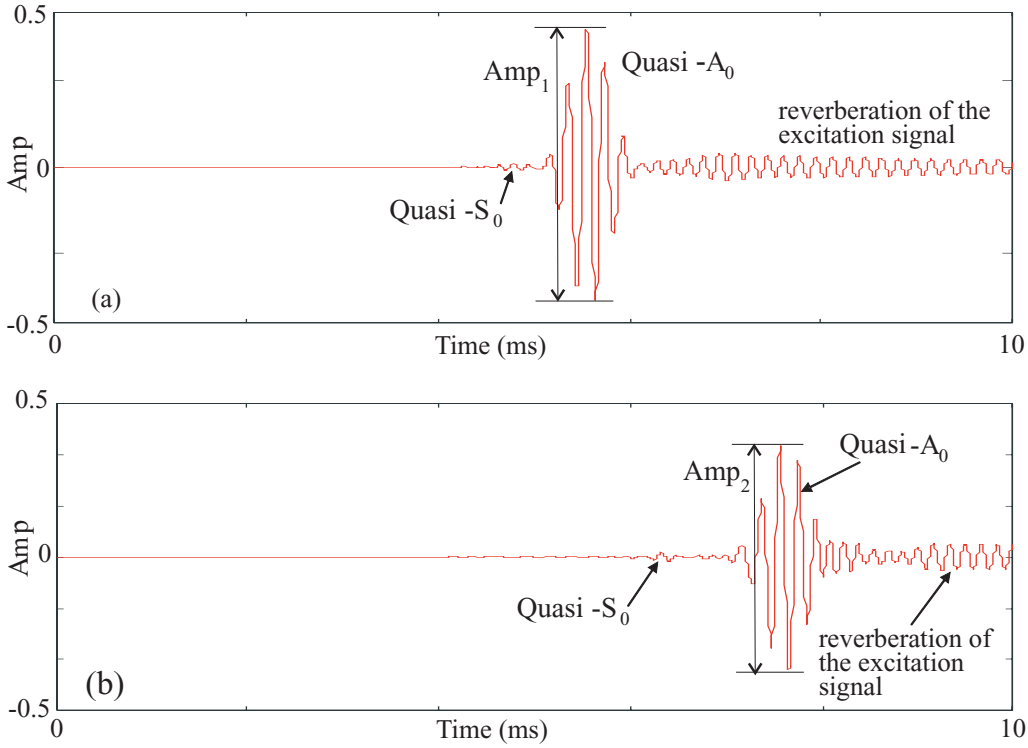

Figure 7.3: Typical FE time-response signals taken from the first (a) and second (b) monitoring points shown in Fig. 7.2(d). The wave signal is excited at 500kHz.

Furthermore, some signals that cannot be correlated to any of the excited wave mode can be observed in Fig. 7.3 at times later than the first arrival of the leaky "quasi-A_0" mode; these signals are likely to be caused by the reverberations of the excitation wave mode or other converted wave modes at the initial straight section, or they can be caused by the re-incident leaky waves after being partially reflected from the absorbing boundaries. As these waves arrive later than the main signal, they should not affect the accuracy in calculating the attenuation of the targeted wave mode.

7.1.2 Results of the FE Validation

The calculation of the attenuation in dB/m of a particular wave mode, due to the energy leakage into the surrounding medium in the curved section of the FE model, can be evaluated easily using the amplitudes of the time-response signals taken at the "monitoring points" 1 and 2. the typical time signal measurements at these monitoring points are shown in Figs. 7.3, and the formula of the attenuation calculation is:

$$Atten(dB/m) = \frac{20}{l} \log\left(\frac{Amp_1}{Amp_2}\right). \tag{7.3}$$

where Amp_i with $i = \{1, 2\}$ corresponds to the peak to peak amplitude of the received signal at the "monitoring points" 1 and 2 (illustrated in Fig. 7.2), and l is the circumferential distance between the two monitoring points (shown Fig. 7.1).

A limitation of using this FE method to calculate the attenuation is that when the curvature radius becomes large, the distance between the two monitoring points increases. This would also increase the amount of energy leakage of the "quasi-modes" as it travels between the two monitoring points. In the limiting case, the amplitude of the "quasi-mode" may not be distinguishable from the reverberative noise mentioned above, and thus the calculation of attenuation would not be possible. For this reason, attenuations of the wave modes in a 3mm steel curved plate due to the energy leakage into the surrounding material are calculated for a range of curvature radii that are restricted to values between 10mm and 110mm if the results are taken only from the principle axes. Alternatively, if the results are to be taken from the curved section, the wave signals may be resolved in directions to obtain the normal amplitude (i.e. $A_x \cos(\theta) + A_y \sin(\theta)$ where $A_{x,y}$ are the motion amplitude along the principle axes x and y).

Figs. 7.4(a)-(d) show the normalised percentage difference in attenuation of the A_0 and S_0 modes calculated using both the analytical method and the FE simulations at 500kHz and 1000kHz, where the results were compared with those of the straight case obtained using Disperse [148]. A greater attenuation compared to the straight case is shown as a positive percentage difference in the y axis, and vice versa.

It can be seen in Fig. 7.4 that the FE simulations predict the percentage difference in attenuation fairly accurately. Nevertheless, a noticeable increase in the level of error can be detected as the curvature radius reduces. This can be linked to the fact that some of the energy reflected from absorbing boundaries in the fluid layer re-enters the plate layer, supplying extra energy to the guiding system. Additionally, this extra supply of energy also provides an explanation for the percentage difference in attenuation of both the A_0 and S_0 modes calculated using the FE simulations always being lower than those predicted analytically.

In general, marginally more energy is expected to re-enter to the plate after reflecting from the edge of the fluid layer, as the curvature radius reduces. This extra energy interferes with the amplitude of the measured signal. A model with a small curvature radius has a short circumferential distance, l, between the two monitoring points, thus allowing a short distance for the re-incident signals and the wave mode of interest to separate in time. Thus the error is believed to be due to the presence of these unwanted re-incident signals.

7.2 Experimental Validation of Curvature Effect in Leaky Cases

In this section, an experimental technique to measure the attenuation of the "quasi-A_0" mode is presented; this technique is applied to fluid loaded pipes with a range of curvature radii, and subsequently used to validate the curvature effect on the attenuation due to the energy leakage into the surrounding material.

7.2.1 Experimental Samples

The experiment was performed using commercially available carbon steel pipes of various sizes. Typical material and acoustical properties of the carbon steel are assumed, and are the same as those used for the analytical solution of the fluid loaded case, investigated in the previous chapter; the material properties of both the carbon steel and the water are listed in Tab. 6.3. To eliminate the dependence of thickness of the pipes when investigating the curvature effect, all pipes were machined in a lathe to the same wall thickness.

The dimensions of commercially available carbon steel pipes of various sizes (i.e. the thickness to radius ratio) are roughly determined by the amount of pressure which the pipes are designed to withstand; typically a large safety factor is also utilised to ensure safety. Therefore these pipes are not required to be manufactured to a high geometrical accuracy. According to the API-51 standard by American Petroleum Institute, pipes with diameter $> 2\frac{3}{8}$ and < 20 inches, the diameter (as a percentage of specified outer diameter) is to be within $\pm 1\%$.

A total of six pipe sizes, labelled from A to F, were investigated, all of which have been carefully machined down to a wall thickness that is as close to 3mm as possible; their dimensions, and the measured maximum and minimum thicknesses around the circumference, which are the positive and negative percentage changes compared to the nominal wall thickness, are listed in Tab. 7.1. In general, the tolerance of the wall thickness increases with the pipe diameter, hence a large pipe is less axially symmetric than one with a smaller diameter, as shown in Tab. 7.1. Every care has been taken to ensure that the

finishing of the pipes is close to perfect, but tiny circumferential grooves can be clearly observed on the machined surfaces due to the turning in the lathe. However, the size of the grooves is much smaller than the wavelength of the excitation mode, and therefore the grooves should have minimal effect on the propagation properties.

Pipe	Inner/Curvature diameter (mm)	Thickness (mm)	Measured min. thickness (% change in thickness)	Measured max. thickness (% change in thickness)
A	53.4	3.0	-2.12	4.91
B	70	3.0	-5.31	7.18
C	80.4	3.0	-2.59	8.83
D	104	3.0	-9.90	6.15
E	156	3.0	-7.75	12.02
F	207	3.0	-5.13	16.12

Table 7.1: Dimensions and their tolerances of pipes of various curvature radii used in the experimental measurement of attenuation due to leakage.

7.2.2 Experimental Technique

To evaluate the attenuation due to leakage into the surrounding medium, the experiment compares the amplitude of wave signal propagating around the circumference of a pipe between the unloaded and loaded cases directly. As a result, it is very important that the positions where the wave mode is excited and detected are fixed for both cases. Compressional PZT circular disc elements were used for the excitation of the wave mode. The material properties of the PZT (see Tab. 5.2) is the same as those used in the validation of the unloaded case; they provide an excellent means of exciting the A_0 mode.

The PZT elements have a diameter of 3mm and thickness of 1mm, and are attached permanently on the outer surface aligned around the circumference as illustrated in Fig. 7.5; these disc elements were subsequently encased in a small amount of silicon to stop any contact with the water when immersed during the second part of the experiment. Typically, more than two PZT elements were placed along the circumference to monitor the signal at several locations as the wave propagates around the circumference. The experimental measurements were taken in a "pitch-catch" configuration.

The pipes are typically cut to a length of approximately 150mm, while the PZT elements are attached on the outer surface of the pipe approximately halfway across the length. Since the A_0 mode propagates in all directions, the length of the pipe above and below the PZT element can act as a "filter length", separating the wave modes reflected from the ends of the pipe from the first arrival of the A_0 mode.

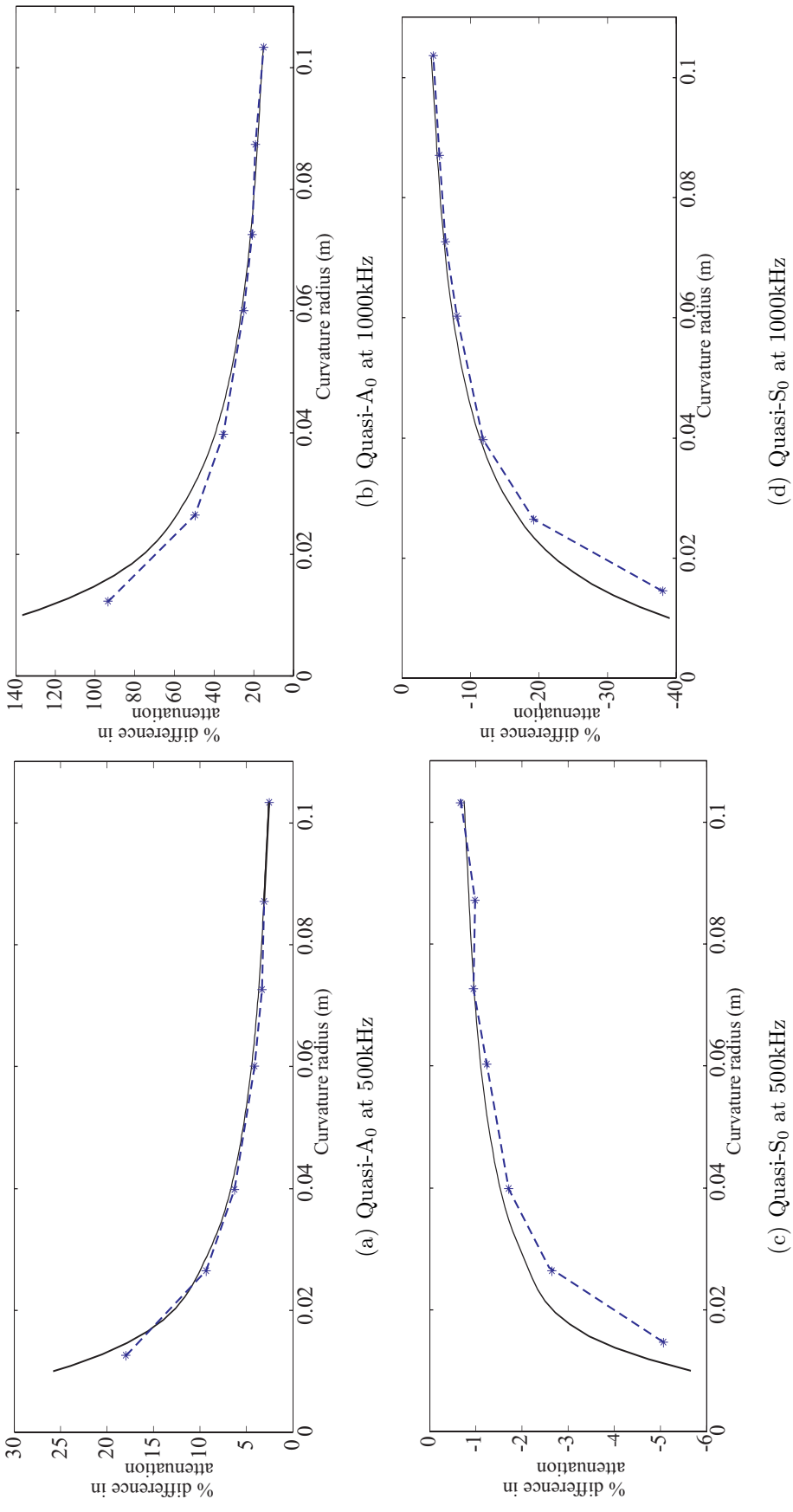

(a) Quasi-A_0 at 500kHz

(b) Quasi-A_0 at 1000kHz

(c) Quasi-S_0 at 500kHz

(d) Quasi-S_0 at 1000kHz

Figure 7.4: Percentage difference in attenuation between straight and curved steel plates (thickness: 3mm) as a function of curvature radius of the curved plate calculated using analytical solution (Black solid lines) and FE simulation (Blue dashed lines). The plates are coupled with a water half space on the outer surface.

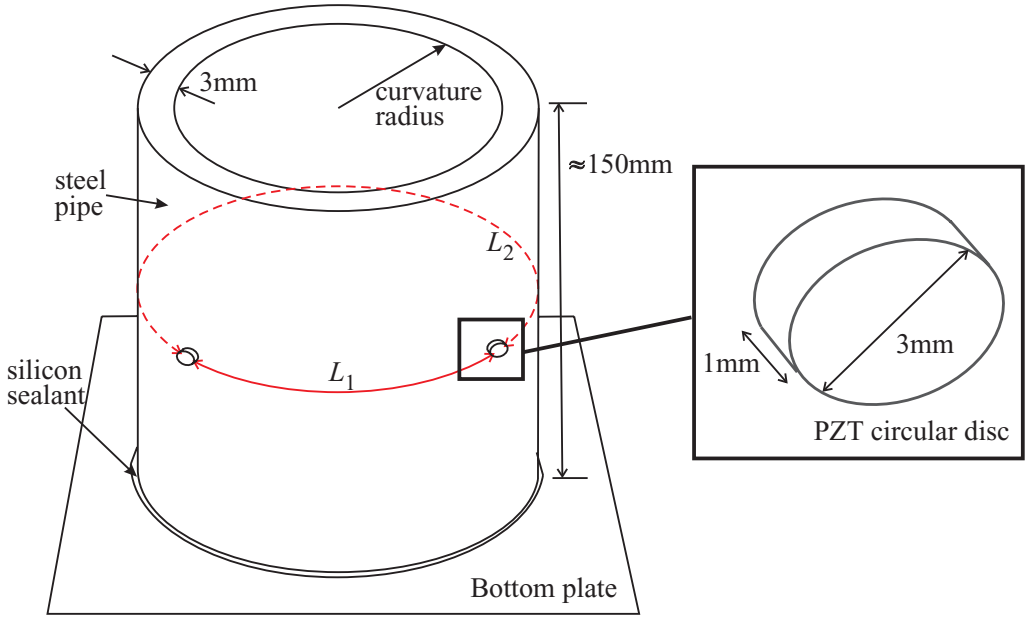

Figure 7.5: Schematic diagram of experimental setup (dry case) where a pipe is attached with PZT circular disc elements for the excitation and detection of the A_0 wave mode that propagates around the circumference.

As demonstrated in the FE simulation earlier, many other wave modes might be simultaneously excited when simply forcing purely in the radial direction on the surface of the pipe. To minimise the number of excitation modes, hence reducing the complication of the received signals, the experiment was carried out at an excitation frequency below the cut-off frequency of the A_1 mode so that only the A_0 and S_0 modes could be excited. Additionally, the PZT elements were carefully positioned in such a way that the arrival times of the wave packet under measurement were not overlapping with those of the other wave packets when it was received using any of the receiver PZT elements.

To carry out the measurement, a 5 cycle toneburst signal, excited using one PZT disc, generated both the A_0 and S_0 modes. These propagated in both directions around the circumference, and were received by all the other PZT elements in turn. Then the sealed pipe was immersed in a water tank (540mm $\times$ 540mm $\times$ 400mm) filled with de-gased tap water, as illustrated in Fig. 7.6. The bottom end of the pipe was sealed with a piece of metal plate to prevent any water from entering the inside of the pipe when immersed; therefore only the outer surface of the pipe was coupled with the water in the tank. Furthermore, the sides of the water tank were laid with acoustical absorbing rubber sheets to prevent any of the leaky signal from re-entering the guiding system. The electronics to drive the toneburst signals were the same as those used in the unloaded validation, illustrated in Fig. 5.26. Once the immersed setup was ready, a second set of measurements was recorded.

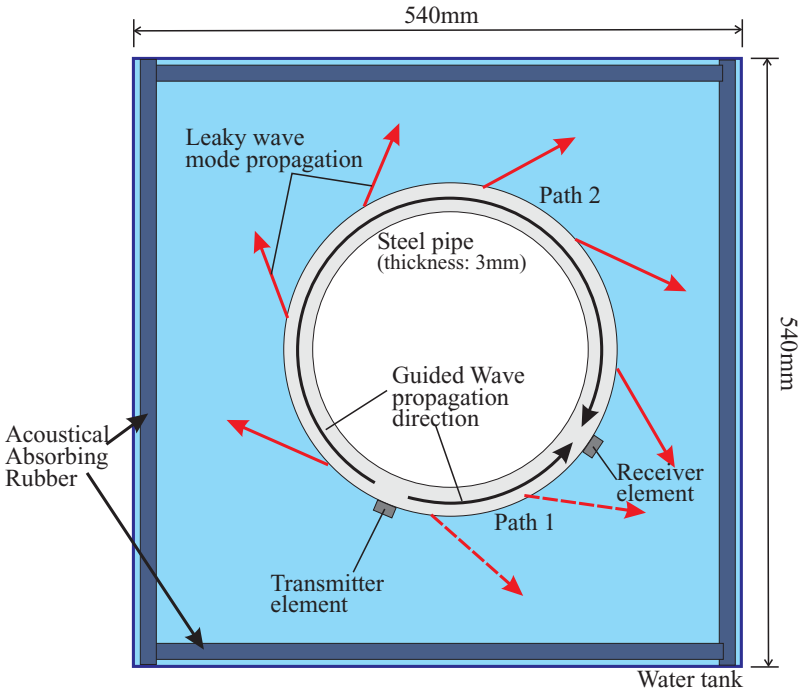

Figure 7.6: Schematic diagram (top view) of experimental setup (wet case) showing a sealed pipe immersed in a water tank, where absorbing rubber was used to prevent reflection of the leaky waves (Diagram is not to scale).

7.2.3 Experimental Results

The attenuation is calculated by dividing the amplitude of the quasi-A_0 time signal of the wet case by that of the dry case. By doing so, the effect of material damping in the steel and beam spreading of the energy can be cancelled out, and any reduction in amplitude is solely attributed to the energy leakage.

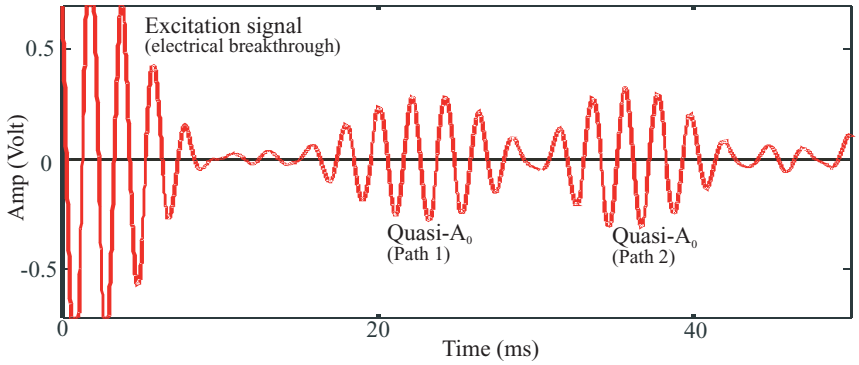

(a) Dry measurement

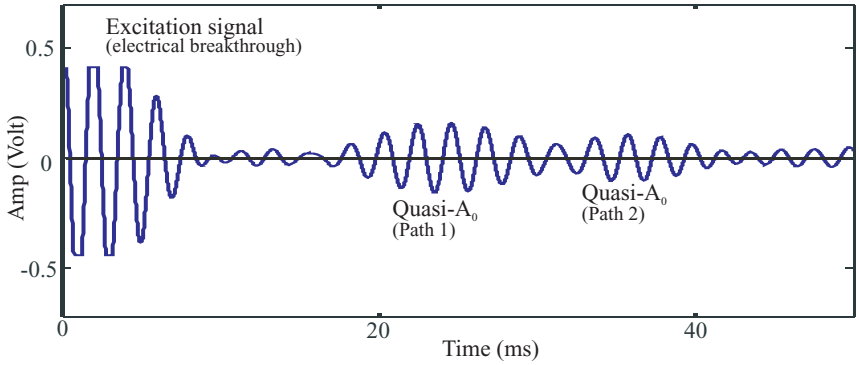

(b) Immersed measurement

Figure 7.7: Typical experimental measurements obtained in "pitch-catch" configuration, where the excitation wave packet propagates in both directions around the circumference along path 1 and 2 shown in Fig. 7.6. These measurements were made on pipe C with a 500kHz signal.

Fig. 7.7 shows two time responses taken from pipe C at 500kHz measured in dry and wet conditions. The first and second arrival wave packets correspond to the propagation of the A_0 mode along the shorter and longer arcs of the circumference respectively (see Fig. 7.6). Knowing the separation distance between the transmitting and receiving PZT disc elements (l), the attenuation value of the A_0 mode of a specific curvature can be calculated using Eqn. 7.3, where Amp_1 and Amp_2 are the peak-to-peak amplitudes of a wave packet measured in the dry and wet cases respectively.

Although the first and second wave packets were both excited and received using the same set of PZT elements, the second received signal (path 2), despite travelling a longer distance, has an unexpectedly higher amplitude than the first (path 1), as shown in

Fig. 7.7(a). This indicates that the sensitivity of the wave mode detection using these PZT disc elements is directional. This may be due to an uneven coupling condition between the PZT elements and pipe surface as discussed before for the unloaded experimental technique in Sec. 5.2.4.

Unfortunately, the wave packet corresponding to the A_0 mode could not be interpreted easily in many of the other measurements. This is generally because of the overlapping of the various wave packets in time, as a result of both the positioning of the PZT elements and the strong excitation of the S_0 mode. The problem is illustrated in Fig. 7.8. This shows that there are numerous propagation paths of different lengths. Nevertheless, since the S_0 and A_0 modes are travelling at different velocities, it can be seen that their corresponding wave packets can eventually separate over a long period of time after travelling around the circumferential more than once. Thus, knowing the length of each of these paths, the attenuation can still be calculated.

The attenuation of the six pipe samples was measured experimentally, using signals at 500kHz and 700kHz; their curvature radius is listed in Tab. 7.1, ranging from 26.7mm to 103.5mm, while the thickness was 3mm. The results are shown in Fig. 7.9, plotted together with those obtained analytically and by the FE method discussed earlier in Sec. 7.1.1. The average values of the experimental measurements are plotted while the distribution of measured values at a particular curvature radius is shown with the vertical error bars.

It can be seen that the curvature effect on the attenuation simulated by the FE models is in generally good agreement with the analytical predictions. The measurements in general match well with the analytical predictions, except for results of pipes with a large radius where they appear to be more inconsistent. One possible reason is that the pipes with a large radius have a high tolerance in axially symmetry as discussed earlier in Sec. 7.2.1, therefore a wider distribution of measured values can be observed as a result of waves propagating along paths with inconsistent thickness.

7.3 Summary

In this chapter, the analytical prediction of the curvature effect has been validated using both FE numerical simulations and experimental measurements.

A two layered leaky FE model with appropriate boundary conditions, simulated in the time-domain, has been used to evaluate the attenuation in a leaky curved plate system. Although it would be impossible to evaluate the attenuation dispersion of each individual mode directly, the model has provided means of validating the amount of energy which leaks into the surrounding medium for a particular wave mode at a given frequency. The curvature effect on both the leaky "quasi-A_0" and "quasi-S_0" modes have been investigated

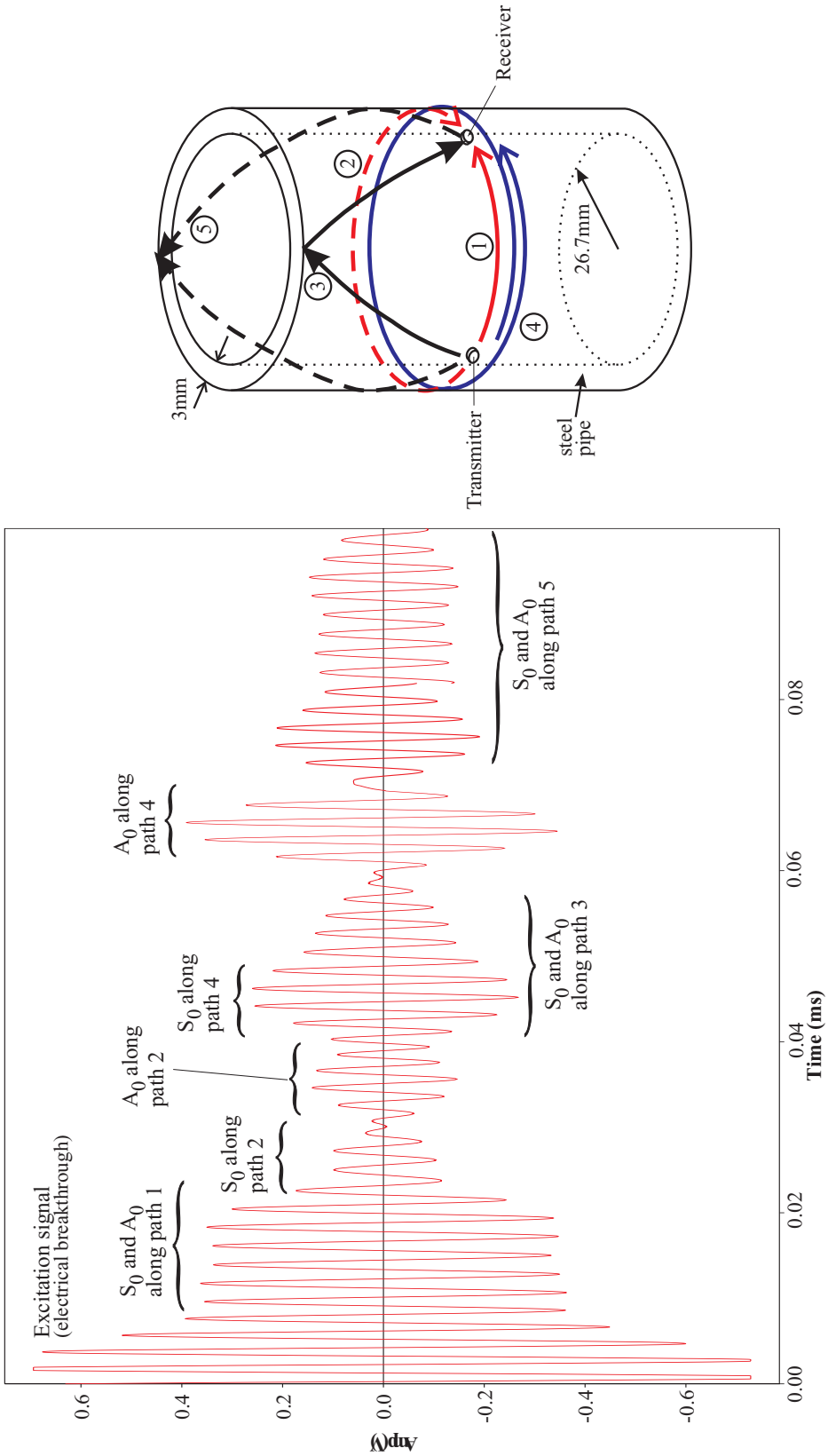

Figure 7.8: Experimental measurements on pipe C using a 500kHz signal. The schematic diagram on the right shows the various paths along which a wave packet can travel between the transmitter and the receiver.

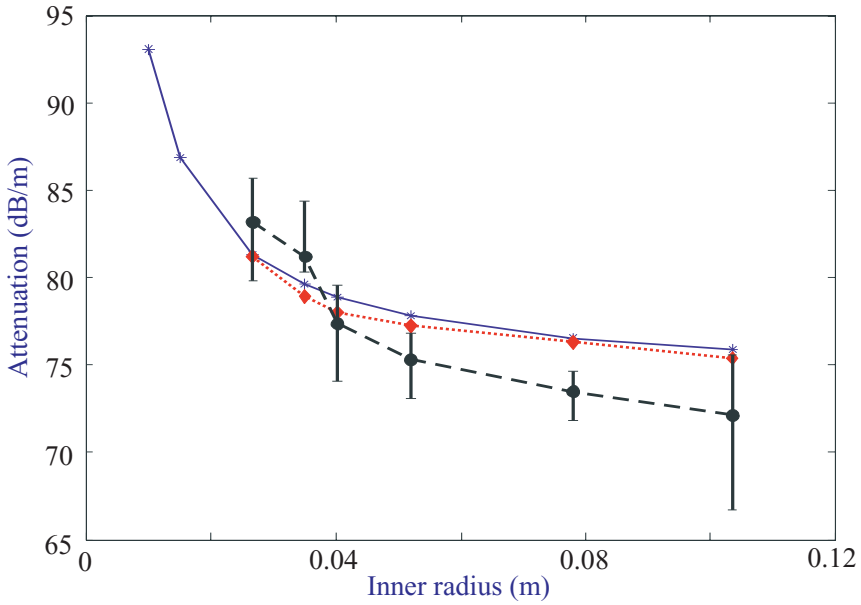

(a) Frequency: 500kHz

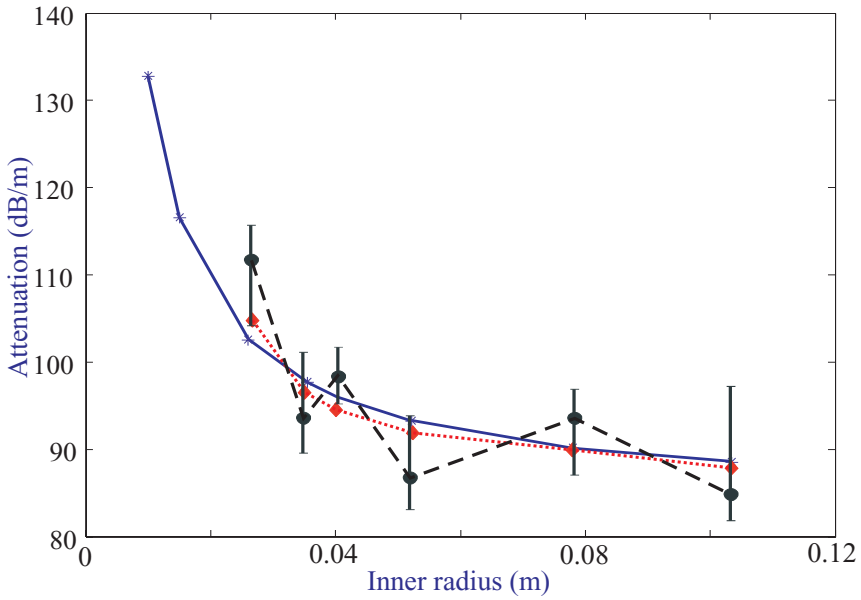

(b) Frequency: 700kHz

Figure 7.9: Attenuation of the leaky quasi-A_0 mode in steel pipes (thickness: 3mm) of various curvature radii, obtained using the analytical model (Blue solid line), FE method (Red dotted line) and experimental measurements (Black dashed line where the dots show the average values while the vertical bars show the distribution of results measured). The pipes are coupled with a water half space on the outer surface.

using this FE method. The FE results generally match well with the analytical predictions, and are very accurate when the curvature radius of the pipes is large. The results become less accurate when the pipes are small. This is caused by the phenomenon of re-incident leaky waves in the fluid layer as a result of imperfection of the adsorbing boundaries used in the FE model.

In the second part of this chapter, a relatively simple experimental technique to validate the curvature effect on the attenuation using pipes with a range of different curvature radii and a fixed wall thickness, has been introduced. PZT elements attached to the wall of the pipe were used to send and receive circumferential guided waves. The attenuation was measured directly by comparing propagated signals between the dry and immersed cases. Despite the difficulty in setting up this experiment, the average attenuation values of these measurements follow the same trend as those predicted by the analytical and FE models over a range of pipe curvature radii.

Chapter 8

Conclusions

This research work focused on the investigation of the curvature effect on the wave propagation properties of guided waves. The findings of such effects are very important for improving the understanding of guided wave inspection techniques in curved embedded engineering structures, such as the original motivation: rockbolts embedded in rock.

In the beginning of this concluding chapter, a general review of this thesis is presented, in which the main findings are highlighted. Secondly, the main contributions to knowledge in this study are summarised. Finally, the future work of this project will be suggested.

8.1 Review of Thesis

The motivation of this research work was presented in Ch. 1; this motivation emerged as a result of unresolved problems in understanding guided wave techniques when inspecting curved structures. A specific example was embedded rockbolts that are curved by the surrounding rock movements. The inspection technique was developed by Beard [2], using an excitation mode and frequency that are chosen in such a way that propagation with low attenuation is obtained. Thus any "breaks" or corrosion of the rockbolt might be identified by the echo signals which reflect from them. However, when the rockbolt is curved, the amplitudes of these signals reduce dramatically due to an increase in the energy leakage which makes the detection of these defects impracticable. Therefore it was important to understand the physics of this observation; the reason for the change of attenuation with curvature.

The exact analytical formulae to calculate the propagation properties of acoustic or elastic waveguides in a curved circular section bar were not developed in this thesis due to their complexity. Nevertheless, many other authors have tried to obtain solutions using

alternative approximation methods. A detailed literature review on these methods was given in Ch. 1.

The main objectives of this work is to improve the understanding the curvature effect on the propagation properties, in particular, where the attenuation of the propagating mode increases after the guiding structure is bent. Since the dispersion relations of plates and circular cross section beams are very similar to each other, the nature of the effects of curvature can therefore be studied using a simpler curved plate geometry, and this was developed in this thesis.

8.1.1 Non-Leaky Circumferential Waves

The historical background of the study of guided waves propagating circumferentially around pipes or curved plates, and their potential engineering applications were reviewed in Ch. 2. Prior to this thesis, the studies of these circumferential plate waves were mostly restricted to those of the non-attenuative nature in the regime of low frequency and small curvature radius. For the attenuative cases, published in few papers, solutions were obtainable only with those that are subjected to heavy assumptions.

In Ch. 2, the analytical formulae for the non-attenuative circumferential case, containing complicated Bessel functions, were generalised to include the multilayered curved plate model for both the SH and the Lamb-type plate wave propagation. In addition, the conditions of the numerical stability of these solutions were evaluated. It was found that the solution becomes unstable when either the frequency or the curvature radius is very large; these numerical instabilities were linked to conditions known as the "large $f - d$" problem and the breakdown of the Bessel functions. The nature of these two numerical instabilities was subsequently investigated thoroughly.

These numerical instabilities were identified and addressed in Ch. 3. Three alternative asymptotic analytical methods: Uniform Asymptotic Method (UAM), Regional Asymptotic Method (RAM) and Simplified Regional Asymptotic Method (SRAM), were derived by the project collaborators at the Mathematics Department, Imperial College, where the specific terms in the solution are either removed or replaced with stable asymptotic equivalent terms. These three schemes were examined and summarised in Ch. 3 by the author.

The UAM replaces the normal Bessel function expression with an asymptotic expression that is uniform for all parameters; although this particular scheme cannot improve the stability of the solution, it significantly increases the robustness of the calculation in the region of frequency-wavenumber domain where the exact solution is stable. On the other hand, the RAM and SRAM express the analytical solution explicitly in individual regions

that depend on the relationship between parameters such as the material and geometrical properties of the system.

All three asymptotic schemes were proven to be extremely accurate except at the very low frequencies, and at the boundaries between analytical regions in the case of RAM and SRAM. Nonetheless the accuracy of these schemes generally increases dramatically with increasing frequency. Therefore, using a combination of the exact and asymptotic methods where the asymptotic solutions are used when the exact solution becomes unstable, the overall accuracy and robustness in obtaining the numerical solutions of a non-leaky case can easily be obtained.

The curvature effect on the propagation and physical properties was investigated in Ch. 4, where the phase velocity and mode shapes of the curved plate wave modes were compared to those of the straight case at a range of curvature radii and frequencies. The results of the phase velocity difference were illustrated in a 3-D landscape plot for each individual mode. The curved plate modes of the lowest four order, "quasi-A_0", "quasi-S_0", "quasi-A_1" and "quasi-S_1" modes, were investigated over a frequency range of 0 - 6MHz, and over a curvature radius range of 0 - 0.1m, showing in general a rapid increase with decreasing curvature radius, and non-linearly dependence on the frequency. An optimal frequency, at which the curvature of the structure in the propagation direction has the minimum effect on the propagation properties in the frequency range investigated, was successfully identified from each of these 3-D plots. Nevertheless, the changes in phase velocity are very small, typically with less than 1% for curvature radius that is larger than 0.01m.

In addition, the mode shapes of several curved plate modes were compared directly with those of the straight case using a "dot-product" method, revealing the similarity of mode shapes between the curved and straight cases, which was termed the "S-factor". It was found that the "S-factor" can in general be related to the difference in phase velocity for a particular curvature radius. The through-thickness energy density of a wave mode shifts towards either the inner or the outer surface, a property which can be exploited to increase the sensitivity of the detection of defects that are situated close to either of these surfaces.

The dispersion curves of curved plates were analysed using the "method of bounds"; a method that provides a visual tool to characterise the major features in the dispersion curves. The dispersion curves of the Lamb-type elastic curved plate waves were shown to be characterised by two sets of so-called "bounds", which simply are dispersion curves corresponding to the uncoupled purely longitudinal and shear plate modes of the same geometry. Unlike the "mode-crossing" phenomenon in the dispersion curves of the straight case, none of the neighbouring modes of the curved plate case cross each other, but instead, after they come close to each other, they subsequently repel at the typical "intersection" points of the straight case.

In Ch. 5, a finite element eigen-modal modelling method to calculate the dispersion curves of the curved plate case was considered. The method, based on a simple axially symmetric model, extracts the natural frequencies corresponding to a pre-ascribed number of circumferential cyclic order which is identical to the angular wavenumber. Additionally, the through-thickness mode shapes can be evaluated using the eigen-vectors of the solution. The curvature effect were investigated using the FE method and presented in the similar 3-D landscape plots as the analytical case, showing the difference in phase velocity as a function of frequency and radius. The FE method was overall found to be very accurate with the level of error typically better than 0.01% in all frequency and curvature ranges for the A_0 and A_1 modes. The only exception is where the curves are close to the cut-off frequency. The FE modelling in general offers an alternative method to evaluate the curvature effect, it is especially useful where the infinitely long structure with a cross section that is too complicated to be formulated analytically.

The effect of curvature on the propagation properties was examined experimentally in the second half of Ch. 5. The experiment involved comparing the arrival times of a toneburst wave packet between the straight and curved cases. The measurements were taken from the end reflection of a thin aluminum strip. A specific curvature of the strip along the propagation direction was achieved by physical bending and held in place by a set of plastic fixtures, while permanently attached PZT elements were used to ensure that the same reference signal was retained for all curvature radius cases. Despite the use of strips with a high "thickness to width" ratio, a significant number of section modes corresponding to those bounded by the width edges, were excited, resulting in both the "width-edges" effect and the excitation of rectangular wave modes. These effects were examined, and the dispersion curves of the rectangular cross section were modelled using finite elements, while their mode shapes at specific frequencies were extracted. Using these dispersion curves and a 2D-Fast Fourier Transform (2DFFT) technique on the experimental results, the type of wave modes being excited in the aluminium strip were successfully identified. It was found that the type of mode which was excited depended on the frequency. In the case of a 0.97mm thick, 30mm wide aluminium strip, an almost pure A_0 wave mode excitation was achieved at 450kHz, 1MHz, 1.1MHz and 1.3MHz, at which the experimental measurements were taken to evaluate the curvature effect. Since the excitation conditions vary greatly from one strip to another, these frequencies are specific to this case and cannot be taken to apply universally.

It was found that the experimental measurements do not agree well with the preliminary analytical predictions. This can be explained by the fact that the differences in phase velocity due to the curvature effect are on average very small. For this reason, any external factors, such as the local changes of stress and density that are introduced during bending, can significantly affect the experimental results, and must be taken into consideration. The experimental results agree well with the analytical prediction when these additional

external factors are included; this improved analytical model contains 9 layers, each of which is assigned with material properties that is relevant to those affected by the external factors at the local position. Furthermore, the phenomenon, where the energy distribution of the A_0 mode shifts towards the outer surface, was validated using two 2mm PZT element cubes attached on opposite sides of the plate surfaces to measure the relative out-of-plane displacement amplitude ratio between the two surfaces. Good agreements were obtained between the analytical prediction and experimental measurements.

8.1.2 Leaky Circumferential Waves

Ch. 6 described the development of an analytical model for a leaky system in which guided waves propagate circumferentially in a curved plate coupled with a half space on the outer surface. A general literature review of these leaky circumferential waves was given. Although the analytical formulation is exactly the same for roots of either complex wavenumber or complex frequency, where the attenuation due to the energy leakage into the surrounding medium can be expressed in terms of the imaginary part of either of these complex parameters, the two cases are in fact associated with completely different physical problems. In this thesis, the leaky guided wave problem was correctly described by the roots composed of complex wavenumber and real frequency.

The analytical characteristic matrix of a leaky curved plate system was assembled using the Global Matrix method and suitable boundary conditions; the characteristic matrix consists of many complicated Bessel functions with complex order that rarely arise in engineering problems. Various numerical methods to solve these Bessel functions were examined, from which a suitable scheme, using a combination of Chebyshev Expansions Technique (CET) and recurrence relations of the Bessel function, was chosen for the numerical calculation of the roots. The roots of this leaky system comprise two independent parameters which can be located using an effective 2-D tracing routine based on a steepest descent method. The numerical tracing routine was illustrated and summarised.

In the leaky curved plate case, although the phase velocity dispersion curves are extremely similar to those of the straight case, the attenuation dispersion curves were found to be dramatically different. The "quasi-A_0" and "quasi-S_0" modes propagating in curved plates that are coupled with an infinite half space were studied in detail. In the leaky curved plate case, the through-thickness energy distribution of the "leaky quasi-A_0" mode shifts towards the outer surface, allowing more energy to be coupled with the half space; thus a higher value of attenuation than that of the corresponding straight case was expected. On the other hand, the "leaky quasi-S_0" mode has its energy distribution shifted towards the inner surface, resulting in less energy available on the outer surface to be coupled with the half space. The shift in energy distribution increases with increasing frequency, and at

very high frequencies, the "quasi-A_0" and "quasi-S_0" modes become the Rayleigh wave on the outer and inner surfaces respectively. It was concluded that the amount of attenuation of a particular mode is typically linked to the concentration of the energy density at the layer-half space interface.

Likewise the same phenomenon was observed with the change of curvature radius of the plate; the shift of the energy distribution towards one surface increases with increasing curvature. Overall, in the ranges of frequency-thickness: 0-3300$Hz-m$ and curvature radius: 0-0.13m, the absolute maximum percentage difference in attenuation of the A_0 and S_0 modes in comparison to a straight plate were calculated to be 157% and -98% respectively, where the negative value indicates a reduction in attenuation.

The inspection range of an embedded structure is determined by the total attenuation experienced by the wave as it propagates. It is therefore important to choose the mode and frequency according to knowledge of the curvature and the attenuation. For example the quasi-S_0 mode would be advantageous for detecting internal surface cracks in a cylindrical structure which is surrounding by fluid. In this case the wave is concentrated near the inner surface which reduces its leakage attenuation. Furthermore its leakage reduces with increase frequency.

In addition to the Lamb-type leaky curved plate modes, a family of highly attenuative fluid-borne wave modes, also known as the Franz modes, that propagate circumferentially at a certain distance away from the curved plate surface, was also investigated in Ch. 6. There is in theory an infinite number of these Franz modes, all of which converge to the bulk speed of the fluid in the half space at high frequencies.

The curvature effect on the attenuation in leaky curved plates was validated numerically and experimentally in Ch. 7. The finite element (FE) modelling comprised a solid metal curved layer of a specific curvature radius, which coupled with a thick fluid layer where absorbing boundary conditions were applied on the free-edges of the layer to eliminate most of the leaking bulk waves. Accurate results of the attenuation due to leakage into the surrounding medium were obtained for both the "quasi-A_0" and the "quasi-S_0" modes. Due to the limitation of the FE model, the curvature radius at which the attenuation was possible to be evaluated, was restricted to a range between 0.01m and 0.11m. The results were compared between the analytical prediction and those measured from the FE models; in general, the FE results predicted well the trend of the curvature effect on the attenuation, but agreement was weaker when the curvature radius considered was small, due to the inefficiency of the absorbing boundaries.

A simple and effective experiment, based on pipes of various diameters and the same thickness, was used to validate the curvature effect on the attenuation of the "quasi-A_0 mode. Using a "pitch-catch" configuration, the amplitudes of the out-of-plane displace-

ment measured from a set of PZT circular disc elements permanently attached on the surface around the circumference of these pipes were measured. The measurements were taken in both the dry condition and when the pipes were immersed in water. Based on these measurements, the attenuation of the "quasi-A_0" mode propagating in pipes of a range of curvature radii was evaluated. The average values of attenuation from roughly 10 measurements of each pipe size, agreed well with the analytical predictions and those obtained using the FE method.

8.2 Main contributions to Knowledge

This work has made a contribution to the understanding of an aspect of guided wave propagation that can be commonly found during NDT guided wave inspection. Although this work does not address the problem which arose directly from the curvature effect in the rockbolt inspection, it deals with the fundamental concept of this curvature effect using a simpler plate system. Using asymptotic methods, it has been demonstrated in this thesis that dispersion curves of an unloaded curved plate can be obtained in the normally unstable region when the frequency and the curvature radius are large.

A thorough assessment of the suitability of the asymptotic methods to eliminate certain types of numerical instabilities was carried out, which led to a novel scheme to trace dispersion curves effectively in all ranges of frequencies and curvature radii. Investigation into the effect of curvature along the propagation direction on the lower order plate modes has established that the difference in phase velocity between the straight and curved cases are both frequency and curvature radius dependent. The curvature effect has been shown to be the same for plates with the same "thickness to curvature radius" ratio.

A novel analysis to relate the changes in the propagation properties to the changes in the through-thickness mode shapes has made the curvature effect more comprehensible. As a rule, the curvature along the propagation direction shifts the energy distribution of a wave mode to either the inner or the outer surface. Although this shift in energy distribution has little effect on the phase velocity of the wave mode in both non-leaky and leaky cases, it has a significant effect on the attenuation in the leaky case, due to a change in the amount of energy available at the guiding medium-half space interface. In general, the same concept can be used to predict the change in attenuation due to leakage of wave modes propagation in beams of any cross section geometry.

An extension of the "method of bounds" has been successfully adapted to analyse various features on the dispersion curves of wave modes in a curved plate. The so-called "bounds" which are asymptotic barriers to the dispersion curves in terms of purely longitudinal or purely shear wave modes satisfying individual boundary conditions, provide a useful tool

to visualise the behaviour and the composition of the wave types at different parts of the curves.

Finally, the development of the analytical solution for the leaky curved plate, based on the Helmholtz decomposition and Global Matrix methods, is novel. As part of the solution, an efficient numerical scheme has been chosen to solve the complicated Bessel function with a complex order. These solutions have subsequently enabled the evaluation of the curvature effect in this kind of leaky system. This is a generic result which has applicability to all sorts of multilayered curved plate structures.

8.3 Project Outlook

Although a substantial amount of work has been done in this thesis to understand the curvature effect on guided wave properties, the entire work has been based on the plate structures. An extension of this study to include the cylindrical geometry is undeniably needed. This would subsequently allow issues, caused when the rock bolts are curved, to be properly addressed.

Again, the study should be carried out in stages, starting with the easier case of a non-leaky system, and then a leaky system. As with the plate case, the analytical solution of the curved cylindrical geometry must first be developed. However, this solution as discussed earlier, is extremely difficult, and thus a close collaboration with the Mathematics Department, Imperial College, would certainly be beneficial.

Using a toroidal geometry, eigen-solutions in a Finite Element (FE) modelling can be effectively used to obtain the dispersion curves of a non-leaky system. Nevertheless, much work is still needed to obtain solutions for the leaky case. The main challenge is to find a method with which the infinite leaky medium can be simulated correctly.

From this study, it is clear that the attenuation of a wave mode is directly linked to the amount of energy available on the interface between the guiding and surrounding mediums. Therefore, once the analytical model for the curved cylindrical geometry is attained, it would allow the mode shapes of the propagating modes to be studied in relation to various frequencies and curvatures.

Ultimately, the aim is to identify a suitable wave mode that contains appropriate properties to carry out inspection on rock bolts which may or may not be curved.

Appendix A

Basic Equations of Elasticity in Cylindrical Coordinates

A.1 Equations of Motion

The equations of motion shown below correspond to the principal directions r, θ and z as defined in figure 2.3.

$$\rho\left(\frac{\partial^2 u_r}{\partial t^2}\right) = \frac{\partial \sigma_{rr}}{\partial r} + \frac{1}{r}\frac{\partial \sigma_{r\theta}}{\partial \theta} + \frac{\partial \sigma_{rz}}{\partial z} + \frac{\sigma_{rr} - \sigma_{\theta\theta}}{r}. \tag{A.1}$$

$$\rho\left(\frac{\partial^2 u_\theta}{\partial t^2}\right) = \frac{\partial \sigma_{\theta r}}{\partial r} + \frac{1}{r}\frac{\partial \sigma_{\theta\theta}}{\partial \theta} + \frac{\partial \sigma_{\theta z}}{\partial z} + 2\frac{\sigma_{r\theta}}{r}. \tag{A.2}$$

$$\rho\left(\frac{\partial^2 u_z}{\partial t^2}\right) = \frac{\partial \sigma_{zr}}{\partial r} + \frac{1}{r}\frac{\partial \sigma_{z\theta}}{\partial \theta} + \frac{\partial \sigma_{zz}}{\partial z} + \frac{\sigma_{zr}}{r}. \tag{A.3}$$

A.2 Strain Tensor Formulation

The strain tensor can be expressed in terms of the displacement vector $\bar{u}$ in the polar coordinate system r, θ, z.

$$\varepsilon_{rr} = \frac{\partial u_r}{\partial r}. \tag{A.4}$$

$$\varepsilon_{\theta\theta} = \frac{1}{r}\frac{\partial u_\theta}{\partial \theta} + \frac{u_r}{r}. \tag{A.5}$$

$$\varepsilon_{zz} = \frac{\partial u_z}{\partial z}. \tag{A.6}$$

$$\varepsilon_{r\theta} = \frac{1}{2}\left(\frac{\partial u_\theta}{\partial r} - \frac{u_\theta}{r} + \frac{1}{r}\frac{\partial u_r}{\partial \theta}\right). \tag{A.7}$$

$$\varepsilon_{\theta z} = \frac{1}{2}\left(\frac{1}{r}\frac{\partial u_z}{\partial \theta} + \frac{\partial u_\theta}{\partial z}\right). \tag{A.8}$$

$$\varepsilon_{zr} = \frac{1}{2}\left(\frac{\partial u_r}{\partial z} + \frac{\partial u_z}{\partial r}\right). \tag{A.9}$$

Appendix B

Exact Dispersion Relations for an Unloaded Single Layer

The elements given here are for an eigen-problem matrix (2.18), D, that satisfies the stress-free boundary conditions at the inner and outer surfaces for the Lamb-type circumferential waves in a single layer curved plate. The elements given here are in their most general form so that they are consistent with those used in the leaky cases given in Ch. 6. However, it is worth noting that a more elegant expression can be obtained using a recurrence relationship of the Bessel functions [63].

$$\left.\begin{aligned} d_{11} &= \tfrac{2\mu i\nu}{r_1}[-\tfrac{1}{r_1}J_\nu(\hat{\omega}_1)+k_L J'_\nu(\hat{\omega}_1)],\\ d_{12} &= \tfrac{2\mu i\nu}{r_1}[-\tfrac{1}{r_1}Y_\nu(\hat{\omega}_1)+k_L Y'_\nu(\hat{\omega}_1)],\\ d_{13} &= \mu[-k_T^2 J''_\nu(\hat{\omega}_3)+\tfrac{k_T}{r_1}J'_\nu(\hat{\omega}_3)-\tfrac{\nu^2}{r_1^2}J_\nu(\hat{\omega}_3)],\\ d_{14} &= \mu[-k_T^2 Y''_\nu(\hat{\omega}_3)+\tfrac{k_T}{r_1}Y'_\nu(\hat{\omega}_3)-\tfrac{\nu^2}{r_1^2}Y_\nu(\hat{\omega}_3)], \end{aligned}\right\} \quad \sigma_{r\theta}|_{r=r_1}. \tag{B.1}$$

$$\left.\begin{aligned} d_{21} &= k_L^2[-\lambda J_\nu(\hat{\omega}_1)+2\mu J''_\nu(\hat{\omega}_1)],\\ d_{22} &= k_L^2[-\lambda Y_\nu(\hat{\omega}_1)+2\mu Y''_\nu(\hat{\omega}_1)],\\ d_{23} &= \tfrac{2\mu i\nu}{r_1}[-\tfrac{1}{r_1}J_\nu(\hat{\omega}_3)+k_T J'_\nu(\hat{\omega}_3)],\\ d_{24} &= \tfrac{2\mu i\nu}{r_1}[-\tfrac{1}{r_1}Y_\nu(\hat{\omega}_3)+k_T Y'_\nu(\hat{\omega}_3)], \end{aligned}\right\} \quad \sigma_{rr}|_{r=r_1}. \tag{B.2}$$

$$\left.\begin{aligned} d_{31} &= \tfrac{2\mu i\nu}{r_2}[-\tfrac{1}{r_2}J_\nu(\hat{\omega}_2)+k_L J'_\nu(\hat{\omega}_2)],\\ d_{32} &= \tfrac{2\mu i\nu}{r_2}[-\tfrac{1}{r_2}Y_\nu(\hat{\omega}_2)+k_L Y'_\nu(\hat{\omega}_2)],\\ d_{33} &= \mu[-k_T^2 J''_\nu(\hat{\omega}_4)+\tfrac{k_T}{r_2}J'_\nu(\hat{\omega}_4)-\tfrac{\nu^2}{r_2^2}J_\nu(\hat{\omega}_4)],\\ d_{34} &= \mu[-k_T^2 Y''_\nu(\hat{\omega}_4)+\tfrac{k_T}{r_2}Y'_\nu(\hat{\omega}_4)-\tfrac{\nu^2}{r_2^2}Y_\nu(\hat{\omega}_4)], \end{aligned}\right\} \quad \sigma_{r\theta}|_{r=r_2}. \tag{B.3}$$

$$\left.\begin{aligned} d_{41} &= k_L^2[-\lambda J_\nu(\hat{\omega}_2)+2\mu J''_\nu(\hat{\omega}_2)],\\ d_{42} &= k_L^2[-\lambda Y_\nu(\hat{\omega}_2)+2\mu Y''_\nu(\hat{\omega}_2)],\\ d_{43} &= \tfrac{2\mu i\nu}{r_2}[-\tfrac{1}{r_2}J_\nu(\hat{\omega}_4)+k_T J'_\nu(\hat{\omega}_4)],\\ d_{44} &= \tfrac{2\mu i\nu}{r_2}[-\tfrac{1}{r_2}Y_\nu(\hat{\omega}_4)+k_T Y'_\nu(\hat{\omega}_4)], \end{aligned}\right\} \quad \sigma_{rr}|_{r=r_2}. \tag{B.4}$$

where $\hat{\omega}_1 = k_L r_1, \quad \hat{\omega}_2 = k_L r_2, \quad \hat{\omega}_3 = k_T r_1, \quad \hat{\omega}_4 = k_T r_2.$

Appendix C

Supplements of Asymptotics Solutions

C.1 Asymptotics of the Bessel Function in Various Regimes [99]

Regime I: $\gamma < x$

$$J_\gamma(x) \sim \sqrt{\frac{2}{\pi}}(x^2-\gamma^2)^{-1/4}\cos\alpha, \quad Y_\gamma(x) \sim \sqrt{\frac{2}{\pi}}(x^2-\gamma^2)^{-1/4}\sin\alpha,$$
$$J'_\gamma(x) \sim -\sqrt{\frac{2}{\pi}}\frac{(x^2-\gamma^2)^{1/4}}{x}\sin\alpha, \quad Y'_\gamma(x) \sim \sqrt{\frac{2}{\pi}}\frac{(x^2-\gamma^2)^{1/4}}{x}\cos\alpha. \tag{C.1}$$

where $\alpha = (x^2-\gamma^2)^{1/2} - \gamma\cos^{-1}(\gamma x) - \pi/4$.

Regime II: $\gamma \approx x$

$$J_\gamma(x) \sim \left(\frac{2}{x}\right)^{1/3} Ai\left\{\left(\frac{2}{x}\right)^{1/3}(\gamma - x)\right\}, \quad Y_\gamma(x) \sim \left(\frac{2}{x}\right)^{1/3} Bi\left\{\left(\frac{2}{x}\right)^{1/3}(\gamma - x)\right\},$$
$$J'_\gamma(x) \sim -\left(\frac{2}{x}\right)^{2/3} Ai'\left\{\left(\frac{2}{x}\right)^{1/3}(\gamma - x)\right\}, \quad Y'_\gamma(x) \sim \left(\frac{2}{x}\right)^{2/3} Bi'\left\{\left(\frac{2}{x}\right)^{1/3}(\gamma - x)\right\}.$$

where Ai and Bi are the Airy functions.

Regime III: $\gamma > x$

$$J_\gamma(x) \sim \frac{1}{\sqrt{2\pi}}\frac{1}{(\gamma^2-x^2)^{1/4}}e^{\beta}, \quad Y_\gamma(x) \sim -\sqrt{\frac{2}{\pi}}\frac{1}{(\gamma^2-x^2)^{1/4}}e^{-\beta},$$
$$J'_\gamma(x) \sim \frac{1}{\sqrt{2\pi}}\frac{(\gamma^2-x^2)^{1/4}}{x}e^{\beta}, \quad Y'_\gamma(x) \sim \sqrt{\frac{2}{\pi}}\frac{(\gamma^2-x^2)^{1/4}}{x}e^{-\beta}. \tag{C.2}$$

where $\beta = (\gamma^2-x^2)^{1/2} - \gamma\cosh^{-1}(\gamma/x$

C.2 Asymptotics for Cross-Products of the Bessel functions [99]

Case $\gamma < x_1$, $\gamma < x_2$

$$
\begin{aligned}
J_\gamma(x_2)Y_\gamma(x_1 - J_\gamma(x_1))Y_\gamma(x_2) &\sim \frac{2}{\pi}\frac{1}{(x_1^2-\gamma^2)^{1/4}}\frac{1}{(x_2^2-\gamma^2)^{1/4}}\sin(\alpha_1-\alpha_2),\\
J'_\gamma(x_2)Y'_\gamma(x_1 - J'_\gamma(x_1))Y'_\gamma(x_2) &\sim \frac{2}{\pi}\frac{(x_1^2-\gamma^2)^{1/4}}{x_1}\frac{(x_2^2-\gamma^2)^{1/4}}{x_2}\sin(\alpha_1-\alpha_2),\\
J_\gamma(x_2)Y'_\gamma(x_1 - J'_\gamma(x_1))Y_\gamma(x_2) &\sim \frac{2}{\pi}\frac{(x_1^2-\gamma^2)^{1/4}}{x_1}\frac{1}{(x_2^2-\gamma^2)^{1/4}}\cos(\alpha_1-\alpha_2),\\
J'_\gamma(x_2)Y_\gamma(x_1 - J_\gamma(x_1))Y'_\gamma(x_2) &\sim -\frac{2}{\pi}\frac{1}{(x_1^2-\gamma^2)^{1/4}}\frac{(x_2^2-\gamma^2)^{1/4}}{x_2}\cos(\alpha_1-\alpha_2).
\end{aligned}
\tag{C.3}
$$

Case $\gamma > x_1$, $\gamma > x_2$

$$
\begin{aligned}
J_\gamma(x_2)Y_\gamma(x_1 - J_\gamma(x_1))Y_\gamma(x_2) &\sim \frac{2}{\pi}\frac{1}{(\gamma^2-x_1^2)^{1/4}}\frac{1}{(\gamma^2-x_2^2)^{1/4}}\sinh(\beta_1-\beta_2),\\
J'_\gamma(x_2)Y'_\gamma(x_1 - J'_\gamma(x_1))Y'_\gamma(x_2) &\sim -\frac{2}{\pi}\frac{(\gamma^2-x_1^2)^{1/4}}{x_1}\frac{(\gamma^2-x_2^2)^{1/4}}{x_2}\sinh(\beta_1-\beta_2),\\
J_\gamma(x_2)Y'_\gamma(x_1 - J'_\gamma(x_1))Y_\gamma(x_2) &\sim \frac{2}{\pi}\frac{(\gamma^2-x_1^2)^{1/4}}{x_1}\frac{1}{\gamma^2-(x_2^2)^{1/4}}\cosh(\beta_1-\beta_2),\\
J'_\gamma(x_2)Y_\gamma(x_1 - J_\gamma(x_1))Y'_\gamma(x_2) &\sim -\frac{2}{\pi}\frac{1}{(\gamma^2-x_1^2)^{1/4}}\frac{(\gamma^2-x_2^2)^{1/4}}{x_2}\cos(\beta_1-\beta_2).
\end{aligned}
\tag{C.4}
$$

where α_i and β_i are defined in 3.17.

C.3 Lamb Dispersion Relation: Transitional Regions of the Regional Asymptotic method [63]

Region II: $\nu \approx \hat{\omega}_1$

$$
\begin{aligned}
&\sqrt{\frac{\pi}{2}}\sin(\alpha_3-\alpha_4)\Big\{\frac{f_5^2 f_6^2}{f_2 f_3 f_4}(\cos\alpha_2 Y_\nu(\hat{\omega}_1)-\sin\alpha_2 J_\nu(\hat{\omega}_1))\\
&-16\nu^4\hat{\omega}_1 f_2 f_3 f_4(\sin\alpha_2 Y'_\nu(\hat{\omega}_1)+\cos\alpha_2 J'_\nu(\hat{\omega}_1))\Big\}\\
&-4\sqrt{\frac{\pi}{2}}\nu^2\cos(\alpha_3-\alpha_4)\Big\{\frac{f_6^2 f_2 f_4}{f_3}(\sin\alpha_2 Y_\nu(\hat{\omega}_1)+\cos\alpha_2 J_\nu(\hat{\omega}_1))\\
&+\frac{f_5^2\hat{\omega}_1 f_3}{f_2 f_4}(\cos\alpha_2 Y'_\nu(\hat{\omega}_1)-\sin\alpha_2 J'_\nu(\hat{\omega}_1))\Big\}+c_3=0.
\end{aligned}
\tag{C.5}
$$

Region IV: $\nu \approx \hat{\omega}_2$

$$
\begin{aligned}
&-\sqrt{\frac{\pi}{2}}\sin(\alpha_3-\alpha_4)\Big\{\frac{f_5^2 f_6^2}{\tilde{f}_1 f_3 f_4}(J_\nu(\hat{\omega}_2)e^{-\beta_1}+Y_\nu(\hat{\omega}_2)\frac{e^{-\beta_1}}{2})\\
&-16\nu^4\hat{\omega}_2\tilde{f}_1 f_3 f_4(J'_\nu(\hat{\omega}_2)e^{-\beta_1}-Y'_\nu(\hat{\omega}_2)\frac{e^{-\beta_1}}{2})\Big\}\\
&-4\sqrt{\frac{\pi}{2}}\nu^2\cos(\alpha_3-\alpha_4)\Big\{\frac{f_6^2\hat{\omega}_2 f_4}{\tilde{f}_1 f_3}(J'_\nu(\hat{\omega}_2)e^{-\beta_1}+Y'_\nu(\hat{\omega}_2)\frac{e^{-\beta_1}}{2})\\
&+\frac{f_5^2\tilde{f}_1 f_3}{f_4}(J_\nu(\hat{\omega}_2)e^{-\beta_1}+Y_\nu(\hat{\omega}_2)\frac{e^{-\beta_1}}{2})\Big\}+c_3=0.
\end{aligned}
\tag{C.6}
$$

Region VI: $\nu \approx \hat{\omega}_3$

$$
\begin{aligned}
&\sqrt{\frac{\pi}{2}}\sinh(\beta_1-\beta_2)\Big\{\frac{f_5^2 f_6^2}{\tilde{f}_1\tilde{f}_2 f_4}(\cos\alpha_4 Y_\nu(\hat{\omega}_3)-\sin\alpha_4 J_\nu(\hat{\omega}_3))\\
&+16\nu^4\hat{\omega}_3\tilde{f}_1\tilde{f}_2 f_4(\sin\alpha_4 Y'_\nu(\hat{\omega}_3)+\cos\alpha_4 J'_\nu(\hat{\omega}_3))\Big\}\\
&-4\sqrt{\frac{\pi}{2}}\nu^2\cosh(\beta_1-\beta_2)\Big\{\frac{f_6^2\tilde{f}_2 f_4}{\tilde{f}_1}(\sin\alpha_4 Y_\nu(\hat{\omega}_3)+\cos\alpha_4 J_\nu(\hat{\omega}_3))\\
&+\frac{f_5^2\hat{\omega}_3\tilde{f}_1}{\tilde{f}_2 f_4}(\cos\alpha_4 Y'_\nu(\hat{\omega}_3)-\sin\alpha_4 J'_\nu(\hat{\omega}_3))\Big\}+c_3=0.
\end{aligned}
\tag{C.7}
$$

Region VIII: $\nu \approx \hat{\omega}_4$

$$
\begin{aligned}
&-\sqrt{\frac{\pi}{2}}\sinh(\beta_1-\beta_2)\Big\{\frac{f_5^2 f_6^2}{\tilde{f}_1\tilde{f}_2\tilde{f}_3}(J_\nu(\hat{\omega}_4)e^{-\beta_3}+Y_\nu(\hat{\omega}_4)\frac{e^{-\beta_3}}{2})\\
&+16\nu^4\hat{\omega}_4\tilde{f}_1\tilde{f}_2\tilde{f}_3(J'_\nu(\hat{\omega}_4)e^{-\beta_3}-Y'_\nu(\hat{\omega}_4)\frac{e^{-\beta_3}}{2})\Big\}\\
&-4\sqrt{\frac{\pi}{2}}\nu^2\cosh(\beta_1-\beta_2)\Big\{\frac{f_6^2\hat{\omega}_4\tilde{f}_2}{\tilde{f}_1\tilde{f}_3}(J'_\nu(\hat{\omega}_4)e^{-\beta_3}+Y'_\nu(\hat{\omega}_4)\frac{e^{-\beta_3}}{2})\\
&+\frac{f_5^2\tilde{f}_1\tilde{f}_3}{\tilde{f}_2}(J_\nu(\hat{\omega}_4)e^{-\beta_3}+Y_\nu(\hat{\omega}_4)\frac{e^{-\beta_3}}{2})\Big\}+c_3=0.
\end{aligned}
\tag{C.8}
$$

where f_i, $\tilde{f}_i$, $\hat{\omega}_i$, α_i, β_i are defined in 3.17.

C.4 Lamb Dispersion Relation: Transitional Regions of the Simplified Regional Asymptotic method [63]

Region IV: $\nu \approx \hat{\omega}_2$

$$
\begin{aligned}
&-\sqrt{\frac{\pi}{2}}\sin(\alpha_3-\alpha_4)\Big\{\frac{f_5^2 f_6^2}{\tilde{f}_1 f_3 f_4}J_\nu(\hat{\omega}_2)-16\nu^4\hat{\omega}_2\tilde{f}_1 f_3 f_4 J'_\nu(\hat{\omega}_2)\Big\}\\
&-4\sqrt{\frac{\pi}{2}}\nu^2\cos(\alpha_3-\alpha_4)\Big\{\frac{f_6^2\hat{\omega}_2 f_4}{\tilde{f}_1 f_3}J'_\nu(\hat{\omega}_2)+\frac{f_5^2\tilde{f}_1 f_3}{f_4}J_\nu(\hat{\omega}_2)\Big\}=0.
\end{aligned}
\tag{C.9}
$$

Region VI: $\nu \approx \hat{\omega}_3$

$$\sqrt{\frac{\pi}{2}}\Big\{\frac{f_5^2 f_6^2}{\tilde{f}_1\tilde{f}_2 f_4}(\cos\alpha_4 Y_\nu(\hat{\omega}_3) - \sin\alpha_4 J_\nu(\hat{\omega}_3)) + 16\nu^4\hat{\omega}_3\tilde{f}_1\tilde{f}_2 f_4(\sin\alpha_4 Y'_\nu(\hat{\omega}_3) + \cos\alpha_4 J'_\nu(\hat{\omega}_3))\Big\} - 4\sqrt{\frac{\pi}{2}}\nu^2\Big\{\frac{f_6^2\tilde{f}_2 f_4}{\tilde{f}_1}(\sin\alpha_4 Y_\nu(\hat{\omega}_3) + \cos\alpha_4 J_\nu(\hat{\omega}_3)) + \frac{f_5^2\hat{\omega}_3\tilde{f}_1}{\tilde{f}_2 f_4}(\cos\alpha_4 Y'_\nu(\hat{\omega}_3) - \sin\alpha_4 J'_\nu(\hat{\omega}_3))\Big\} = 0. \tag{C.10}$$

Region VIII: $\nu \approx \hat{\omega}_4$

$$-\sqrt{\frac{\pi}{2}}\frac{(f_6^2 - 4\nu^2\tilde{f}_1^2\tilde{f}_3^2)}{\tilde{f}_1\tilde{f}_2\tilde{f}_3}[f_5^2 J_\nu(\hat{\omega}_4) - 4\nu^2\hat{\omega}_4\tilde{f}_2^2 J_\nu(\hat{\omega}_4)] = 0.$$

where f_i, $\tilde{f}_i$, $\hat{\omega}_i$, α_i, β_i are defined in Equation 3.17.

References

[1] O. C. Zienkiewicz and K. G. Stagg, *Rock Mechanics* (John Wiley & Sons, 1972).

[2] M. Beard, "Guided Wave Inspection of Embedded Cylindrical Structures," Ph.D. thesis, University of London (2002).

[3] M. Beard, M. Lowe, and P. Cawley, "Inspection of Rock Bolts using Guided Ultrasonic Waves," in D. Thompson and D. Chimenti, editors, *Review of Progress in Quantitative NDE* (American Institute of Physics, New York, 2001), vol. 20, 1156–1163.

[4] B. Pavlakovic, M. Lowe, and P. Cawley, "High Frequency Low Loss Ultrasonic Modes in Embedded Bars," Jounral of Applied Mechanics **68**, 67–75 (2001).

[5] B. Auld, *Acoustic Fields and Waves in Solids*, vol. 2 (Krieger Publishing Company, Malabar, Florida, 1990).

[6] P. D. Wilcox, "Lamb Wave Inspection of Large Structures using Permanently Attached Transducers," Ph.D. thesis, University of London (1998).

[7] C. Valle, J. Qu, and L. Jacobs, "Guided Circumferential Waves in layered Cylinders," International Journal of Engineering Science **37**, 1369–1387 (1999).

[8] H. Lamb, "On Waves in an Elastic Plate," Proceeding of Royal Society London, Series A 114–128 (1917).

[9] M. Lowe, "Plate Waves for the NDT of Diffusion Bonded Titanium," Ph.D. thesis, University of London, UK (1993).

[10] K. Graff, *Wave Motion in Elastic Solids* (Dover Publicaitons inc., New York, 1973).

[11] J. Miklowitz, *Theory of Elastic Waves and Waveguides* (North-Holland, Amsterdam, 1978).

[12] D. Chimenti, "Guided Waves in Plates and their Use in Materials Characterization," Applied Mechanical Review **50**, 247–284 (1997).

[13] D. Gazis, "Three Dimensional Investigation of the Propagation of Waves in Hollow Circular Cylinders. I. Analytical Foundation," The Journal of the Acoustical Society of America **31**, 568–578 (1959).

[14] B. Pavlakovic, "Leaky Guided Ultrasonic Waves in NDT," Ph.D. thesis, University of London (1998).

[15] R. Kumar, "Flexural Vibrations of Fluid-Filled Circular Cylindrical Shells," Acustica **24**, 137–146 (1971).

[16] Y.-H. Pao and R. Mindlin, "Dispersion of Flexural Waves in an Elastic, Circular Cylinder," Jounral of Applied Mechanics **27**, 513–520 (1960).

[17] R. Thurston, "Elastic Waves in Rods and Clad Rods," The Journal of the Acoustical Society of America **64**, 1–37 (1978).

[18] A. Nayfeh, *Wave Propagation in Layered Anisotropic Media with Application to Composites* (Elsevier, 1995).

[19] W. Ewing, W. Jardetzky, and F. Press, *Elastic Waves in Layered Media* (McGraw-Hill, 1957).

[20] N. Haskell, "The Dispersion of Surface Waves on Multi-Layered Media," Bulletin of the American Seismological Society **43**, 17–34 (1953).

[21] B. Hosten and M. Castings, "Transfer Matrix of Multilayered Absorbing and Anisotropic Media - Measurements and Simulations of Ultrasonic Wave Propagation through Composite Materials," The Journal of the Acoustical Society of America **94**, 1488–1495 (1993).

[22] W. Karunasena, A. Shah, and S. Datta, "Wave Propagation in a Multilayered Laminated Cross-Ply Composite Plate," Jounral of Applied Mechanics **58**, 1028–1032 (1991).

[23] J. Rose and A. Pilarski, "Surface and Plate Waves in Layered Structures," Material Evaluation **46**, 598–605 (1988).

[24] B. Auld, D. Chimenti, and P. Shull, "SH Wave Propagation in Periodically Layered Composites," IEEE transactions on ultrasonics, ferroelectrics, and frequency control **43**, 319–325 (1996).

[25] V. Buchwald, "Rayleigh Waves in Anisotropic Media," Quarterly Journal of Mechanics and Applied Mathematics **41**, 461–469 (1961).

[26] C. Chang and W. Sachse, "Analysis of Elastic Wave Signals from an Extended Source in a Plate," The Journal of the Acoustical Society of America **77**, 1335–1341 (1985).

[27] W. Karunasena, A. Shah, and S. Datta, "Elastic Wave Propagation in Laminated Composite Plates," The Journal of the Acoustical Society of America **113**, 411–418 (1991).

[28] Y. Li and B. Thompson, "Influence of Anisotropy on the Dispersion Characteristics of Guided Ultrasonic Plate Modes," The Journal of the Acoustical Society of America **87**, 1911–1931 (1990).

[29] D. Chimenti and A. Nayfeh, "Leaky Lamb Waves in Fibrous Composite Laminates," Jounral of Applied Physics **58** (1985).

[30] D. Chimenti and A. Nayfeh, "Ultrasonic Leaky Waves in a Solid Plate Separating a Fluid and Vacuum," The Journal of the Acoustical Society of America **85**, 555–560 (1989).

[31] V. Dayal and V. Kinra, "Leaky Lamb Waves in an Anisotropic Plate. 2. Non-Destructive Evaluation of Matrix Cracks in Fibre-Reinforced Composites," The Journal of the Acoustical Society of America **89**, 1590–1598 (1991).

[32] J. Achenbach, *Wave propagation in Elastic Solids* (North-Holland, New York, 1984).

[33] B. Auld, *Acoustic Fields and Waves in Solids*, vol. 1 (Krieger Publishing Company Malabar, Florida, 1990).

[34] R. Waldron, "Theory of the Helical Waveguide of Rectangular Cross Section," Journal of British Institute in Radio Engineering **17**, 577–592 (1957).

[35] F. E. Grigor'yan, "Theory of Sound Wave Propagation in Curvilinear Waveguides," Soviet Physics - Acoustics **14**, 315–321 (1969).

[36] W. Rostafinski, "On Propagation of Long Waves in Curved Ducts," The Journal of the Acoustical Society of America **52**, 1411–1420 (1971).

[37] W. Osborne, "Higher Mode Propagation of Sound in Short Curved Bends of Rectangular Cross-Section," Journal of Sound and Vibration **45**, 39–52 (1976).

[38] A. Cummings, "Sound Transmission in Curved Duct Bends," Journal of Sound and Vibration **35**, 451–477 (1974).

[39] P. Morse and H. Feshbach, *Methods of Theoretical Physics* (McGraw-Hill Book Company, 1953).

[40] A. Cabelli, "The Acoustic Characteristics of Duct Bends," Journal of Sound and Vibration **68**, 369–388 (1980).

[41] C. Fuller and D. Bies, "Propagation of Sound in a Curved Bend Containing a Curved Axial Partition," The Journal of the Acoustical Society of America **63**, 681–686 (1978).

[42] K. D.H. and A. Benade, "Wave Propagation in Strongly Curved Ducts," The Journal of the Acoustical Society of America **74**, 320–332 (1983).

[43] L. Ting and M. Miksis, "Wave Propagation through a Slender Curved Tube," The Journal of the Acoustical Society of America **74**, 631–639 (1983).

[44] S. Félix and V. Pagneux, "Sound Propagation in Rigid Bends: A Multimodal Approach," The Journal of the Acoustical Society of America **110**, 1329–1337 (2001).

[45] S. Félix and V. Pagneux, "Multimodal Analysis of Acoustic Propagation in Three-Dimensional Bends," Wave Motion **36**, 157–168 (2002).

[46] S. Félix and V. Pagneux, "Ray-Wave Correspondence in Bent Waveguides," Wave Motion **41**, 339–355 (2005).

[47] L. Morley, "Elastic Waves in a Naturally Curved Rod," Quarterly Journal of Mechanics and Applied Mathematics **14**, 155–172 (1961).

[48] F. Crowley, J. Phillips, and C. Taylor, "Pulse Propagation in Straight and Curved Beams - Theory and Experiment," Journal of Applied Mechanics **41**, 71–76 (1974).

[49] W. Wittrick, "On Elastic Wave Propagation in Helical Springs," International Journal of Mechanical Sciences **8**, 25–47 (1966).

[50] W. Britton and G. Langley, "Stress Pulse Dispersion in Curved Mechanical Waveguides," Journal of Sound and Vibration **7**, 417–430 (1968).

[51] W. Britton and G. Langley, "Stress Pulse Dispersion in Helical Springs," Journal of Sound and Vibration **18**, 247–259 (1971).

[52] D. Hsieh and J. Lee, "Experimental Study of Pulse Propagation in Curved Elastic Rods," The Journal of the Acoustical Society of America **54**, 1052–1055 (1973).

[53] T. Bryant Moodie, C. Rogers, and D. Clements, "Large Wavelength Pulse Propagation in Curved Elastic Rods," The Journal of the Acoustical Society of America **59**, 557–563 (1976).

[54] C. Wu and B. Lundberg, "Reflection and Transmission of the Energy of Harmonic Elastic Waves in a Bent Bar," Journal of Sound and Vibration **190**, 645–659 (1996).

[55] R. Beccu, C. Wu, and B. Lunderg, "Reflection and Transmission of the Energy of Transient Elastic Extensional Waves in a Bent Bar," Journal of Sound and Vibration **191**, 261–272 (1996).

[56] D. Alleyne, B. Pavlakovic, M. Lowe, and P. Cawley, "Rapid, Long Range Inspection of Chemical Plant Pipework using Guided Waves," Insight **43**, 93–96,101 (2001).

[57] A. Demma, P. Cawley, and M. Lowe, "Mode Conversion of Longitudinal and Torsional Guided Modes Due to Pipe Bends," in D. Thompson and D. Chimenti, editors, *Review of Progress in Quantitative NDE* (American Institute of Physics, 2001), vol. 20, 172–179.

[58] A. Demma, P. Cawley, and M. Lowe, "Guided Waves in Curved Pipes," in D. Thompson and D. Chimenti, editors, *Review of Progress in Quantitative NDE* (American Institute of Physics, 2002), vol. 21, 157–164.

[59] M. Bromley and B. Esry, "Propagation of Ultracold Atoms through Bends in Waveguides," Physical Review A **68**, 043609 (2003).

[60] S. Qu and M. Geller, "Mesoscopic Electron and Phonon Transport through a Curved Wire," Physical Review B **70**, 085414 (2004).

[61] G. Kino, *Acoustic Waves : Devices, Imaging and Analogue Signal Processing* (Prentice-Hall Inc, New Jersey, 1987).

[62] B. Rulf, B. Z. Robinson, and P. Rosenau, "Asymptotic Expansions of Guided Elastic Waves," Transactions of the ASME 378 – 384 (1972).

[63] D. Gridin, R. V. Craster, J. Fong, M. Lowe, and M. Beard, "The High-Frequency Asymptotic Analysis of Guided Waves in a Circular Elastic Annulus," Wave Motion **38**, 67–90 (2003).

[64] J. D. Achenbach, A. K. Gautesen, and H. McMaken, *Ray Methods for Waves in Elastic Solids*, Monographs and studies in mathematics (Pitman Advanced Publishing Program, London, 1982).

[65] F. Nanny, *JWKB Approximation: Contributions to the Theory* (North-Holland, 1965).

[66] B. Fornberg, *A Practical Guide to Pseudospectral Methods* (Cambridge University Press, Cambridge UK, 1996).

[67] J. P. Boyd, *Chebyshev and Fourier Spectral Methods* (Dover, new York, 2001), 2nd ed.

[68] Engineering and Physical Sciences Research Council (EPSRC), 'Distorted Elastic Waveguides: Theory and Application', *Research contract awarded to Imperial College London* (2001).

[69] K. Sezawa, "Dispersion of Elastic Waves Propagated on the Surface of Stratified Bodies and on Curved Surfaces," Bulletin of the Earthquake Research Institute **3**, 1–18 (1927).

[70] K. Sezawa, "On the Propagation of Rayleigh Waves on Plane and Spherical Surfaces," Bulletin of the Earthquake Research Institute **2**, 21–28 (1927).

[71] I. Viktorov, "Rayleigh-Type Waves on Cylindrical Surfaces," The Journal of the Acoustical Society of America **4**, 131–136 (1958).

[72] J. Keller and F. Karal Jr., "Geometrical Theory of Elastic Surface-Wave Excitation and Propagation," The Journal of the Acoustical Society of America **36**, 32–40 (1964).

[73] L. M. Brekhovskikh, "Surface Waves Confined to the Curvature of the Boundary in Solids," Soviet Physics Acoustics **13**, 462–472 (1968).

[74] B. Rulf, "Rayleigh Waves on Curved Surfaces," The Journal of the Acoustical Society of America **45**, 493–499 (1968).

[75] U. Kawald, C. Desmet, W. Lauriks, C. Glorieux, and J. Thoen, "Investigation of the Dispersion Relations of Surface Acoustic Waves Propagating on Layered Cylinder," The Journal of the Acoustical Society of America **99**, 926–930 (1996).

[76] C. W. Horton, W. R. King, and K. J. Diercks, "Theoretical Analysis of the Scattering of Short Acoustic Pulses by a Thin-Walled Metallic Cylinder in Water," The Journal of the Acoustical Society of America **34**, 1929–1932 (1962).

[77] I. Viktorov and O. Zubova, "Normal Plate Modes in a Solid Cylindrical Layer," Soviet Physics Acoustics **9**, 15–17 (1963).

[78] O. D. Grace and R. R. Goodman, "Circumferential Waves on Solid Cylinders," The Journal of the Acoustical Society of America **39**, 173–174 (1966).

[79] J. Qu, Y. Berthelot, and L. Li, "Dispersion of Guided Circumferential Waves in a Circular Annulus," in D. Thompson and D. Chimenti, editors, *Review of Progress in Quantitative NDE* (Plenum Press, New York, 1996), 169–176.

[80] G. Liu and J. Qu, "Guided Circumferential Waves in a Circular Annulus," Jounral of Applied Mechanics **65**, 424–430 (1998).

[81] M. Kley, C. Valle, L. Jacobs, J. Qu, and J. Jarzynski, "Development of Dispersion Curves for Two-Layered Cylinders using Laser Ultrasonics," The Journal of the Acoustical Society of America **106**, 582–588 (1999).

[82] G. Maze, J. Cheek, X. Li, and Z. Wang, "Coupled Guided Acoustic Modes in Water-Filled Thin-Walled Tubes," The Journal of the Acoustical Society of America **110**, 2295–2300 (2001).

[83] X. Zhao and J. Rose, "Guided Circumferential Shear Horizontal Waves in an Isotropic Hollow Cylinder," The Journal of the Acoustical Society of America **115**, 1912–1916 (2004).

[84] S. Towfighi, T. Kundu, and M. Ehsani, "Elastic Wave Propagation in Circumferential Direction in Anisotropic Cylindrical Curved Plates," Jounral of Applied Mechanics **41**, 283–291 (2002).

[85] S. Towfighi and T. Kundu, "Elastic Wave Propagation in Anisotropic Spherical Curved Plates," International Journal of Solids and Structures **40**, 5496–5510 (2003).

[86] V. Babich and V. Lukyanov, "Wave propagation along a Curved Piezoelectric Layer," Wave Motion **28**, 1–11 (1998).

[87] J. Sharma and V. Pathania, "Generalized Thermoelastic Wave Propagation in Circumferential Direction of Transversely Isotropic Cylindrical Curved Plates," Journal of Sound and Vibration **281**, 1117–1131 (2005).

[88] P. Wilcox, M. Lowe, and P. Cawley, "An EMAT Array for the Rapid Inspection of Large Structures using Guided Waves," in D. Thompson and D. Chimenti, editors, *Review of Progress in Quantitative NDE* (American Institute of Physics, New York, 2003, in press).

[89] G. Alers, "Application of Special Wave Modes to Industrial Inspection Problems," Wave Propagation and Emerging Technologies, ASME **188**, 1–9 (1994).

[90] M. Hirao and H. Ogi, "An SH-Wave EMAT Technique for Gas Pipeline Inspection," NDT&E International **32**, 127–132 (1999).

[91] P. Nagy, M. Blodgett, and M. Golis, "Weep Hole Inspection by Circumferential Creeping Waves," NDT&E Int **27**, 131–142 (1994).

[92] W. Hassan and P. Nagy, "Circumferential Creeping Waves around a Fluid-Filled Cylindrical Cavity in an Elastic Medium," The Journal of the Acoustical Society of America **101**, 2496–2503 (1997).

[93] J. Cheeke, X. Li, and Z. Wang, "Observation of Flexural Lamb Waves (A_0 Mode) on Water-Filled Cylindrical Shells," The Journal of the Acoustical Society of America **104**, 3678–3680 (1998).

[94] Z. Li and Y. Berthelot, "Propagation of Transient Ultrasound in Thick Annular Waveguides: Modeling, Experiments, and Application," NDT&E International **33**, 225–232 (2000).

[95] C. Valle, M. Niethammer, J. Qu, and L. Jacobs, "Crack Characterization using Guided Circumferential Waves," The Journal of the Acoustical Society of America **110**, 1282–1290 (2001).

[96] J. Qu and L. J. Jacobs, "Guided Circumferential Waves and Their Applications in Characterizing Cracks in Annular Components," Materials Evaluation **61**, 85–93 (2003).

[97] X. Chen and M. Wan, "Parameter Measurement of the Cylindrically Curved Thin Layer using Low-Frequency Circumferenctial Lamb Waves," Ultrasonics **43**, 357–364 (2004).

[98] M. Lowe, "Matrix Techniques for Modeling Ultrasonic Waves in Mutilayered Media," IEEE transactions on ultrasonics, ferroelectrics, and frequency control **42**, 525–542 (1995).

[99] M. Abramowitz and I. Stegun, *Handbook of Mathematical Functions - with Formulas, Graphs and Mathematical Tables* (Dover Publications inc., New York, 1970).

[100] G. N. Watson, *A Treatise on the Theory of Bessel Functions* (Cambridge at the University Press, 1952).

[101] J. Fong, M. J. S. Lowe, D. Gridin, and R. V. Craster, "Fast Techniques for Calculating Dispersion Relations of Circumferential Waves in Annular Structures," in D. Thompson and D. Chimenti, editors, *Review of Progress in Quantitative NDE* (American Institute of Physics, 2003), 213–220.

[102] L. Solie and B. Auld, "Elastic Waves in Free Anisotropic Plates," The Journal of the Acoustical Society of America **54**, 50–65 (1973).

[103] W. Press, B. Flannery, S. Teukolsky, and W. Vetterling, *Numerical Recipes in C* (Cambridge University Press, 1987).

[104] E. Kreyszig, *Advanced Engineering Mathematics* (John Wiley + Sons, inc., 1993).

[105] J. Fong and M. J. S. Lowe, "Curvature Effect on the Properties of Guided Waves in Plates," in D. Thompson and D. Chimenti, editors, *Review of Progress in Quantitative NDE* (American Institute of Physics, 2004), 126–133.

[106] J. Dickey and H. Überall, "Whispering Gallery Wave Modes on Elastic Cylinders," The Journal of the Acoustical Society of America **59**, 1339–1346 (1976).

[107] R. Mindlin, "Mathematical Theory of Vibrations of Elastic Plates," in *Proceedings of the 11th Annual Symposium on Frequency Control* (U.S. Army Signal Engineering Laboratories, Fort Monmouth, NJ., 1957), 1–4.

[108] Q. Zhu and W. Mayer, "On the crossing Points of Lamb Wave Velocity Dispersion Curves," The Journal of the Acoustical Society of America **93**, 1893–1895 (1993).

[109] H. Überall, B. Hosten, M. Deschamps, and A. Gerard, "Repulsion of Phase-Velocity Dispersion Curves and the Nature of Plate Vibrations," The Journal of the Acoustical Society of America **96**, 908–917 (1994).

[110] K.-J. Bathe, *Finite Element Procedures in Engineering Analysis* (Prentice-Hall, Englewood Cliffs, New Jersey, 1982).

[111] P. N. Marty, M. J. S. Lowe, and P. Cawley, "Finite Element Predictions of Guided Ultrasonic Wave Fields Generated by Piezoelectric Transducers," in D. Thompson and D. Chimenti, editors, *Review of Progress in Quantitative NDE* (American Institute of Physics, New York, 2001), vol. 20, 829–836.

[112] O. Diligent, T. Grahn, A. Boström, P. Cawley, and M. Lowe, "The Low-Frequency Reflection and Scattering of the S_0 Lamb Mode from a Circular Through-Thickness Hole in a Plate: Finite Element, Analytical and Experimental Studies," The Journal of the Acoustical Society of America **112**, 2589–2601 (2002).

[113] B. Hosten and M. Castings, "Finite Elements Methods for Modeling the Guided Waves Propagation in Structures with Weak Interfaces," The Journal of the Acoustical Society of America **117**, 1108–1132 (2005).

[114] L. Garlic, "Computation of Propagative Waves in Free Rail Using a Finite Element Technique," Journal of Sound and Vibration **185**, 531–543 (1995).

[115] P. Wilcox, M. Evans, O. Diligent, M. Lowe, and P. Cawley, "Dispersion and Excitability of Guided Acoustic Waves in Isotropic Beams with Arbitrary Cross Section," in D. Thompson and D. Chimenti, editors, *Review of Progress in Quantitative NDE* (Plenum Press, New York, 2002), vol. 21, 203–210.

[116] D. Hitchings, "FE77 User Manual," Tech. Rep., Imperial College of Science, Technology and Medicine, London, UK (1994).

[117] L. F. Mondolfo, *Aluminium Alloys: Structures and Properties* (Butterworth, London, 1976).

[118] O. M. Mukdadi, Y. M. Desai, S. K. Datta, A. H. Shah, and A. J. Niklasson, "Elastic Guided Waves in a Layered Plate with Rectangular Cross Section," The Journal of the Acoustical Society of America **112**, 1766–1779 (2002).

[119] Macro Design Ltd., 16 Palewell Park, East Sheen, London SW14 8JG, UK.

[120] P. Fromme, "Defect Detection in Plates using Guided Waves," Ph.D. thesis, ETH Zurich - Swiss Federal Institute of Technology (2001).

[121] D. Gazis and R. D. Mindlin, "Influence of Width on Velocities of Long Waves in Plates," Journal of Applied Mechanics **24**, 541–546 (1957).

[122] D. Alleyne and P. Cawley, "A two-dimensional Fourier transform method for the measurement of propagating multimode signals," The Journal of the Acoustical Society of America **89**, 1159–1168 (1991).

[123] R. Smith, "Stress-Induced Anisotropy in Solids - the Acousto-Elastic Effect," Ultrasonics 135–147 (1963).

[124] F. D. Murnaghan, *Finite Deformation of an Elastic Solid* (Wiley, 1951).

[125] V. Kesava Raju and P. Jayarama Reddy, "Third-Order Elastic Moduli of Polycrystalline Al-Mg and Al-Cu Alloys," Journal of Physics D: Applied Physics **14**, 65–70 (1981).

[126] R. A. Toupin and B. Bernstein, "Sound Waves in Deformed Perfectly Elastic Materials - Acousto-Elastic Effect," The Journal of the Acoustical Society of America **33**, 216 (1961).

[127] J. L. Rousselot, "Comportement Acoustique D'un Tube Cylindrique Mince en Basse fréquence," Acustica **58**, 291–297 (1985).

[128] J. Fong and M. J. S. Lowe, "Leaky Quasi Modes in Curved Plates," in D. Thompson and D. Chimenti, editors, *Review of Progress in Quantitative NDE* (American Institute of Physics, 2005), Submitted in September 2004.

[129] M. Osborne and S. Hart, "Transmission, Reflection, and Guiding of an Exponential Pulse by a Steel Plate in Water 1. Theory," The Journal of the Acoustical Society of America **17** (1945).

[130] A. Bernard, M. Deschamps, and M. Lowe, "Simulation of a Transient Bounded Beam Incident on an Immersed Istropic Plate for the Reconstruction of Lamb Waves Dispersion Curves either in Complex Frequency and Real Slowness or in Real Frequency and Complex Slowness," in D. Thompson and D. Chimenti, editors, *Review of Progress in Quantitative NDE* (Plenum Press, New York, 2001), vol. 20, 73–80.

[131] M. Talmant and G. Quentin, "Backscattering of a Short Ultrasonic Pulse from Thin Cylindrical Shells," Jounral of Applied Physics **63**, 1857–1863 (1988).

[132] J. D. Murphy, E. D. Breitenbach, and H. Überall, "Resonance scattering of Acoustic Waves from Cylindrical Shell," The Journal of the Acoustical Society of America **64**, 677–683 (1978).

[133] E. D. Breitenbach, H. Überall, and K. B. Yoo, "Resonant Acoustic Scattering from Elastic Cylindrical Shells," The Journal of the Acoustical Society of America **74**, 1267–1273 (1983).

[134] R. D. Doolittle and H. Überall, "Sound Scattering by Elastic Cylindrical Shells," The Journal of the Acoustical Society of America **39**, 272–275 (1966).

[135] G. C. Gaunaurd and D. Brill, "Acoustic Spectrogram and Complex-Frequency Poles of a Resonantly Excited Elastic Tube," The Journal of the Acoustical Society of America **75**, 1680–1693 (1984).

[136] M. Talmant, G. Quentin, J. L. Rousselot, J. V. Subrahmanyam, and H. Überall, "Acoustic Resonances of Thin Cylindrical Shells and the Resonance Scattering Theory," The Journal of the Acoustical Society of America **84**, 681–688 (1988).

[137] G. Maze, F. Léon, and H. Überall, "Repulsion Phenomena in the Phase-Velocity Dispersion Curves of Circumferential Waves on Elastic Cylindrical Shells," The Journal of the Acoustical Society of America **105**, 1695–1701 (1999).

[138] X. Bao, K. Raju, and H. Überall, "Circumferential Waves on an Immersed, Fluid-Filled Elastic Cylindrical Shell," The Journal of the Acoustical Society of America **105**, 2704–2709 (1990).

[139] A. C. Ahyi, P. Pernod, O. Gatti, V. Latard, A. Merlen, and H. Überall, "Experimental Demonstration of the pseudo-Rayleigh (A_0) Wave," The Journal of the Acoustical Society of America **104**, 2727–2732 (1998).

[140] G. V. Frisk, J. W. Dickey, and H. Überall, "Surface Wave Modes on Elastic Cylinders," The Journal of the Acoustical Society of America **58**, 996–1008 (1975).

[141] G. V. Frisk and H. Überall, "Creeping Waves and Lateral Waves in Acoustic Scattering by Large Elastic Cylinders," The Journal of the Acoustical Society of America **59**, 46–54 (1976).

[142] R. E. Bunney, R. R. Goodman, and S. W. Marshall, "Rayleigh and Lamb Waves on Cylinders," The Journal of the Acoustical Society of America **46**, 1223–1233 (1969).

[143] W. Hassan and P. Nagy, "On the Anomalously Low Attenuation of the Leaky Rayleigh Wave in a Fluid-Filled Cylindrical Cavity," The Journal of the Acoustical Society of America **104**, 1246–1255 (1998).

[144] R. E. Langer, "On the Asymptotic Solutions of Differential Equations, with an Application to the Bessel Functions of Large Complex Order," Transactions of the American Mathematical Society **34**, 447–479 (1932).

[145] V. S. Sastry, "Algorithms for the Computation of Hankel Functions of Complex Order," Numerical Algorithms **5**, 621–628 (1993).

[146] M. Kodama, "Numerical Calculation of the Bessel Function of Complex Order using the Recurrence Method," IEICE Trans. Fundamental **E78-A**, 506–516 (1995).

[147] I. Thompson and A. R. Barnett, "Coulomb and Bessel Functions of Complex Arguments and Order," Jounral of Computational Physics **64**, 490–509 (1986).

[148] B. Pavlakovic, M. Lowe, D. Alleyne, and P. Cawley, "DISPERSE: A General Purpose Program for Creating Dispersion Curves," in D. Thompson and D. Chimenti, editors, *Review of Progress in Quantitative NDE* (Plenum Press, New York, 1997), vol. 16, 185–192.

[149] W. Franz, "Über die Greeschen Funktionen des Zylinders Und der Kugel," Zeits. Naturforsch. **9a**, 705–716 (1954).

[150] J. Rose, *Ultrasonic Waves in Solid Media* (Cambridge University Press, 1999).

[151] B. Engquist and A. Majda, "Absorbing Boundary Conditions for the Numerical Simulation of Waves," Mathematics of Computation **31**, 629–651 (1977).

List of Publications

D. Gridin, R.V. Craster, J. Fong, M.J.S. Lowe and M. Beard, "The high-frequency asymptotic analysis of guided waves in a circular elastic annulus", Wave Motion **38**, 67-90 (2003).

J. Fong, M.J.S. Lowe, D. Gridin, R.V. Craster, "Fast techniques for calculating dispersion relations of circumferential waves in annular structures", in D. Thompson and D. Chimenti, editors, Review of Progress in Quantitative NDE (American Institute of Physics),**22**, 213-220 (2003).

J. Fong, M.J.S. Lowe, "Curvature effect on the properties of guided waves in plates", in D. Thompson and D. Chimenti, editors, Review of Progress in Quantitative NDE (American Institute of Physics), **23**, 126-133 (2004).

J.Fong, M.J.S. Lowe, "Leaky quasi modes in curved plates", in D. Thompson and D. Chimenti, editors, Review of Progress in Quantitative NDE (American Institute of Physics), in print (2005).

J.Fong, M.J.S. Lowe, "A Study of the effect of plate curvature on the properties of Lamb waves", in preparation.

J.Fong, M.J.S. Lowe, "Leaky circumferential waves: theory and experiment", in preparation.